ISSN 2408-2384 (ONLINE)

Environment and Natural Resources Journal

Volume 23 Number 1 January -February 2025

View of Kumana National Park from the Bambaragasthalawa rocky mountain. Tropical dry mixed evergreen forest habitats with rocky clusters are clearly visible

Source: Rodrigo P, Gunathilaka C, Jayasekara D, Mahaulpatha D. Habitat categorization and vegetation mapping of Kumana National Park, Sri Lanka. Page 525-534.

Environment and Natural Resources Journal (EnNRJ)
Volume 23, Number 1, January - February 2025 ISSN: 2408-2384 (Online)

AIMS AND SCOPE

The Environment and Natural Resources Journal is a peer-reviewed journal, which provides insight scientific knowledge into the diverse dimensions of integrated environmental and natural resource management. The journal aims to provide a platform for exchange and distribution of the knowledge and cutting-edge research in the fields of environmental science and natural resource management to academicians, scientists and researchers. The journal accepts a varied array of manuscripts on all aspects of environmental science and natural resource management. The journal scope covers the integration of multidisciplinary sciences for prevention, control, treatment, environmental clean-up and restoration. The study of the existing or emerging problems of environment and natural resources in the region of Southeast Asia and the creation of novel knowledge and/or recommendations of mitigation measures for sustainable development policies are emphasized.

The subject areas are diverse, but specific topics of interest include:

- Biodiversity
- Climate change
- Detection and monitoring of polluted sources e.g., industry, mining
- Disaster e.g., forest fire, flooding, earthquake, tsunami, or tidal wave
- Ecological/Environmental modelling
- Emerging contaminants/hazardous wastes investigation and remediation
- Environmental dynamics e.g., coastal erosion, sea level rise
- Environmental assessment tools, policy and management e.g., GIS, remote sensing, Environmental Management System (EMS)
- Environmental pollution and other novel solutions to pollution
- Remediation technology of contaminated environments
- Transboundary pollution
- Waste and wastewater treatments and disposal technology

Schedule

Environment and Natural Resources Journal (EnNRJ) is published 6 issues per year in January-February, March-April, May-June, July-August, September-October, and November-December.

Publication Fees

An article publication fee in the Environment and Natural Resources Journal is set at a rate of 250 USD per article, payable after the final acceptance of the manuscript.

Ethics in publishing

EnNRJ follows closely a set of guidelines and recommendations published by Committee on Publication Ethics (COPE).

Environment and Natural Resources Journal (EnNRJ)

Volume 23, Number 1, January - February 2025 ISSN: 2408-2384 (Online)

Editorial Office Address
Research and Academic Service, Research Management Unit,
Faculty of Environment and Resource Studies, Mahidol University
999, Phutthamonthon Sai 4 Road, Salaya, Phutthamonthon, Nakhon Pathom, Thailand, 73170
Phone +662 441 5000 ext. 2108
Website: https://ph02.tci-thaijo.org/index.php/ennrj/index
E-mail: ennrjournal@gmail.com

Environment and Natural Resources Journal (EnNRJ)

Volume 23, Number 1, January - February 2025 ISSN: 2408-2384 (Online)

CONTENT

Environment and Natural Resources Journal

Volume 23
Issue 1
2025

Mapping Subsurface and Surface Characteristics of the Recent Pesanggrahan Landslide, Central Java, Indonesia, for Landslide Hazard Management

Anastasia Neni Candra Purnamasari[1,2], Eddy Hartantyo[3*], Junun Sartohadi[4,5], and Hazqial Hafazhah[3]

[1]*Department of Environmental Sciences, Graduate School, Universitas Gadjah Mada, Indonesia*
[2]*Faculty of Engineering, Universitas Proklamasi 45, Indonesia*
[3]*Department of Physics, Faculty of Natural Sciences, Universitas Gadjah Mada, Indonesia*
[4]*Department of Soil, Faculty of Agriculture, Universitas Gadjah Mada, Indonesia*
[5]*Research Center for Land Resources Management, Universitas Gadjah Mada, Indonesia*

ARTICLE INFO

Received: 5 Jun 2024
Received in revised: 4 Nov 2024
Accepted: 16 Nov 2024
Published online: 3 Dec 2024
DOI: 10.32526/ennrj/23/20240163

Keywords:
Thick materials/ Material layers/ Landslide/ Seismic refraction/ Geotechnical assessment

*** Corresponding author:**
E-mail: hartantyo@ugm.ac.id

ABSTRACT

Regions prone to deep landslides are characterized by thick materials exceeding 10 m and frequent natural disasters. This research aims to analyze the recent occurrence of Pesanggrahan landslide in Central Java, Indonesia, which is a region consisting of both settlements and rice fields. Surface mapping was conducted using aerial photos and direct field observations. Additionally, subsurface conditions to identify the unconsolidated material layers below the landslide surface have been analyzed using the seismic refraction method. The primary velocity (Vp) values are represented in 2D subsurface cross sections. Differences in Vp values corresponded to different geological layers. There were four distinct layers: Top Soil (TS), Clay (CL), Weathered Bedrock (WB), and Tuff Breccia (TB) within the 2D seismic refraction cross-section with Vp values ranging from 150 to 1,800 m/s. The ranges of Vp are: 150-600 m/s for Top Soil (TS), 600-1,200 m/s for Clay (CL), 1,200-1,800 m/s for Weathered Bedrock (WB), and values exceeding 1,800 m/s for Tuff Breccia (TB). The material layer is critical for sustainable land management strategies aimed to control landslides. Furthermore, the potential depth of the sliding plane was managed through effective environmental management practices, including proper disposal of household waste and minimizing the cutting of steep slopes.

1. INTRODUCTION

Landslide is a natural disaster that often occurs in Indonesia (Ariyanto et al., 2019; Usman et al., 2020; Sadisun et al., 2021), comprising several types based on mass movement and direction of materials such as rock, earth or debris down a slope (Lee and Jones, 2004). This natural disaster is also divided into shallow and deep landslides, depending on the thickness of the material (Pratiwi et al., 2019). However, the research location characterized by the appearance of an outcrop with a material thickness greater than 10 m tend to encounter deep landslide. Residents at the base have diverse agricultural lands covered by the extremely thick material from the natural disaster. Although it remains in the transition zone, the materials mainly possesses Clay (CL) texture (Pulungan and Sartohadi, 2017; Sartohadi et al., 2018; Noviyanto et al., 2020). Therefore, to properly assess the impact of lanslide, it is crucial to identify and understand the thickness of the materials.

In landslide environment, both surface and subsurface components can be investigated and identified by testing soil samples or mapping for risk disaster with Geographic Information System (GIS)

Citation: Purnamasari ANC, Hartantyo E, Sartohadi J, Hafazhah H. Mapping subsurface and surface characteristics of the recent Pesanggrahan Landslide, Central Java, Indonesia, for landslide hazard management. Environ. Nat. Resour. J. 2025;23(1):1-13. (https://doi.org/10.32526/ennrj/23/20240163)

(Iscan and Guler, 2021; Budha et al., 2020; Ming and Zawawi, 2021; Putra et al., 2021; Thongley and Vansarochana, 2021; Intarat et al., 2024), and the use of geophysical methods, respectively (Sana et al., 2021; Galone et al., 2024; Jin et al., 2024). In addition, the methods often used to identify subsurface layers include geoelectric (electrical resistivity tomography/ERT), seismic refraction tomography (SRT), and multichannel analysis surface wave (MASW) (Zainal et al., 2021; Amanatidou et al., 2022; Butchibabu et al., 2023; Karaaslan et al., 2023). Seismic refraction can be used to identify geological faults and fractures beneath the surface (Sichugova and Fazilova, 2024). Subsurface mapping in the form of cross-sections showing the layers is often used in environmental applications. Asides from landslide, it can also be used for mining and petroleum geology analyses (Jaysaval et al., 2021; Punzo et al., 2021; Rahimi et al., 2021), resulting in the generation of both 2D and 3D visualizations of subsurface cross-sectional results (Imani et al., 2021b; Sana et al., 2021; Whiteley et al., 2021).

This present research used seismic refraction to obtain a cross-section of the surface beneath landslide. According to Telford et al. (1990), and Reynolds (1997), the waves in various soil or rock layers with varying densities were refracted. Meanwhile, dissimilarities in the density of material layers tend to show differences in Vp values. Preliminary research used seismic refraction method to determine subsurface characteristics of landslide and the volume of materials (Samyn et al., 2012; Whiteley et al., 2020; Imani et al., 2021a).

The occurrence of landslide posed potential risk to the surrounding environment, caused by the unconsolidated super thick materials. Therefore, the current research focused on the layers, which tended to transition into slip areas, considered a major cause of landslide.

The subsurface cross-section was interpreted into multiple strata connected to geological and geomorphological data, through direct field observations and information from prior research. Layer interpretation was used to determine the characteristics of landslide materials, while differentiating Vp values from the results of seismic refraction measurement helped to identify the properties of diverse material layers. Furthermore, landslide was controlled through sustainable land management based on the properties of the materials.

2. METHODOLOGY

Surveys were carried out to determine the research location and geophysical measurement trajectories. Furthermore, three geophysical trajectories were determined after conducting direct field observations. Measuring the length of a possible path in landslide depended on whether the surface had undulations.

Direct field observations were carried out to obtain geomorphological and geological data to support seismic refraction interpretation. The outcrops or open material were carefully analyzed to obtain the actual appearance of the layer beneath the surface. These were found under large landslide and in several other parts.

Surface mapping was carried out using aerial photography taken above Pesanggrahan landslide with DJI Phantom. This landslide is located in Bogowonto watershed, with Sumbing Volcano situated upstream. Meanwhile, the surface morphology around Bogowonto watershed was characterized by several thick deposits of material and erosion (Maulana et al., 2023), leading to frequent landslide in Ngasinan research location. Direct field observations carried out in Ngasinan showed many creeps, dormants and landslide outcrops. Furthermore, super thick soil material was observed in this transition area, impacted by tertiary and quarter zones (Pulungan and Sartohadi, 2017; Pulungan and Sartohadi, 2018; Sartohadi et al., 2018; Prayitno et al., 2019). Thick layered soil properties were produced due to the formation of materials from many geological periods and sources.

Landslide outcrops, including those influenced by human activities such as cutting hillsides, showed layers of extremely thick soil material. Furthermore, layers originating from volcanic eruption deposits of Sumbing and weathering of parent rock have different characteristics. Figure 1 shows the exact location of landslide outcrops, in Bogowonto Watershed Basin in Ngasinan Village.

Seismic refraction is a geophysical method that can be used to determine differences in deeper layers. The principle of this method depends on the propagation of refracted seismic waves at the boundary of the layer, thereby depicting the difference in primary velocity (Vp) (Reynolds, 1997). Additionally, seismic refraction was obtained using the Snell's law formula in equation (1) (Telford et al., 1990).

$$\frac{\sin\theta_1}{V_1} = \frac{\sin\theta_2}{V_2} = p \quad (1)$$

The quantity p is called the raypath parameter.

Seismic refraction method was used to describe subsurface conditions in accordance with the Vp model. However, in the case of landslide, the existence of field boundaries was identified through the contrast in Vp between the solid and weathered material.

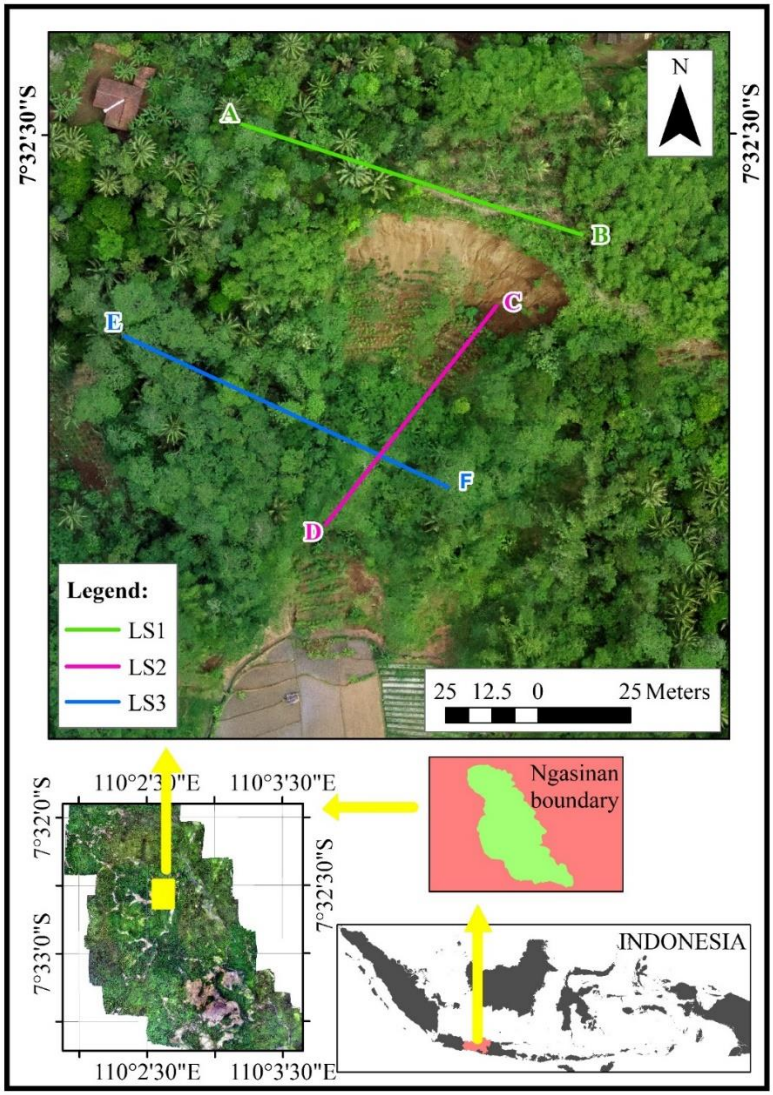

Figure 1. Research location and seismic refraction trajectory in the landslide area

Seismic refraction was measured using three trajectories in the landslide area. The first trajectory LS1 was positioned at the crown of the landslide, tending towards the West-East. The second trajectory LS2 was positioned on the body, heading North-South, in the same direction as the landslide movement. While, the third trajectory LS3 was positioned at the foot of landslide tending towards West-East. Detailed seismic refraction measurement parameters are shown in Table 1. Additionally, field acquisition activities in Figure 2 show seismic trajectory and the tool used, namely Doremi 24 channels.

Table 1. Seismic refraction measurement parameters

Trajectory	Length (m)	Interval (m)	Shot number	Geophone number	Record time (s)	Sampling rate (Hz)
LS1 (AB)	98.5	4.5	5	22	0.25	5,000
LS2 (CD)	76.5	3.5	5	22	0.25	5,000
LS3 (EF)	98.5	4.5	5	22	0.25	5,000

(a) (b)

Figure 2. Seismic refraction measurement: (a) one of seismic trajectories, and (b) measurement tools Doremi 24 channels

Seismic refraction data processing flowchart and method are shown in Figures 3 and 4. In addition, three seismic trajectories produced a 2D cross-section of Vp values. Data was processed with Seisimager package software, comprising Pickwin and Plotrefa programs (Figure 4). The main task of the Pickwin program is to pick the first arrival time, including editing the geometry, and turning off bad traces. The picked data is saved and opened in the Plotrefa program, where the T-X curve tends to be displayed (Figure 3). Furthermore, data quality control was performed by editing the position of the picking point to comply with the rules of refraction. Elevation data were inputted in this program, whose main task was to perform tomographic inversion. In this research, an initial model of 10 layers, maximum depth of 30 m, and five iterations served as the parameters of the inversion process.

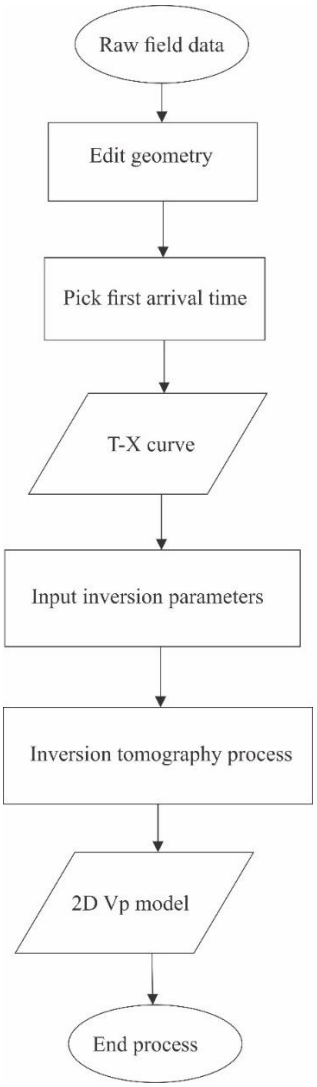

Figure 3. Flowchart of seismic refraction data processing

3. RESULTS AND DISCUSSION

3.1 Material layers interpretation

Seismic refraction measurements were used to generate 2D cross-sectional Vp values from the subsurface of the Pesanggrahan landslide. Layered variations in Vp values were shown in 2D cross-section, depicting various material deposit layers, as proven by the results of the inversion in Figure 5. Seismic refraction data on 2D cross-section of LS1, LS2, and LS3 trajectories suggested that each had a depth of approximately 25 to 30 m.

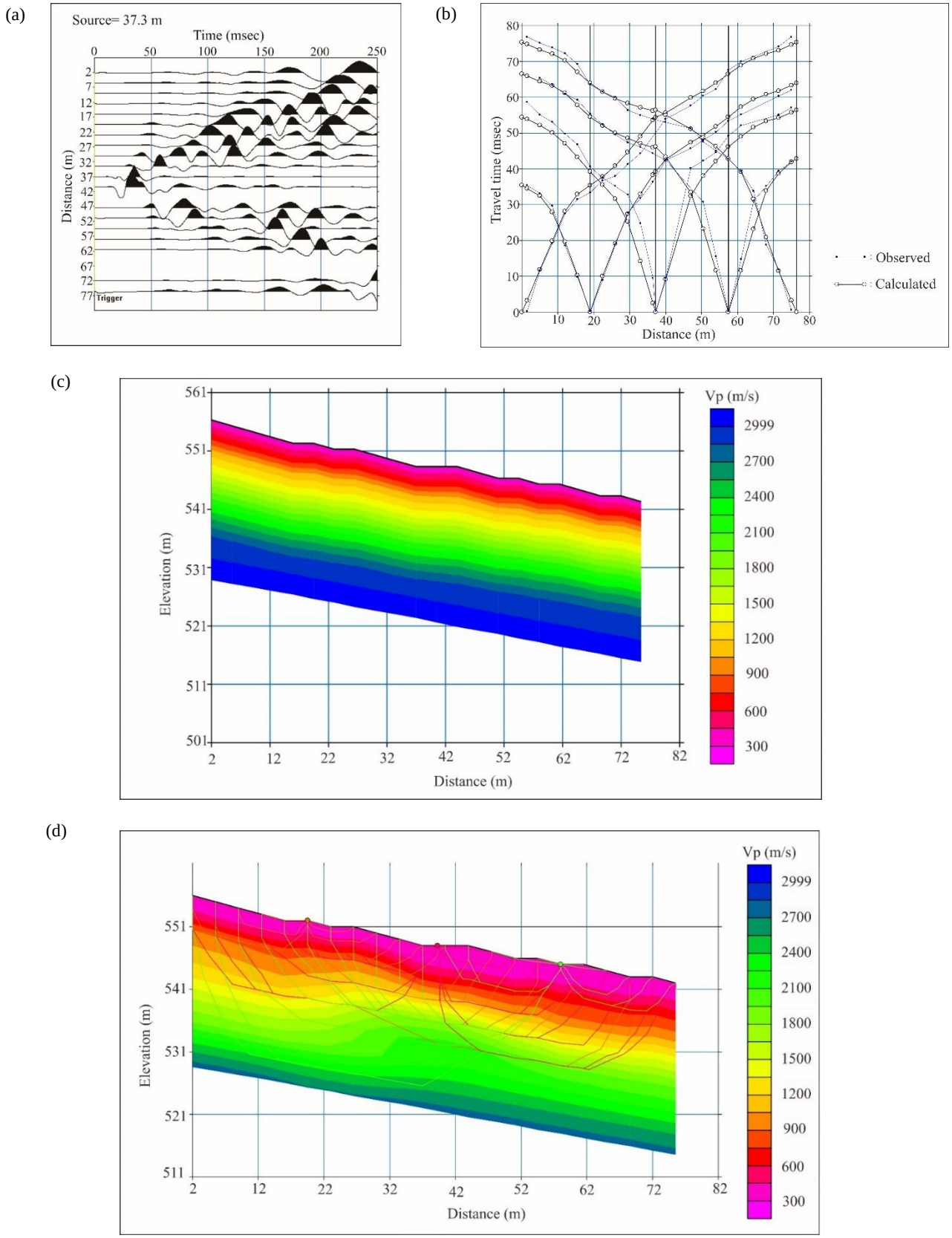

Figure 4. Seismic data processing: (a) raw data, (b) traveltime graphic, (c) initial model, and (d) inversion result

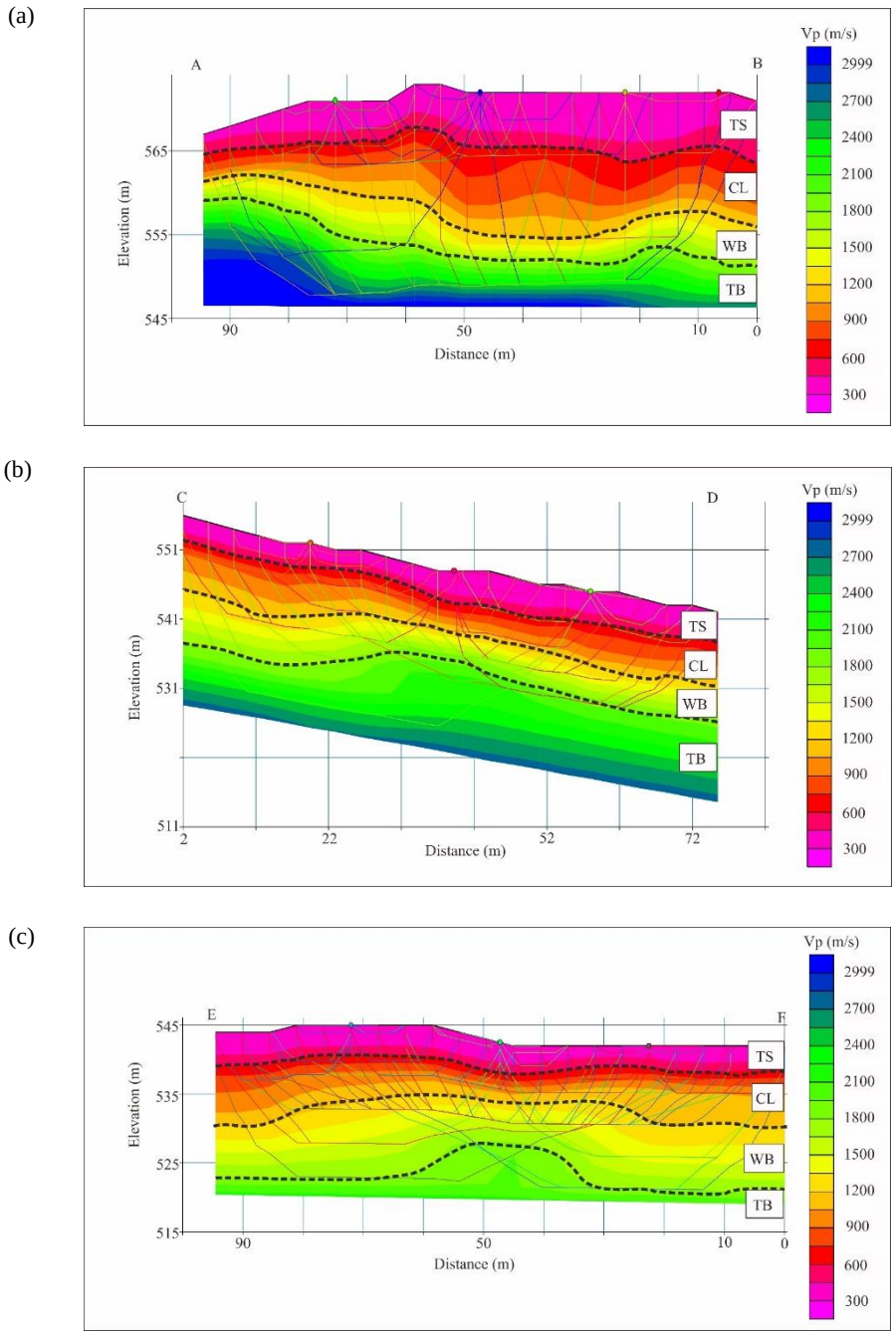

Figure 5. Inversion results: (a) LS1, (b) LS2, and (c) LS3 trajectories

2D seismic refraction sections obtained Vp values between 150 m/s and 2,999 m/s. Patanduk (2020), conducted a research on the transition zone, and reported that Vp within the range of 200 and 700 m/s were categorized as Top Soil (TS), while values between 700 and 1,000 m/s, 1,000 and 1,800 m/s, and greater than 1,800 m/s were referred to as CL, Weathered Bedrock (WB), and Tuff Breccia (TB), respectively. In accordance with previous research (Patanduk, 2020) and direct geomorphological observations conducted in the field, the interpreted seismic section contained four large layers. TS constituted the top layer, followed by CL, WB, and TB with Vp values within the range of 150 to 600 m/s, 600 to 1,200 m/s, 1,200 to 1,800 m/s, and greater than 1,800 m/s, respectively.

Direct field observation led to the discovery of WB outcrop at the foot of landslide, characterized by soft hardness, mixed lump structure, and red appearance. WB originated from breccia material altered as a result of weathering. Figure 6 shows WB outcrop at the foot of a landslide, approximately 20 m below LS3 trajectory. When viewed from an elevated position, WB outcrop was approximately 50 m below

LS1 track. This direct observation data strengthened the interpretation of 2D seismic refraction layer.

Although landslide has not yet covered TB outcrop, this structure was discovered in nearby areas. TB outcrop has an elevation of 517 m, implying that the interpretation of 2D seismic refraction section was correct because TB was below WB layer. Furthermore, TB outcrop was characterized by a grayish-white color, sand-border texture and softness, with the location shown in Figure 7.

TS, CL, WB, and TB layers were depicted in the interpretation of 2D seismic refraction cross-section. Each of the four layers had a different thickness, for example TS, CL, WB, and TB ranged from 2 to 8 m, 3 to 10 m, 2 to 12 m and greater than 15 m. Sequentially, each layer had a depth surface of 0-5 m, 5-15 m, 15-20 m and greater than 20 m. Table 2 shows the layers derived from seismic refraction findings and direct field observations.

The loose uppermost layer, TS was found on both the surface and crown of landslide, covered with many types of plants. CL layer was characterized by CL texture based on the outcrops surrounding landslide. Meanwhile, the red WB layer is loose, having a similar appearance to the outcrop in Figure 6. This layer is formed from a combination of previously occurring landslide material and weathering of subsurface rock. TB layer contains material impacted by volcanic eruptions (tuff), including rock deposit from pre-existing outcrops as shown in Figure 7. The prior material was moved and deposited by river currents, forming breccia rock units. Furthermore, WB and TB layers were characterized by the CL texture and ability to hold large quantity of water when tested. This implied that the material had weathered, proven by the altered physical and chemical qualities.

Table 2. Super thick material layers in deep landslide

Layer	Depth (m)	Vp (m/s)	Thickness (m)
TS	0-5	150-600	2-8
CL	5-15	600-1,200	3-10
WB	15-20	1,200-1,800	2-12
TB	>20	>1,800	>15

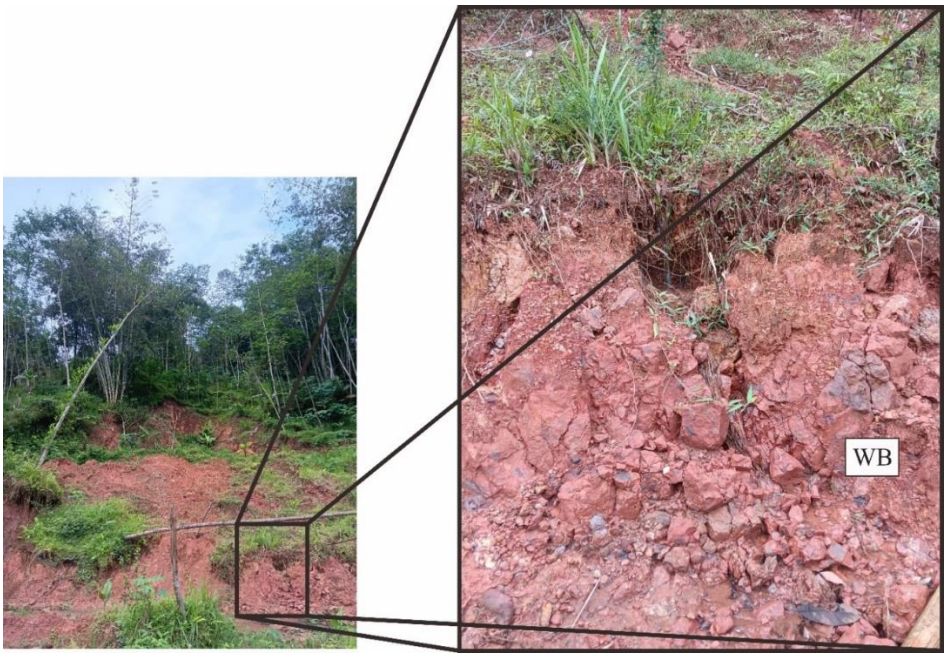

Figure 6. WB at the foot of landslide

In geology, weathered or altered material is related to hydrothermal variations around volcanoes (Kereszturi et al., 2021; Douglas et al., 2022; Kanakiya et al., 2022; Heap et al., 2023). The altered material was produced as a result of magma activity, generating heat beneath the surface. However, this volcanic activity occurred earlier leading to the formation of younger eruption strata (Sambodo and Arpornthip, 2021). Material from several eras formed layers that were deposited into super thick material, such as at the research location.

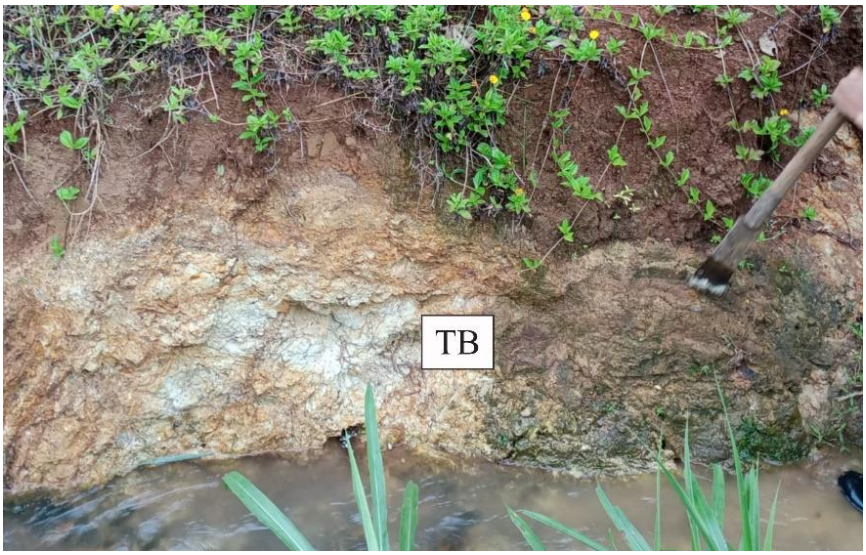

Figure 7. TB in Ngasinan research area

The distinct properties of the layers make thick materials prone to landslide. However, the susceptibility to this natural disaster was controlled by the thickness, and characteristics of the material, including varying physical and chemical contents. Texture is a physical quality, as well as fissures and the loose materials found at the research location (Teh et al., 2023). The chemical features include the mineralogical content influenced by the rapid occurrence of the weathering process (Pandarinath, 2022). Furthermore, the altered material contains CL minerals namely smectite, illite, quartz, etc (Weisenberger et al., 2020; González-Partida et al., 2022), leading to the formation of a pseudo-sliding plane. The characteristics of a super thick material layer that can form a pseudo-sliding plane include CL texture, high CEC value, easy absorption of water and low resistivity value (Purnamasari et al., 2024).

A specific finding of this research is the identification of layers in unconsolidated super thick material. The finding differs from previous recent investigations that adopted seismic refraction methods. Table 3 shows the differences between the present findings and past research. Meanwhile, layers of super thick material interpreted in detail at deep landslide locations are critical for environmental management. The combination of subsurface, and surface mapping, as well as direct field observation is a research method that integrates numerous scientific disciplines.

Table 3. Previous research that used seismic refraction method

Tittle	Research result
Engineering geotechnical evaluation of soil for foundation purposes using shallow seismic refraction and MASW in 15th Mayo, Egypt.	Subsurface mapping with massive materials for building construction (Mohammed et al., 2020).
Landslide monitoring using seismic refraction tomography - The importance of incorporating topographic variations.	Determination of the near-surface soil layer below landslide with a thin soft layer (Whiteley et al., 2020).
Electrical resistivity and refraction seismic tomography in the detection of near-surface Qadimah Fault in Thuwal-Rabigh area, Saudi Arabia.	Subsurface identification of structures such as faults (AlQahtani et al., 2021).
Determination of Weathered Layer Thickness Around the Landslide Zone using Seismic Refraction Method.	The refraction method used was simple, only two layers were obtained, namely weathered and massive (Hadi et al., 2021).
Application of combined electrical resistivity tomography (ERT) and seismic refraction tomography (SRT) methods to investigate Xiaoshan District landslide site Hangzhou, China.	The slip interpretation of landslide area with contact boundary characterized by clearly thin weathered material (Imani et al., 2021b).

Table 3. Previous research that used seismic refraction method (cont.)

Tittle	Research result
Assessment of spatiotemporal changes in water contents of landslide zone by geophysical methods: a case study.	Integration of geological and geophysical data to determine water content under landslide (Imani et al., 2021a).
Characteristics and rippability conditions of near-surface lithologic units (Penang Island, Malaysia) derived from multimethod geotomographic and geostatistics models.	Subsurface ground water and infrastructure (Akingboye and Bery, 2022).
Hydromechanical assessment of a complex landslide through geophysics and numerical modeling toward an upgrade for the Villerville landslide (Normandy, France).	Identify the subsurface geology of landslide on a large scale enabling the visibility of the structural extent (Thirard et al., 2022).
Integrated analysis of geophysical methods for slope failure characterization.	Geophysical method for measuring the subsurface characterized by the massive nature, creep landslide type, and rock borders found in the research area (Zakaria et al., 2022).
Identification of surface layer structure using seismic refraction for landslide reduction in Tandikek region, West Sumatra Indonesia.	The simple seismic method was used to obtain two layers with clear boundaries between the weathered and massive layers (Draini et al., 2023).
Integrated geophysics for investigation of landslide-affected site located near Alemketema Town, Central Ethiopia.	Large-scale subsurface mapping showed massive rock layers (Genetu and Mewa, 2023).
Landslide assessment through integrated geoelectrical and seismic methods a case study in Thungsong Site, Southern Thailand.	Subsurface mapping of landslide area containing massive material, distinguished by three layers with thin weathered material, in addition, sandstone was found at a depth of less than 5 m (Sujitapan et al., 2024).

3.2 Hazard environment management

Data on thickness and depth of subsurface layers are useful for managing the environment around the landslide. Different Vp values representing material density were found in layers determined by seismic refraction measurements. This parameter is related to porosity, which was used to determine whether fluids such as water could easily pass through the material (Schaetzl and Anderson, 2005). Additionally, porosity is also associated with the vegetation on the surface (Birkeland, 1984), including the type of roots, as well as the appropriateness to the properties of the deposited material (Purwaningsih et al., 2020). Direct field observations showed that the vegetation type commonly found around landslide was characterized by tap roots and fibers. Therefore, the reinforcement of soil by roots is a complex synergy of root-soil me- chanical properties, and morphology, including plant-induced alterations, leading to a considerable enhancement in slope stability (Lann et al., 2024).

Direct field observations were also used to identify the environment around landslide. Based on Figure 8, the area surrounding landslide was characterized by mixed vegetation, rice fields, and settlements, found in elevated position above landslide. Meanwhile, the rice fields were located below the landslide (Figure 8). Settlements, rice fields and mixed vegetation exposed lands to this natural disaster.

Some causes of landslide are sedimentary material characterized by low density (not massive), thick material deposits, sliding plane, varying surface undulations that tend to be steep and high rainfall (Jäger et al., 2013; Chae et al., 2017; Abdullah et al., 2020). Furthermore, the rainfall were projected and used to evaluate subsequent alterations in landslide susceptibility, and the frequency of these events exceeded the empirical thresholds (Lin et al., 2022). The sliding plane was identified based on the layers resulting from the interpretation of geophysical measurements. The morphology was determined by directly observing the location of settlements and rice fields on undulating land.

Based on this perspective, an increase in population growth, enlarges the settlement area. Furthermore, the surrounding area of landslide tends to be affected by the increasing quantity of settlements. Land used as settlement may be vulnerable or have an impact on existing landslide (Servanzi et al., 2023). The material deposits underneath will also be affected by water from household waste. When this wastewater directly enters the sedimented material or soil, it tend to hinder vegetation growth. Many fruit plants with mixed vegetation in Ngasinan do not bear fruit even though the plants are healthy, due to the inappropriate chemical content of the soil (Birkeland, 1984). In addition, non-fruiting of local vegetation has an economic impact on the community.

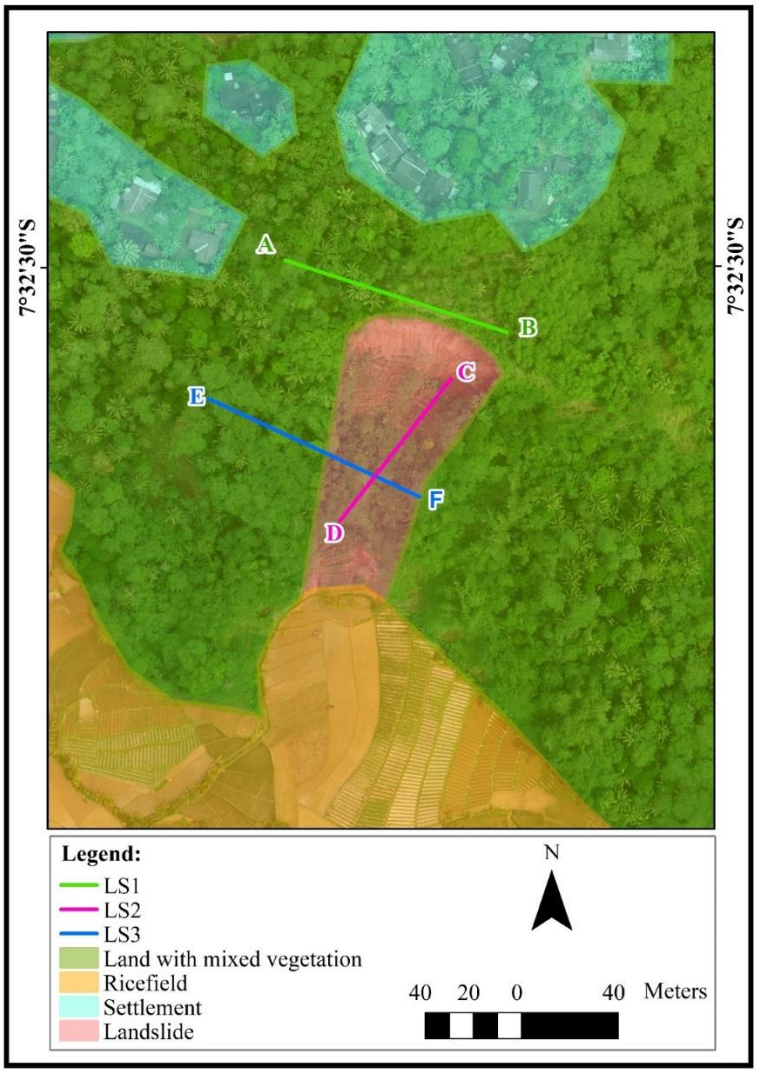

Figure 8. The surrounding environment of landslide

Landslide risk reduction depends on the perceptions of local communities in the affected areas, which is closely associated with the economic and social conditions (Qasim et al., 2018). Ngasinan people were unable to understand the geomorphological or subsurface conditions of the region. It is necessary to provide advice regarding proper land management to reduce or control the impact of landslide. Pipes or similar instruments must be used to convey the management of domestic waste flows. Furthermore, waste management needs to be carried out to prevent garbage from entering the soil or material deposits directly. Appropriate land management on slopes prone to landslide also needs to be conveyed to Ngasinan community, specifically those whose homes are located in landslide-prone locations. Land management can be started by planting vegetation that suits the characteristics of the subsurface material, and cuts on steep slopes also need to be minimized. Appropriate land use such as afforestation, reforestation, and proper agricultural practices can help stabilize slopes, reducing the risk of landslide (Poddar and Roy, 2024). Therefore, comprehending the connection between land use and land cover alterations, as well as the vulnerability to landslide is crucial in managing the risk of this disaster in mountainous regions (Poddar and Roy, 2024).

4. CONCLUSION

In conclusion, seismic refraction data were used to identify subsurface layers that extend to a depth of approximately 25 to 30 m. Layers with varying Vp values were observed in 2D seismic refraction section showing dissimilar material layering. TS, CL, WB, and TB constituted the four major layers, arranged from top to bottom (surface). TS, CL, WB, and TB layers had Vp values in the range of 150-600 m/s, 600-1,200 m/s, 1,200-1,800 m/s, and greater than

1,800 m/s, respectively. Landslide minimization or the investigation of control methods was enhanced by the subsurface interpretation of seismic data. The selection of appropriate vegetation, an environmental management method helped prevent landslide. Determining the type of vegetation also required data on the characteristics, both physical and chemical properties of soil. Managing household waste and reducing the cutting of steep slopes should be performed to reduce the risk of landslides. The results proved effective for future research on landslide minimization applications. Additionally, the layering and thickness of the material could serve as a reference. In future research, ERT and other geophysics method should be used on all trajectories.

ACKNOWLEDGEMENTS

The authors are grateful to the Center for Higher Education Funding (BPPT), Faculty of Math and Nat Sciences Grant 2023 and Indonesia Endowment Funds for Education (LPDP) for the funding provided. This research is part of a dissertation entitled Environmental Geopedophysics Studies in Landslide Areas around Ngasinan Village, Purworejo, Central Java.

REFERENCES

Abdullah NH, Mohamed JIB, Awang H. Geophysical method exploration for slope failure investigation. IOP Conference Series: Materials Science and Engineering 2020;917(1):1-11.

Akingboye AS, Bery AA. Characteristics and rippability conditions of near-surface lithologic units (Penang Island, Malaysia) derived from multimethod geotomographic models and geostatistics. Journal of Applied Geophysics 2022; 204:Article No. 104723.

AlQahtani HH, Fnais MS, Almadani SA, Alhumimidi MS, Abdelrahman K. Electrical resistivity and refraction seismic tomography in the detection of near-surface Qadimah Fault in Thuwal-Rabigh Area, Saudi Arabia. Arabian Journal of Geosciences 2021;14(12):Article No. 1153.

Amanatidou E, Vargemezis G, Tsourlos P. Combined application of seismic and electrical geophysical methods for karst cavities detection: A case study at the campus of the new University of Western Macedonia, Kozani, Greece. Journal of Applied Geophysics 2022;196:Article No. 104499.

Ariyanto SV, Zuhri MD, Kasanova R, Darmawan I, Hari NH. Investigation of landslide zones with geoelectric methods for disaster mitigation in Pamekasan. IOP Conference Series: Earth and Environmental Science 2019;243(1):1-9.

Birkeland PW. Soils and Geomorphology. Vol. 122, Geological Magazine. New York: Oxford University Press; 1984. p. 372.

Budha PB, Rai P, Katel P, Khadka A. Landslide hazard mapping in panchase mountain of central Nepal. Environment and Natural Resources Journal 2020;18(4):387-99.

Butchibabu B, Jha PC, Sandeep N, Sivaram YV. Seismic refraction tomography using underwater and land based seismic data for evaluation of foundation of civil structures. Journal of Applied Geophysics 2023;210:Article No. 104934.

Chae BG, Park HJ, Catani F, Simoni A, Berti M. Landslide prediction, monitoring and early warning: A concise review of state-of-the-art. Geosciences Journal 2017;21(6):1033-70.

Draini DP, Syafriani, Akmam, Dwiridal L. Identification of surface layer structure using seismic refraction for landslide mitigation in Tandikek region, West Sumatra Indonesia. IOP Conference Series: Earth and Environmental Science 2023;1228(1):1-12.

Douglas A, Kereszturi G, Schaefer LN, Kennedy B. Rock alteration mapping in and around fossil shallow intrusions at Mt. Ruapehu New Zealand with laboratory and aerial hyperspectral imaging. Journal of Volcanology and Geothermal Research 2022;432:Article No. 107700.

Galone L, Villani F, Colica E, Pistillo D, Baccheschi P, Panzera F, et al. Integrating near-surface geophysical methods and remote sensing techniques for reconstructing fault-bounded valleys (Mellieha valley, Malta). Tectonophysics 2024;875:Article No. 230263.

Genetu M, Mewa G. Integrated geophysics for investigation of landslide-affected site located near to Alemketema town, Central Ethiopia. Journal of Applied Geophysics 2023; 216:Article No. 105162.

González-Partida E, Camprubí A, López-Hernández A, Santoyo E, Izquierdo-Montalvo G, Pandarinath K, et al. Distribution of hypogene alteration and fluid evolution in the Los Humeros Geothermal Field (Puebla, Mexico): Multiple sourced fluids, interrelations, and processes in a superhot system. Applied Geochemistry 2022;136:Article No. 105159.

Hadi AI, Brotopuspito KS, Pramumijoyo S, Hardiyatmo HC. Determination of weathered layer thickness around the landslide zone using the seismic refraction method. IOP Conference Series: Earth and Environmental Science 2021;830(1):1-12.

Heap MJ, Wadsworth FB, Jessop DE. The thermal conductivity of unlithified granular volcanic materials: The influence of hydrothermal alteration and degree of water saturation. Journal of Volcanology and Geothermal Research 2023;435:Article No. 107775.

Imani P, Tian G, EL-Raouf AA. Assessment of spatiotemporal changes in water contents of landslide zone by geophysical methods: A case study. Arabian Journal of Geosciences 2021a;14(14) :Article No. 1380.

Imani P, Tian G, Hadiloo S, El-Raouf AA. Application of combined electrical resistivity tomography (ERT) and seismic refraction tomography (SRT) methods to investigate Xiaoshan District landslide site: Hangzhou, China. Journal of Applied Geophysics 2021b;184:Article No. 104236.

Intarat K, Yoomee P, Hussadin A, Lamprom W. Assessment of landslide susceptibility in the Intermontane Basin Area of Northern Thailand. Environment and Natural Resources Journal 2024;22(2):158-70.

Iscan F, Guler E. Developing a mobile GIS application related to the collection of land data in soil mapping studies. International Journal of Engineering and Geosciences 2021;6(1):27-39.

Jäger D, Sandmeier C, Schwindt D, Terhorst B. Geomorphological and geophysical analyses in a landslide area near

Ebermannstadt, Northern Bavaria. Quaternary Science Journal 2013;62(2):150-61.

Jaysaval P, Robinson JL, Johnson TC. Stratigraphic identification with airborne electromagnetic methods at the Hanford Site, Washington. Journal of Applied Geophysics 2021;192:Article No. 104398.

Jin L, Luan X, Raveendrasinghe TD, Jiang L, Xue Y, Wei X, et al. Influence of sedimentary processes and fault tectonics on the evolution of submarine canyons in the East Andaman Basin: Insights from high-resolution seismic data analysis. Geomorphology 2024;454:Article No. 109179.

Kanakiya S, Adam L, Rowe MC, Esteban L, Lerner GA, Lindsay JM. Petrophysical and elastic properties of altered lavas from Mt. Taranaki: Implications for dome stability. Journal of Volcanology and Geothermal Research 2022;432:Article No. 107693.

Karaaslan H, Silahtar A, Ramazanoglu S. Characterization of an active landslide structure with integrated electrical resistivity tomography and multi-channel analysis of surface waves methods in Değirmendere District, Sakarya (Türkiye). Earth Surface Processes and Landforms 2023;48(15):3170-80.

Kereszturi G, Schaefer L, Mead S, Miller C, Procter J, Kennedy B. Synthesis of hydrothermal alteration, rock mechanics and geophysical mapping to constrain failure and debris avalanche hazards at Mt. Ruapehu (New Zealand). New Zealand Journal of Geology and Geophysics 2021;64(2-3):421-42.

Lann T, Bao H, Lan H, Zheng H, Yan C, Peng J. Hydro-mechanical effects of vegetation on slope stability: A review. Science of the Total Environment 2024;926:Article No. 171691.

Lee EM, Jones DKC. Landslide Risk Assessment. London: Thomas Telford Publishing; 2004.

Lin Q, Steger S, Pittore M, Zhang J, Wang L, Jiang T, et al. Evaluation of potential changes in landslide susceptibility and landslide occurrence frequency in China under climate change. Science of the Total Environment 2022;850:Article No. 158049.

Maulana E, Sartohadi J, Setiawan MA. Soil conservation at the gully plot scale in the tropical volcanic landscape of Sumbing. AIMS Environmental Science 2023;10(6):832-46.

Ming PLH, Zawawi AA. Analysis of landslide occurrence using dtm-based weighted overlay: A case study in tropical mountainous forest of Cameron highlands, Malaysia. Environment and Natural Resources Journal 2021;19(5): 358-70.

Mohammed MA, Abudeif AM, Abd el-aal AK. Engineering geotechnical evaluation of soil for foundation purposes using shallow seismic refraction and MASW in 15th Mayo, Egypt. Journal of African Earth Sciences 2020;162:Article No. 103721.

Noviyanto A, Sartohadi J, Purwanto BH. The distribution of soil morphological characteristics for landslide-impacted Sumbing Volcano, Central Java - Indonesia. Geoenvironmental Disasters 2020;7(1):Article No. 25.

Pandarinath K. Application potential of chemical weathering indices in the identification of hydrothermally altered surface volcanic rocks from geothermal fields. Geosciences Journal 2022;26(3):415-42.

Patanduk A. Integration of Aerial Photography, GNSS, and Refraction Seismic to Identify the Characteristic of Surface Cracks on the Kalisari Landslide Area, Bompon River Basin. [project report]. Universitas Gadjah Mada, Indonesia; 2020. (in Bahasa Indonesia)

Poddar I, Roy R. Application of GIS-based data-driven bivariate statistical models for landslide prediction: A case study of highly affected landslide prone areas of Teesta River Basin. Quaternary Science Advances 2024;13:Article No. 100150.

Pratiwi ES, Sartohadi J, Wahyudi. Geoelectrical prediction for sliding plane layers of rotational landslide at the volcanic transitional landscapes in Indonesia. IOP Conference Series: Earth and Environmental Science 2019;286(1):Article No. 012028.

Prayitno A, Sartohadi J, Nurudin M. Utilization of soil function information for assessing soil quality of rice field in the quaternary-tertiary volcanic transitional zones in Central Java. SAINS TANAH - Journal of Soil Science and Agroclimatology 2019;16(2):Article No. 169.

Pulungan NA, Sartohadi J. Variability of soil development in Hilly Region, Bogowonto Catchment, Java, Indonesia. International Journal of Soil Science 2017;13(1):1-8.

Pulungan NA, Sartohadi J. New approach to soil formation in the transitional landscape zone: Weathering and alteration of parent rocks. Journal of Environments 2018;5(1):1-7.

Punzo M, Cianflone G, Cavuoto G, De Rosa R, Dominici R, Gallo P, et al. Active and passive seismic methods to explore areas of active faulting. The case of Lamezia Terme (Calabria, southern Italy). Journal of Applied Geophysics 2021; 188:Article No. 104316.

Purnamasari A, Sartohadi J, Hartantyo E. Pseudo sliding plane in super-thick soil materials deposit at Ngasinan Deep Landslide Area. Revista Brasileira de Geomorfologia 2024;25(2):e2540.

Purwaningsih R, Sartohadi J, Anggri M. Trees and crops arrangement in the agroforestry system based on slope units to control landslide reactivation on volcanic foot slopes in Java, Indonesia. Land 2020;9(9):Article No. 327.

Putra AN, Nita I, Jauhary MRAl, Nurhutami SR, Ismail MH. Landslide risk analysis on agriculture area in pacitan regency in east java indonesia using geospatial techniques. Environment and Natural Resources Journal 2021;19(2):141-52.

Qasim S, Qasim M, Shrestha RP, Khan AN. Socio-economic determinants of landslide risk perception in Murree hills of Pakistan. AIMS Environmental Science 2018;5(5):305-14.

Rahimi MR, Mohammadi SD, Heidari M, Jalali SH. Correlation between mineral composition and P-wave velocity, strength and textural properties of sulfate rocks in dry and saturated conditions. Journal of Applied Geophysics 2021;192:Article No. 104397.

Reynolds JM. An Introduction to Applied and Environmental Geophysics. Vol. 148. West Sussex: John Wiley and Sons Ltd; 1997.

Sadisun IA, Prasaja DB, Kartiko RD, Dinata IA. Landslide susceptibility zonation of Rongga District and Surrounding Areas using weight of evidence (WoE) method. IOP Conference Series: Earth and Environmental Science 2021;873(1):1-7.

Sambodo AP, Arpornthip T. Increasing the Efficiency of Detailed Soil Resource Mapping on Transitional Volcanic Landforms Using a Geomorphometric Approach. Applied and Environmental Soil Science 2021;2021:Article No. 8867647.

Samyn K, Travelletti J, Bitri A, Grandjean G, Malet JP. Characterization of a landslide geometry using 3D seismic refraction traveltime tomography: The La Valette landslide case history. Journal of Applied Geophysics 2012;86:120-32.

Sana H, Taborik P, Valenta J, Bhat FA, Flašar J, Štěpančíkova P, et al. Detecting active faults in intramountain basins using electrical resistivity tomography: A focus on Kashmir Basin, NW Himalaya. Journal of Applied Geophysics 2021; 192:Article No. 104395.

Sartohadi J, Pulungan HJNA, Nurudin M, Wahyudi W. The ecological perspective of landslides at soils with high clay content in the middle bogowonto watershed, central Java, Indonesia. Applied and Environmental Soil Science 2018;2018(1):Article No. 2648185.

Schaetzl R, Anderson S. Soils Genesis and Geomorphology. Cambridge: Cambridge University Press; 2005.

Servanzi L, Quadroni S, Espa P. Hydro-morphological alteration and related effects on fish habitat induced by sediment management in a regulated Alpine River. International Journal of Sediment Research 2023;39(4):514-30.

Sichugova L, Fazilova D. Study of the seismic activity of the Almalyk-Angren industrial zone based on lineament analysis. International Journal of Engineering and Geosciences 2024;9(1):1-11.

Sujitapan C, Kendall JM, Chambers JE, Yordkayhun S. Landslide assessment through integrated geoelectrical and seismic methods: A case study in Thungsong site, southern Thailand. Heliyon 2024;10(2):e24660.

Teh YY, Wong JL, Lee ML. Effect of fines content on soil moisture responses to wetting and drying cycles. Physics and Chemistry of the Earth 2023;129:Article No. 103313.

Telford WM, Geldart LP, Sheriff RE, Keys DA. Applied Geophysics. New York: Press Syndicate of the Cambridge University Press; 1990.

Thirard G, Thiery Y, Gourdier S, Grandjean G, Maquaire O, François B, et al. Hydromechanical assessment of a complex landslide through geophysics and numerical modeling: Toward an upgrade for the Villerville landslide (Normandy, France). Engineering Geology 2022;297:Article No. 106516.

Thongley T, Vansarochana C. Spatial zonation of landslide prone area using information value in the geologically fragile region of samdrup jongkhar-tashigang national highway in bhutan. Environment and Natural Resources Journal 2021; 19(2):122-31.

Usman FCA, Manyoe IN, Duwingik RF, Kasim DNP. Geophysical survey of landslide movement and mechanism in Gorontalo Outer Ring Road, Gorontalo. IOP Conference Series: Earth and Environmental Science 2020;589(1):1-9.

Weisenberger TB, Ingimarsson H, Hersir GP, Flóvenz ÓG. Cation-exchange capacity distribution within hydrothermal systems and its relation to the alteration mineralogy and electrical resistivity. Energies 2020;13(21):1-19.

Whiteley JS, Chambers JE, Uhlemann S, Boyd J, Cimpoiasu MO, Holmes JL, et al. Landslide monitoring using seismic refraction tomography - The importance of incorporating topographic variations. Engineering Geology 2020;268: Article No. 105525.

Whiteley JS, Watlet A, Uhlemann S, Wilkinson P, Boyd JP, Jordan C, et al. Rapid characterisation of landslide heterogeneity using unsupervised classification of electrical resistivity and seismic refraction surveys. Engineering Geology 2021; 290:Article No. 106189.

Zainal M, Munir B, Marwan. The electrical resistivity tomography technique for landslide characterization in Blangkejeren Aceh. Journal of Physics: Conference Series 2021;1825(1):Article No. 012022.

Zakaria MT, Mohd Muztaza N, Zabidi H, Salleh AN, Mahmud N, Rosli FN. Integrated analysis of geophysical approaches for slope failure characterisation. Environmental Earth Sciences 2022;81(10):1-21.

Environment and Natural Resources Journal

Volume 23
Issue 1
2025

Analyzing Drought Propagation and Its Influential Factors in the Upper Nan Watershed, Thailand

Muhammad Chrisna Satriagasa, Piyapong Tongdeenok*, and Naruemol Kaewjampa

Watershed and Environmental Management Program, Faculty of Forestry, Kasetsart University, Bangkok 10900, Thailand

ARTICLE INFO

Received: 15 Jul 2024
Received in revised: 4 Oct 2024
Accepted: 16 Oct 2024
Published online: 11 Dec 2024
DOI: 10.32526/ennrj/23/20240202

Keywords:
Meteorological drought/ Hydrological drought/ Drought propagation/ Upper Nan Watershed/ Forest conservation

*** Corresponding author:**
E-mail: fforppt@ku.ac.th

ABSTRACT

Understanding drought propagation is essential for effective water resource management. This study employs an innovative approach to examine the transition from meteorological drought (MD) to hydrological drought (HD) in the Upper Nan Watershed (UNW), Thailand, using the standardized precipitation evapotranspiration index (SPEI) and standardized streamflow index (SSI). Cross-wavelet transform (XWT) and Pearson's correlation analyses reveal a significant positive correlation between MD and HD, with the drought propagation time (DPT) ranging from 2 to 5 months, notably shorter during the dry season. The eastern UNW (Zone I) has the longest DPT, while the western UNW (Zone III) has the shortest. This study is distinguished by its integration of global teleconnection factors, such as El Niño-Southern Oscillation (ENSO), the Dipole Mode Index (DMI), and Pacific Decadal Oscillation (PDO), alongside local factors like climate, slope, and watershed morphometry. This dual focus provides a comprehensive analysis of drought dynamics, enhancing the understanding of drought propagation and its complexities. The integration of global and local influences provides insights applicable across diverse water resource management contexts. It highlights the critical role of forests in regulating water flow and extending the DPT, emphasizing the need for forest conservation and land use regulation in the headwaters. Despite challenges associated with highland meteorological data, findings offer improvements to existing drought monitoring and early warning systems, underscoring the importance of combining global and local factors in effective drought management strategies.

1. INTRODUCTION

Drought, characterized by insufficient rainfall, leads to significant water shortages that affect agriculture, the environment, and society and result in substantial economic losses (Dalezios et al., 2012). The types of drought include meteorological drought (MD), agricultural drought, hydrological drought (HD), and socioeconomic drought, occurring when water supply fails to meet demand (Abbas and Kousar, 2021). Understanding the transition from MD to HD is critical for water resource management. However, previous studies have not explored the combination of global and local factors affecting drought propagation, especially in the context of Thailand's Upper Nan Watershed (UNW). This study bridges that gap by offering an innovative and detailed analysis of the dynamics between global teleconnection factors and local watershed conditions to predict drought propagation.

Previous studies have explored drought propagation, with Ding et al. (2021a) finding stronger propagation from agricultural drought (AD) to HD in northern China during summer and autumn; Huang et al. (2017) noting a time lag between MD and HD in the Wei River Basin, influenced by atmospheric anomalies such as El Niño-Southern Oscillation (ENSO) and Arctic Oscillation (AO); and Gu et al. (2020) showing that droughts increase in duration and severity as they propagate, particularly in the Yangtze and Yellow River basins. This research contributes to

Citation: Satriagasa MC, Tongdeenok P, Kaewjampa N. Analyzing drought propagation and its influential factors in the Upper Nan Watershed, Thailand. Environ. Nat. Resour. J. 2025;23(1):14-27. (https://doi.org/10.32526/ennrj/23/20240202)

the field by focusing on the UNW, a drought-prone area in Thailand where the specific dynamics of MD-to-HD propagation are not yet well understood. Climate change intensifies droughts, affecting water availability and agricultural productivity (Wan et al., 2018; Xu et al., 2019). Land use changes such as deforestation and urbanization worsen drought impacts by disrupting hydrological cycles and reducing water retention (Fedele et al., 2018).

The UNW in northern Thailand flows from north to south, merging with the Wang, Ping, and Yom Watersheds to form the Chao Phraya Watershed. This study presents an innovative approach by examining the spatiotemporal mechanisms of drought propagation in the UNW and identifying the factors affecting the drought propagation time (DPT). This novel combination of global factors (e.g., ENSO, DMI, and PDO) with local conditions such as topography and land use provides a fresh perspective on drought management. Using the SPEI, the SSI, cross-wavelet transform (XWT), and Pearson's correlation analyses, this research aims to improve drought monitoring and early warning systems. The findings will inform land use policies and forest conservation to reduce the socio-economic impacts of drought in the UNW and similar watersheds, delivering insights for enhancing integrated drought management strategies globally.

2. METHODOLOGY

2.1 Study area

This study was conducted in the Upper Nan Watershed (UNW) in northern Thailand; it spans the coordinates 18°27′55.72″ N to 19°38′26.97″ N and 100°21′39.14″ E to 101°21′7.52″ E, covering an area of 4,588.4 km² (Figure 1). The UNW experiences a dry season (January to March and November to December) with 9.7 to 64.4 mm of rainfall and a wet season (April to October) with 102.7 to 269 mm, often receiving rainstorms from the South China Sea during the northeast monsoon. The landscape includes hilly upstream and midstream regions and low-lying flatland downstream, where the town of Nan is located. The headwaters are critical due to the thin soil from intensive erosion on steep slopes, which limits moisture retention and increases drought susceptibility. Agriculture is vital in the UNW, with rice and maize being the primary crops. Forests have been cleared for maize cultivation due to its higher economic returns, leading to reduced soil moisture retention, increased runoff, and soil erosion, heightening drought vulnerability (Paiboonvorachat and Oyana, 2011). The region heavily relies on agriculture, stressing water resources and necessitating sustainable management for long-term environmental and economic stability (Plangoen and Babel, 2014; Satriagasa et al., 2023).

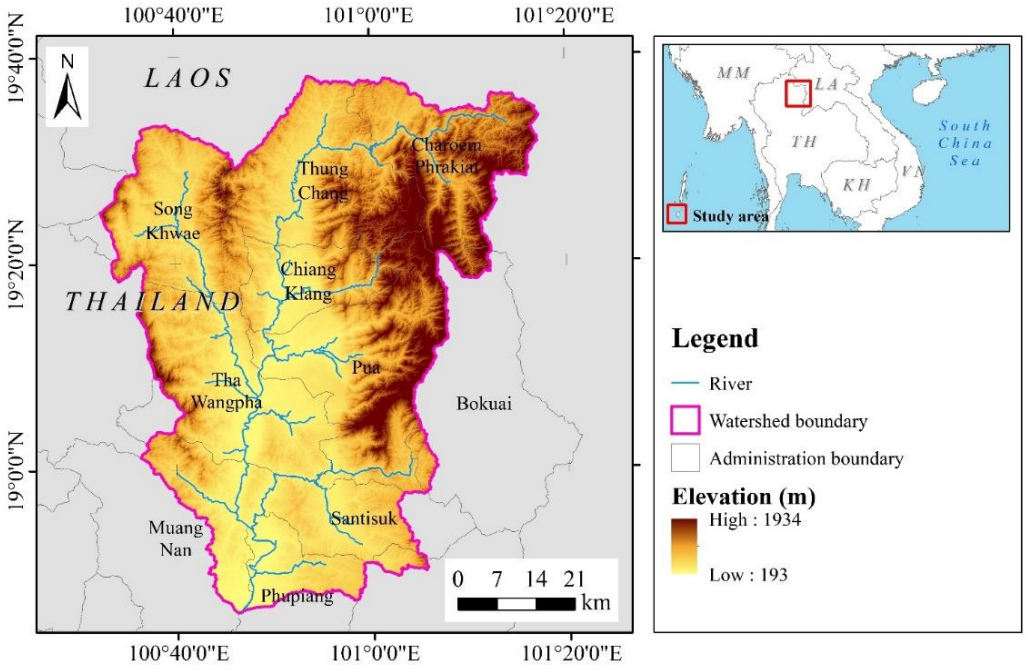

Figure 1. Map of Upper Nan Watershed

2.2 Data collection

Several types of data were used in this study, detailed in Table 1.

The data used in this study span the period from 2000 to 2020, covering 21 years. While a 30-year or longer time series is generally recommended for calculating drought indices to better assess long-term trends, the selection of this period was driven by several key considerations.

First, data availability was a significant factor. Reliable and continuous meteorological and hydrological data, particularly for highland areas within the Upper Nan Watershed, only became consistently available in 2000. Prior to this, there were substantial gaps in the dataset, which could have introduced uncertainty and reduced the accuracy of the drought index calculations.

Second, the selected period provides consistent and continuous datasets for both meteorological and hydrological parameters, ensuring the reliability of the cross-wavelet transform (XWT) and Pearson's correlation analyses performed in this study. Extending the dataset beyond 2000 would require incorporating older, inconsistent data that could negatively affect the robustness of the results.

Table 1. Data used in this study, period, and data source

No	Data	Period	Source
1	Rainfall data from CHIRPS imagery	2000-2020	Climate Hazard Center UC Santa Barbara (https://chc.ucsb.edu/data/chirps)
2	Air temperature data from ERA5 imagery	2000-2020	Copernicus (https://cds.climate.copernicus.eu/), acquired in Google Earth Engine
3	Sea surface temperature (SST) data	2000-2020	Physical Science Laboratory of the NOAA (https://psl.noaa.gov/gcos_wgsp/Timeseries/)
4	Dipole mode index (DMI) data	2000-2020	
5	Pacific decadal oscillation (PDO) data	2000-2020	National Center for Environmental Information of the NOAA(https://www.ncei.noaa.gov/access/monitoring/pdo/)
6	Streamflow data	2000-2020	Observed streamflow data from Thailand Royal Irrigation Department (RID) (https://www.hydro-1.net/), SWAT-modeled streamflow from (Satriagasa et al., 2023)
7	Hansen Global Forest Change	2000-2020	Hansen et al. (2013)
8	DEM SRTM 30 m	-	USGS (https://www.usgs.gov/)

Finally, this period captures recent climate trends, particularly the increasing frequency and intensity of drought events influenced by global teleconnection factors such as ENSO, the DMI, and PDO. Focusing on the period from 2000 to 2020 allows for a more relevant assessment of recent drought propagation dynamics and provides insights that are applicable to current and future drought management strategies.

For rainfall data, this study used CHIRPS satellite-based precipitation estimates from the Climate Hazard Center at UC Santa Barbara. While CHIRPS provides extensive spatial and temporal coverage, we did not conduct a formal validation process comparing CHIRPS data to local measurements. However, CHIRPS has been widely used and validated in similar regions, including Southeast Asia, for its ability to represent precipitation patterns and drought conditions. Although satellite-based estimates have limitations, they offer significant advantages in areas such as the Upper Nan Watershed, where ground-based meteorological stations are sparse.

In choosing CHIRPS data, we balanced data consistency and availability with the need to capture relevant drought events and climatic trends during the study period. Future studies could enhance these findings by conducting additional validations with local rainfall measurements.

While a longer time series would be ideal for long-term trend analysis, the 21-year period used in this study represents a balance among data quality, consistency, and relevance to the changing climatic conditions in the region.

2.3 Drought indices

2.3.1 Standardized precipitation evapo-transpiration index (SPEI)

The standardized precipitation evapo-transpiration index (SPEI) is widely used for detecting meteorological drought (MD). As proposed by Vicente-Serrano et al. (2010), it incorporates temperature-induced evapotranspiration with rainfall,

enhancing drought detection accuracy. The SPEI calculation involves computing the difference between precipitation (P) and potential evapotranspiration (PET) for each month (Equation 1), aggregating these values over different timescales (1 to 12 months), fitting the accumulated values to a log-logistic probability distribution (Equation 2), and converting them into a standardized index with a mean of zero and a standard deviation of one (Equation 3). This study used the SPEI to assess MD in the UNW from 2000 to 2020 over 1- to 12-month periods, with calculations performed using the SPEI package in RStudio for rapid, accurate, and reliable results.

$$D = P - PET \quad (1)$$

$$F(x) = \frac{1}{1+\left(\frac{\alpha}{x-\gamma}\right)^{\beta}} \quad (2)$$

$$SPEI = \frac{W-\mu}{\sigma} \quad (3)$$

Where; F(x) is the cumulative probability, x is the water balance, and α, β, and γ are the scale, shape, and location parameters, respectively; W is the log-logistically normalized water balance, μ is the mean, and σ is the standard deviation.

2.3.2 Standardized streamflow index (SSI)

The standardized streamflow index (SSI) captures hydrological drought (HD) by analyzing streamflow discharge. On the basis of monthly streamflow data modeled using the soil and water assessment tool (SWAT) for the period from 2000 to 2020, the SSI was calculated for the Upper Nan Watershed (UNW) following the standardized precipitation index (SPI) method. The steps include collecting monthly streamflow data, aggregating it over the chosen timescale, normalizing it to a probability distribution (typically log-normal), and standardizing it to a mean of zero and standard deviation of one, resulting in SSI values (Equation 4).

$$SSI = \frac{Q-\mu}{\sigma} \quad (4)$$

Where; Q is the monthly streamflow value, μ is the mean of the streamflow over the reference period, and σ is the standard deviation of the streamflow.

The SWAT model was run with a warm-up period from 1980 to 1984 to initialize the model. Calibration was conducted for 1985 to 2005 and validation for 2006 to 2020 using observed streamflow data from the Thailand Royal Irrigation Department (RID). The model's performance was assessed using the Nash-Sutcliffe Efficiency (NSE), the ratio of the root-mean-square error to the standard deviation (RSR), and the Kling-Gupta Efficiency (KGE). The calibration results showed an NSE of 0.83 (very good), an RSR of 0.59 (good), and a KGE of 0.45 (poor). For the validation period, the model achieved an NSE of 0.87 (very good), an RSR of 0.5 (very good), and a KGE of 0.53 (intermediate). These results confirmed that the SWAT model performed well in simulating streamflow during both the calibration and validation periods, providing confidence in its reliability for drought analysis in the UNW.

One month of SSI data was focused on to detect the propagation time from meteorological drought (MD) to HD using the SPEI/SPI package in RStudio. The SSI's reliability in hydrological drought assessment has previously been validated in various regions (Kartika and Wijayanti, 2023).

2.4 Drought propagation time

The drought propagation time (DPT) was determined using the maximum Pearson's correlation coefficient (MPCC) method. The SPEI was used to represent MD, and the SSI was used to represent HD. The MPCC—the highest Pearson correlation coefficient between the SPEI and SSI—then indicated the specific month of drought propagation. The MPCC values were calculated for 176 grid cells (each cell being 5.5 × 5.5 km) to determine the spatial distribution. Seasonal variations were captured by computing MPCC values for the entire year, dry season, and wet season.

The spatial distribution of the DPT in the study area showed notable variation across different parts of the watershed. To capture these variations more effectively, the area was divided into four distinct regions based on a combination of parameters. These parameters included the spatial distribution of the DPT itself, as well as other key environmental factors such as slope and topography, land use patterns, and forest cover. Regions with steeper slopes tended to have faster runoff and shorter DPTs, while flatter areas exhibited longer DPTs. Similarly, differences in land use—particularly between agricultural and forested areas—played a role in shaping water retention and flow dynamics, with areas of higher forest cover typically experiencing longer DPTs due to their better water retention capabilities. Areas with significant deforestation, in contrast, showed quicker drought

propagation. By combining these factors, each of the four regions reflects a distinct set of environmental conditions that influence drought behavior. This classification also provides a foundation for more targeted, region-specific drought mitigation strategies.

2.5 Drought propagation relationship

The relationship between meteorological drought (MD) and hydrological drought (HD) was analyzed using cross-wavelet transform (XWT) on data from 25 sub-watersheds in the UNW with RStudio. XWT identifies phase relationships between the standardized precipitation evapotranspiration index (SPEI) and the standardized streamflow index (SSI), showing drought propagation over time. The analysis assumed stationarity in the time series data and significant wavelet coherence. Figure 2 details the XWT procedure for characterizing drought propagation.

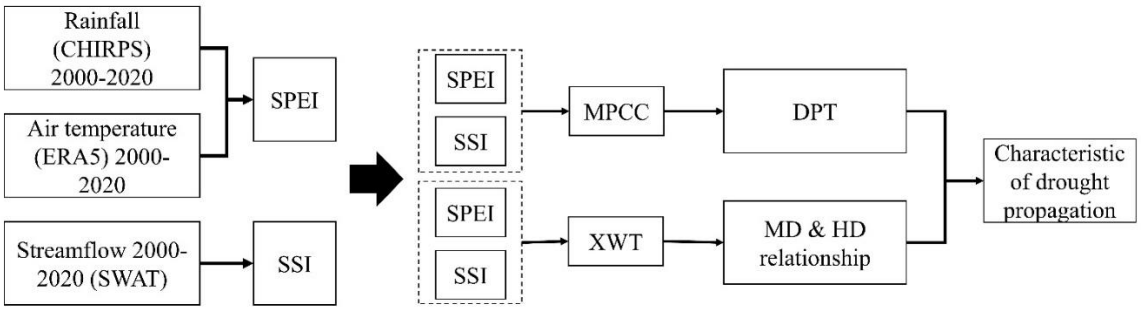

Figure 2. Procedure for characterizing drought propagation

2.6 Factor influencing drought propagation

Several factors influencing drought propagation were analyzed, including climatic, ecological, physical, and anthropogenic factors. The selection of El Niño-Southern Oscillation (ENSO), the Dipole Mode Index (DMI), and Pacific Decadal Oscillation (PDO) as teleconnection indices was based on their well-established influence on precipitation and temperature patterns in Southeast Asia, including Thailand. These indices were obtained from publicly available datasets, with ENSO data sourced from the National Oceanic and Atmospheric Administration (NOAA), DMI from the Physical Science Laboratory of NOAA, and PDO from the National Centers for Environmental Information (NCEI). The analysis involved correlating these teleconnection indices with local climate data by using cross-wavelet transform (XWT) to examine how variations in the teleconnection factors influenced drought propagation patterns over time. This approach allowed us to identify phase relationships and time lags between global teleconnection factors and local drought conditions.

Ecological and anthropogenic factors, such as forest cover, forest loss, and land use, were examined using data from Hansen Global Forest Change (Hansen et al., 2013) and Google Earth Engine. Forest cover change and deforestation rates were spatially analyzed to assess their influence on water retention and drought propagation. This was performed by overlaying forest cover maps onto drought propagation data and identifying regions where forest loss accelerated drought conditions. Anthropogenic activities, including land use changes for agriculture, were assessed using land use classifications provided by national databases and satellite imagery, with a focus on how these changes disrupted hydrological cycles.

Physical factors, including slope and watershed morphometry, were analyzed using high-resolution digital elevation models (DEMs) from the United States Geological Survey (USGS). A slope analysis was performed using ArcGIS to quantify how the topography influenced runoff and water retention in different sub-watersheds. The watershed morphometry was calculated using standard hydrological metrics, such as the drainage density, elongation ratio, and relief ratio, to evaluate how the physical structure of the watershed affected the speed and extent of drought propagation. These analyses provided a comprehensive understanding of drought propagation mechanisms in the UNW, integrating spatial and temporal assessments to determine their impacts.

3. RESULTS AND DISCUSSION

3.1 Result

3.1.1 Drought propagation time (DPT)

The drought propagation time (DPT) is the duration of the transition from meteorological drought (MD) to hydrological drought (HD). In this study, the

DPT was assessed in monthly steps from 1 to 12 months. Based on the maximum Pearson's correlation coefficient (MPCC) analysis, the DPT in the Upper Nan Watershed (UNW) ranges from 2 to 11 months (Figure 3(a)). The most common DPT is 2 to 5 months, with a 2-month DPT covering nearly 46% of the UNW, primarily in the middle part of the watershed. Upstream areas show greater variability, with four months dominating the west and three months dominating the east. Downstream, the DPT extends to five months. The MPCC values ranged from 0.35 to 0.64, indicating the strength of the relationship between the standardized precipitation evapotranspiration index (SPEI) and the standardized streamflow index (SSI). The highest MPCC values were found in the western upstream and midstream areas, while the rest of the watershed had low to medium values (Figure 4).

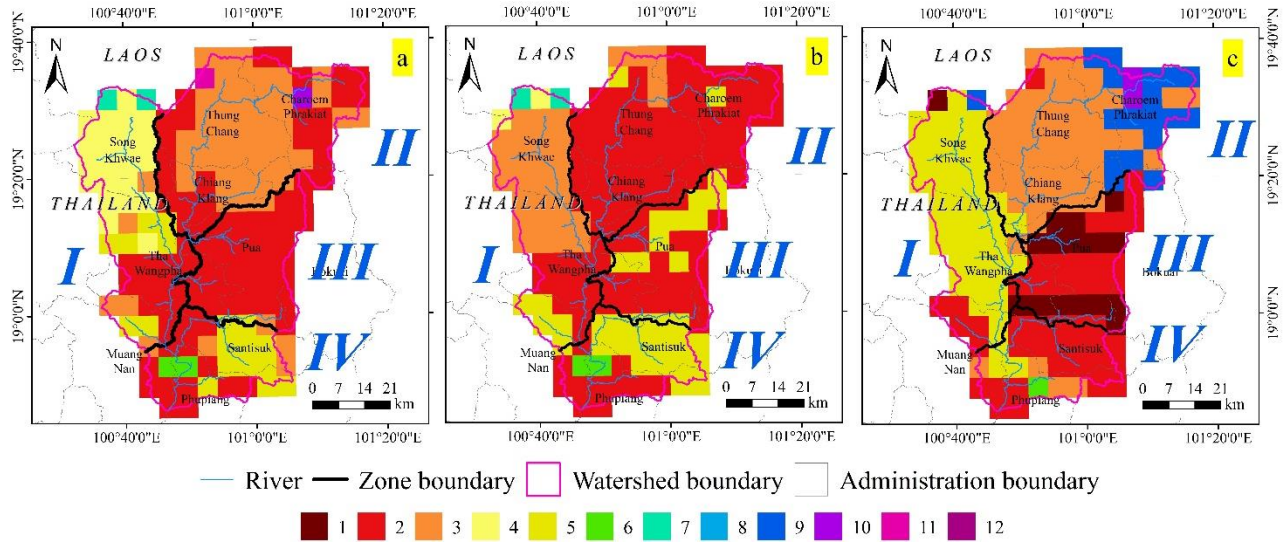

Figure 3. Spatial distribution of drought propagation time in month: (a) all seasons, (b) dry season, and (c) wet season

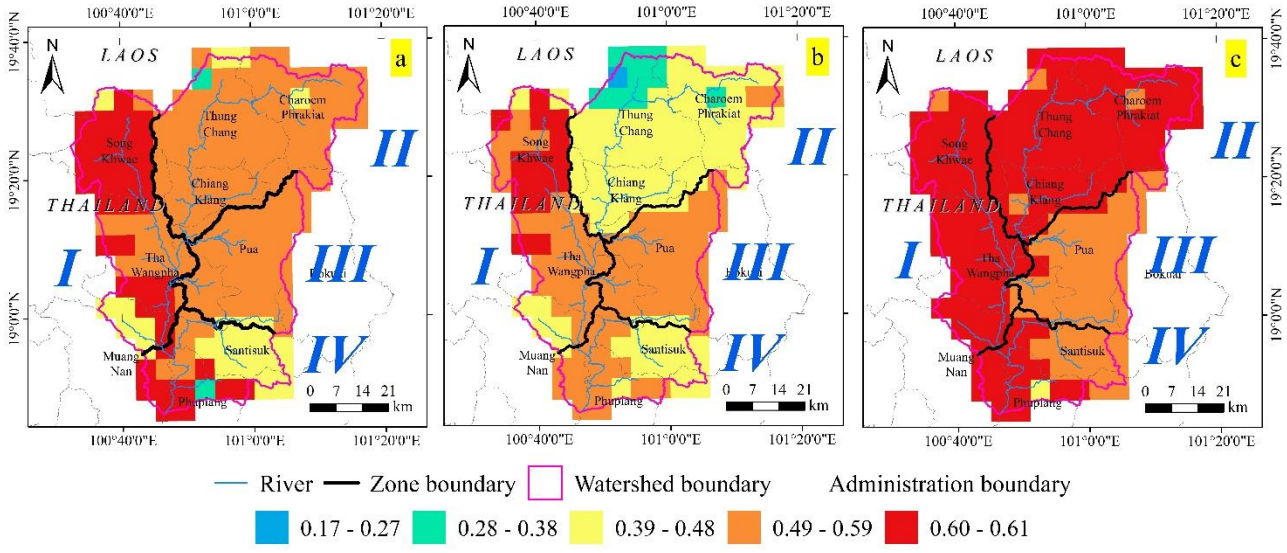

Figure 4. Spatial distribution of MPCC between SPEI and SSI: (a) all seasons, (b) dry season, and (c) wet season

3.1.2 Seasonal drought propagation time

To understand seasonal variations in the DPT, the standardized precipitation evapotranspiration index (SPEI) and standardized streamflow index (SSI) were analyzed for the dry (October-March) and wet (April-September) seasons. In the dry season, the DPT ranges from 2 to 7 months, with a 2-month DPT covering 60% of the watershed, indicating quicker drought propagation due to lower rainfall and higher temperatures. In the wet season, the DPT ranges from

1 to 10 months, with a 3-month DPT covering 30% of the watershed, suggesting that increased rainfall and soil moisture delay hydrological drought. The spatial distribution of the DPT reveals four distinct zones within the UNW, with MPCC values ranging from 0.17 to 0.61 in the dry season and 0.39 to 0.69 in the wet season, being highest in the western watershed. These patterns highlight the varying influences of precipitation, temperature, streamflow, and soil moisture on drought propagation.

3.1.3 Meteorological and hydrological drought relationship

A cross-wavelet transform (XWT) analysis of 25 SPEI and SSI dataset pairs revealed a positive correlation between MD and HD. Four representative XWT charts for the different zones show this correlation, with phase arrows predominantly pointing to the right (Figure 5). For full cross-wavelet transforms between SPEI and SSI, please refer to Figure S1 in the appendix section.

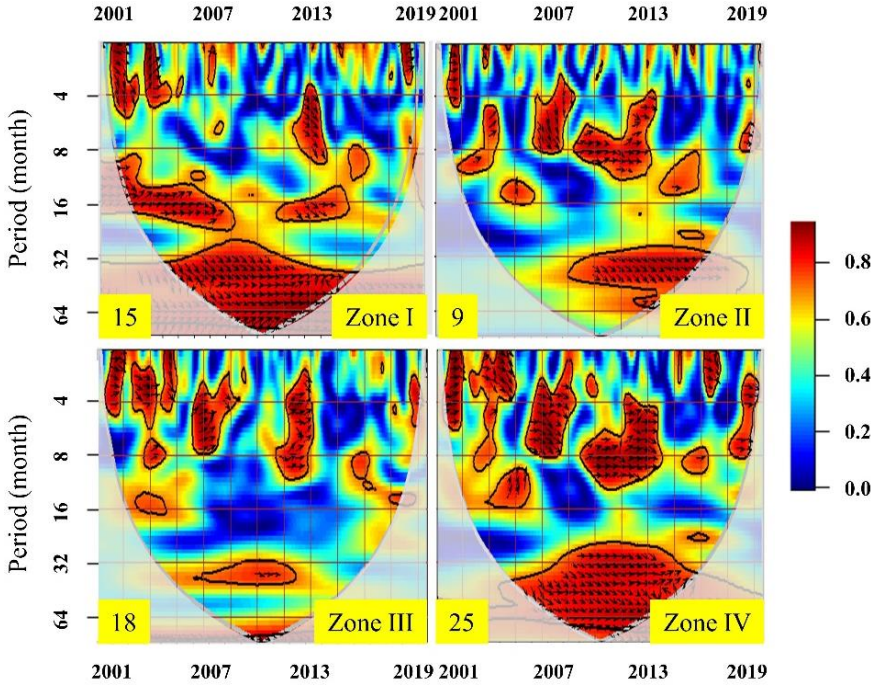

Figure 5. The cross-wavelet transforms between SPEI and SSI of zones I to IV. The arrows indicate the relative phase relationship, with right-pointing arrows representing positive correlations.

3.1.4 Factor influencing the drought propagation characteristics

Several factors influence drought propagation in the UNW, including climatic, ecological, physical, and anthropogenic factors. Our analysis primarily focused on the spatial relationships between these factors and drought propagation, using tools such as XWT and spatial overlays, rather than conducting a detailed quantitative analysis to ascertain the specific contribution of each factor. While statistical modeling could provide more precise measurements of each factor's impact, the current study aimed to identify and visualize spatial patterns that influence drought propagation.

Climatic factors, such as rainfall and air temperature, and global teleconnection indices, such as El Niño-Southern Oscillation (ENSO), the Indian Ocean Dipole (IOD), and Pacific Decadal Oscillation (PDO), significantly impact the region's water balance. El Niño phases reduce rainfall and raise temperatures, exacerbating drought conditions, while La Niña phases increase rainfall, mitigating drought. Similarly, positive IOD phases and warm PDO phases reduce precipitation and increase temperatures, worsening drought, while negative IOD and cool PDO phases alleviate drought. The temporal (Figure 6(a)) and spatial (Figure 7) rainfall patterns illustrate how these teleconnection factors affect the UNW's water balance by influencing the timing and severity of drought propagation.

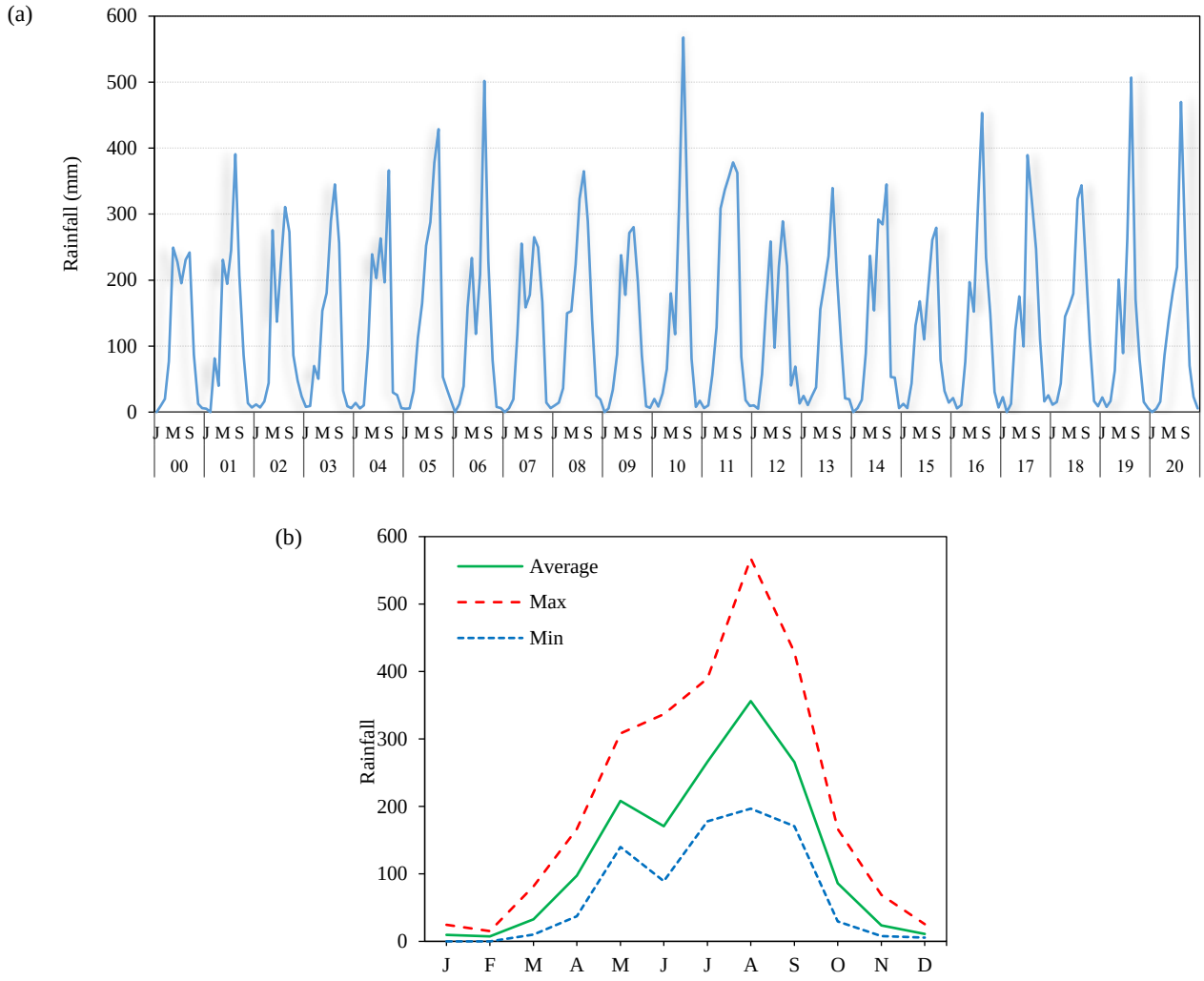

Figure 6. Temporal rainfall pattern of UNW: (a) annual and (b) monthly

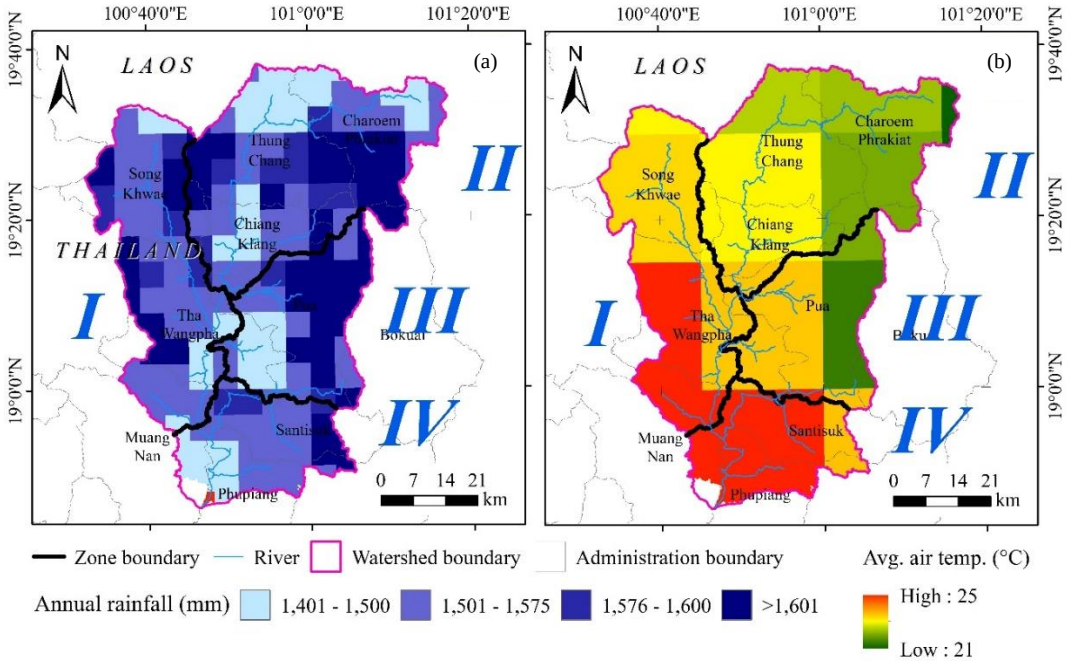

Figure 7. Spatial distribution of (a) annual rainfall and (b) average annual air temperature in the UNW

The annual rainfall in the UNW varies, with mountainous areas receiving over 1,600 mm and lowland areas near the outlet receiving 1,400-1,500 mm. The average temperatures range from 21°C upstream to 25°C downstream. Teleconnection factors such as ENSO, the DMI, and PDO exacerbate drought conditions. Understanding these factors is crucial for effective water management and climate adaptation. The XWT analysis showed significant negative correlations between all teleconnection factors, rainfall, and evaporation in the UNW (Figure 8).

Ecological factors, such as forest cover and forest loss, also play a critical role in regulating water retention and drought propagation. As shown in Figure 9(a), Zones I, II, and III have high tree cover with low forest loss, which helps delay drought propagation, while Zone IV, with extensive forest loss and dryland farming, experiences faster drought propagation. Although our analysis effectively highlights these spatial patterns, further quantitative analyses of the specific contributions of these factors could be explored in future studies.

The slope and watershed morphometry affect the DPT, with gentler slopes retaining water for longer and steep slopes causing rapid runoff (Figure 9(b)). Table 2 provides the detailed morphometric characteristics of selected sub-watersheds within the UNW, highlighting key metrics such as the maximum stream order (MSO), drainage density (DD), circulatory ratio (CR), elongation ratio (ER), and relief ratio (RR). These metrics help to explain why certain sub-watersheds, such as SW13, are highly prone to drought: their high relief ratio and low drainage density accelerate runoff and reduce water retention. For full Upper Nan Watershed morphometry, please refer to Table S1 in the appendix section.

In contrast, sub-watersheds such as SW15 and SW25 have gentler slopes, lower relief ratios, and better water retention capabilities, making them less prone to HD. Understanding these morphometric differences are crucial in determining how the physical characteristics of the watershed influence drought vulnerability and propagation, as reflected in the DPT across the various sub-watersheds. These physical characteristics were analyzed using DEMs and other spatial analysis techniques. While the spatial analysis effectively highlighted these relationships, a more detailed quantitative analysis of the specific contributions of each factor could be explored in future studies to provide a clearer understanding of the factors' impacts on drought propagation.

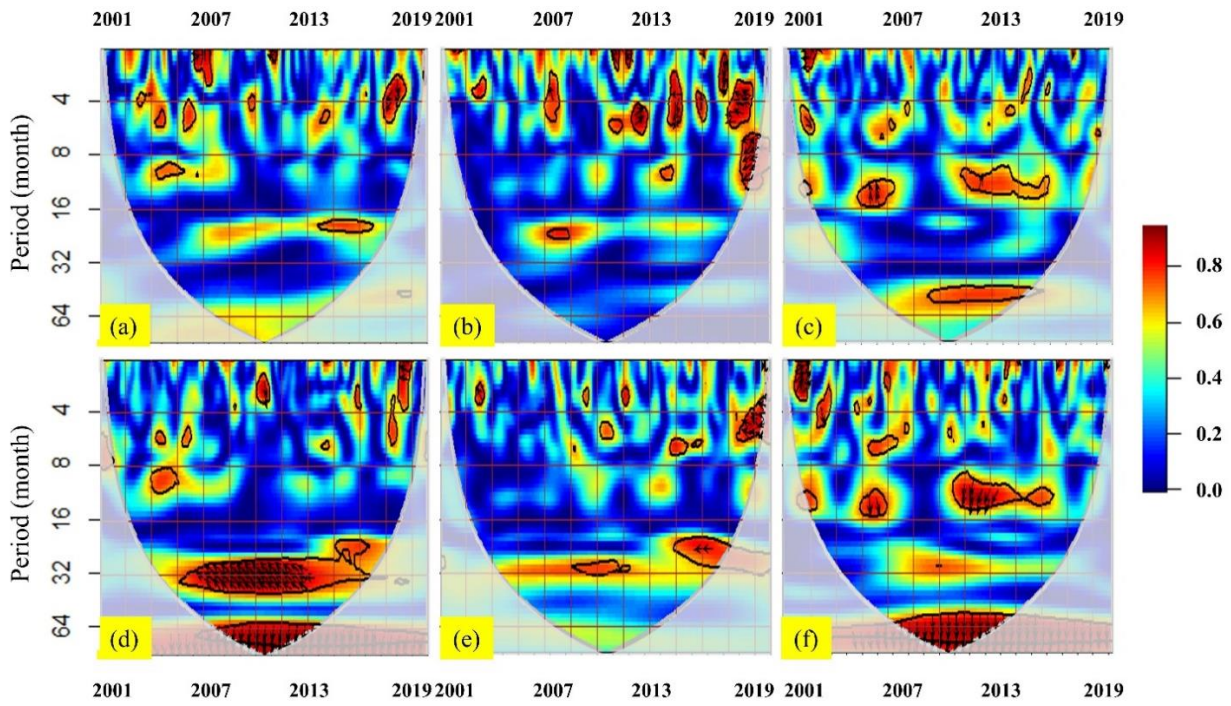

Figure 8. The cross wavelet transforms between (a) ATE and ENSO, (b) ATE and DMI, (c) ATE and PDO (d) rainfall and ENSO, (e) rainfall and DMI, and (f) rainfall and PDO.

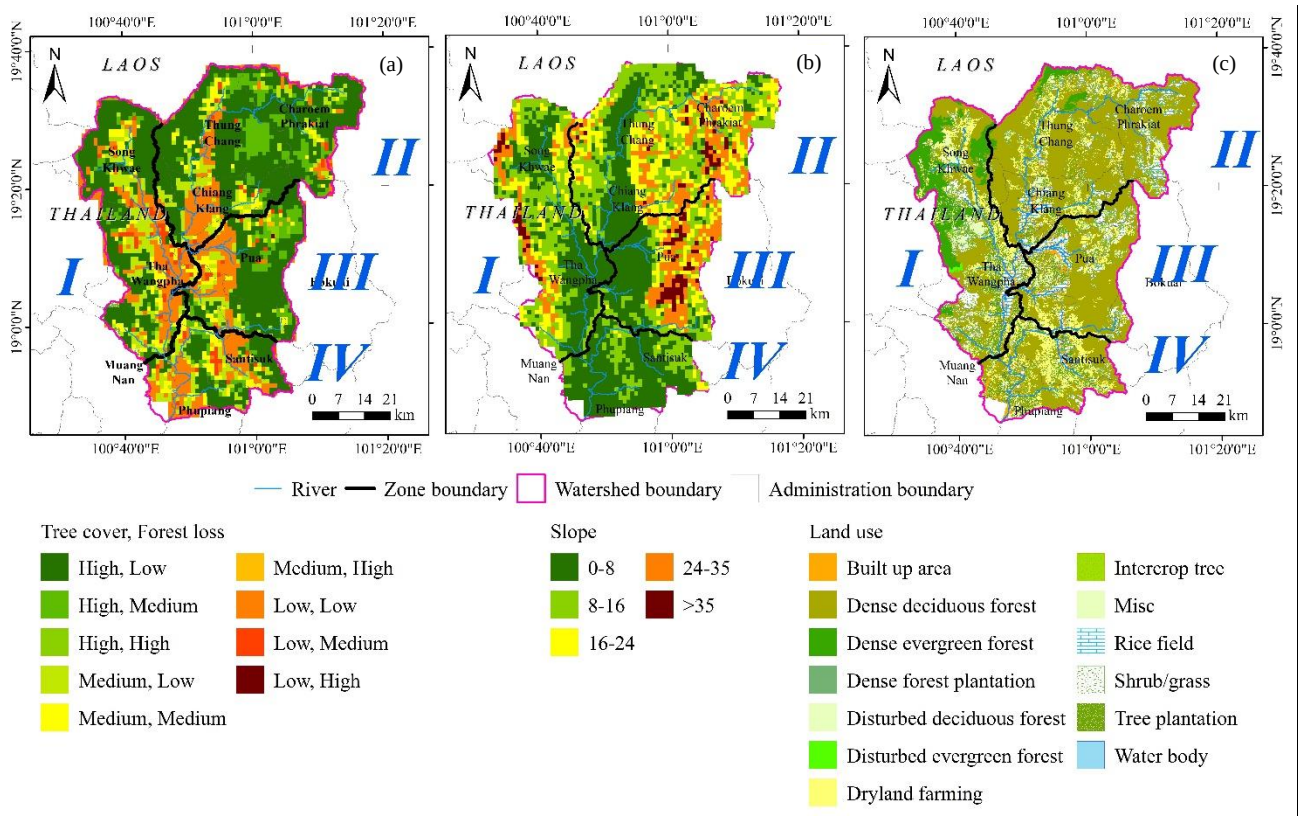

Figure 9. Ecological and anthropogenic factors: (a) tree cover and forest loss, (b) slope, and (c) land use

Table 2. Upper Nan Watershed morphometry

Sub-W	MSO	DD	CR	ER	RR
13	2	0.32	0.23	0.63	95.8
14	3	0.49	0.10	0.62	81.7
15*	4	0.28	0.24	0.57	34.6
25*	5	0.35	0.18	0.59	13.7

Note: MSO, maximum stream order; DD, drainage density; CR, circulatory ratio; ER, elongation ratio; RR, relief ratio; *, lowest.

3.2 Discussion

3.2.1 Correlation between meteorological and hydrological drought

Our analysis revealed a significant positive correlation between MD and HD in the UNW, with the strongest correlation observed during the wet season. This finding aligns with the results of previous studies, such as the works by Huang et al. (2017) and Xu et al. (2021) in China, which identified similar patterns between MD and agricultural drought.

The identified DPT in the UNW ranges from 2 to 11 months, with a predominant period of 2 to 5 months. This range aligns with those found in previous studies in Asian regions, highlighting similarities and nuanced differences. For instance, Li et al. (2022) reported DPTs in the Arid Region of Northeast Asia (ARNA) of 1-3 months in summer and autumn and 5-12 months in spring and winter. The shorter DPTs in summer and autumn align with the findings for the UNW during the wet season, while the longer DPTs in the ARNA reflect its extreme climatic conditions. Ding et al. (2021b) observed a DPT range of 1-12 months across their study area in China, reflecting diverse local conditions similar to those in the UNW. Luo et al. (2023), in the neighboring Lancang-Mekong River Basin, found DPTs of 2-11 months with a predominant period of 2-5 months; considering the similar climatic conditions, their result reinforces our findings for the UNW. While the similar lag times between the UNW and other watersheds can be attributed to common monsoon patterns, local factors such as the soil characteristics, land use, and watershed morphometry lead to differences in specific DPT values. Understanding these nuances is crucial for developing effective, region-specific drought management strategies.

The similar lag times between the UNW and other watersheds are due to common regional climatic patterns and monsoon-influenced hydrological processes. However, local factors such as soil characteristics, land use, and watershed morphometry cause differences in the specific DPT values. For instance, the ARNA's extreme climatic conditions result in greater seasonal DPT variations compared to the more stable UNW. Understanding these nuances is crucial for tailoring region-specific drought management strategies.

The transition from MD to HD is driven by several mechanisms:

Soil moisture depletion: During periods of reduced rainfall (MD), soil moisture decreases significantly, leading to reduced groundwater recharge (Cao et al., 2016; Khaki et al., 2018). This depletion of soil moisture affects surface water flow, contributing to the onset of HD.

Evapotranspiration: High temperatures associated with MD increase evapotranspiration rates, further depleting soil moisture and reducing surface water availability (Condon et al., 2020; Vahmani et al., 2021). This accelerated loss of water from the soil and water bodies intensifies HD conditions.

Runoff reduction: Reduced rainfall during MD leads to decreased runoff into rivers and streams (Bai et al., 2023; Nippgen et al., 2016). With less water entering the watershed's hydrological system, streamflow diminishes, exacerbating HD.

These mechanisms collectively explain the observed correlation between MD and HD and the identified DPTs in the UNW. Understanding these processes is crucial for effective drought management and mitigation strategies.

3.2.2 Influence of global and local climatic factors

This study highlights the significant impact of global teleconnection factors, such as ENSO, DMI, and PDO, on drought conditions in the UNW. Our XWT analysis showed a statistically significant negative correlation between these factors and both rainfall and evaporation. Ueangsawat and Jintrawet (2013) also noted ENSO's influence on short-term rainfall patterns in northern Thailand. However, the UNW's mountainous location may lessen the overall effect of these factors. Local climatic factors, particularly rainfall, have a more substantial impact on the DPT than air temperature. Higher-rainfall areas tend to have a decreased DPT, supporting Luo et al.'s (2023) findings that lower rainfall correlates with shorter DPTs. The lack of a consistent spatial pattern between the air temperature and DPT may be due to the coarse resolution of ERA5 satellite imagery, indicating a need for higher-resolution data to better understand these dynamics.

3.2.3 Role of physical and ecological factors

Physical characteristics such as the slope and watershed morphometry significantly influence the DPT. Zones with steep slopes and thin soils, such as Zone III, exhibit shorter DPTs (1-2 months) due to their rapid runoff and limited water retention. Conversely, zones with gentler slopes and better soil retention, such as Zone I, show longer DPTs, as water is retained for longer, delaying the transition from MD to HD. This aligns with results from Lin et al. (2023), who found that steep slopes accelerate drought propagation by facilitating rapid water movement and reducing infiltration. Factors such as the drainage density and watershed shape also play crucial roles, with more compact and better-draining watersheds experiencing faster drought propagation due to their efficient water conveyance.

Ecological factors, particularly forest cover, play a complex role in drought dynamics. High evapotranspiration rates in forests can lead to shorter DPTs, but forests also provide water regulation services that can extend DPTs. Studies by Ding et al. (2021c) and Tarigan et al. (2018) supported the assertion that forests enhance base flow and reduce runoff velocity, mitigating the impacts of drought. Forested areas tend to have longer DPTs due to their improved soil moisture retention and slower runoff, while regions with significant forest loss exhibit shorter DPTs due to their faster runoff and lower groundwater recharge. These findings indicate that areas with higher forest cover and lower forest loss, such as Zones I, II, and III, experience longer DPTs than areas with significant forest loss, such as Zone IV.

3.2.4 Impact of anthropogenic activities

Human activities such as dryland farming and deforestation exacerbate drought by reducing DPTs. In Zone IV, extensive dryland farming and significant forest loss have led to shorter DPTs, contrasting with studies highlighting forests' role in water retention. Zone III's agricultural practices further intensify drought conditions. Yang et al. (2023) found that reservoir regulation reduced the likelihood of meteorological droughts becoming hydrological by

16% and decreased the duration and severity of long-lasting hydrological droughts by 18% and 37%, respectively. Li et al. (2021) reported that human activities influence seasonal drought dynamics, especially in winter, alleviating hydrological drought severity. Shah et al. (2021) noted that intensive irrigation, reservoir storage, and groundwater pumping in India significantly impact agricultural and hydrological droughts. Wang et al. (2021) observed that high percentages of cropland shorten the DPT due to increased water consumption. In the Upper Nan Watershed, deforestation and dryland farming in Zone IV have led to shorter DPTs, in accordance with Wang et al.'s (2021) findings, while the extensive agricultural practices in Zone III align with Shah et al.'s (2021) observations. These studies highlight the significant impact of human activities on DPTs and underscore the importance of sustainable practices to mitigate drought in regions such as the Upper Nan Watershed.

3.2.5 Practical implication and future research

Understanding DPTs in the UNW is crucial for effective water management and climate adaptation. Maintaining forest cover and regulating land use are vital for mitigating drought impacts, while sustainable agriculture and forest conservation enhance resilience. The study provides valuable insights but has its limitations, including the coarse ERA5 satellite imagery resolution and a focus on general patterns that may overlook fine-scale climatic variations. The findings could be further refined by including soil properties, groundwater dynamics, and detailed land use data.

Additionally, the use of the soil and water assessment tool (SWAT), a semi-distributed hydrological model, imposes limitations on capturing the spatial heterogeneity of regional moisture at a fine scale. Since the SWAT operates on hydrological response units (HRUs) rather than individual grid cells, it does not fully account for moisture variability across different spatial regions. Future studies could consider using fully distributed models such as the Variable Infiltration Capacity (VIC) model, which provides a higher spatial resolution and better captures moisture dynamics. This could improve the accuracy of drought simulations and allow for a more detailed understanding of spatial variability in moisture and water retention across the watershed.

The maximum Pearson's correlation coefficient (MPCC) may not fully capture non-linear relationships between meteorological and hydrological droughts, and model calibration could affect the accuracy. Deeper analyses are required to examine specific land use changes and agricultural practices, and findings specific to the UNW may not be generalizable to other regions.

Policymakers should focus on forest conservation, sustainable land use, adaptive agriculture, and efficient water management strategies, while considering regional and seasonal DPT variability. An understanding of global teleconnection factors and local climatic conditions can inform climate adaptation strategies. Integrated watershed management, robust drought monitoring, community engagement, and policy coordination are essential for comprehensive drought management, enhancing water security, and building resilience in the UNW and similar regions.

4. CONCLUSION

This study provides insights into the transition from meteorological drought (MD) to hydrological drought (HD) in the Upper Nan Watershed (UNW), Thailand, using the SPEI, the SSI, cross-wavelet transform (XWT), and Pearson's correlation analyses. A positive correlation between MD and HD was found, with drought propagation times (DPTs) that ranged from 2 to 5 months and were shorter during the dry season. Zones with high tree cover and low forest loss exhibited longer DPTs, while areas with significant deforestation and dryland farming had shorter DPTs, highlighting the impact of land use on drought severity. These results underscore the need for reforestation, sustainable forest management, and water-efficient agricultural practices to enhance water retention and reduce drought severity. Land use regulations must be implemented to prevent deforestation and conserve critical watershed areas. Future research should use higher-resolution data, explore soil properties, and establish long-term monitoring programs. Policymakers should integrate these findings into their decision making, prioritize comprehensive drought management plans, and invest in data collection and analysis infrastructure to enhance drought resilience, mitigate socio-economic impacts, and promote sustainable development in the UNW and similar regions.

ACKNOWLEDGEMENTS

We extend our gratitude to DAAD and the Southeast Asian Regional Center for Graduate Study

and Research in Agriculture (SEARCA) for funding this research.

REFERENCES

Abbas S, Kousar S. Spatial analysis of drought severity and magnitude using the standardized precipitation index and streamflow drought index over the Upper Indus Basin, Pakistan. Environment Development Sustainability 2021;23(10):15314-40.

Bai X, Zhao W, Liu H, Zhang Y, Yang Q, Liu J, et al. Effects of precipitation changes and land-use alteration on streamflow: A comparative analysis from two adjacent catchments in the Qilian Mountains, arid northwestern China. Frontiers in Environmental Science 2023;11:Article No. 1097049.

Cao G, Scanlon BR, Han D, Zheng C. Impacts of thickening unsaturated zone on groundwater recharge in the North China Plain. Journal of Hydrology 2016;537:260-70.

Condon LE, Atchley AL, Maxwell RM. Evapotranspiration depletes groundwater under warming over the contiguous United States. Nature Communications 2020;11:Article No. 873.

Dalezios NR, Blanta A, Spyropoulos NV. Assessment of remotely sensed drought features in vulnerable agriculture. Natural Hazards and Earth System Science 2012;12(10):3139-50.

Ding Y, Gong X, Xing Z, Cai H, Zhou Z, Zhang D, et al. Attribution of meteorological, hydrological and agricultural drought propagation in different climatic regions of China. Agricultural Water Management 2021a;255:Article No. 106996.

Ding Y, Xu J, Wang X, Cai H, Zhou Z, Sun Y, et al. Propagation of meteorological to hydrological drought for different climate regions in China. Journal of Environmental Management 2021b;238:Article No. 111980.

Ding Y, Wang F, Mu Q, Sun Y, Cai H, Zhou Z, et al. Estimating land use/land cover change impacts on vegetation response to drought under 'Grain for Green' in the Loess Plateau. Land Degradation and Development 2021c;32(17):5083-98.

Fedele G, Locatelli B, Djoudi H, Colloff MJ. Reducing risks by transforming landscapes: Cross-scale effects of land-use changes on ecosystem services. PLoS One 2018;13(4): e0195895.

Gu L, Chen J, Yin J, Xu C-Y, Chen H. Drought hazard transferability from meteorological to hydrological propagation. Journal of Hydrology 2020;585:Article No. 124761.

Hansen MC, Potapov PV, Moore R, Hancher M, Turubanova SA, Tyukavina A, et al. High-resolution global maps of 21st-century forest cover change. Science 2013;342(6160):850-3.

Huang S, Li P, Huang Q, Leng G, Hou B, Ma L. The propagation from meteorological to hydrological drought and its potential influence factors. Journal of Hydrology 2017;547:184-95.

Kartika FD, Wijayanti P. Drought disaster modeling using drought index: A systematic literature review. IOP Conference Series: Earth and Environmental Science 2023;1190:Article No. 012026.

Khaki M, Forootan E, Kuhn M, Awange JL, van Dijk AIJM, Schumacher M, et al. Determining water storage depletion within Iran by assimilating GRACE data into the W3RA hydrological model. Advanced in Water Resources 2018;114:1-18.

Li C, Zhang X, Yin G, Xu Y, Hao F. Evaluation of drought propagation characteristics and influencing factors in an Arid Region of Northeast Asia (ARNA). Remote Sensing 2022;14(14):Article No. 3307.

Li Z, Huang S, Zhou S, Leng G, Liu D, Huang Q, et al. Clarifying the propagation dynamics from meteorological to hydrological drought induced by climate change and direct human activities. Journal of Hydrometeorology 2021;22(9):2359-78.

Lin Q, Wu Z, Zhang Y, Peng T, Chang W, Guo J. Propagation from meteorological to hydrological drought and its application to drought prediction in the Xijiang River Basin, South China. Journal of Hydrology 2023;617:Article No. 128889.

Luo X, Luo X, Ji X, Ming W, Wang L, Xiao X, et al. Meteorological and hydrological droughts in the Lancang-Mekong River Basin: Spatiotemporal patterns and propagation. Atmospheric Research 2023;293:Article No. 106913.

Nippgen F, McGlynn BL, Emanuel RE, Vose JM. Watershed memory at the Coweeta Hydrologic Laboratory: The effect of past precipitation and storage on hydrologic response. Water Resources Research 2016;52(3):1673-95.

Paiboonvorachat C, Oyana TJ. Land-cover changes and potential impacts on soil erosion in the Nan Watershed, Thailand. International Journal of Remote Sensing 2011;32(21):6587-609.

Plangoen P, Babel M. Projected rainfall erosivity changes under future climate in the Upper Nan Watershed, Thailand. Journal of Earth Science and Climatic Change 2014;5(10):Article No. 242.

Satriagasa MC, Tongdeenok P, Kaewjampa N. Assessing the implication of climate change to forecast future flood using SWAT and HEC-RAS model under CMIP5 climate projection in Upper Nan Watershed, Thailand. Sustainability 2023;15(6):Article No. 5276.

Shah D, Shah HL, Dave HM, Mishra V. Contrasting influence of human activities on agricultural and hydrological droughts in India. Science of the Total Environment 2021;774:Article No. 144959.

Tarigan S, Wiegand K, Sunarti, Slamet B. Minimum forest cover required for sustainable water flow regulation of a watershed: A case study in Jambi Province, Indonesia. Hydrology and Earth System Sciences 2018;22(1):581-94.

Ueangsawat K, Jintrawet A. The impacts of ENSO phases on the variation of rainfall and stream flow in the Upper Ping River Basin, Northern Thailand. Environment and Natural Resources Journal 2013;11(2):97-119.

Vahmani P, Jones AD, Li D. Will Anthropogenic warming increase evapotranspiration? examining irrigation water demand implications of climate change in California. Earth's Future 2021;10:e2021EF002221.

Vicente-Serrano SM, Beguería S, López-Moreno JI. A multiscalar drought index sensitive to global warming: The standardized precipitation evapotranspiration index. Journal of Climate 2010;23(7):1696-718.

Wan W, Zhao J, Li H, Mishra A, Hejazi M, Lu H, et al. A holistic view of water management impacts on future droughts: A global multimodel analysis. Journal of Geophysical Research Atmospheres 2018;123:5947-72.

Wang J, Wang W, Cheng H, Wang H, Zhu Y. Propagation from meteorological to hydrological drought and its influencing

factors in the Huaihe River Basin. Water 2021;13(14):Article No. 1985.

Xu Y, Zhang X, Hao Z, Singh VP, Hao F. Characterization of agricultural drought propagation over China based on bivariate probabilistic quantification. Journal of Hydrology 2021;598:Article No. 126194.

Xu Y, Zhang X, Wang X, Hao Z, Singh VP, Hao F. Propagation from meteorological drought to hydrological drought under the impact of human activities: A case study in Northern China. Journal of Hydrology 2019;579:Article No. 124147.

Yang H, Ma F, Yuan X. The role of human activities in the weakening of the propagation relationship between meteorological and hydrological droughts in the Heihe River Basin. Hydrological Process 2023;37(7):e14946.

Environment and Natural Resources Journal

Volume 23
Issue 1
2025

Habitat Categorization and Vegetation Mapping of Kumana National Park, Sri Lanka

Pasindu Rodrigo, Charani Gunathilaka, Dulan Jayasekara, and Dharshani Mahaulpatha*

Department of Zoology, Faculty of Applied Sciences, University of Sri Jayewardenepura, Sri Lanka

ARTICLE INFO

Received: 15 Apr 2024
Received in revised: 9 Oct 2024
Accepted: 16 Oct 2024
Published online: 12 Dec 2024
DOI: 10.32526/ennrj/23/20240104

Keywords:
Maximum likelihood classification/ Protected area/ Remote sensing/ Sentinel 2/ Vegetation classification

*** Corresponding author:**
E-mail: mahaulpatha@sjp.ac.lk

ABSTRACT

Remote sensing constitutes a broad and influential discipline that has assumed a significant role in vegetation mapping on a global scale in recent years. The availability of an accurate vegetation map assists future ecological studies and the management of protected areas. This study was conducted to identify and map the available habitats in Kumana National Park (KNP), Sri Lanka. We utilized multiple environmental covariates obtained via field surveys and remote sensing techniques for the initial categorization of habitats based on principal component analysis. Vegetation maps for KNP were generated by applying multiple classification algorithms to Sentinel 2 multispectral satellite imagery. The maximum likelihood classification (MLC) model generated the most accurate and detailed vegetation map for KNP, which was verified with ground truth data (overall accuracy of 93%; Kappa, 87%). The study's findings furnish precise insights into the vegetation cover of KNP, thereby augmenting knowledge on the spatial distribution of habitats to support the future work of researchers and park managers. This map offers significantly improved resolution and spatial detail compared to previous maps. It also increased the number of identified habitat types from four to six. These findings can be used to identify critical areas for both terrestrial and aquatic fauna within KNP and support habitat conservation and management strategies in the park.

1. INTRODUCTION

Vegetation is an attribute that describes the land use on Earth (Roy et al., 2015). Remote sensing has been important in vegetation mapping for the past few decades (Langley et al., 2001; Raynolds et al., 2019; Schindler et al., 2021; Mucsi and Bui, 2023). Past studies have been conducted to evaluate National Park vegetation to assess the land cover (Brown de Colstoun et al., 2003; Jiménez and Díaz-Delgado, 2015; Martinez del Castillo et al., 2015; Urban et al., 2018). These vegetation maps categorize the different types of vegetation that play a vital role in managing natural resources (Xiao et al., 2004), evaluating land use changes and management (Beuchle et al., 2015) and contributing to the conservation measures by generating remote sensed vegetation maps (Rose et al., 2015). The main goal of vegetation categorization is to group plant communities assumed to be similar, making it easier to describe the vegetation patterns in a particular geographic area. Traditional methods such as field surveys, literature studies, map interpretation, and collateral and supplementary data analysis are ineffective for acquiring vegetation cover when compared to novel remote sensing techniques due to the long-time consumption and frequently high cost (Xie et al., 2008). Moreover, the development and availability of various land use classification algorithms and models have made remote sensing techniques more versatile in this aspect (Otukei and Blaschke, 2010; Rodriguez-Galiano et al., 2012; Lyons et al., 2018; Mercier et al., 2019).

Remote sensing-based vegetation classification can be identified as the most effective method for generating habitat maps for larger protected areas where ground access is often restricted. There are several remote sensing approaches initiated for habitat

Citation: Rodrigo P, Gunathilaka C, Jayasekara D, Mahaulpatha D. Habitat categorization and vegetation mapping of Kumana National Park, Sri Lanka. Environ. Nat. Resour. J. 2025;23(1):28-39. (https://doi.org/10.32526/ennrj/23/20240104)

mapping in Sri Lanka (Dahdouh-Guebas et al., 2000; Nandasena et al., 2023), and this technology has been utilized for forest management and monitoring since (Jewell and Legg, 1993). However, only a handful of studies are available where in-depth analyses have been conducted regarding the vegetation classification and habitat mapping using remote sensing methods restricted to several protected areas, such as Wilpattu (Sandamali and Welikanna, 2018), Maduru Oya (Jayasekara et al., 2021), Horton Plains (Jayasekara et al., 2021) and Udawalawe (Perera et al., 2021) governed by the Department of Wildlife and Conservation (DWC) Sri Lanka. Furthermore, we have observed a lack of remote sensing tools utilization for identifying the types of vegetation in national parks located in the eastern and southern regions due to the unavailability of ground-truth observed data for verification. While Jayasekara et al. (2021) have comprehensively illustrated a vegetation map for Maduru Oya, a dry zone national park located near the border of eastern and Uva provinces we observed that detailed vegetation/habitat maps are not available for the national parks located in eastern and southern regions of the island. This motivated us to map the vegetation in Kumana National Park (KNP) located in the south-eastern dry zone of Sri Lanka utilizing remote sensing techniques.

Kumana National Park is a protected area under the Department of Wildlife Conservation and is ranked sixth in terms of park area. Previously, Kasige et al. (2020) have identified several habitat types (Water bodies, Forests, Grasslands, Bare lands, and Coastlands) in KNP to determine the habitat cover change over 15 years using NDVI data. However, our preliminary ground observations suggested that the map generated by Kasige et al. (2020) needs further improvements to illustrate the complex vegetation of KNP supported by ground reference data. NDVI is a method mostly used for vegetation categorization as well as the healthiness of vegetation (Mtibaa and Irie, 2016). The current study incorporated the NDVI to identify the photosynthetic (Healthy) vegetation inside the park. Furthermore, we incorporated the ground reference data, and composites of high-resolution multispectral satellite bands to conduct advanced vegetation mapping and classification.

Two main types of classifications can be identified in environmental land use mapping: unsupervised and supervised classification (Wu, 2018). The Maximum Likelihood Classification (MLC) algorithm is an effective model for the supervised classification technique (Ali et al., 2018; Navin and Agilandeeswari, 2019). However, vegetation mapping through Random Forest (RF) (Mohammadpour et al., 2022), k-Nearest Neighbours (kNN) (Sun et al., 2018) and Support Vector Machine (SVM) (Shi and Yang, 2015) have been identified as other alternative machine learning algorithms (Thanh Noi and Kappas, 2017). Forest-based classification is a multiple raster regression model that analyses multiple rasters such as NDVI along with satellite images while other applications are available as single raster models in ArcGIS Pro (ESRI, Redlands). As per the previous literature available for KNP, the previous identification of vegetation types was based on an unsupervised iso-cluster method (Kasige et al., 2020).

The present study aims to categorize the vegetation of KNP with the highest possible spatial accuracy. We aim to assess the applicability and accuracy of multiple classification algorithm models to generate a detailed vegetation map for the area. Due to the in-depth remote sensing analysis and comprehensive ground truth assessment and verification, we are convinced that the results of our research would be valuable from both a remote sensing and ecological perspective.

2. METHODOLOGY

2.1 Study area

The study was conducted from August 2022 to March 2023, for 8 months in KNP located in Ampara district along the southeast coast of Sri Lanka (Figure 1). The KNP was previously designated as Yala-East National Park in 1970, and the present name was declared in 2006 (Krishan et al., 2020). The park spreads over an area of 35,665 ha (357 km^2). KNP borders Kumbukkan Oya from the south and Panama-Kudumbigala sanctuary from the north (Krishan et al., 2020). The Kumana National Park belongs to the dry zone of Sri Lanka which has an altitude of the ranges from sea level to 90 meters. The vegetation of the park is mainly dry mixed evergreen forest (Figure 2), scrublands, and dunes (Krishan et al., 2020). The dry season in Kumana generally runs from February to September and the wet season runs from October to December while the mean annual temperature is 27.30°C and the area receives 1,300 millimeters of annual rainfall (MoMD&E, 2016).

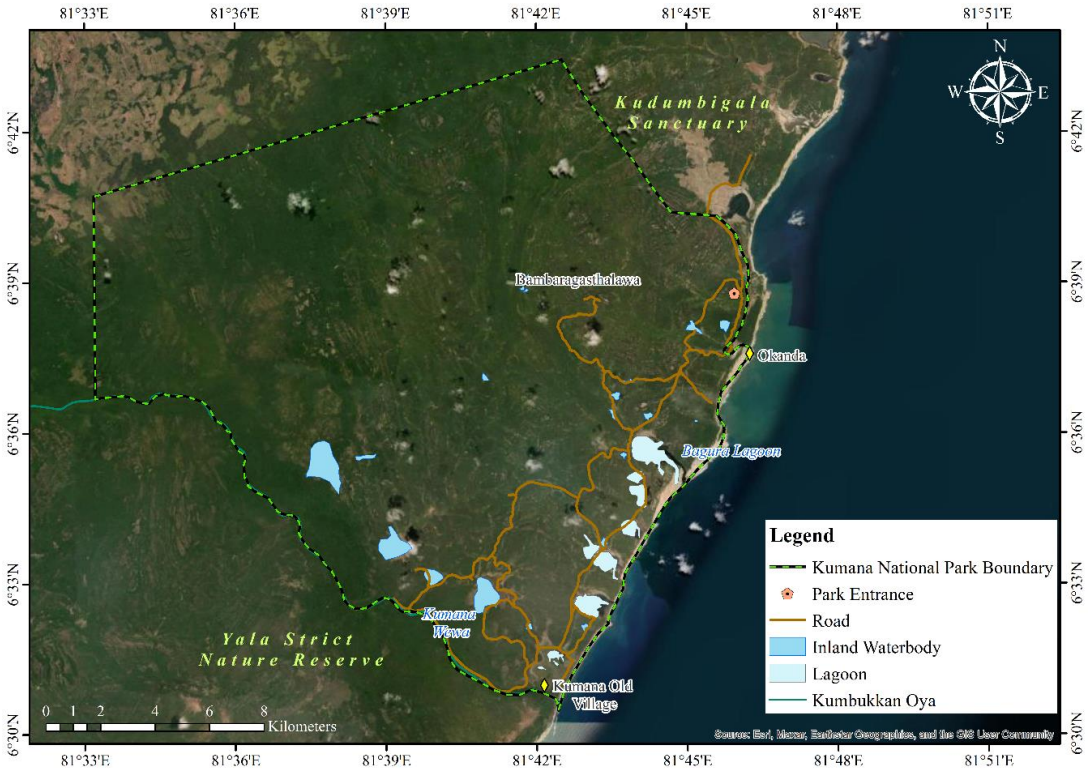

Figure 1. General map of the Kumana National Park

Figure 2. View of Kumana National Park from the Bambaragasthalawa rocky mountain. Tropical dry mixed evergreen forest habitats with rocky clusters are clearly visible

2.2 Survey for the habitat categorization

A preliminary survey was conducted based on the available literature (Gunatilleke and Gunatilleke, 1990; Gunatilleke et al., 2008; Kasige et al., 2020) to identify the nomenclature used for the vegetation types of the region. With the aid of online ArcGIS (Esri, Redlands, USA) base maps, the general borders of the major vegetation types were created on a physiognomic basis (Dias et al., 2004). Sampling quadrats of 10×10 m were selected randomly within

larger 2×2 km^2 plots ensuring the representation of different habitat types within the KNP. Most of the sampling was conducted within the eastern region of the park due to the limitations in ground accessibility. We traversed the area by 4×4 vehicles and ground trekking up to six km to establish 90 quadrats. At each quadrat, the environmental parameters were obtained in a standard manner following the methods explained in Table 1. Principal component analysis (PCA) in R version 4.3.3 (R Core Team, 2024) was performed to create clusters of similar vegetation/land cover types.

Table 1. Environmental covariate and the standard method

Environmental parameter	Abbreviation	Standard method
Canopy cover (%)	CC	CC was calculated by photo point analysis using TinEye Online Color Extractor and eCognition software package
Litter cover (%)	LC	LC was estimated by obtaining the litter cover inside 1×1 m^2 quadrats ocularly within a 10×10 m^2 plot
Litter depth (cm)	LD	LD was measured with a metal ruler within multiple 1×1 m^2 quadrats and averaged
Horizontal visibility (%)	HV	HV was measured ocularly by visualizing an object 30 m far from the observer in the habitat and the visibility was ranked numerically from 1 to 10 10=Maximum 0=Minimum
Ground vegetation cover (%)	GV	GV was estimated by observing the ground vegetation less than 10 cm (<10 cm) height within 10×10 m^2 quadrats ocularly and averaged.
Rock availability (%)	RA	RA was estimated ocularly by observing the rocks in the selected location using 10×10 m^2 quadrats ranked 0 -10 0=Minimum 10=Maximum
Canopy height (m)	CH	CH was measured using a Rangefinder and ranked 0 -10 0=Minimum 10=Maximum

2.3 Generation of the vegetation map using different classification models

Atmospherically corrected SR (Surface reflectance) satellite images from the Sentinel 2A dataset were used to determine the spatial distribution of habitat/vegetation types of the study site. The images were obtained from the Copernicus Open Access Hub database (https://scihub.copernicus.eu/) for the NDVI and vegetation analysis. Google Earth Engine (GEE) geospatial processing service in the Google Cloud Platform was used to filter the satellite images captured from January 1, 2018 to December 31, 2023. Cloud and cirrus correction were obtained using the "maskS2clouds" function in GEE. The mosaic function in Google Earth Engine (GEE) was used to combine multiple images into a single image using the filtered image collection with low cloud cover for the corresponding period. A multiband composite image was generated including the spectral bands B1, B2, B3, B4, B5, B6, B7, and B8. The generated multispectral composite image was downloaded from the GEE and further analyzed in Arc GIS Pro (ESRI, Redlands). Different band combinations such as 4,3,2 (True color), 8,4,3 (False color infrared), 5,4,3 (Color Infrared-Vegetation), 5,6,4 (Land/water), etc. were utilized to identify and gather detailed information about the vegetation and water areas (Mtibaa and Irie, 2016; Simonetti et al., 2014). The Normalized Difference Vegetation Index (NDVI) was used to assess the healthiness of the vegetation and greenness (Chlorophyll content). NDVI was determined using the formula: (NIR - Red)/(NIR + Red) where NIR and Red are the near-infrared and red bands respectively (Mtibaa and Irie, 2016).

Before image classification, training samples were created using the ground observation taken from January 2023 to March 2023. The supplementary training data was obtained utilizing ArcGIS base map imaginary data (Esri, Digital Globe) for inaccessible areas and outside the eastern region of the park. Five different classification functions namely, Maximum Likelihood Classification (MLC), Random Forest (RF), k-nearest Neighbour (kNN), Support Vector Machine (SVM), and Forest Based Classification (FBC) algorithm were carried out (da Silveira et al., 2022) ArcGIS Pro 3.2. The software extrapolated the

given ground truth data and used the supervised classification algorithm to create complete land cover/vegetation cover maps of KNP. Post-classification processing was conducted on the classified images using the tools majority filter, boundary clean, region group, and nibble for the noise removal and smoothing of the generated maps. ArcMap area calculation option in ArcGIS Pro 3.2 was aided to estimate the area of each habitat category. The overall framework for the vegetation mapping is illustrated in Figure 3.

2.4 Accuracy assessment of generated maps

The forecasted outcomes were compared to ground reference data as part of an accuracy assessment. Observations collected on the ground and base-map imagery were used to verify the accuracy of the map. Arc Map was used to build the error matrix and calculate the Kappa coefficient (κ) (Abbas and Jaber, 2020), and the accuracy of generated maps using different models was compared to select the most accurate classification model.

$$\text{Kappa coefficient } (\kappa) = \frac{(TS \times TCS) - \Sigma(\text{Column Total} \times \text{Row Total})}{(TS \times TS) - \Sigma(\text{Column Total} \times \text{Row Total})} \times 100 \quad (1)$$

(While; TS=total samples; TCS=total corrected samples)

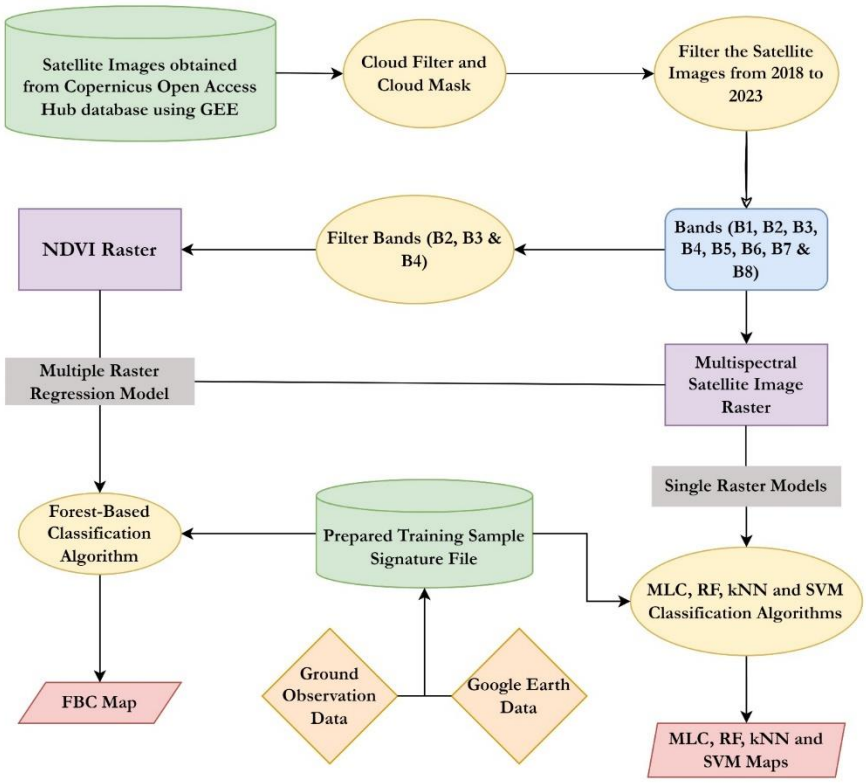

Figure 3. Overall research framework for the vegetation mapping analysis

3. RESULTS AND DISCUSSION

3.1 Habitat categorization of KNP

The principal component analysis (PCA) clustered five vegetation types in KNP namely: Tropical dry-mixed evergreen forest, Tropical thorn forest (Scrubland), Dry riverine forest, Seasonal grassland, and Rocky outcrops (Figure 4(b)). The tropical dry mixed evergreen forests are dominated by *Manilkara hexandra* ('Palu') and *Drypetes sepiaria* ('Veera') while *Diospyros quaesita* ('Kalu Madiriya') and *Diospyros ovalifolia* ('Kunumella') were also present in this habitat. The tropical thorn forest comprised of thorny shrubs such as *Dichrostachys cinerea* ('Andara'), *Bauhinia racemosum* ('Mila'), *Salvadora persica* ('Maliththan'), *Carissa spinarum* ('Heen Karaba'), and *Ziziphus oenoplia.* ('Heen Eraminiya'). *Terminalia arjuna* ('Kumbuk') was dominant in the dry riverine forest whereas tiny clusters of *Walsura trifoliolata* ('Kiri Koon') and *Drypetes sepiaria* ('Veera') were located along with the riverbanks and the adjacent area (Table 2). Most of these dry riverine forests get flooded during the rainy

season. Seasonal grasslands and bare land areas are profoundly located around the water bodies of the park. Most of these areas are swamped occasionally and temporal shifts can be observed turning them into either seasonal grasslands or bare lands based on the rainfall and water levels. Rocky outcrops were identified as areas with a mosaic distribution of rocks within the forest clusters including several rocky mountain areas that emerge above the generally plain surrounding forested landscape. The vegetation of these habitats was like the tropical dry mixed evergreen forests and tropical dry thorn forests (Figure 5).

Table 2. Prominent plant species of each forest habitat types located in KNP

Forest habitat type	Prominent plant species	Plant family	Local name (*'In Sinhala'*)
Tropical dry mixed Evergreen forest	*Manilkara hexandra*	Sapotaceae	Palu
	Drypetes sepiaria	Putranjivaceae	Veera
	Diospyros quaesita	Ebenaceae	Kalu Madiriya
	Diospyros ovalifolia	Ebenaceae	Kunumella
Tropical thorn forest	*Dichrostachys cinerea*	Fabaceae	Andara
	Bauhinia racemosum	Fabaceae	Mila
	Salvadora persica	Salvadoraceae	Maliththan
	Carissa spinarum	Apocynaceae	Heen Karaba
	Ziziphus oenoplia	Rhamnaceae	Heen Eraminiya
Dry riverine forest	*Terminalia arjuna*	Combretaceae	Kumbuk
	Walsura trifoliolata	Meliaceae	Kiri Koon

According to the loading plot (Figure 4(a)) the canopy height, litter cover, and horizontal visibility were the significant contributing factors to shape the structure of tropical dry-mixed evergreen forests. The tropical dry-mixed evergreen forest and scrublands are composed of several shared features, but the two habitats can be distinctly identified. The ground vegetation and canopy cover negatively influenced the tropical thorn forest (Scrublands). The dry riverine forest cluster was separated via litter depth and the canopy height. Seasonal grasslands indicated a low canopy cover and litter cover with a high horizontal visibility. Rock availability exhibited a positive influence on the determination of rocky outcrops.

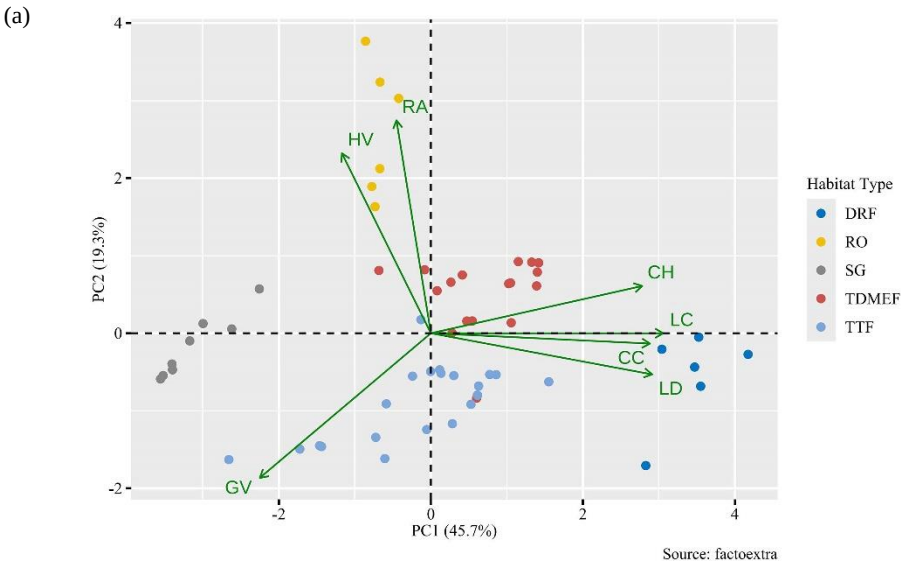

Figure 4. (a) Loading plot and (b) Score plot of PCA conducted for KNP through a field survey [*TDMEF - Tropical Dry Mixed Evergreen Forest, SG - Seasonal Grassland and DRF - Dry Riverine Forest, TTF - Tropical Thorn Forest, RO - Rocky Outcrops]

(b)

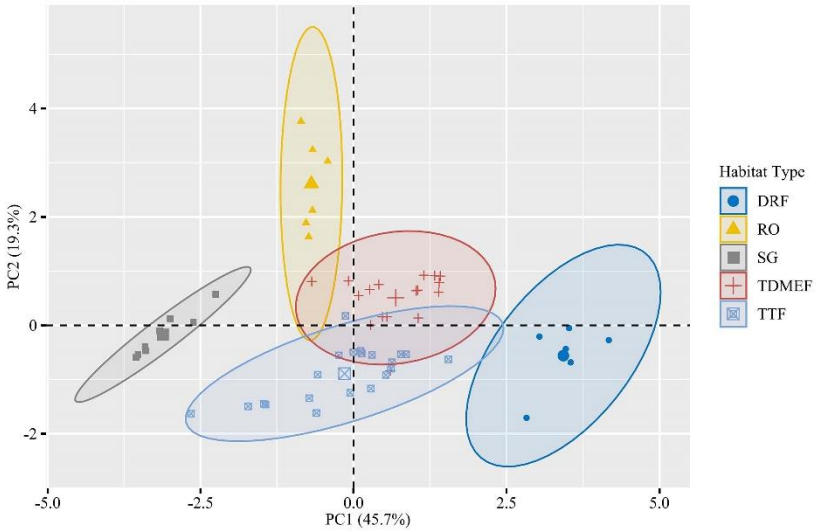

Figure 4. (a) Loading plot and (b) Score plot of PCA conducted for KNP through a field survey [*TDMEF - Tropical Dry Mixed Evergreen Forest, SG - Seasonal Grassland and DRF - Dry Riverine Forest, TTF - Tropical Thorn Forest, RO - Rocky Outcrops] (cont.)

Figure 5. Terrestrial habitats in Kumana National Park; (a) Tropical Dry-mixed Evergreen Forest; (b) Tropical Thorn Forest; (c) Rocky Outcrops; (d) Dry Riverine Forest; (e) Seasonal Grassland; and (f) Sand and Dunes along the coastline

3.2 Generation of classified habitat maps using supervised data

Four post-processed maps were generated through Maximum Likelihood Classification (MLC), Random Forest (RF), k-Nearest Neighbour (kNN), and Support Vector Machine (SVM) classification models. The Forest-Based Classification (FBC) model was not post-processed due the poor accuracy. Five terrestrial habitats and two aquatic habitats were classified in the generated maps. Terrestrial habitats were, namely, Tropical Dry-mixed Evergreen Forests, Tropical Thorn Forests (Scrublands), Seasonal Grasslands, Rocky Outcrops, and Sand Dunes (Figure 5). All seasonal and permanent waterbodies including rivers (Kumbukkan Oya and estuaries) were considered as aquatic habitats. The dry riverine forest area near the Kumbukkan Oya River remained as undefined in the categorized map probably due to the minor proportion of this forest type along a small stretch beside the river. From all the terrestrial habitats, Tropical dry-mixed evergreen forests accounted for an area of 28,562 ha followed by Tropical thorn forests (Scrublands) which covered 5,218 ha. The tropical dry-mixed evergreen forests covered 77.9% of the park followed by the tropical thorn forests, rocky outcrops, and seasonal grasslands covering 14.3%, 1.9%, and 1.3% of the park respectively (Table 4). Waterbodies cover 1.4% of the total park which are situated mostly within the eastern region of the park. Sand dunes and river areas accounted for a relatively smaller area (<1%) (Table 3).

3.3 Accuracy assessment of generated maps

The maximum value of the Kappa coefficient (κ) was achieved for the classified map using the maximum likelihood classification model (MLC) which had an overall accuracy of 91% (Figure 6). Other maps had a lower accuracy with Kappa coefficients less than 0.87 (κ<0.87). Each classified map was visually compared with satellite images obtained from ArcGIS Pro 3.2 imagery data for further verification (Figure 7).

Table 3. Accuracy assessment table for the Maximum Likelihood Classification (MLC) model

	Dry-mixed Evergreen	Tropical Thorn	Rocky Outcrop	Bare/Grass land	Waterbody	River	Sand and Dunes	Total (User)	User Accu (%)
Dry-mixed Evergreen	62	0	0	0	0	0	0	62	100
Tropical Thorn	5	11	0	0	0	0	1	17	64.7
Rocky Outcrop	1	0	6	0	0	0	0	7	85.7
Bare/Grass land	0	0	0	4	0	0	0	4	100
Waterbody	0	0	0	0	4	0	0	4	100
River	0	0	0	0	0	3	0	3	100
Sand and Dunes	0	0	0	0	0	0	3	3	100
Total (Producer)	68	11	6	4	4	3	4	100	-
Producer Accu (%)	91.2	100	100	100	100	100	75	-	91

Table 4. Habitat availability based on vegetation mapping in KNP

Habitat categories in KNP	Area proportion (%)	Area (ha)
Tropical dry-mixed evergreen forest	77.9	28,562
Tropical thorn forest (Scrubland)	14.3	5,218
Rocky outcrops	1.9	692
Bare land and Seasonal grass	1.3	461
Waterbodies	1.4	508
Sand and dunes	0.7	262
River	0.2	68
Total area		35,773

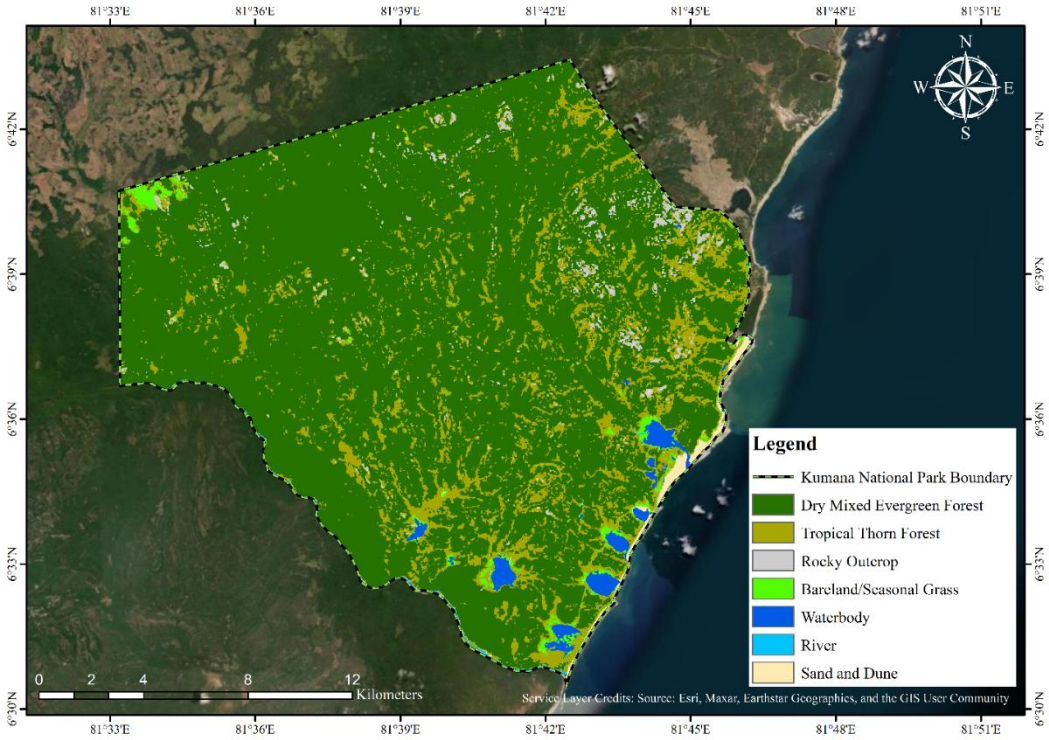

Figure 6. Categorized map using Maximum Likelihood Classification (MLC) model with available habitat types in Kumana National Park

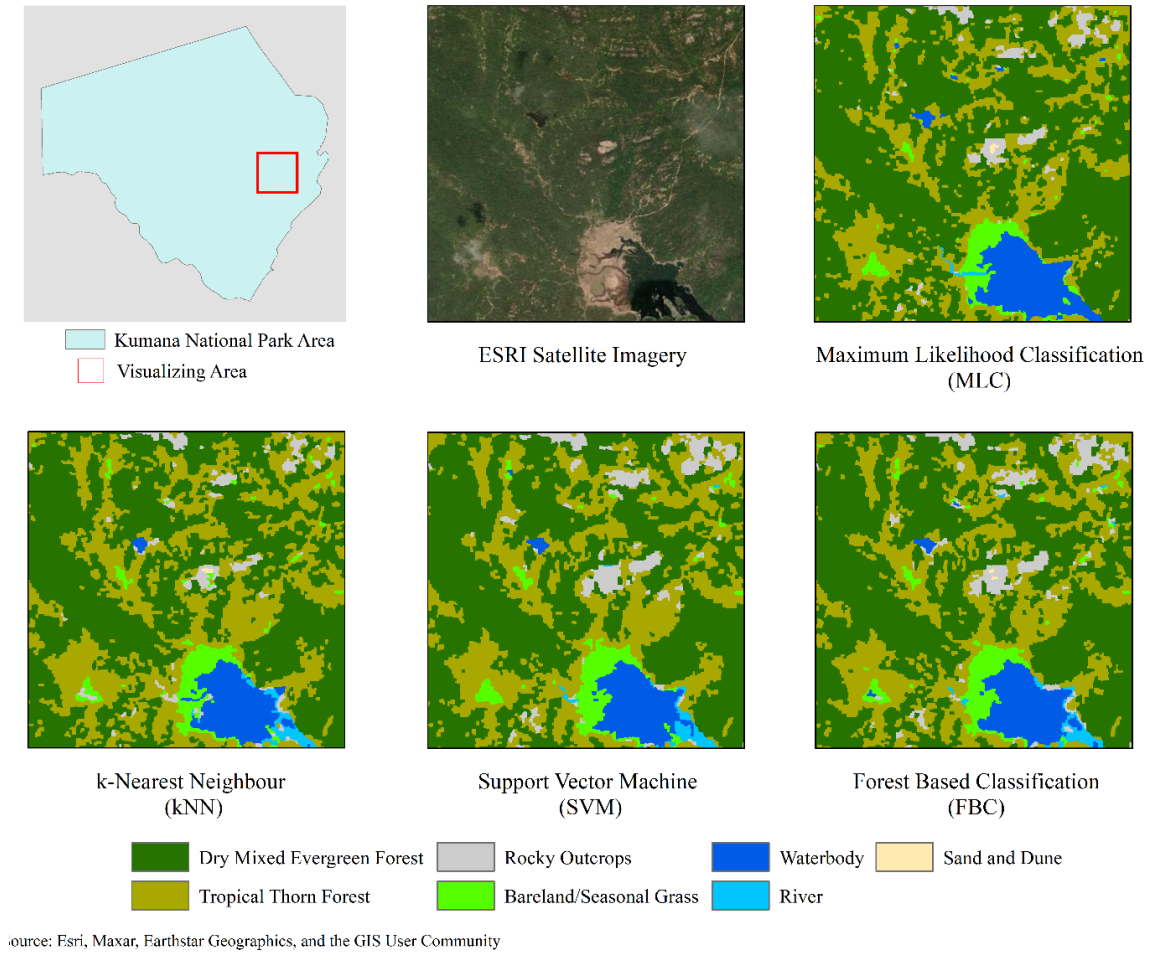

Figure 7. Vegetation maps developed using different models for the Kumana National Park

4. DISCUSSION

Our study presents a detailed habitat map for Kumana National Park (KNP), which can be utilized for park management decisions and future ecological research. This map offers significantly improved resolution and spatial detail compared to the previous map by Kasige et al. (2020). By incorporating multispectral data and ground-based surveys, we achieved a higher accuracy level. While Kasige et al. (2020) identified four habitat types, our study identified six: 1) Dry-mixed evergreen forest, 2) Tropical thorn forest, 3) Rocky outcrop, 4) Dry riverine forest, and 5) Seasonal grasslands through PCA analysis. Sand dunes were excluded from the PCA due to their low area percentage.

Despite the PCA identifying the dry riverine forest adjacent to the Kumbukkan Oya River, none of the classification models were able to distinguish it as a unique habitat type. Consequently, this habitat was excluded from our final map due to misidentification with dry-mixed evergreen forest and its relatively low spatial distribution. Our findings contrast sharply with the habitat areas reported for 2019 by Kasige et al. (2020), who noted only 124.43 km² of forest cover and 57.80 km² of grasslands. In contrast, we identified a forested area of 337.8 km², encompassing both dry-mixed evergreen and tropical thorn forests, while grasslands cover only 4.61 km². This discrepancy likely arises from our identification of tropical thorn forests as a distinct habitat type and the enhanced clarity achieved through improved spatial resolution and mosaicking of spectral data, resulting in a temporally representative satellite image instead of a single-point NDVI raster.

Our study highlights Google Earth Engine's (GEE) potential for filtering, preprocessing, and raster mosaicking over a time range, which significantly improved the classification's overall accuracy by reducing temporal bias. Accurate habitat classification is crucial for park managers, enabling them to make more informed and effective management decisions.

However, Kumana National Park currently generates significant revenue, largely due to its appeal to tourists interested in its diverse mammalian and avian fauna (SLTDA, 2019). Therefore, our study offers valuable insights for managing the recreational road network and camping sites maintained by the Department of Wildlife Conservation (DWC). We recommend an integrated approach that balances visitor satisfaction with habitat conservation to ensure sustainable tourism within the park. Our findings can assist in spatially identifying areas with high potential for wildlife viewing, while also safeguarding more sensitive and critical habitats. The use of freely available satellite data allowed us to conduct this study cost-effectively (Gil et al., 2011), and the use of remote sensing multispectral products, combined with verification through Google Earth and Arc basemaps, overcame accessibility limitations.

Gunatilleke et al. (2008) observed that most of Sri Lanka's natural forest area is covered by tropical dry mixed evergreen forest. Similarly, we found that approximately 75% of KNP is covered by this forest type, primarily located away from recreational roads and within the park's interior. These forests, characterized by a 12-meter canopy height with prominent species such as *Manilkara hexandra*, *Diospyros quaesita*, and *Diospyros ovalifolia*, provide critical habitats for elusive mammalian species. In contrast, the tropical thorn forests, which are the second-largest habitat type in KNP, feature thorny vegetation and are primarily found near recreational roads and aquatic bodies. This habitat includes species such as *Dichrostachys cinerea* and *Ziziphus* sp., along with other characteristic flora.

The dry riverine forest, although less spatially extensive, is another significant habitat along KNP's southern boundary, nourished by the Kumbukkan River. Dominated by *Terminalia arjuna* (Kumbuk), these forests exhibit a denser canopy near the riverbanks, withstanding seasonal floods and creating a shaded environment with lower ground vegetation than the tropical dry-mixed evergreen forests. Grasslands in KNP, consisting of short seasonal grasses, are primarily located near major water bodies and are subject to seasonal flooding. These grasslands, which are most visible during the dry season, are easily distinguishable in satellite images due to their high ground vegetation cover and lack of a canopy layer. Seasonal grasslands and bare lands with open soil and mudflats cluster together due to similar pixel values.

Initially, we used LANDSAT 9 satellite imagery from the United States Geological Survey (USGS) for vegetation classification. However, due to its low resolution, we opted for Sentinel-2A images from the Copernicus Open Access Hub. Among the various classification models we tested, Maximum Likelihood Classification (MLC), after post-modification, produced the most accurate map, as evaluated using the kappa coefficient. This map accurately depicted the physical features of the area,

including forest habitats, rocky outcrops, grasslands, and water bodies. Thus, we propose the vegetation map (Figure 7) for KNP using the MLC algorithm. Despite the availability of newer classification algorithms, the MLC model remains highly competent in achieving high accuracy. We believe our study will support decision-makers and relevant authorities in managing protected areas more effectively.

5. CONCLUSION

The findings of this study offer modern solutions for vegetation categorization in future ecological research. Kumana National Park is predominantly covered by dry mixed evergreen forest, followed by tropical thorn forest, resulting in a substantial forest cover of 92.2%. The habitat map we generated, along with the associated spatial parameters, can be used to identify critical areas for both terrestrial and aquatic fauna within KNP. These findings can be effectively utilized to support habitat conservation and management strategies in the park.

ACKNOWLEDGEMENTS

We appreciate the support received from all the staff of Kumana National Park, Sri Lanka. We thank the Department of Wildlife Conservation for granting permission to conduct our research under Permit No: WL/3/2/44/22. We would also like to express our sincere gratitude to the Department of Zoology, the University of Sri Jayewardenepura, the Wildlife Circle, and the Rufford small grant program (Grant ID: 38961-2) for the facilities and equipment provided. We humbly appreciate Mr. R.A.D. Samaranayaka (Park Warden - KNP), Mr. Wasantha Disanayaka (Wildlife Range Assistant), and Mr. Ajith Kumara (Volunteer Guide) for the field assistance throughout our work.

REFERENCES

Abbas Z, Jaber HS. Accuracy assessment of supervised classification methods for extraction land use maps using remote sensing and GIS techniques. IOP Conference Series Material Science Engineering 2020;745:Article No. 012166.

Ali MZ, Qazi W, Aslam N. A comparative study of ALOS-2 PALSAR and Landsat-8 imagery for land cover classification using maximum likelihood classifier. The Egyptian Journal of Remote Sensing and Space Science 2018;21:29-35.

Beuchle R, Grecchi RC, Shimabukuro YE, Seliger R, Eva HD, Sano E, et al. Land cover changes in the Brazilian Cerrado and Caatinga biomes from 1990 to 2010 based on a systematic remote sensing sampling approach. Applied Geography 2015;58:116-27.

Brown de Colstoun E, Story MH, Thompson C, Commisso K, Smith TG, Irons JR. National Park vegetation mapping using multitemporal Landsat 7 data and a decision tree classifier. Remote Sensing Environment 2003;85(3):316-27.

Dahdouh-Guebas F, Hettiarachchi S, Koedam N. Four-decade vegetation dynamics in Sri Lankan mangroves as detected from sequential aerial photography: A case study in Galle. Bulletin of Marine Science 2000;67(2):741-59.

Dias E, Elias RB, Nunes V. Vegetation mapping and nature conservation: A case study in Terceira Island (Azores). Biodiversity Conservation 2004;13(8):1519-39.

Gil A, Yu Q, Lobo A, Lourenço P, Silva L, Calado H. Assessing the effectiveness of high resolution satellite imagery for vegetation mapping in small islands protected areas. Journal of Coast Research 2011;64(2):1663-7.

Gunatilleke N, Gunatilleke S. Distribution of floristic richness and its conservation in Sri Lanka on JSTOR. Conservation Biology 1990;4(1):21-31.

Gunatilleke N, Pethiyagoda R, Gunatilleke S. Biodiversity of Sri Lanka. Journal of National Science Foundation 2008; 36:25-62.

Jayasekara D, Kumara P, Mahaulpatha W. Mapping the vegetation cover and habitat categorization of *Maduru Oya* and Horton Plains National Parks using LANDSAT 8 (OLI) imagery to assist the ecological studies. WILDLANKA 2021;9(1):122-35.

Jewell N, Legg CA. A remote sensing/GIS database for forest management and monitoring in Sri Lanka. Proceedings of the 1993 ESRI User Conference for Southeast Asia: Kuala Lumpur, Malaysia; 1993.

Jiménez M, Díaz-Delgado R. Towards a standard plant species spectral library protocol for vegetation mapping: A case study in the Shrubland of Doñana National Park. ISPRS International Journal of Geoinformation 2015;4(4):2472-95.

Kasige RH, Wijesinghe M, Niroshan JJ. Habitat-cover assessment in the Kumana National Park, Sri Lanka using multi temporal satellite data. Proceedings of the 9th Young Scientists Forum (YSF) Research Symposium; 2020.

Krishan K, Wijesinghe M, Ransika Gulegoda C, Ranasinghe T. Protected area offences in Sri Lanka: A case study of the Kumana National Park and Panama-Kudumbigala Sanctuary. WILDLANKA 2020;8(3):108-19.

Langley SK, Cheshire HM, Humes KS. A comparison of single date and multitemporal satellite image classifications in a semi-arid grassland. Journal of Arid Environments 2001; 49(2):401-11.

Lyons MB, Keith DA, Phinn SR, Mason TJ, Elith J. A comparison of resampling methods for remote sensing classification and accuracy assessment. Remote Sensing of Environment 2018;208:145-53.

Martinez del Castillo E, García-Martin A, Longares Aladrén LA, de Luis M. Evaluation of forest cover change using remote sensing techniques and landscape metrics in Moncayo Natural Park (Spain). Applied Geography 2015;62:247-55.

Mercier A, Betbeder J, Rumiano F, Baudry J, Gond V, Blanc L, et al. Evaluation of Sentinel-1 and 2 time series for land cover classification of forest-agriculture mosaics in temperate and tropical landscapes. Remote Sensing 2019;11(8):Article No. 979.

Mohammadpour P, Viegas DX, Viegas C. Vegetation mapping with random forest using Sentinel 2 and GLCM texture feature: A case study for Lousã Region, Portugal. Remote Sensing 2022;14(18):rticle No. 4585.

Ministry of Mahaweli Development and Environment (MoMD&E). National Biodiversity Strategic Action Plan 2016-2022. Colombo, Sri Lanka: MoMD&E; 2016.

Mtibaa S, Irie M. Land cover mapping in cropland dominated area using information on vegetation phenology and multi-seasonal Landsat 8 images. Euro-Mediterranean Journal of Environmental Integration 2016;1(1):Article No. 6.

Mucsi L, Bui DH. Evaluating the performance of multi-temporal synthetic-aperture radar imagery in land-cover mapping using a forward stepwise selection approach. Remote Sensing Applications: Society and Environment 2023;30:Article No. 100975.

Nandasena WDKV, Brabyn L, Serrao-Neumann S. Monitoring invasive pines using remote sensing: A case study from Sri Lanka. Environmental Monitoring and Assessment 2023;195(2):Article No. 347.

Navin MS, Agilandeeswari L. Land use land cover change detection using K-means clustering and maximum likelihood classification method in the Javadi Hills, Tamil Nadu, India. International Journal of Engineering and Advanced Technology 2019;9(13):51-6.

Otukei JR, Blaschke T. Land cover change assessment using decision trees, support vector machines and maximum likelihood classification algorithms. International Journal of Applied Earth Observation and Geoinformation 2010;12:27-31.

Perera WPTA, Prematilaka PHKLA, Haseena MHA, Athapaththu AHLCM, Wijesinghe MR. Changes in habitat coverage from 2005 to 2019 in the Udawalawe National Park, Sri Lanka. Ceylon Journal of Science 2021;50(4):Article No. 467.

R Core Team. R: A Language and Environment for Statistical Computing. Vienna, Austria: R Foundation for Statistical Computing; 2024.

Raynolds MK, Walker DA, Balser A, Bay C, Campbell M, Cherosov MM, et al. A raster version of the Circumpolar Arctic Vegetation Map (CAVM). Remote Sensing of Environment 2019;232:Article No. 111297.

Rodriguez-Galiano VF, Ghimire B, Rogan J, Chica-Olmo M, Rigol-Sanchez JP. An assessment of the effectiveness of a random forest classifier for land-cover classification. ISPRS Journal of Photogrammetry and Remote Sensing 2012; 67:93-104.

Rose RA, Byler D, Eastman JR, Fleishman E, Geller G, Goetz S, et al. Ten ways remote sensing can contribute to conservation. Conservation Biology 2015;29:350-9.

Roy PS, Behera MD, Murthy MSR, Roy A, Singh S, Kushwaha SPS, et al. New vegetation type map of India prepared using satellite remote sensing: Comparison with global vegetation maps and utilities. International Journal of Applied Earth Observation and Geoinformation 2015;39:142-59.

Sandamali KUJ, Welikanna DR. Deforestation or reforestation, a time series remote sensing perspective of Wilpattu National Park, Sri Lanka. Journal of Applied Mathematics and Computation 2018;2(10):473-82.

Schindler J, Dymond JR, Wiser SK, Shepherd JD. Method for national mapping spatial extent of southern beech forest using temporal spectral signatures. International Journal of Applied Earth Observation and Geoinformation 2021;102:Article No. 102408.

Shi D, Yang X. Support Vector Machines for Land Cover Mapping from Remote Sensor Imagery. In: Monitoring and Modelling of Global Changes: A Geomatics Perspective. Dordrecht, Springer; 2015.

da Silveira VA, Veloso GV, de Paula HB, dos Santos AR, Schaefer CEGR, Fernandes-Filho EI, et al. Modelling and mapping of Inselberg habitats for environmental conservation in the Atlantic Forest and Caatinga domains, Brazil. Environmental Advances 2022;8:Article No. 100209.

Simonetti D, Preatoni D, Simonetti E. Phenology-Based Land Cover Classification Using Landsat 8 Time Series. Publications Office of the European Union; 2014.

Sri Lanka Tourism Development Authority (SLTDA). Annual Statistical Report of Sri Lanka Tourist Development Authority. Sri Lanka: SLTDA; 2019.

Sun H, Wang Q, Wang G, Lin H, Luo P, Li J, et al. Optimizing kNN for mapping vegetation cover of arid and semi-arid areas using Landsat images. Remote Sensing 2018; 10(8):Article No. 1248.

Thanh Noi P, Kappas M. Comparison of random forest, k-Nearest Neighbor, and support vector machine classifiers for land cover classification using Sentinel-2 imagery. Sensors 2017;18(2):Article No. 18.

Urban M, Berger C, Mudau T, Heckel K, Truckenbrodt J, Onyango Odipo V, et al. Surface Moisture and Vegetation Cover Analysis for Drought Monitoring in the Southern Kruger National Park Using Sentinel-1, Sentinel-2, and Landsat-8. Remote Sensing 2018;10(9):Article No. 1482.

Wu Q. GIS and Remote Sensing Applications in Wetland Mapping and Monitoring. In: Huang B, editor. Comprehensive Geographic Information Systems, Vol. 2. Elsevier; 2018. p. 140-57.

Xiao X, Zhang Q, Braswell B, Urbanski S, Boles S, Wofsy S, et al. Modeling gross primary production of temperate deciduous broadleaf forest using satellite images and climate data. Remote Sensing of Environment 2004;91(2):256-70.

Xie Y, Sha Z, Yu M. Remote sensing imagery in vegetation mapping: A review. Journal of Plant Ecology 2008;1(1):9-23.

Environment and Natural Resources Journal

Volume 23
Issue 1
2025

The Effectiveness of an Anoxic-Oxic-Anoxic-Oxic Sequencing Batch Reactor System (A2/O2-SBR) to Treat Electroplating Wastewater and the Bacterial Community within the System

Tanta Suriyawong[1], Sasidhorn Buddhawong[1*], Thanit Swasdisevi[2], and Suntud Sirianuntapiboon[3]

[1]*Division of Environmental Technology, School of Energy, Environment and Material, King Mongkut's University of Technology Thonburi, Thailand*
[2]*Division of Thermal Technology, School of Energy, Environment and Material, King Mongkut's University of Technology Thonburi, Thailand*
[3]*Office of the Election Commission of Thailand, The Government Complex Commemorating His Majesty, Bangkok, Thailand*

ARTICLE INFO

Received: 3 May 2024
Received in revised: 9 Oct 2024
Accepted: 16 Oct 2024
Published online: 25 Dec 2024
DOI: 10.32526/ennrj/23/20240134

Keywords:
Sequencing batch reactor/ Anoxic:oxic/ A2/O2-SBR/ Heavy metals/ Electroplating wastewater/ Bacterial community

*** Corresponding author:**
E-mail:
sasidhorn.bud@kmutt.ac.th

ABSTRACT

This study presents an examination of the effectiveness of an anoxic-oxic-anoxic-oxic sequencing batch reactor (A2/O2-SBR) for treating electroplating wastewater (EPWW). The A2/O2-SBR was monitored for 60 days and the bacterial composition in the treatment system was determined. The system consisted of four reactors, which had the following anoxic/oxic ratios: reactor-I, 0:9 h; reactor-II, 2:7 h; reactor-III, 4.5:4.5 h; and reactor-IV, 7:2 h. The combined cycle time of the reactors was 12 h, the hydraulic retention time (HRT) was five days, and the total volume of mixed liquor suspended solids (MLSS) was 2,000 mg/L. The results demonstrate the importance of an anoxic period for the treatment of heavy metals. Most of the ammonium nitrogen (NH_4^+-N), Total Kjeldahl nitrogen (TKN), and total nitrogen (TN) were removed during the oxic period. However, as the anoxic period increased, the amounts of TKN, nitrite nitrogen (NO_2^--N), nitrate nitrogen (NO_3^--N), and TN declined. Reactor-IV showed a high removal efficiency for heavy metals (Zn^{2+}, 89.74%; Cd^{2+}, 81.37%), TKN (89.20%), and TN (84.25%), and also effectively treated NH_4^+-N (78.84%), biochemical oxygen demand (BOD_5; 93.5%), and chemical oxygen demand (COD; 84.9%). Reactor-IV showed an appropriate difference in the dissolved oxygen (DO) concentration between the anoxic period and oxic period (2.12-2.00 mg/L). The main bacterial phyla in the treatment system were Proteobacteria, Actinobacteria, and Firmicutes, while *Pseudomonas vancouverensis* and *Cryobacterium arcticum* were the most common species. The anoxic period and bacterial community have significantly demonstrated the ability to remove Zn^{2+} and Cd^{2+} for effective treatment of EPWW.

1. INTRODUCTION

Heavy metals are common in various industries, including galvanizing, electroplating, leather tanning, and film photography. Galvanization is an electroplating process in which zinc is used to coat steel and increase its corrosion resistance. EPWW contains heavy metals and nutrients that can contaminate the environment (Coelho et al., 2021; Wang et al., 2021). Therefore, treating EPWW is necessary (Marques et al., 2013). Biological processes can be used to eliminate heavy metals and are both cost-effective and environmentally friendly (James and Vijayanandan, 2022).

Sequencing batch reactor (SBR) systems enhance the activated sludge process for wastewater treatment. However, wastewater characteristics may influence pollution removal efficiency (Singh et al., 2022). SBR systems demonstrate exceptional stability

Citation: Suriyawong T, Buddhawong S, Swasdisevi T, Sirianuntapiboon S. The effectiveness of an anoxic-oxic-anoxic-oxic sequencing batch reactor system (A2/O2-SBR) to treat electroplating wastewater and the bacterial community within the system. Environ. Nat. Resour. J. 2025;23(1):40-54. (https://doi.org/10.32526/ennrj/23/20240134)

and adaptability, making them efficient for biological wastewater treatment (Zhang et al., 2023). The reaction phase in SBR systems includes both anoxic and oxic periods, and enhances pollution removal (Liu et al., 2017; Gao et al., 2021). An abundance of oxygen (O_2) allows aerobic organisms to perform nitrification, using O_2 as an electron acceptor. Conversely, microorganisms utilize NO_3^--N as an electron acceptor under anoxic conditions, resulting in denitrification (Yan et al., 2019). Heavy metals, nitrogen compounds, phosphates, and COD are reduced in industrial wastewater under anoxic conditions (Feng et al., 2013; Jena et al., 2020; Lu et al., 2021). Preserving both anoxic and oxic processes helps to accelerate pre-denitrification in anoxic phase. This inhibits the development of NO_3^--N and NO_2^--N within the system (Gong et al., 2012; Lu et al., 2021). The anoxic/oxic system removes nitrogen through nitrification, denitrification, ammonification, and anaerobic ammonium oxidation (anammox) process.

The anoxic/oxic process can be used to treat EPWW, removing organic matter (OM) and nitrogen compounds (Yan et al., 2018; Gao et al., 2021). Feng et al. (2013) reported that an anoxic/aerobic-membrane bioreactor (A/O-MBR) can remove 80-95% of heavy metals like zinc (Zn^{2+}), copper (Cu^{2+}), lead (Pb^{2+}), and cadmium (Cd^{2+}). By using ion exchange, extracellular precipitation, and intracellular accumulation, denitrifying bacteria remove heavy metals better than nitrifying bacteria (Wang et al., 2016; Su et al., 2020). Moreover, microorganism multiplication in various environments demonstrates the need for DO. Microorganisms determine wastewater treatment system efficiency (Quan et al., 2012). The main phyla in anoxic/oxic habitats are Proteobacteria, Bacteroidetes, Firmicutes, Chloroflexi, Acidobacteria, and Verrucomicrobia (Xie et al., 2024). Yong et al. (2018) found that *Pseudomonadaceae* generate organic acids to chelate and precipitate heavy metals.

The anoxic-oxic-anoxic-oxic (A2/O2-SBR) process was demonstrated to effectively treat less heavy metal contaminated in EPWW (Yan et al., 2018; Gao et al., 2021). This study examines how different oxic and anoxic conditions change the bacterial communities in EPWW that contains heavy metals, as well as how they affect the removal of heavy metals, the breakdown of OM, and the growth of bacteria. Pilot-scale experiments are necessary to advance practical applications of the A2/O2-SBR process. Managing the wastewater treatment system requires monitoring DO levels during anoxic and oxic phases. The goal of this study was to evaluate A2/O2-SBR system, which constantly treats EPWW, and identify the best anoxic/oxic ratios. Additionally, studying the diversity of microbial populations during wastewater treatment will improve our understanding of these systems.

2. METHODOLOGY

2.1 Wastewater characteristics

EPWW from electro-galvanized steel production was obtained from the electroplating industry in southern Thailand. The production process is not continuous and the wastewater is occasionally released, resulting in a single collection during peak production to evaluate the efficiency of the A2/O2-SBR in reducing high pollution levels. Table 1 presents the characteristics of the EPWW.

Table 1. The EPWW characteristics

Parameter	Value
Cadmium (Cd^{2+})	20.57±0.21 mg/L
Zinc (Zn^{2+})	30.62±0.13 mg/L
Ferrous (Fe^{2+})	0.273±0.120 mg/L
Manganese (Mn^{2+})	0.120±0.110 mg/L
Nickel (Ni^{2+})	0.052±0.160 mg/L
Copper (Cu^{2+})	0.004±0.100 mg/L
Biochemical Oxygen Demand (BOD_5)	285.0±3.0 mg/L
Chemical Oxygen Demand (COD)	402.0±2.5 mg/L
Ammonium-nitrogen (NH_4^+-N)	3.31±0.04 mg/L
Total Kjeldahl Nitrogen (TKN)	14.50±0.13 mg/L
Nitrite-nitrogen (NO_2^--N)	0.34±0.02 mg/L
Nitrate-nitrogen (NO_3^--N)	0.43±0.01 mg/L
Total nitrogen (TN)	15.73±0.25 mg/L
pH	7.43±0.04

2.2 A2/O2 SBR operation

Activated sludge was obtained from domestic wastewater treatment plants in Bangkok, Thailand. The four reactors in this study were made from clear acrylic plastic cylinders, with each reactor having a diameter of 18 cm, a height of 40 cm, and a working volume of 7.5 L (Figure 1(a)). The mixer system used a 60-rpm gear motor and paddle agitator. Air was diffused to the reactor, and the mixing and air pump were timed.

Four reactors were used with a cycle time of 12 h, an HRT of 5 days, and a MLSS concentration of 2,000 mg/L. All reactors were run for 9 h during the reaction phase and operated for 60 days. During the reaction phase, reactor-I, reactor-II, reactor-III, and reactor-IV had different anoxic/oxic ratios (0:9 h, 2:7 h, 4.5:4.5 h, and 7:2 h, respectively) as depicted in Figure 1(b).

(a) SBR reactors in the experiment

(b) Operational coditions of the A2/O2-SBR at different anoxic/oxic ratios

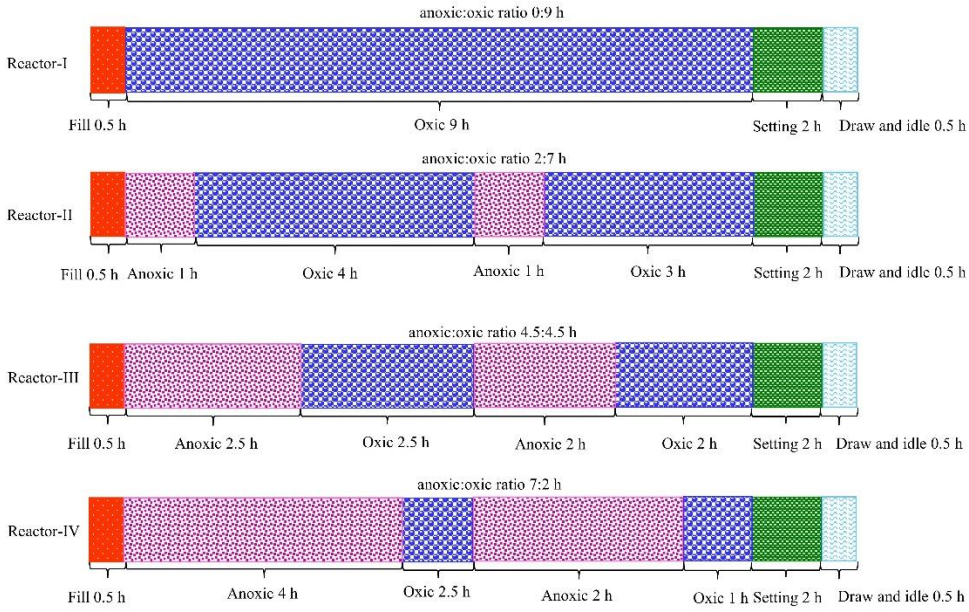

Figure 1. Experimental of A2/O2-SBR for treating EPWW (a) SBR reactors in the experiment, (b) Operational conditions of the A2/O2-SBR at different anoxic/oxic ratios

2.3 Analytical methods

The BOD_5, COD, TKN, NH_4^+-N, NO_2^--N, and NO_3^--N were measured following standard methods used for examining water and wastewater (Rice et al., 2012). The concentrations of heavy metals were determined using an atomic absorption spectrophotometer (AA). The sample sludge from reactor-I and the most effective reactor were used on

Day 0 (blank) and Day 60 to investigate bacterial diversity. The GF-1 kit from Vivantis technologies was used to extract bacterial DNA from the sludge after 20 min of centrifugation at 10,000 rpm. DNA was amplified, purified, and sequenced using 16S rRNA primers, following the Illumina 16S metagenomics protocol.

3. RESULTS AND DISCUSSION

3.1 Heavy metal removal

The results of this study are shown the AA machine was unable to detect Fe^{2+}, Mn^{2+}, Ni^{2+}, and Cu^{2+} in the effluent wastewater, indicating that low levels of heavy metals can be removed with the treatment system. The concentrations of Zn^{2+} and Cd^{2+} in all reactors decreased over time, as represented in Figure 2(a) and Figure 2(c), because activated sludge could be a process for removing heavy metals through active and passive mechanisms involving intracellular accumulation and cellular metabolism processes (Ayangbenro and Babalola, 2017). Several researchers have reported that the physicochemical properties of anionic functional groups in extracellular polymeric substances (EPS) and cell surfaces act as adsorbents for sludge. Zn^{2+} and Cd^{2+} accumulate within cells through the Zn-transported system (Zhang et al., 2022; Bi et al., 2014).

The metal ions that fill the active binding sites make the biosorption process more challenging due to their slow adsorption rate until they reach the saturation point, which ultimately results in an equilibrium state (Fathollahi et al., 2021; Kalita and Baruah, 2023). The type of microorganisms and their resistance to heavy metals influence their capacity to adsorb and precipitate heavy metals on the cell surface. Numerous studies indicate that denitrifying bacteria exhibit greater resistance to heavy metals than nitrifying organisms (Feng et al., 2013; Su et al., 2020). Therefore, the oxic and anoxic conditions of the treatment system influence the remediation of heavy metals. According to Sirianuntapiboon (2013), SBR incorporating an anoxic phase can eliminate cyanide and Zn^{2+}. The investigation revealed that *Nitrobacter* sp. was the most affected nitrifying bacteria, while heterotrophic or denitrifying bacteria showed no signs of damage. Moreover, Cd^{2+} has demonstrated higher toxicity to nitrifying bacteria in comparison to denitrifying microbes (Feng et al., 2013; Dai et al., 2019).

Figure 2(b) and Figure 2(d) demonstrate that all reactors removed up to 58% of Zn^{2+} and 49% of Cd^{2+} from the first period (Anoxic1) due to the presence of more vacant and unoccupied active biosorption sites on the biosorbent surfaces. However, the second anoxic period (Anoxic2) was the most effective treatment for Zn^{2+} and Cd^{2+}, surpassing the first and second oxic periods (Oxic1 and Oxic2). The results confirmed that the bio-sludge kept more Zn^{2+} and Cd^{2+} as the anoxic period increased, as shown in Figures 2(e) and Figure 2(f).

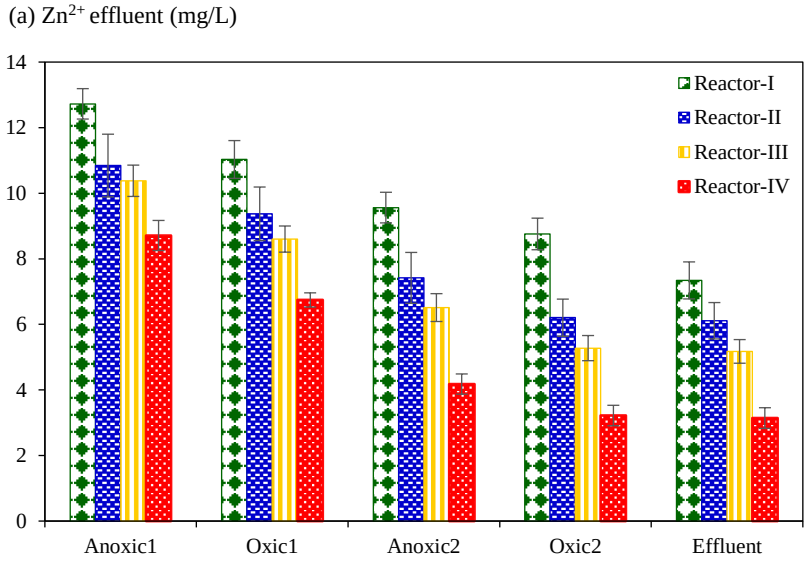

Figure 2. Heavy metal concentrations, removal efficiency in wastewater and heavy metal concentrations in bio-sludge of A2/O2-SBR for EPWW treatment (a) Zn^{2+} concentrations, (b) Zn^{2+} removal efficiencies, (c) Cd^{2+} concentrations, and (d) Cd^{2+} removal efficiencies, (e) Zn^{2+} concentrations and (f) Cd^{2+} concentrations in bio-sludge

(b) Zn^{2+} removal efficiency (%)

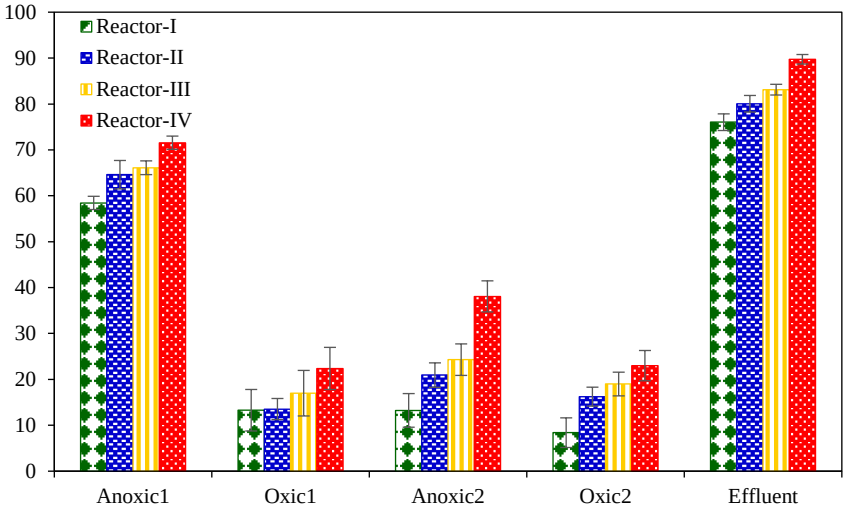

(c) Cd^{2+} concentrations (mg/L)

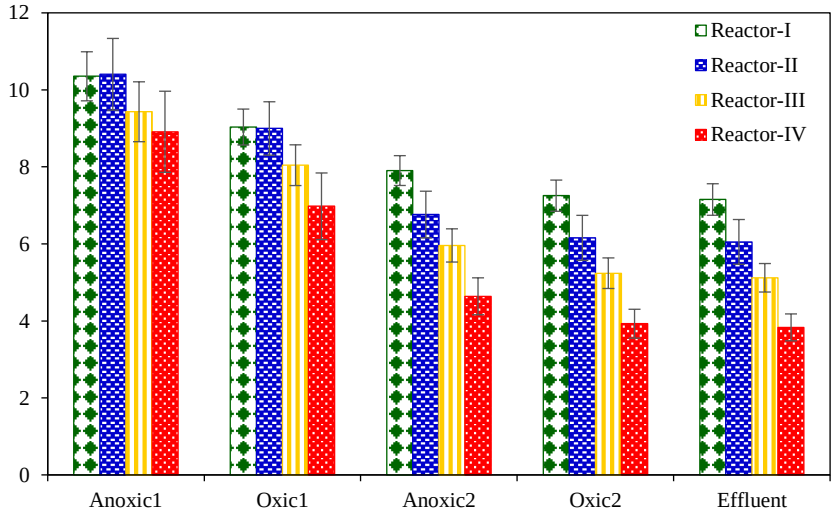

(d) Cd^{2+} removal efficiencies (%)

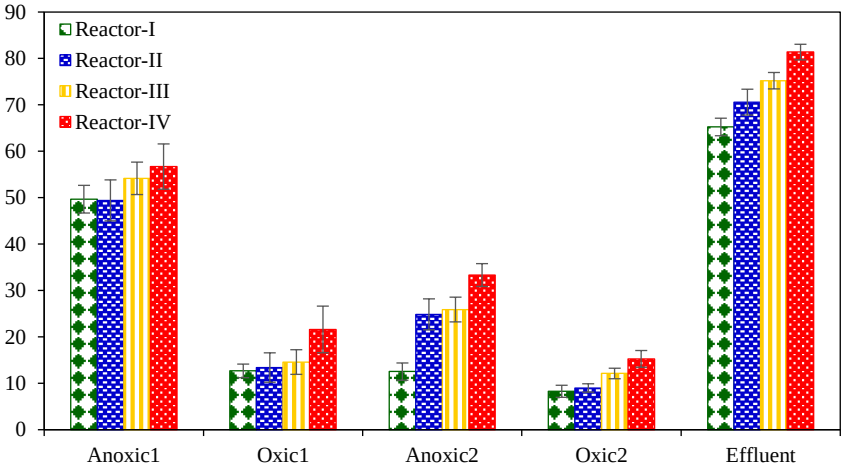

Figure 2. Heavy metal concentrations, removal efficiency in wastewater and heavy metal concentrations in bio-sludge of A2/O2-SBR for EPWW treatment (a) Zn^{2+} concentrations, (b) Zn^{2+} removal efficiencies, (c) Cd^{2+} concentrations, and (d) Cd^{2+} removal efficiencies, (e) Zn^{2+} concentrations and (f) Cd^{2+} concentrations in bio-sludge (cont.)

(e) Zn^{2+} concentrations in bio-sludge

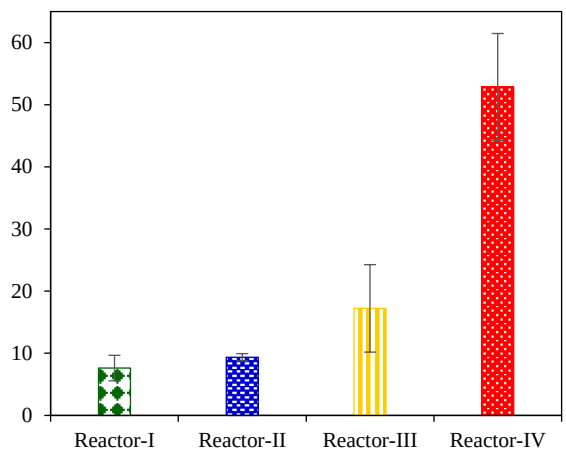

(f) Cd^{2+} concentrations in bio-sludge

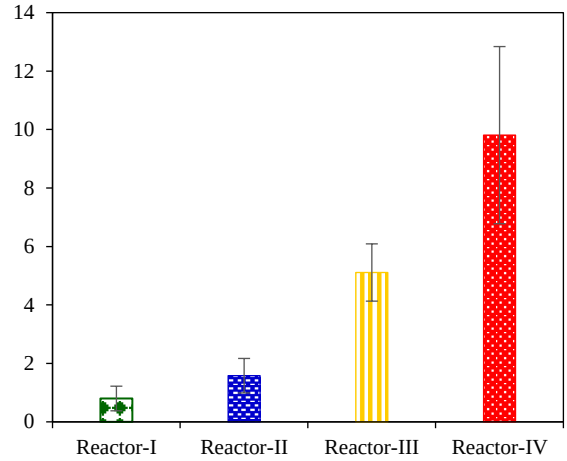

Figure 2. Heavy metal concentrations, removal efficiency in wastewater and heavy metal concentrations in bio-sludge of A2/O2-SBR for EPWW treatment (a) Zn^{2+} concentrations, (b) Zn^{2+} removal efficiencies, (c) Cd^{2+} concentrations, and (d) Cd^{2+} removal efficiencies, (e) Zn^{2+} concentrations and (f) Cd^{2+} concentrations in bio-sludge (cont.)

3.2 BOD_5 and COD removal

Figure 3(a) and Figure 3(c) show that most BOD_5 and COD values decreased after the first period of the reaction phase and slightly decreased in the later period because bacteria require OM for growth. OM is oxidized by heterotrophic bacteria to carbon dioxide, after which the nitrogen compounds can be decomposed by autotrophic bacteria, especially nitrifying bacteria, through the process of decomposing inorganic compounds. All of the above processes occurred under oxic conditions. During anoxic periods, low DO levels inhibit microbial activity, leading to reductions in OM removal (Yan et al., 2018). The oxic phase is more effective than the anoxic phases in reducing BOD_5 and COD because autotrophic bacteria do most of the work in oxic conditions (Gabarro et al., 2014; Gao et al., 2021).

The COD degradation by the A2/O2-SBR occurred when aerobic microorganisms oxidized OM under aerobic conditions, while heterotrophic bacteria utilized organic carbon as an electron donor under anoxic conditions (Huang et al., 2020; Guo et al., 2023). Reducing the length of the oxic period in wastewater treatment process led to a lower BOD_5 and COD removal efficiency. However, the BOD_5 and COD removal efficiencies were greater than 90% and 84% (Figure 3(b) and Figure 3(d)). This result is consistent with that of Li et al. (2018), who reported a COD removal efficiency of 89.1% at a Cd^{2+} concentration of 40 mg/L. Zhang et al. (2022) reported that activated sludge could reduce COD by 73.64% when the Zn^{2+} concentration was 20 mg/L. In addition, Liu et al. (2017) reported that a two-step anoxic/oxic membrane bioreactor system effectively treated landfill leachate and removed 80.1% of COD.

3.3 Nitrogen compound removal

3.3.1 NH_4^+-N and TKN removal

Figure 4 (a) shows the concentrations of NH_4^+-N. Most NH_4^+-N is removed under oxic conditions but can also be removed under anoxic conditions through these processes. Under oxic conditions, in the nitrification process, ammonia-oxidizing bacteria (AOB) convert ammonia into NO_2^--N in the first step, and then, NO_2^--N is oxidized to NO_3^--N by nitrite-oxidizing bacteria (NOB) (Wang et al., 2016). Under anoxic conditions, in the ammonium oxidation process (anammox), anammox bacteria use NO_2^--N instead of O_2 to convert NH_4^+-N. and NO_2^--N into N_2 (Jaroszynski et al., 2011; Lu et al., 2021). In addition, Figure 4(b) shows that the NH_4^+-N removal efficiency of reactor-I steadily decreased over time due to the absence of OM. However, reactor-II, reactor-III, and reactor-IV had greater NH_4^+-N removal efficiencies in the oxic periods than in the anoxic periods because most NH_4^+-N was treated during the oxic periods. However, when anoxic period increased in length, the efficiency of NH_4^+-N removal decreased due to the decreased DO levels, leading to the inhibition of ammonification process (Tang et al., 2021; Lu et al., 2021). Additionally, Cd^{2+} and Zn^{2+} inhibited the ammonium oxidation enzyme activity of the nitrifying and AOB (Marques et al., 2013; Bi et al., 2014; Li et al., 2018).

(a) BOD_5 concentrations (mg/L)

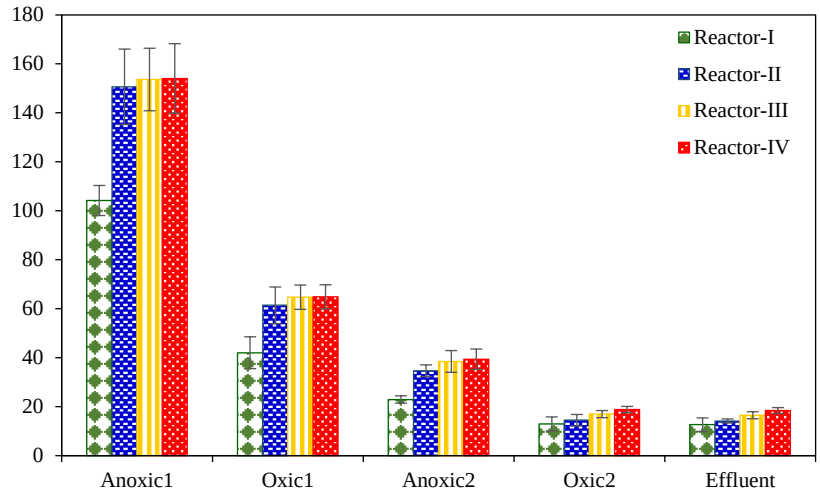

(b) BOD_5 removal efficiencies (%)

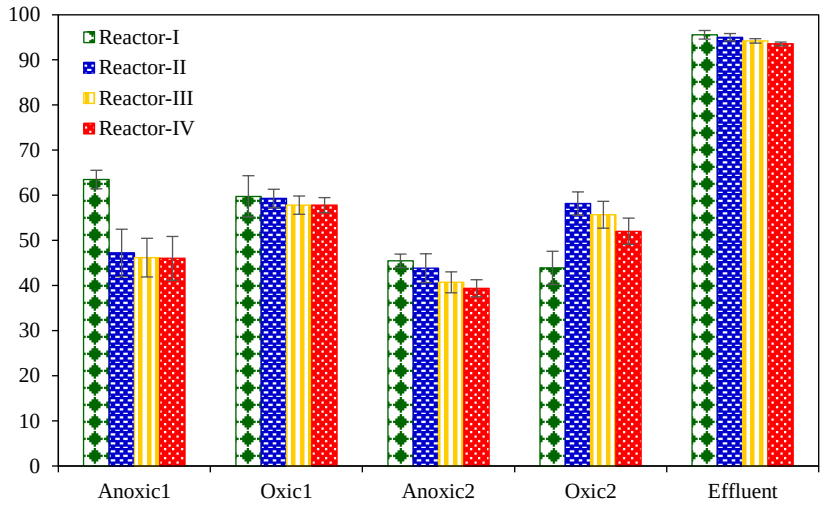

(c) COD concentrations (mg/L)

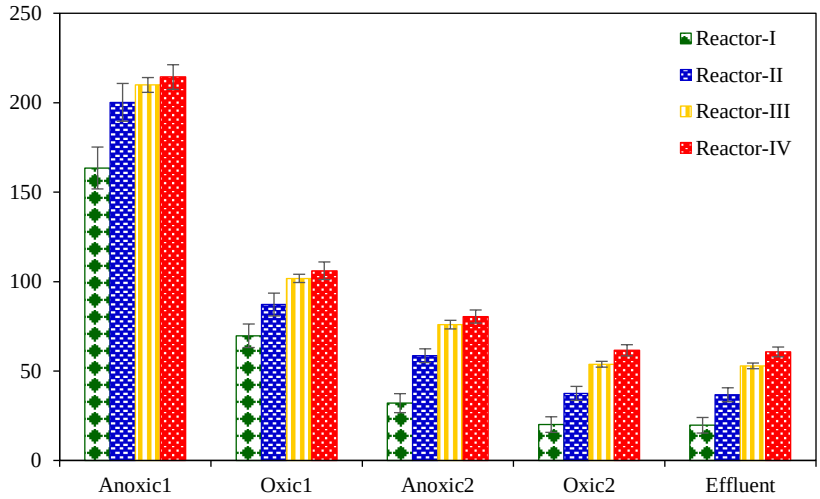

Figure 3. BOD_5 and COD concentrations and their removal efficiency of A2/O2-SBR for EPWW treatment (a) BOD_5 concentrations, (b) BOD_5 removal efficiencies, (c) COD concentrations, and (d) COD removal efficiencies

(d) COD removal efficiencies (%)

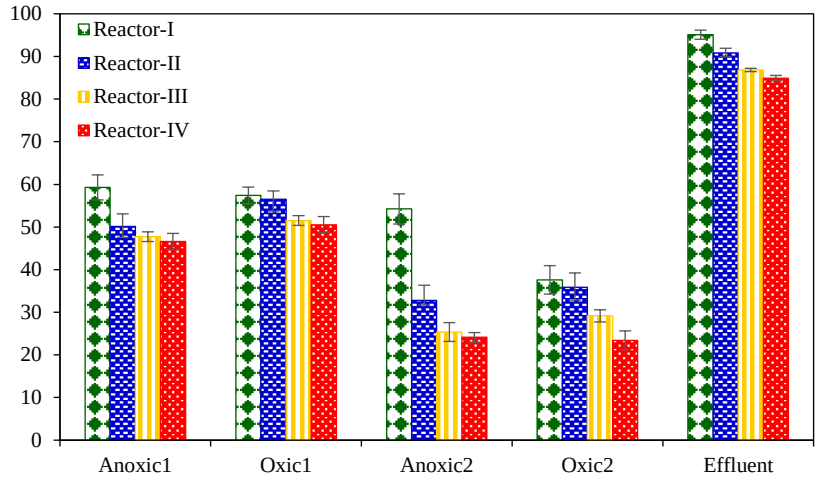

Figure 3. BOD_5 and COD concentrations and their removal efficiency of A2/O2-SBR for EPWW treatment (a) BOD_5 concentrations, (b) BOD_5 removal efficiencies, (c) COD concentrations, and (d) COD removal efficiencies (cont.)

However, during the anoxic periods of reactor-II, reactor-III, and reactor-IV, NH_4^+-N removal efficiencies were 39-42% due to the anammox process (Jaroszynski et al., 2011). This result was observed in the A2/O2-SBR treatment system when the anoxic period increased in length, resulting in a decreased NH_4^+-N removal efficiency. Similarly, Hu et al. (2011) reported that in an anoxic/aerobic SBR, the removal efficiency of NH_4^+-N decreased as the anoxic period increased.

TKN concentrations in this study are shown in Figure 4(c), which shows that TKN concentrations decreased after the first period. Figure 4(d) shows that TKN removal efficiency of reactor-I continuously decreased at 6 h and began to stabilize at 9 h, while adding anoxic periods in other reactors improved TKN removal efficiencies during the oxic period. However, increasing the anoxic ratios for these systems increased TKN removal efficiency. In addition, the results show that most TKN is eliminated by autotrophic nitrifying bacteria under oxic conditions (Guo et al., 2023). Under anoxic conditions, TKN is eliminated by denitrification process, and anammox process.

When comparing the removal efficiency of NH_4^+-N with that of TKN during every period, it was found that when the anoxic period increased in length, NH_4^+-N removal efficiency decreased. On the other hand, TKN removal efficiency in anoxic period was less than that in oxic period, but TKN removal efficiency in the effluent increased with an increasing anoxic ratio in A2/O2-SBR. The results showed that A2/O2-SBR, which increased anoxic ratio was promoted the removal of organic nitrogen.

(a) NH_4^+-N concentrations (mg/L)

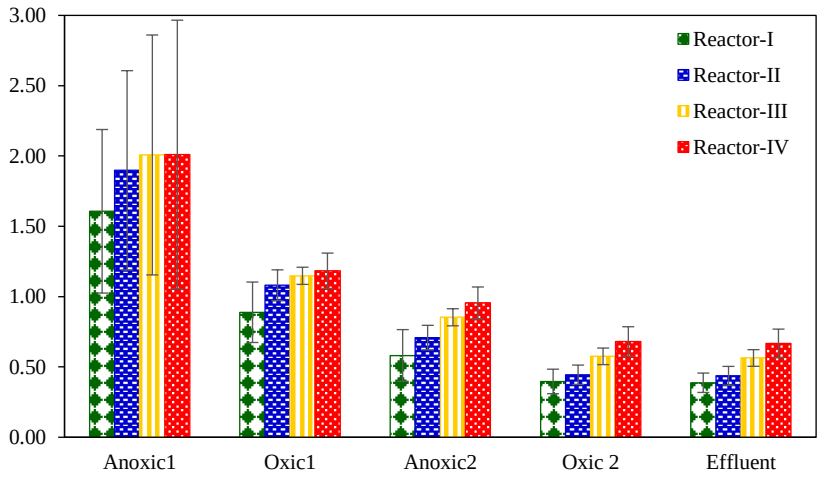

Figure 4. NH_4^+-N and TKN concentrations and their removal efficiency of A2/O2-SBR for EPWW; (a) NH_4^+-N concentrations, (b) NH_4^+-N removal efficiencies (c), TKN concentrations, and (d) TKN removal efficiencies

(b) NH_4^+-N removal efficiencies (%)

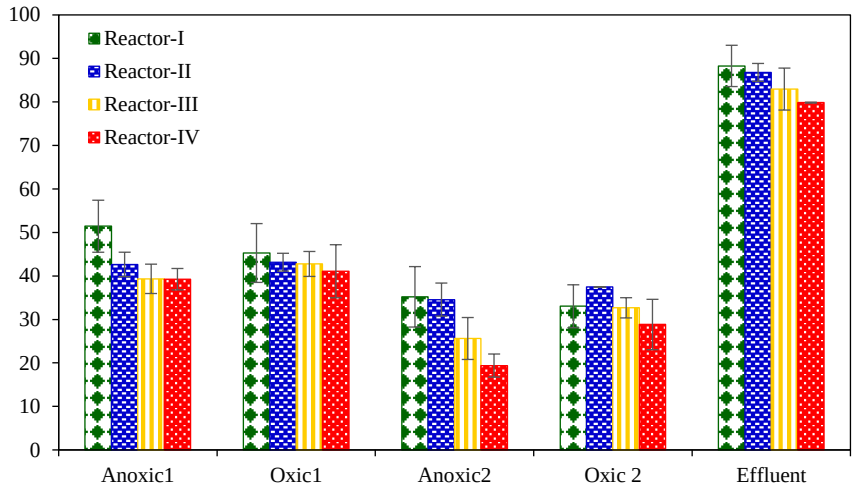

(c) TKN concentrations (mg/L)

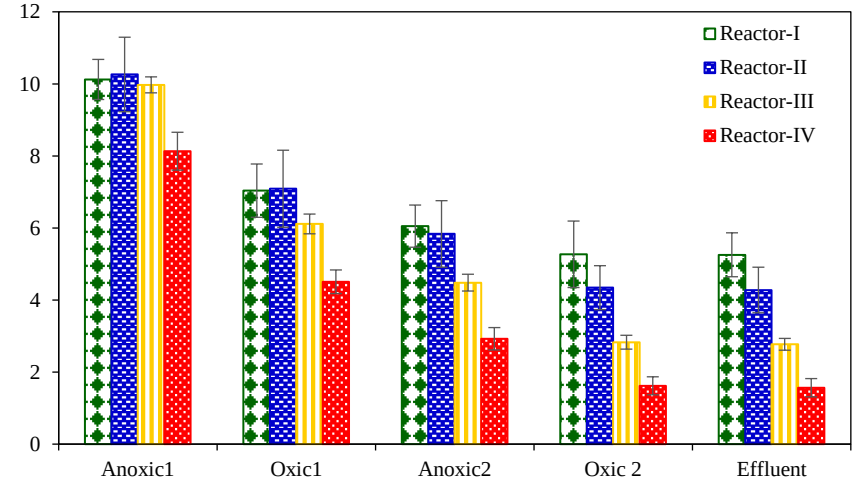

(d) TKN removal efficiencies (%)

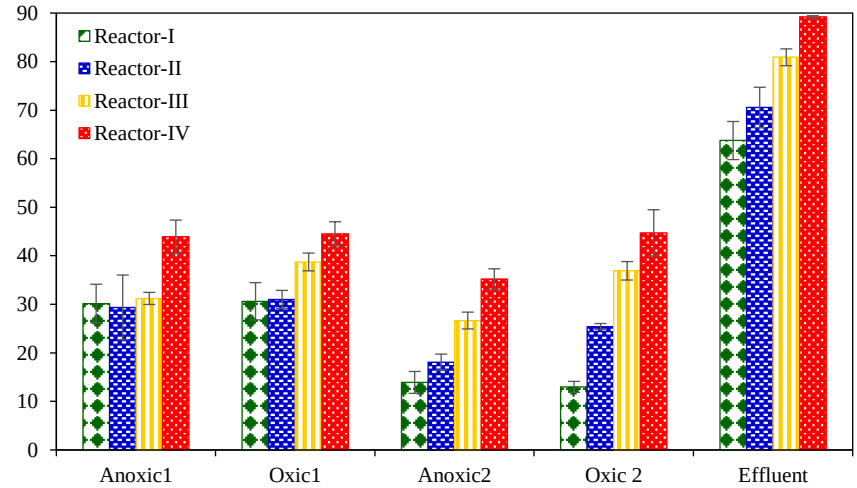

Figure 4. NH_4^+-N and TKN concentrations and their removal efficiency of A2/O2-SBR for EPWW; (a) NH_4^+-N concentrations, (b) NH_4^+-N removal efficiencies (c), TKN concentrations, and (d) TKN removal efficiencies

3.3.2 NO_2^--N and NO_3-N removal

NO_2^--N and NO_3^--N concentrations in EPWW were 0.34±0.20 and 0.43±0.10 mg/L. Figure 5(a) and Figure 5(b) show that NO_2^--N and NO_3-N concentrations increased in reactor-I but decreased in other reactors. Nitrification occurred in reactor-I, causing the accumulation of NO_2^--N and NO_3^--N in this reactor. However, reactor-II, reactor-III, and reactor-IV experienced increases in the anoxic period combined with denitrification, with NO_3^--N being converted into N_2O or N_2, which reduced the accumulation of NO_2^--N and NO_3^--N. This result is consistent with that of Wu et al. (2018), who reported that the secondary-stage A/O process of a pilot-scale two-stage anoxic/oxic process was effective in removing nitrogen by reducing NO_3^--N to N_2. However, Cd^{2+} toxicity has a detrimental effect on microorganism activity, leading to reductions in NO_2^--N and NO_3^--N removal (Su et al., 2019), which caused NO_2^--N and NO_3^--N to accumulate in this study.

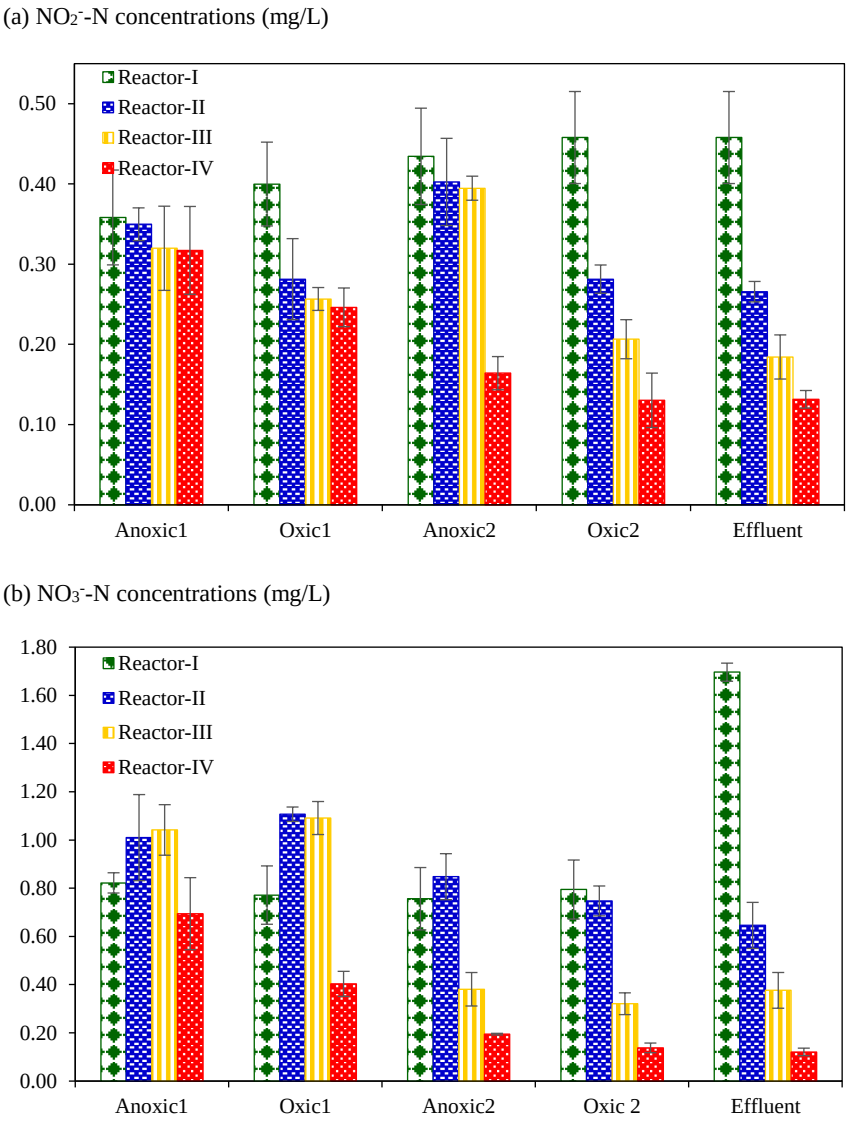

Figure 5. Concentrations of NO_2^--N and NO_3^--N in EPWW treated using the A2/O2-SBR (a) NO_2^--N concentrations and (b) NO_3^--N concentrations

3.3.3 TN removal

TN is the sum of NO_3^--N, NO_2^--N, and TKN. This study showed that TN concentrations in all reactors gradually decreased over time, as shown in Figure 6(a). TN removal efficiencies of the A2/O2-SBR reactors are shown in Figure 6(b). Reactor-I removed most of TN within the first 6 h, and only a small amount remained after treatment. However, in other reactors, the nitrification process converted most of NH_4^+-N and TKN to NO_3^--N under oxic conditions, leading to the removal of most TN under oxic conditions (Huang et al., 2020). Increasing the anoxic

period in the system improved the efficiency of TN removal during every period of the reaction phase. The continuous operation of anoxic/oxic systems affects the treatment of nitrogen compounds (Zheng et al., 2021; Hu et al., 2011). Yan et al. (2018) reported that the first-stage anoxic/oxic cycle in a two-stage anoxic/oxic process transforms most TN into NO_3^--N through complete nitrification and incomplete denitrification, followed by the conversion of NO_2^--N to NO_3^--N. EPWW contains Zn^{2+} and Cd^{2+}, which are toxic to nitrifying bacteria and denitrifying bacteria (Su et al., 2019; Zhang et al., 2023); however, the findings show that reactor-IV had the highest TN removal efficiency at 84.25±6.10%. According to research by Hu et al. (2020), the efficiency of TN removal in the anoxic/oxic process was greater than 80%.

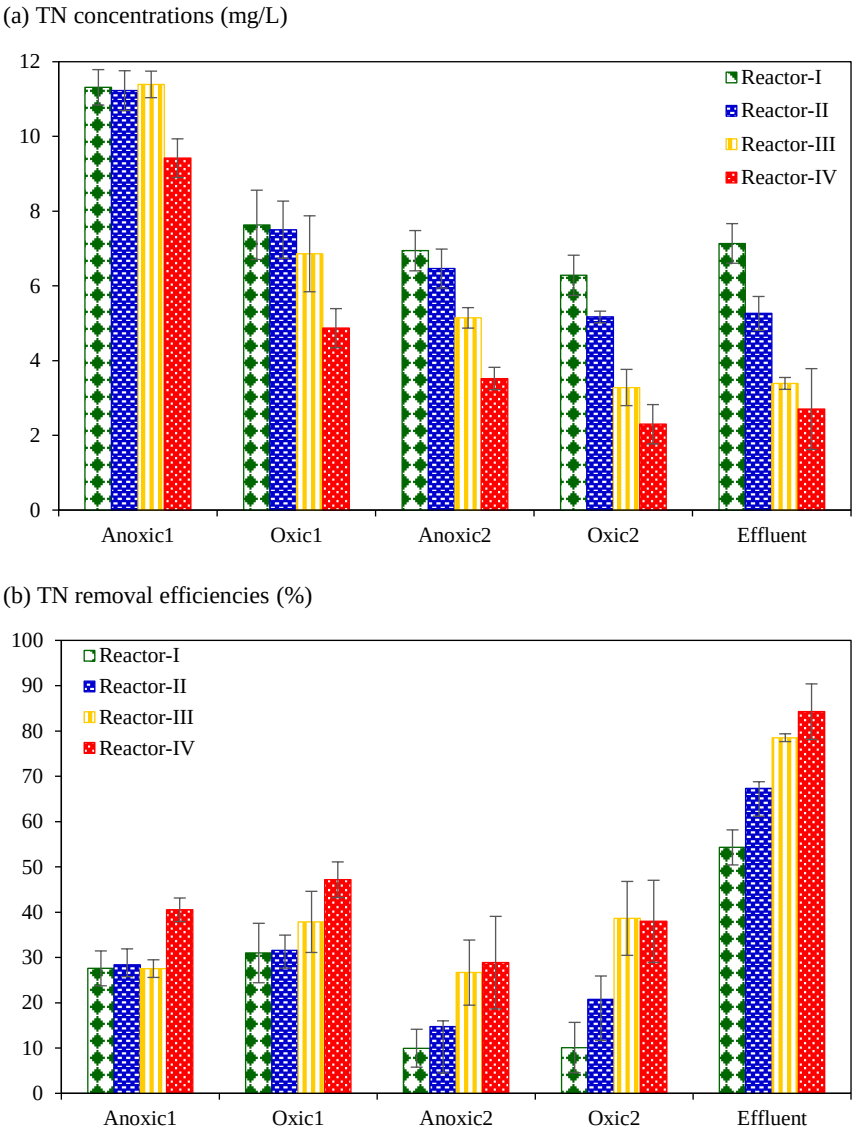

Figure 6. Concentrations and removal efficiency of TN in EPWW treated using the A2/O2-SBR (a) TN concentrations and (b) TN removal efficiencies

3.4 DO levels

Table 2 displays the DO levels in this study. The average DO concentration was 0.1-0.4 mg/L during the anoxic periods and 2.2-6.5 mg/L during oxic periods, which was adequate for denitrifying and nitrifying bacteria (Yan et al., 2019). Anammox bacteria can also grow at DO concentrations below 2.5 mg/L (Kimura et al., 2011). Raising the anoxic/oxic ratio during the reaction phase of these systems reduced the difference in DO levels between the two periods. Between anoxic and oxic periods, reactor-I had DO values of 6.5-6.6 mg/L, and reactor-II, reactor-III, and reactor-IV had DO values of 5.3-5.4, 5.3-5.5, and 2.1-2.2 mg/L, respectively. Increasing the

anoxic period while decreasing the oxic period resulted in greater Zn^{2+}, Cd^{2+}, TKN, and TN elimination. Over 80% of BOD_5 and COD were removed.

Minor DO concentration differences between oxic and anoxic periods affect both obligate aerobic and facultative anaerobic bacteria. Yong et al. (2018) observed a close relationship between DO levels and OM elimination, as high DO levels during oxic and short anoxic periods impeded denitrification. Gao et al. (2021) found that excess DO (3-4 mg/L) from oxic unit to anoxic unit damaged denitrifying microorganisms. In a single reactor wastewater treatment system, regulating DO levels to suit different microbial taxa is crucial. A2/O2 reduced DO variations between oxic and anoxic phases, improving nitrogen and OM removal. Increasing the anoxic period in reactor-IV effectively removed Zn^{2+} (89.74%) and Cd^{2+} (81.37%), with BOD_5 and COD removal efficiencies greater than 93.55% and 84.9%, respectively.

3.5 Sludge properties

Table 3 shows A2/O2-SBR performance. As anoxic period increased, excess sludge and suspended particles decreased, but sludge retention time (SRT) increased due to lower biomass output (Jena et al., 2016). High SRT improves sludge flocculation (Singh et al., 2022). Sludge settled well with sludge volume index (SVI) values of 48-55. The food to microorganism ratios (F/M) in this investigation were 0.22-0.26 kg BOD/kg MLSS.

Table 2. DO values of the A2/O2-SBR for treatment of EPWW

Reaction phase steps	Reactor-I*	Reactor-II	Reactor-III	Reactor-IV
Anoxic1	6.5±0.1 mg/L	0.4±0.1 mg/L	0.2±0.1 mg/L	0.1±0.1 mg/L
Oxic1	6.6±0.1 mg/L	5.8±0.1 mg/L	5.7±0.1 mg/L	2.3±0.2 mg/L
Anoxic2	6.5±0.1 mg/L	0.4±0.1 mg/L	0.3±0.1 mg/L	0.1±0.1 mg/L
Oxic2	6.6±0.1 mg/L	5.7±0.1 mg/L	5.6±0.1 mg/L	2.2±0.1 mg/L

Remark * Reactor-I controlled the oxic conditions throughout the study.

Table 3. Sludge properties in the A2/O2 SBR for the treatment of EPWW

Parameter	Reactor-I	Reactor-II	Reactor-II	Reactor-IV
Excess sludge (mg/d)	529±217	364±123	206±50	147±34
SVI (mL/g)	54±9	55±6	48±5	50±4
SRT (days)	5±2	7±2	12±4	15±4
SS (mg/L)	57.29±5.70	51.14±5.00	50.43±5.00	49.07±4.40
F/M (kg_{BOD}/Kg_{MLSS})	0.22±0.10	0.24±0.10	0.25±0.10	0.26±0.10
pH	7.02±0.20	7.17±0.10	7.29±0.10	7.33±0.20

3.6 Microbial community

Proteobacteria, Bacteroidetes, Actinobacteria, Firmicutes, and Verrucomicrobia were the most common phyla in the samples (Figure 7(a)). Reactor-IV also contained Deinococcus-Thermus and Planctomycetes. In reactor-IV, under anoxic conditions, Proteobacteria constituted 60.8%, while under oxic conditions, they comprised 58.5%. Actinobacteria were more common in oxygenated (17.4%) than anoxic (6.1%) conditions, which suggests that they prefer environments with less O_2 for the metal-removal process. Firmicutes exhibited a higher prevalence in anoxic conditions, with a representation of 12.4% compared to 8.3% in oxic environments. Gram-negative bacteria possessing lipopolysaccharide surfaces exhibit resistance to Cd (Huang et al., 2017; Su et al., 2020). These results indicate a high removal efficiency of heavy metals under anoxic conditions (Figure 2). Furthermore, Firmicutes and Thermomonas are involved in the digestion of ammonia nitrogen (Chen et al., 2019; Jin et al., 2022).

Figure 7(b) depicts the microbial species present in reactor-I and reactor-IV. In reactor-I, *Thermomonas heamalytica* and *Bacillus funiculus* were the most common bacteria. In reactor-IV, *Pseudomonas vancouverensis*, *Clostridium pasterurianum*, and *Sulfuriflexus mobiliz* were the most common bacteria. Hussain et al. (2022) showed that many bacteria, such as those in the genera *Bacillus*, *Staphylococcus*, and *Pseudomonas*, can facilitate Zn^{2+} fixation. Reactor-IV had a high abundance of nitrifying and denitrifying bacteria,

especially *P. vancouverensis*, which likely helped with nitrogen and metal removal. *Pseudomonas* species can also remove Cd^{2+} (Igbinosa et al., 2012; Abbas et al., 2014). *T. heamalytica* facilitates nitrogen removal, while *B. funiculus* removes heavy metals, demonstrating the critical role of bacteria in reactor-I. In reactor-IV, *Pseudomonas* reached a relative abundance of 20% and a metal removal efficiency of over 30% when DO levels were low.

DO concentrations and time period affect bacterial proliferation (Liu et al., 2022), which in turn affects the removal efficiency of A2/O2-SBR. Bacterial taxonomy is linked to the removal of heavy metals (Fathollahi et al., 2021). Microorganisms are crucial for wastewater, nitrogen, and heavy metal treatment. Improved Proteobacteria and Actinobacteria populations may help remove metals from the wastewater, having different roles in oxygenated and anoxic environments.

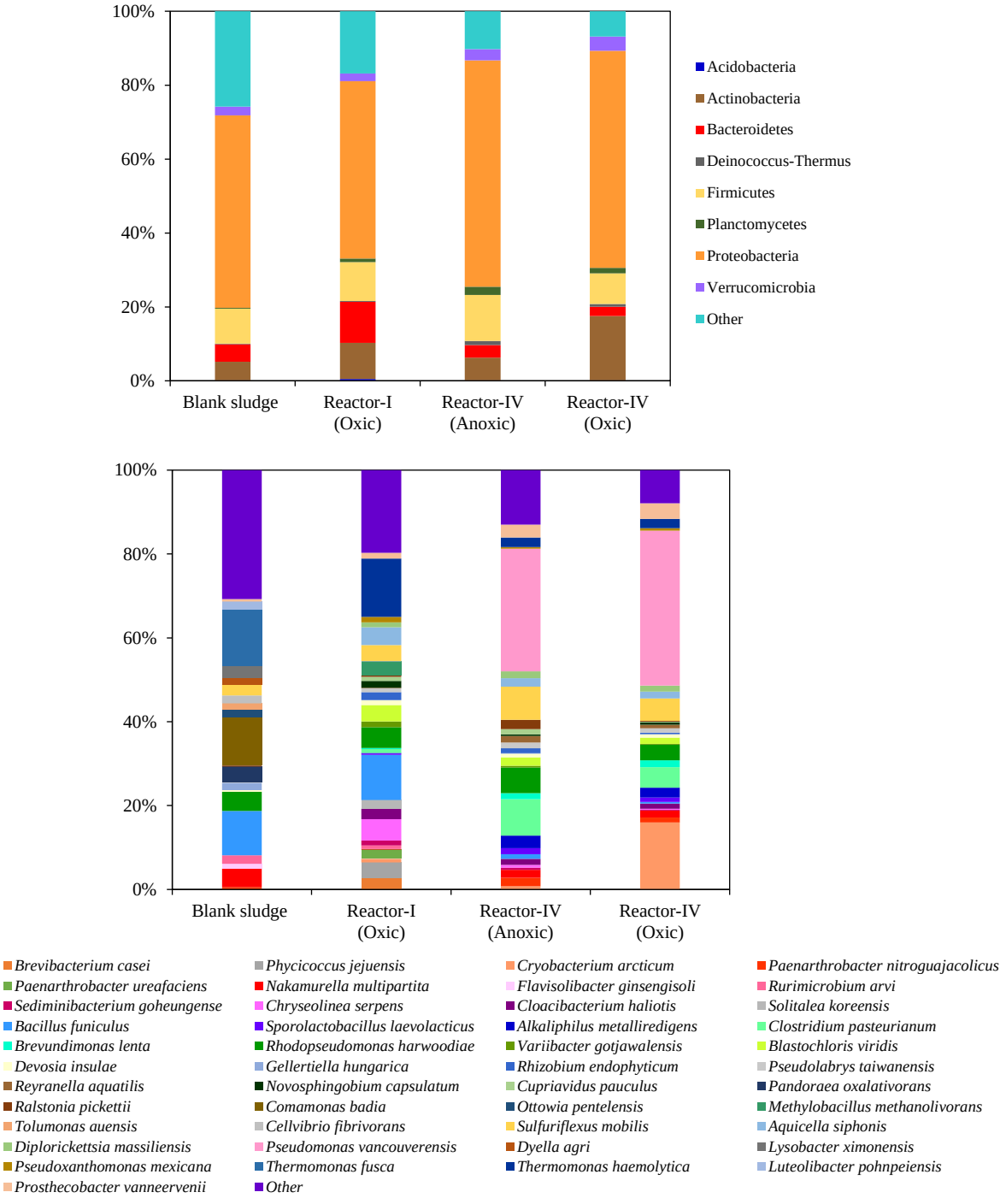

Figure 7. Relative abundances of bacterial in the blank sludge, reactor-I, and reactor-IV (with relative abundances greater than 1%) (a) phyla and (b) species

4. CONCLUSION

This study demonstrates that A2/O2-SBR system cleans electroplating effluent. Heavy metals (Zn^{2+} 89.74%, Cd^{2+} 81.37%), TKN (89.20%), and TN (84.25%) were removed at the best rates in reactor-IV, likely because it had a longer anoxic phase. Keeping the concentration of DO between 2.1 and 2.2 mg/L was beneficial for bacteria like *P. vancouverensis*, *R. harwoodiae*, and *S. mobilis*, which removed nitrogrn and heavy metals, improving the wastewater treatment. The A2/O2-SBR is a reliable and adaptable wastewater treatment technology. This study provides valuable insights for metal contamination management, including the importance of specific bacterial species for the elimination of heavy metals and nitrogen compounds and how the bacterial community can be modified to improve reactor performance. Future pilot studies should focus on the development and implementation of the A2/O2-SBR system in industrial wastewater treatment.

ACKNOWLEDGEMENTS

This research project was supported by King Mongkut's University of Technology Thonburi and the Thailand Science Research and Innovation (TSRI) Basic Research Fund: Fiscal year 2022 under project number FRB650048/0164.

REFERENCES

Abbas S, Rafatullah M, Ismail N, Lalung J. Isolation, identification, and characterization of cadmium resistant *Pseudomonas* sp. M3 from industrial wastewater. Journal of Waste Management 2014;2014(1):Article No. 160398.

Ayangbenro A, Babalola O. A new strategy for heavy metal polluted environments: A review of microbial biosorbents. International Journal of Environmental Research and Public Health 2017;14(1): Article No. 94.

Bi Z, Qiao S, Zhou J, Tang X, Cheng Y. Inhibition and recovery of Anammox biomass subjected to short-term exposure of Cd, Ag, Hg, and Pb. Chemical Engineering Journal 2014;244:89-96.

Chen J, Xu Y, Li Y, Liao J, Ling J, Li J, et al. Effective removal of nitrate by denitrification re-enforced with a two-stage anoxic/oxic (A/O) process from a digested piggery wastewater with a low C/N ratio. Journal of Environmental Management 2019;240:19-26.

Coelho F, Oliveira V, Araujo E, Balarini J, Konzen C, Salum A, et al. Treatment of a wastewater from a galvanizing industry containing chromium (VI) and zinc (II) by liquid surfactant membranes technique. Journal of Environmental Science and Health, Part A 2021;56(3):289-302.

Dai M, Zhou G, Ng H, Zhang J, Wang Y, Li N, et al. Diversity evolution of functional bacteria and resistance genes (CzCA) in aerobic activated sludge under Cd(II) stress. Journal of Environmental Management 2019;250:Article No. 109519.

Fathollahi A, Khasteganan N, Coupe S, Newman A. A meta-analysis of metal biosorption by suspended bacteria from three phyla. Chemosphere 2021;268:Article No. 129290.

Feng B, Fang Z, Hou J, Ma X, Huang Y, Huang L. Effects of heavy metal wastewater on the anoxic/aerobic-membrane bioreactor bioprocess and membrane fouling. Bioresource Technology 2013;142:32-8.

Gabarro J, Gonzalez-Carcamo P, Ruscalleda M, Ganigue R, Gich F, Balaguer M, et al. Anoxic phases are main N_2O contributor in partial nitritation reactors treating high nitrogen loads with alternate aeration. Bioresource Technology 2014;163:92-9.

Gong L, Jun L, Yang Q, Wang S, Ma B, Peng Y. Biomass characteristics and simultaneous nitrification-denitrification under long sludge retention time in an integrated reactor treating rural domestic sewage. Bioresource Technology 2012;119:277-84.

Guo H, Yao H, Huang Q, Lia T, Show D, Ling M, et al. Anaerobic-anoxic-oxic biological treatment of high-strength, highly recalcitrant polyphenylene sulfide wastewater. Bioresource Technology 2023;371:Article No. 128640.

Gao J, Duan C, Huang X, Yu J, Cao Z, Zhu J. The tolerance of anoxic-oxic (A/O) process for the changing of refractory organics in electroplating wastewater: Performance, optimization and microbial characteristics. Processes 2021; 9(6):Article No. 962

Hu B, Wang Y, Quan J, Huang K, Gua X, Zhu J, et al. Effects of static magnetic field on the performances of anoxic/oxic sequencing batch reactor. Bioresource Technology 2020;309:Article No. 123299.

Hu Z, Zhang J, Xie H, Li S, Wang J, Zhang T. Effect of anoxic/aerobic phase fraction on N_2O emission in a sequencing batch reactor under low temperature. Bioresource Technology 2011;102(9):5486-91.

Huang X, Zhu J, Duan W, Gao J, Li W. Biological nitrogen removal and metabolic characteristics in a full-scale two-staged anoxic-oxic (A/O) system to treat optoelectronic wastewater. Bioresource Technology 2020;300:Article No. 122595.

Huang Z, Liu D, Zhao H, Zhang Y, Zhang Y, Zhou W. Performance and microbial community dynamic membrane bioreactor enhanced by Cd(II)-accumulating bacterium in Cd(II)-containing wastewater treatment. Chemical Engineering Journal 2017;317:368-75.

Hussain S, Khan M, Sheikh T, Mumtaz M, Chohan T, Shamim S, et al. Zinc Essentiality, toxicity, and its bacteria bioremediation. Frontiers in Microbiology 2022;13:Article No. 900740.

Igbinosa I, Nwodo U, Sosa A, Tom M, Okoh A. Commensal *Pseudomonas* Species isolated from wastewater and freshwater Milieus in the Eastern Cape Province, South Africa, as reservoir of antibiotic resistant determinants. International Journal of Environmental Research and Public Health 2012;9(7):2537-49.

James S, Vijayanandan A. Anoxic-aerobic-anoxic sequencing batch reactor for enhanced nitrogen removal. Bioresource Technology 2022;363:Article No. 127892.

Jaroszynski LW, Cicek N, Sparling R, Oleszkiewicz JA. Importance of the operating pH in maintaining the stability of anoxic ammonium oxidation (anammox) activity in moving bed biofilm reactors. Bioresource Technology 2011;102(14): 7051-6.

Jena J, Kumarb R, Saifuddina M, Dixitb A, Das T. Anoxic-aerobic SBR system for nitrate, phosphate and COD removal from high-strength wastewater and diversity study of microbial communities. Biochemical Engineering Journal 2016;105:80-9.

Jena J, Narward N, Das T, Dhotre D, Sarkar U, Souche Y. Treatment of industrial effluents and assessment of their impact on the structure and function of microbial diversity in a unique anoxic-aerobic sequencing bath reactor (AnASBR). Journal of Environmental Management 2020;261:Article No. 110241.

Jin Y, Xiong W, Zhou N, Xiao G, Wang S, Su H. Role of initial bacterial community in the aerobic sludge granulation and performance. Journal of Environmental Management 2022;309:Article No. 114706.

Kalita N, Baruah P. Cyanobacteria as a potent platform for heavy metals biosorption: Uptake, responses and removal mechanisms. Journal of Hazardous Materials Advances 2023; 11:Article No. 100349.

Kimura Y, Isaka K, Kazama F. Tolerance level of dissolved oxygen to feed into anaerobic ammonium oxidation (anammox) reactor. Journal of Water and Environment Technology 2011;9(2):171-8.

Li S, Xu Q, Ma B, Guo L, She Z, Zhao Y, et al. Performance evaluation and microbial community of a sequencing batch reactor under divalent cadmium (Cd(II)) stress. Chemical Engineering Journal 2018;336:325-33.

Liu J, Zhang H, Zhang P, Wu Y, Gou X, Song Y, et al. Two-stage anoxic/oxic combined membrane bioreactor system for landfill leachate treatment: Pollutant removal performances and microbial community. Bioresource Technology 2017; 243:738-46.

Liu Y, Ma B, Liu Z. Application of partial nitrogen lab-scale sequencing batch reactor for the treatment of organic wastewater and its N_2O production pathways, and the microbial mechanism. Sustainability 2022;14(3):Article No. 1457.

Lu W, Ma B, Wang Q, Wei Y, Su Z. Feasibility of achieving advance nitrogen removal via endogenous denitrification/ annamox. Bioresource Technology 2021;325:Article No. 124666.

Marques A, Duque A, Bessa V, Mesquita R, Rangel A, Castro P. Performance of an aerobic granular sequencing batch reactor fed with wastewater contaminated with Zn^{2+}. Journal of Environmental Management 2013;128:877-82.

Quan Y, Han H, Zheng S. Effect of dissolved oxygen concentration (microaerobic and aerobic) on selective enrichment culture for bioaugmentation of acidic industrial wastewater. Bioresource Technology 2012;120:1-5.

Rice E, Baird R, Eaton A, Clesceri L. Standard Methods for the Examination of Water and Wastewater. Washington DC, USA: American Public Health Association, American Water Works Association, Water Environment Federation; 2012.

Singh A, Srivastava A, Saidulu D, Gupta A. Advancements of sequencing batch reactor for industrial wastewater treatment: Major focus on modifications, critical operational parameters, and future perspectives. Journal of Environment Management 2022;317:Article No. 115305.

Sirianuntapiboon S. Effect of the dilution rate and hydraulic retention time on the efficiency of the sequencing batch reactor (SBR) system with electroplating wastewater. Journal of Environmental Chemical Engineering 2013;1(4):786-94.

Su J, Wang Z, Huang T, Zhang H, Zhang H. Simultaneous removal of nitrate, phosphorus and cadmium using a novel multifunctional biomaterial immobilized aerobic strain *Proteobacteria cupriavidus* H29. Bioresource Technology 2020;307:Article No. 123196.

Su J, Xue L, Huang T, Wei L, Gao C, Wen Q. Performance and microbial community of simultaneous removal of NO_3^--N, Cd^{2+}, and Ca^{2+} in MBBR. Journal of Environmental Management 2019;250:Article No. 109548.

Tang G, Li B, Zhang B, Wang C, Zeng G, Zheng X, et al. Dynamics of dissolved organic matter and dissolved organic nitrogen during anaerobic/anoxic/oxic treatment process. Bioresource Technology 2021;331:Article No. 125026.

Wang W, Cui J, Li J, Du J, Chang Y, Cui J, et al. Removal effects of difference emergent-aquatic-plant groups on Cu, Zn, and Cd compound pollution from simulated swine wastewater. Journal of Environmental Management 2021;296:Article No. 113251.

Wang Y, Ji M, Zhao Y, Zhai H. Recovery of nitrification in cadmium-inhibited activated sludge system by bio-accelerators. Bioresource Technology 2016;200:812-9.

Wu D, Zhang Z, Yu Z, Zhu L. Optimization of F/M ratio for stability of aerobic granular process via quantitative sludge discharge. Journal of Bioresource Technology 2018;252:150-6.

Xie Y, Zhang Q, Wu Q, Zhang J, Dzakpasu M, Wang X. Nitrogen removal efficiency and mechanisms of an improved anaerobic-anoxic-oxic system for decentralized sewage treatment. Bioresource Technology 2024;393:Article No. 129976.

Yan L, Liu S, Liu Q, Zhang M, Liu Y, When Y, et al. Improved performance of simultaneous nitrification and denitrification via nitrite in an oxygen-limited SBR by alternating the DO. Bioresearch Technology 2019;275:153-62.

Yan X, Zhu C, Huang B, Yan Q, Zhang G. Enhanced nitrogen removal from electroplating tail wastewater through two-staged anoxic-oxic (A/O) process. Bioresource Technology 2018;247:157-64.

Yong Z, Bashir M, Ng C, Sethupathi S, Lim J. A sequential treatment of intermediate tropical landfill leachate using a sequencing batch reactor (SBR) and coagulation. Journal of Environmental Management 2018;205:244-52.

Zhang H, Yan D, Zhu Y, Li Y, Zhang G, Jiao Y, et al. Effect of Cd(II) shock loading on performance, microbial enzymatic activity and microbial community in a sequencing batch reactor. Journal of Environmental Management 2023; 342:Article No. 118108.

Zhang L, Liu Y, Wang C, Guo J, Ma D, Liu S, et al. The effects of varying Zn^{2+} on the activated sludge properties and its distribution patterns. Bioresource Technology Reports 2022;17:Article No. 100990.

Zheng Z, Ali A, Su J, Zhang S, Fan Y, Sun Y. Self-immobilized biochar fungal pellet combined with bacterial strain H29 enhanced the removal performance of cadmium and nitrate. Bioresource Technology 2021;341:Article No. 125803.

Environment and Natural Resources Journal

Volume 23
Issue 1
2025

Ammonium, Nitrate, and Phosphate in Coastal Waters of Red River Biosphere Reserve, Vietnam

Luu Viet Dung[1,2*], Nguyen Tai Tue[1,2], Tran Dang Quy[1,2], and Mai Trong Nhuan[1,2]

[1]VNU Key Laboratory of Geoenvironmental and Climate Change Response, University of Science,Vietnam National University, Hanoi, Vietnam
[2]Faculty of Geology, University of Science, Vietnam National University, Hanoi, Vietnam

ARTICLE INFO

Received: 30 Apr 2024
Received in revised: 22 Oct 2024
Accepted: 11 Nov 2024
Published online: 10 Jan 2025
DOI: 10.32526/ennrj/23/20240128

Keywords:
Mangroves/ Coastal nutrient dynamic/ Eutrophication/ Red River Biosphere Reserve

*** Corresponding author:**
E-mail: dungluuviet@gmail.com

ABSTRACT

Nutrient availability in coastal areas plays a crucial role in supporting primary producers and maintaining the aquatic food chain. The spatial variation of nutrients, including ammonium, nitrate, and phosphate, can significantly influence coastal ecosystems' structure, leading to both positive and negative results. This study examines the fine-scale spatial variation of physicochemical parameters and nutrient concentrations in shrimp ponds and adjacent coastal waters from two wetland areas: Ba Lat Estuary (BLE) and Thai Thuy (TTW) in the Red River Delta, Vietnam. Ammonium concentrations ranged from 155.80 to 1,500.80 µg/L, with an average value of 666.83±260.02 µg/L. Nitrate concentrations varied from 25.10 to 996.40 µg/L, averaging of 285.42±255.05 µg/L, while phosphate concentrations exhibited significant variability, ranging from 0.70 to 128.70 µg/L. Nutrient concentrations in the RRD were relatively high compared to other regions globally. The findings revealed that tidal dynamics and aquaculture activities significantly influence nutrient variations in coastal waters. The increasing nutrient concentrations in the coastal marine environment of the Red River Biosphere could lead to eutrophication risks, which could adversely affect mangroves, estuarine areas, and other coastal ecosystems. This results emphasize the critical need to reduce nutrient discharge and implement wastewater treatment from anthropogenic activities to safeguard ecosystems and protect the coastal estuary environment. Further research is essential to investigate the spatial and temporal dynamics of nutrients in this region to fully understand their impacts on coastal marine ecosystems.

1. INTRODUCTION

The coastal zone is a highly dynamic area with many important economic activities such as industry, seaports, aquaculture, and tourism. However, this area is susceptible to pollution originating from the mainland, leading to risks of environmental degradation and vulnerability. The overabundance of nutrients such as nitrogen, phosphorus, and silicate can cause negative impacts on the coastal marine environment, such as eutrophication, degradation of estuaries and coastal areas, loss of marine habitats, and biodiversity degradation (Barcellos et al., 2019; Fauzi et al., 2013; Fauzi et al., 2014). Potential nutrient pollution sources affecting the marine environment include industrial activities, urban wastewater, agricultural production, domestic waste, and coastal aquaculture. Studies in Brazil and India showed that the increase in phosphorus discharge might cause deterioration of water quality, sediments, and biodiversity in mangrove areas (Barcellos et al., 2019; Manna et al., 2010; Mukhopadhyay et al., 2006). However, the increase in nutrient concentrations also shows positive effects, such as maintaining mangrove forests (Dangremond et al., 2019) and improving mangroves' growth rate and biomass (Hayes et al., 2017). These nutrients also play an essential role in the

Citation: Dung LV, Tue NT, Quy TD, Nhuan MT. Ammonium, nitrate, and phosphate in coastal waters of Red River Biosphere Reserve, Vietnam. Environ. Nat. Resour. J. 2025;23(1):55-64. (https://doi.org/10.32526/ennrj/23/20240128)

growth of phytoplankton, contributing to maintaining food webs in coastal ecosystems. The inland nutrient sources have supported and maintained marine ecosystems, including mangroves, estuaries, and coastal tidal flats. Nutrients in the coastal marine environment serve both beneficial and detrimental functions. Therfore, it is important to effectively manage pollution in these areas to ensure the sustainable use of natural resources and the protection of the surrounding environment.

A study on nutrient loads in the Red River Delta (RRD), Vietnam showed that agricultural irrigation activities and leakage from the soil environment are the primary causes leading to the increase in nitrogen and phosphorus content in the Red River water sources (Luu et al., 2012). Recent studies also show that nitrogen, phosphorus and silicate concentrations in the Red River water has gradually reached the limit point of eutrophication (Le et al., 2014). Therefore, determination of the role and impact of nutrients in the Red River Delta are necessary to protect the ecosystems and biodiversity in the future. However, the fine-scale spatial assessment has not been conducted on the nutrients in coastal waters, highlighting the neccesary for updated information in the RRD. The present study aims to determine the distribution of nutrients such as ammonium, nitrate, and phosphate, and other physiochemical parameters in the Red River Delta Biosphere Reserve, Vietnam. Study results will provide invaluable information for mangrove conservation and efforts to reduce the impact of anthropogenic activities in the RRD and other similar regions worldwide.

2. METHODOLOGY

2.1 Study site

The Red River Delta Biosphere Reserve in northern Vietnam is recognized as one of the country's largest mangrove forest and wetland conservation areas. This area encompasses a range of habitats, including mangroves, wetlands, salt marshes, estuaries, beaches, etc., supporting a high biodiversity with more than 30 different mangrove and mangrove-associated species. These ecosystems serve as habitats for numerous rare and endangered species of flora and fauna. Additionally, they play an important role in stabilizing sediment, protecting coastlines, and mitigating the impacts of climate change. The sampling sites were Ba Lat Estuary (BLE) and Thai Thuy Wetland Area (TTW) in Red River Delta Biosphere Reserve, Vietnam (Figure 1). The BLE was the largest estuary in Northern Vietnam, which provided an essential stopover for migratory birds and waterfowl. The BLE is the first Ramsar site in Vietnam and plays a critical role in biodiversity conservation and supporting local peoples' livelihoods. The BLE and TTW are situated in the tropical monsoon climate region, with the rainy season from May to October and the dry season from November to April. Mangroves are widely distributed along coastlines of BLE and TTW, with dominant mangrove species are *Kandelia obovata*, *Soneratia caseolaris*, *Rhizophora stylosa*, *Aegiceras corniculatum*, and *Avicennia marina*. The TTW is located at the north of the Red River Delta Biosphere Reserve and is rich in wetland resources such as mangroves, tidal flats, and estuary areas. The aquaculture activities are highly developed in both regions, with the main products being black tiger shrimps, white legs shrimp, clams, and sea bass. The extensive and eco-oriented shrimp farming is widespread in Ba Lat Estuary (BLE) and Thai Thuy wetlands (TTW). Intensive (or industrial) shrimp farming is the second largest production activity, distributed unevenly in the study areas. Shrimp farming developed from the 1990s to the 2010s, with the massive mangrove forest loss due to land conversion (Long et al., 2021).

2.2 Field sampling

Coastal seawater samples were collected and surveyed in three environment types, including creeks and estuaries, intensive shrimp farming ponds, and extensive shrimp ponds along the coastal zone of Red River Delta Biosphere Reserve. In the present study, the Ba Lat Estuary (BLE) and Thai Thuy Wetlands area (TTW) in the RRD were sampling locations to analyze nutrient concentration in coastal waters. Samples in BLE were collected in December 2020, including 31 water samples in coastal waters (Cw), 31 water samples in extensive ponds (EcoP), and 5 water samples in intensive shrimp ponds (InsP) (Figure 1). In TTW, a total of 11, 2, and 4 samples were collected in coastal waters, extensive shrimp ponds, and intensive shrimp ponds, respectively (Figure 1). Water samples were stored in primary polyethylene plastic bottles, stored in iceboxes, and transported to the laboratory for laboratory analysis. Physiochemical parameters such as pH, TDS, Eh, DO, and salinity were measured in-situ immediately during sampling.

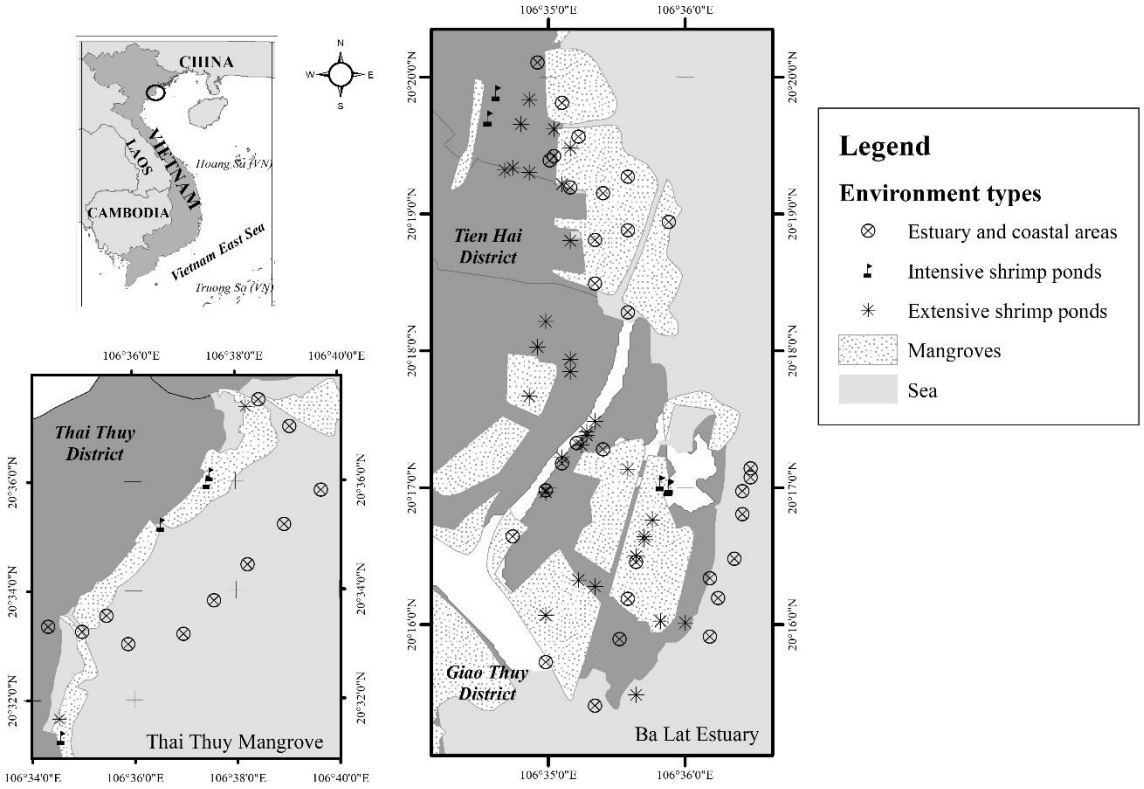

Figure 1. Sampling location in Ba Lat estuary (BLE) and Thai Thuy wetlands (TTW)

2.3 Measurement of physiochemical parameters

The physicochemical parameters of the coastal water environment, including pH, TDS, Eh, DO, and salinity, were measured directly in the field by the Horiba WQC 330 handheld system. The seawater's pH, salinity, and TDS were measured by 300-PH2 and 300-C2 digital electrodes, respectively. The seawater's redox potential was measured by glass electrode 9300-10D with Horiba digital converter. The accuracy of instruments was 0.5% and 0.1 mV for digital and glass electrodes, respectively.

2.4 Nutrient analysis

Ammonium, nitrate, and phosphate concentrations in seawater were analyzed using a CFA Skalar SAN++ continuous flow automated analysis system (Skalar Analytical BV, Breda, The Netherlands) at the VNU key laboratory of geoenvironment and response climate change, faculty of geology, university of science, Vietnam National University, Hanoi. Before conducting the analysis, the water sample was filtered through a quantitative filter paper to remove suspended matter in the solution. After filtering, water samples were kept in ice buckets and analyzed on the same day after filtration. The analysis of nutrient concentration in water was performed according to Skalar Analytical guidelines (Skalar Analytical B.V., 2019). The analytical detection limit for nitrate, ammonium, and phosphate are 15, 5, and 2 µg/L, respectively. Samples with expected ammonium, nitrate, and phosphate concentrations above 500 µg/L should be diluted at least two times before analysis. After ten samples were analyzed in a batch, a standard sample was repeated for peak correction during analysis. The system was operated automatically by Skalar's Flow Access V3 control software (Skalar Analytical B.V., 2019). Standard samples were evaluated to ensure that the change in detector signal was not more than 5% and the R-value of the analytical standard curve was higher than 0.990.

2.5 Statistical analysis

The General Linear Model (GLM) was applied to test the differences in physiochemical parameters and nutrient concentrations among locations (BLE and TTW) and environment types. Principal component analysis (PCA) assessed the relationship between physiochemical parameters and nutrient concentrations in the Thai Thuy Wetlands and Ba Lat estuary regions. IBM SPSS v20.0 and Microsoft Excel were applied to perform statistical tests in the present study. The statistical differences were confirmed with p values<0.05.

3. RESULTS AND DISCUSSION

3.1 Physiochemical parameters of coastal water

The values of water quality parameters such as pH, redox potential (Eh), TDS, and salinity are shown in Figure 2. The pH of coastal waters in TTW and BLE ranged from 7.5 to 8.3 and 6.5 to 9.4, respectively. The mean pH values of coastal waters were 7.88±0.30 and 7.57±0.44 for TTW and BLE, respectively. The DO of coastal waters in TTW and BLE ranged from 5.4 to 9.2 and 4.1 to 8.8, with average values of 7.07±1.07 and 7.89±0.76 for TTW and BLE, respectively. The pH and DO values in TTW were higher than BLE, but a statistical difference was not observed between the two sampling locations (Table 1, $p>0.05$). The redox potential of coastal waters in TTW and BLE ranged from 163.3 to 212.2 and 127.0 to 224.5 mV, respectively. The mean redox potential values of coastal waters were 190.79±13.55 and 179.02±17.90 for TTW and BLE, respectively. TTW and BLE's total dissolved solids ranged from 5.3 to 15.0 and 3.8 to 31.5 mg/L with average values of 11.44±3.33 and 17.76±7.05 (g/L) for TTW and BLE, respectively. The mean salinity was 13.46±4.14 and 18.22±7.35 (‰) for coastal water from TTW and BLE, respectively. The statistical difference between the two study sites was observed in redox potential, salinity, and TDS (Table 1, GLM test, $p<0.05$).

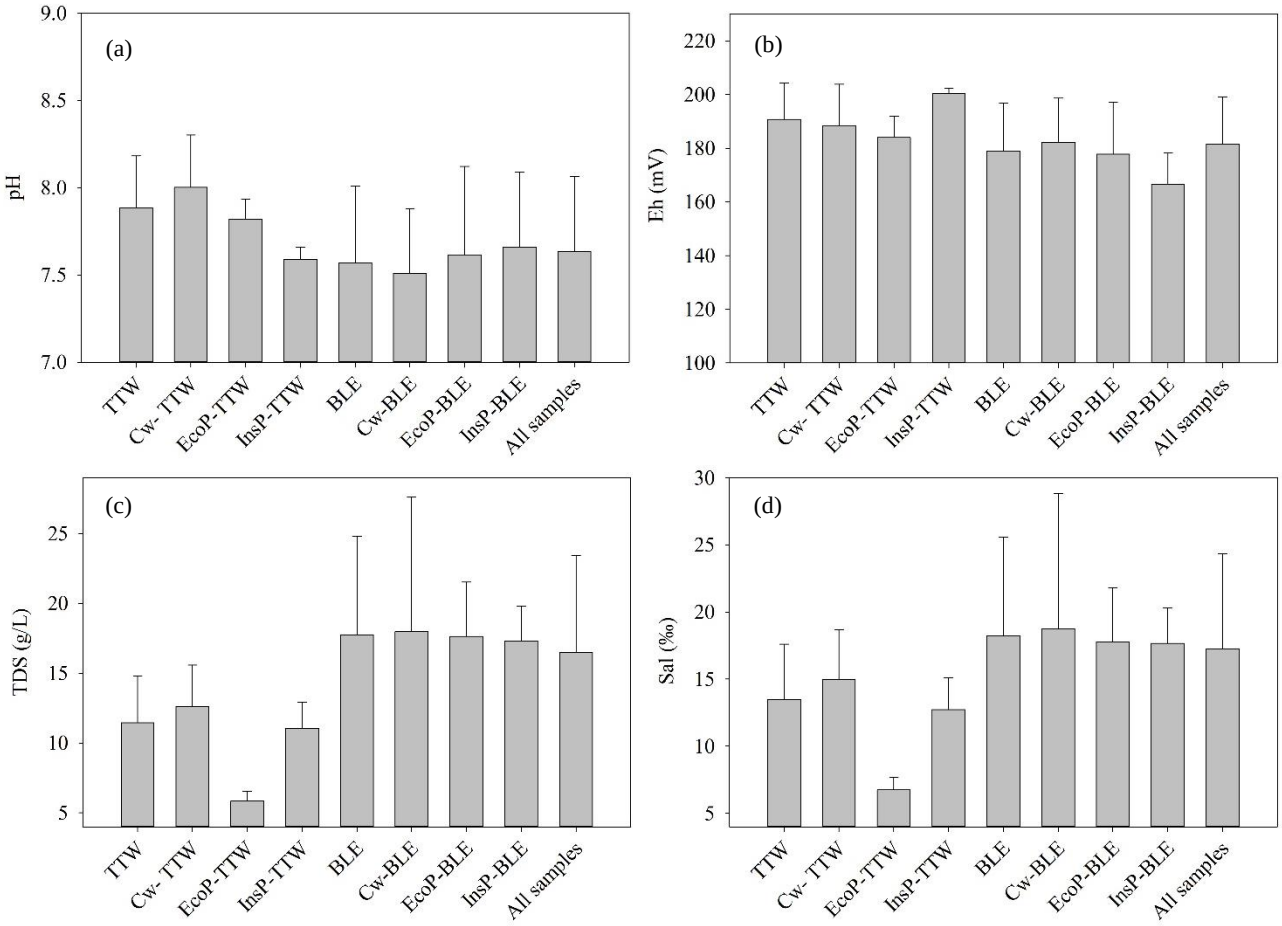

Figure 2. Water quality parameters in TTW and BLE: (a) pH, (b) redox potential, (c) total dissolved solids, and (d) salinity. Error bars represent the standard deviation (SD) of the mean. Acronyms are shown in Table 1.

The PCA results of water quality parameters showed that the first factors accounted for 57.20% and 32.07% of the variance for TTW and BLE, respectively. The second factor accounted for 19.39% in TTW and 23.06% of the variance in BLE. High loading of the first factor was observed in TDS, salinity, DO, and pH of samples from TTW, whereas the BLE observed high loading of the first factor in salinity and TDS. The PCA results suggested that TDS, salinity, DO, and pH from TTW have a strong relationship (Figure 3).

Table 1. The concentrations of ammonium, nitrate, and phosphate in BLE and TTW

Location	Ammonium (µg/L)		Nitrate (µg/L)		Phosphate (µg/L)		n
	Mean	SD	Mean	SD	Mean	SD	
Thai Thuy Wetlands (TTW)	558.27	343.29	316.57	171.42	18.77	35.06	17
Coastal and estuary (Cw)	461.91	157.94	270.08	120.87	5.79	3.62	11
Extensive shrimp ponds (EcoP)	903.22	-	644.63	-	73.87	-	2
Intensive shrimp ponds (InsP)	650.80	427.21	280.38	111.93	26.92	32.77	4
Ba Lat Estuary (BLE)	694.38	229.46	276.26	272.67	9.76	17.34	67
Cw	750.99	251.12	443.80	309.38	6.75	5.92	31
EcoP	680.70	158.11	127.12	97.79	10.99	22.26	31
InsP	428.16	305.65	162.10	176.07	20.79	27.34	5
All samples	666.83	260.02	284.42	255.05	11.58	22.12	84

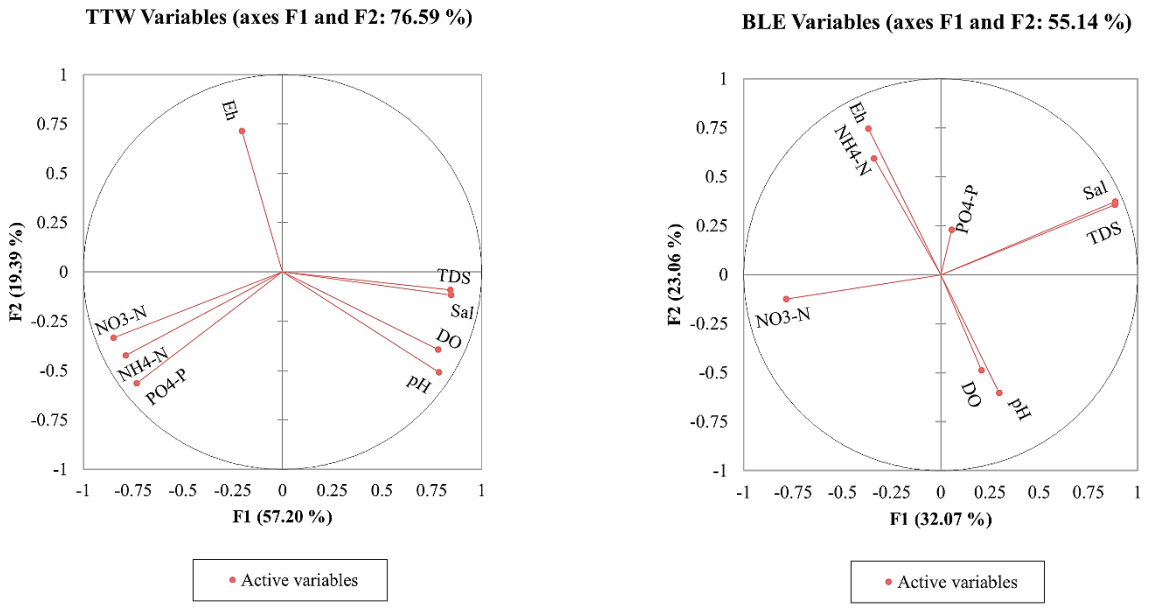

Figure 3. Principle component analysis results of physiochemical characteristics and nutrients in BLE and TTW

3.2 Nutrient concentration in coastal waters of Red River Delta

The concentration of ammonium (NH_4-N), nitrate (NO_3-N), and phosphate (PO_4-P) are shown in Table 1. In the TTW, the mean values of ammonium were 461.9±57.9, 903.2±845.1, and 650.8±427.2 µg/L for coastal waters, extensive shrimp ponds, and intensive shrimp ponds, respectively. The significant variation in ammonium concentration of waters in extensive shrimp ponds resulted from small sample sizes or differences in water retention time. The mean ammonium concentration in BLE was 751.0±251.1, 680.7±158.1, and 428.2±305.6 µg/L for coastal waters, extensive shrimp ponds, and intensive shrimp ponds, respectively. In the TTW, the mean concentration of ammonium decreased from EcoP through InsP to Cw sites, whereas in the BLE, ammonium concentration decreased in the order of Cw, EcoP, and InsP (Figure 5).

The mean concentration of nitrate (NO_3-N) was 316.6±171.0 and 276.3±272.7µg/L TTW and BLE, respectively. The average nitrate concentration in BLE were 443.8±309.4, 127.1±97.8, and 162.1±176.1 µg/L for coastal waters, extensive shrimp ponds, and intensive shrimp ponds, respectively. In the TTW, the mean concentration of nitrate decreased from EcoP through InsP to Cw with average values of 644.6±205.5, 280.4±11.9, and 270.1±120.9 µg/L, respectively (Figure 4). The phosphate concentration in water ranged from 2.8 to 137.6 and from 0.7 to 127.9 µg/L for TTW and BLE, respectively. However, the phosphate concentration has a large variation in EcoP samples, with the highest and lowest values observed in this sampling site (Table 1).

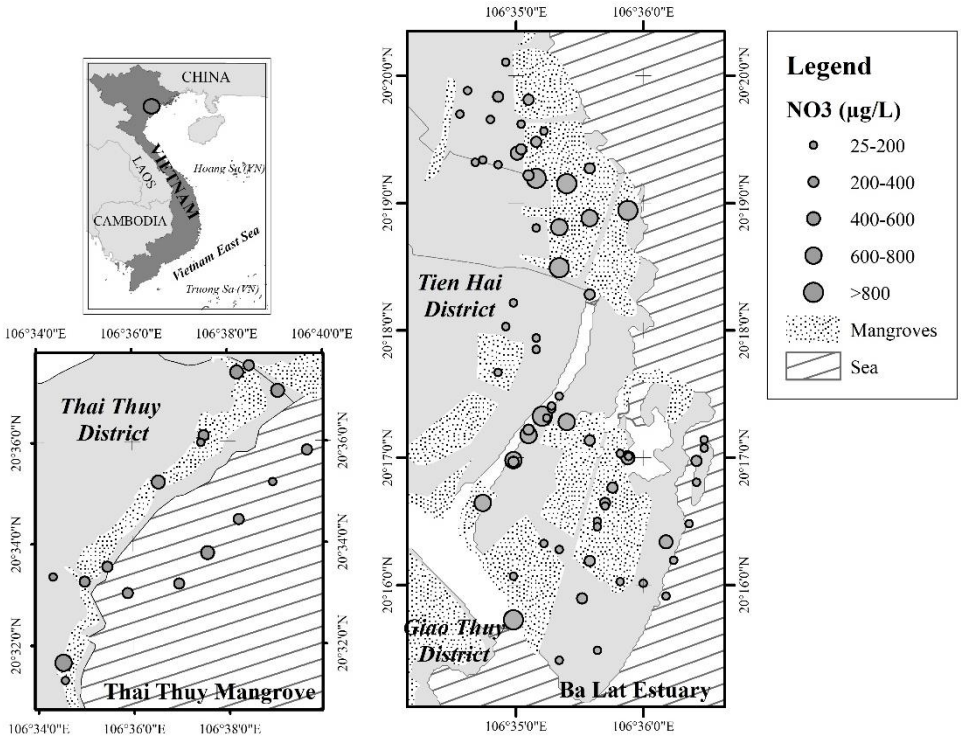

Figure 4. Nitrate concentration in the coastal waters of TTW and BLE in the Red River Biospheres Reserve

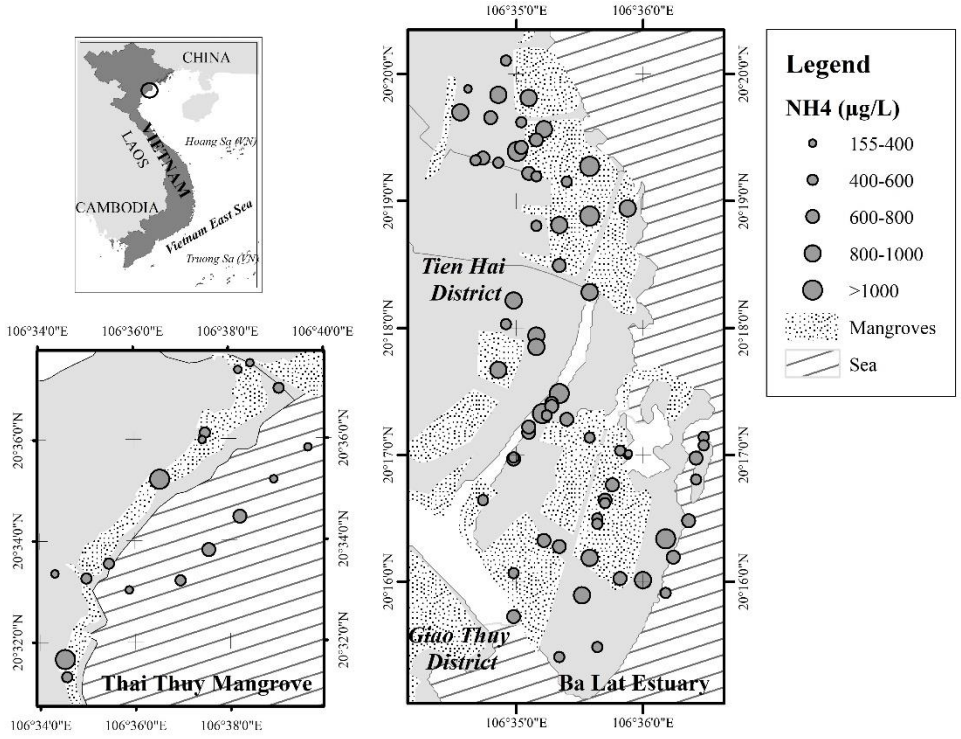

Figure 5. Ammonium concentration in coastal waters of TTW and BLE in Red River Biosphere Reserve

The PCA analysis result in TTW showed that the ammonium, nitrate, and phosphate have a strong relationship (Figure 3). A similar trend was not observed in BLE, with Eh and ammonium having a strong relationship in PCA analysis. High-loading factors of nutrients in TTW may be related to the sources of the nutrient environment. The PCA results of BLE showed that the nutrient concentration in this area might be influenced by various factors rather than anthropogenic sources from the mainland. The GLM

test showed that phosphate concentration showed a statistical difference between sampling locations, environment types, and two factors interaction (GLM, $p<0.05$). The nitrate and ammonium concentrations in each location showed statistical differences among the environment types (GLM, $p<0.05$) (Table 2). In the BLE, we observed the strong relationship between redox potential and ammonium in coastal water, which may relate to the denitrification process in mangrove and wetland ecosystems.

Table 2. The GLM analysis results of physiochemical parameters and nutrients in BLD and TTW

Source	Parameters	Type III Sum of Squares	df	Mean Square	F	Sig.
Location	NH_4-N	22,035.781	1	22,035.8	0.4	0.540
	NO_3-N	193,146.606	1	193,146.6	4.3	0.042
	PO_4-P	4,188.972	1	4,189.0	10.8	0.002
	pH	0.353	1	0.4	2.0	0.156
	DO	60.476	1	60.5	2.3	0.134
	Eh	1,944.789	1	1,944.8	6.8	0.011
	Sal	353.491	1	353.5	7.4	0.008
	TDS	495.983	1	496.0	11.5	0.001
Environmental types	NH_4-N	285,418.036	2	142,709.0	2.5	0.092
	NO_3-N	149,986.078	2	74,993.0	1.7	0.195
	PO_4-P	8,825.278	2	4,412.6	11.3	0.000
	pH	0.120	2	0.1	0.3	0.706
	DO	10.388	2	5.2	0.2	0.822
	Eh	133.394	2	66.7	0.2	0.793
	Sal	133.605	2	66.8	1.4	0.252
	TDS	78.809	2	39.4	0.9	0.406
Location* Environmental types	NH_4-N	713,335.224	2	356,667.6	6.1	0.003
	NO_3-N	776,757.509	2	388,378.8	8.6	0.000
	PO_4-P	6,258.984	2	3,129.5	8.0	0.001
	pH	0.595	2	0.3	1.7	0.185
	DO	7.360	2	3.7	0.1	0.870
	Eh	1,389.489	2	694.7	2.4	0.096
	Sal	79.981	2	40.0	0.8	0.435
	TDS	63.700	2	31.8	0.7	0.482

4. DISCUSSION

4.1 Factors influencing physiochemical parameters of coastal waters

The redox potential, salinity, and TDS showed a clear spatial variation trend between TTW and BLE, with the salinity and TDS in TTW significantly lower than those of BLE and vice versa for redox potential. These patterns resulted from tidal dynamics and water exchange between mangroves, shrimp ponds, and coastal water. The salinity and TDS in TTW showed a significant variation among Cw, InsP, and, EcoP zones, whereas salinity and TDS in BLE were more stable in all sampling areas (Table 1). The lower values of salinity and TDS in TTW may be related to water discharge from low salinity aquaculture activities (sea bass production) in TTW, which led to the decreasing trend of salinity and TDS in adjacent shrimp ponds. The physiochemical parameters of coastal and estuarine seawater have seasonal and tidal fluctuations (Trang et al., 2013; Wösten et al., 2003) and seasonal variation was also considered an important influencing factor of physiochemical parameters in river estuaries (Fatema et al., 2014; Pham, 2017; Prabu et al., 2008; Saravanakumar et al., 2008). A study in Pichavaram mangroves showed that the monsoon, river discharge, and tidal variation strongly influence physiochemical parameters in coastal waters (Prabu et al., 2008). In the present study, water samples in the RRD were collected in the dry season, and physiochemical parameters may be

strongly affected by tidal flushing rather than river discharge from the mainland. The seasonal variation analysis of nutrient dynamics should be determined in the future research. Additionally, physiochemical parameters are also affected by the water exchange process between the aquaculture ponds and coastal waters in this region. According to tidal cycles, local people will drain wastewater from inside aquaculture ponds into the adjacent tidal creeks at low tide and receive fresh supply water at high tide. Overall, physiochemical parameters of coastal water in this area are influenced by three factors of aquaculture wastewater, mangroves exchange water, and tidal seawater. This pattern is a complex exchange process in coastal estuaries, especially in the RRD. Therefore, long-term monitoring is necessary to assess changes of these parameters in future studies.

4.2 Nutrient variation in the coastal ecosystems of the Red River Delta

The nutrients content in the RRD was higher than those of coastal areas in Vietnam and worldwide (Table 3). The ammonium and nitrate concentrations in the RRD were relatively high compared to Cam and Bach Dang estuaries in northern Vietnam (Trang et al., 2013), and equivalent to Can Gio Area, Ho Chi Minh City (Pham, 2017), Paguil Bay, Philippines, and Merbok estuary, Malaysia (Canini et al., 2013; Fatema et al., 2014). The sources of these nutrients are mainly from human-caused anthropogenic activities such as agriculture, aquaculture, industry, urban waste, etc., and a small part due to natural processes such as the decomposition of organic matter and growth of microorganisms (Downing, 1999; Reopanichkul et al., 2010).

Table 3. The concentration of nutrients in selected study sites in the world

Location	Environment types	NH_4-N (µg/L)	NO_3-N (µg/L)	PO_4-P (µg/L)	References
Red River Delta	Extensive shrimp ponds	305.6-1,500.8	25.1-789.9	0.7-137.6	Current study
	Intensive shrimp ponds	155.8-1,274.9	37.5-472.5	5.3-75.8	
	Estuary and coastal areas	239.1-1,413.6	64.4-996.4	2.2-24.0	
Hai Phong (Vietnam)	Estuary	16.5-571.5	86.7-285.4	8.81-39.00	Trang et al. (2013)
Can Gio (Vietnam)	Estuary	150-300	600-1,500	150-320	Pham (2017)
Phuket (Thailand)	Nearshore water	0.00-93.15	0.00-41.30	0.00-81.30	Reopanichkul et al. (2010)
Panguil Bay (Philipines)	Coastal water	-	300-900	100-500	Canini et al. (2013)
Merbok (Malaysia)	Estuary	100-1,180	50-210	60-80	Fatema et al. (2014)
Allowable limit (local)		100 (Vietnam technical regulation on Marine water quality QCVN10:2023)	60 (ASEAN)	200 (Vietnam technical regulation on Marine water quality QCVN10:2023)	ASEAN-Secretariat (2008)

The distribution of ammonium in coastal water showed a large variation in both TTW and BLE in the RRD. The highest ammonium value was observed in the EcoP site in TTW, whereas the lowest was InsP from BLE. In both areas, the mean ammonium concentration in the EcoP site was higher than in the InsP and Cw samples. This pattern may be related to the decomposition of organic matter and shrimp waste in extensive shrimp ponds, which usually lack of waste water treatment system. Intensive shrimp ponds use water propellers to provide oxygen in water, enhancing the nitrification process and reducing ammonia concentration. The other reason is organic matter ammonification in EcoP with a high density of mangrove trees surrounding the aquaculture ponds (Alongi, 2018; Feller et al., 2003; Taillardat et al., 2020). The high availability of mangrove litter in EcoP will enhance loads of organic matter decomposition, leading to increased ammonium concentration in water (Taillardat et al., 2020). The strong relationship between ammonium concentration and redox potential in BLE supported this pattern (Miao et al., 2006). The ammonium concentration in coastal water of BLE and TTW showed an opposite trend, with the ammonium values of Cw samples in BLE higher than those of EcoP and InsP and vice versa for samples from TTW regions. This trend resulted from the natural characteristics of BLE and TTW regions. The BLE is

large estuary with complex tidal creek systems and receives a massive amount of ammonium from adjacent shrimp ponds and mangrove forests (Taillardat et al., 2020), causing the increase of ammonium in the water column.

The nitrate concentration in the RRD showed an opposite trend with ammonium in coastal environments, with the mean concentration in the BLE lower than those of TTW areas. The strong relationship between ammonium, nitrate, and phosphate in the TTW (Figure 3) suggested that the nutrients in this area may originate from the same sources. This pattern was not observed in water samples from BLE, with the nitrate having high loading in PC1. In contrast, ammonium has high loading in PC2 (Figure 3). These results indicated that the nitrate sources in the BLE and TTW may be originated from mainland discharge and local sources, respectively. The BLE received nutrient loads from the urban and industrial areas in northern Vietnam, which led to the high concentration of nitrate in water. Furthermore, the decrease of water discharge volume in the dry season may lead to a weak nutrient dilution process in estuaries, causing an increase trend in nutrient concentration from coastal water adjacent to mangrove forests and aquaculture ponds.

A previous study in the RRD showed that mangrove forests play essential roles in nutrient composition exchange between estuarine and coastal waters. Mangroves in this area were considered net sinks of nutrients from the mainland, where nutrients are assimilated for biomass growth and preserved nutrients in the sediment stratum (Wösten et al., 2003). However, the increase in nutrient discharge may lead to an increased mortality rate of mangroves and degrade other coastal ecosystems (Lovelock et al., 2009). The aquaculture in the coastal zone was also considered an important factor influencing the nutrient dynamic in this region. The effluent from shrimp ponds (both EcoP and InsP) may be led to eutrophic risks in mangrove forests and adjacent coastal waters (Páez-Osuna, 2001; Queiroza et al., 2019; Robertson, 1995). Therefore, reducing nutrient sources from the mainland is necessary for treating aquaculture wastewater in the coastal zone. In addition, the conservation of mangroves is also a solution to reduce nutrient loads released into the marine environment due to filtering pollutants and net sinks of nutrients in the coastal estuary area (Lin and Dushoff, 2004; Tanaka and Choo, 2000).

5. CONCLUSION

Ammonium, nitrate, and phosphate in coastal waters were influenced by tidal flushing, aquaculture discharge, and nutrient exchange between mangrove forests and estuarine water in the Red River Delta. The variation of nutrients in coastal waters and shrimp ponds from the RRD resulted from three main sources of mainland discharge, aquaculture activities, and decomposition of organic matter in coastal zone. Even though the nutrient concentration in intensive shrimp ponds was lower than those of extensive shrimp ponds and adjacent coastal waters, the effluent discharge from this area could be a significant source of nitrogen and phosphorus discharge to the environment. This research indicated that there had been an increase in nutrient concentrations (ammonium, nitrate) in the coastal waters and adjacent aquaculture ponds of the RRD. The prolonged elevation of nutrient levels in the coastal marine environment is expected to result in eutrophication, which will have adverse effects on mangrove forests, tidal flats, estuaries, and other coastal ecosystems. Therefore, spatial and temporal monitoring is necessary to clarify the variation and dynamics of nutrients in coastal marine environments in the future.

ACKNOWLEDGEMENTS

The authors are grateful to staffs of University of Science, Vietnam National University, Hanoi for their support during field sampling. This research is supported by the Ministry of Natural Resources and Environment, Vietnam (MONRE) under project number TNMT.2018.06.16 and partially supported by project TXTCN.21.26 of Vietnam National University, Hanoi.

We express our gratitude to two anonymous reviewers for their invaluable feedback and comments, which have contributed to the enhancement of this manuscript.

REFERENCES

Alongi DM. Impact of global change on nutrient dynamics in mangrove forests. Forests 2018;9(10):Article No. 596.

ASEAN-Secretariat. ASEAN Marine Water Quality Management Guidelines and Monitoring Manual. Australia: Australia Marine Science and Technology Ltd. (AMSAT); 2008.

Barcellos D, Queiroz HM, Nóbrega GN, de Oliveira Filho RL, Santaella ST, Otero XL. Phosphorus enriched effluents increase eutrophication risks for mangrove systems in northeastern Brazil. Marine Pollution Bulletin 2019;142: 58-63.

Canini ND, Metillo EB, Azanza RV. Monsoon-influenced phytoplankton community structure in a Philippine mangrove estuary. Tropical Ecology 2013;54(3):331-43.

Dangremond EM, Simpson LT, Osborne TZ, Feller IC. Nitrogen enrichment accelerates mangrove range expansion in the temperate-tropical ecotone. Ecosystems 2019;23(4):703-14.

Downing JA, McClain M, Twilley R, Melack JM, Elser J, Rabalais NN, et al. The impact of accelerating land-use change on the N-Cycle of tropical aquatic ecosystems: Current conditions and projected changes. Biogeochemistry 1999;46:109-48.

Fatema K, Wan Omar WM, Isa MM. Spatial and temporal variation of physico-chemical parameters in the Merbok Estuary, Kedah, Malaysia. Tropical Life Sciences Research 2014;25(2):1-19.

Fauzi A, Skidmore AK, Gils Hv, Schlerf M, Heitkönig IMA. Shrimp pond effluent dominates foliar nitrogen in disturbed mangroves as mapped using hyperspectral imagery. Marine Pollution Bulletin 2013;76(1):42-51.

Fauzi A, Skidmore AK, Heitkonig IM, van Gils H, Schlerf M. Eutrophication of mangroves linked to depletion of foliar and soil base cations. Environmental Monitoring and Assessment 2014;186(12):8487-98.

Feller IC, Whigham DF, McKee KL, Lovelock CE. Nitrogen limitation of growth and nutrient dynamics in a disturbed mangrove forest, Indian River Lagoon, Florida. Oecologia 2003;134(3):405-14.

Hayes MA, Jesse A, Tabet B, Reef R, Keuskamp JA, Lovelock CE. The contrasting effects of nutrient enrichment on growth, biomass allocation and decomposition of plant tissue in coastal wetlands. Plant and Soil 2017;416(1):193-204.

Le TPQ, Billen G, Garnier J, Chau VM. Long-term biogeochemical functioning of the Red River (Vietnam): Past and present situations. Regional Environmental Change 2014; 15(2):329-39.

Lin BB, Dushoff J. Mangrove filtration of anthropogenic nutrients in the Rio Coco Solo, Panama. Management of Environmental Quality: An International Journal 2004;15(2):131-42.

Long C, Dai Z, Zhou X, Mei X,Van CM. Mapping mangrove forests in the Red River Delta, Vietnam. Forest Ecology and Management 2021;483:Article No. 118910.

Lovelock CE, Ball MC, Martin KC, Feller ICF. Nutrient enrichment increases mortality of mangroves. PLoS One 2009; 4(5):e5600.

Luu TNM, Garnier J, Billen G, Le TPQ, Nemery J, Orange D, et al. N, P, Si budgets for the Red River Delta (Northern Vietnam): How the delta affects river nutrient delivery to the sea. Biogeochemistry 2012;107(1):241-59.

Manna S, Chaudhuri K, Bhattacharyya S, Bhattacharyya M. Dynamics of Sundarban estuarine ecosystem: Eutrophication induced threat to mangroves. Saline Systems 2010; 6(1):Article No. 8.

Miao S, DeLaune RD, Jugsujinda A. Influence of sediment redox conditions on release/solubility of metals and nutrients in a Louisiana Mississippi River deltaic plain freshwater lake. Science of the Total Environment 2006;371(1-3):334-43.

Mukhopadhyay S, Biswas H, De T, Jana T. Fluxes of nutrients from the tropical River Hooghly at the land-ocean boundary of Sundarbans, NE Coast of Bay of Bengal, India. Journal of Marine Systems 2006;62(1-2):9-21.

Páez-Osuna F. The environmental impact of shrimp aquaculture: Causes, effects, and mitigating alternatives. Environmental Management 2001;28(2):131-40.

Pham TL. Environmental gradients regulate the spatio-temporal variability of phytoplankton assemblages in the Can Gio Mangrove Biosphere Reserve, Vietnam. Ocean Science Journal 2017;52(4):537-47.

Prabu VA, Rajkumar M, Perumal P. Seasonal variations in physico-chemical characteristics of Pichavaram mangroves, southeast coast of India. Journal of Environmental Biology 2008;29(6):945-50.

Queiroza HM, Artur AG, Taniguchic CAK, da Silveirac MRS, Nascimento JCd, Nóbregad GN, et al. Hidden contribution of shrimp farming effluents to greenhouse gas emissions from mangrove soils. Estuarine, Coastal and Shelf Science 2019;221:8-14.

Reopanichkul P, Carter RW, Worachananant S, Crossland CJ. Wastewater discharge degrades coastal waters and reef communities in southern Thailand. Marine Environmental Research 2010;69(5):287-96.

Robertson AIPM. Mangroves as filters of shrimp farm effluent: Predictions and biogeochemical research needs. Hydrobiologia 1995;293:311-9.

Saravanakumar A, Rajkumar M, Serebiah JS, Thivakaran GA. Seasonal variations in physico-chemical characteristics of water, sediment and soil texture in arid zone mangroves of Kachchh-Gujarat. Journal of Environmental Biology 2008; 29(5):725-32.

Skalar Analytical B.V. Skalar SAN++ User Quide. Breda, The Netherlands: 2019.

Taillardat P, Marchand C, Friess DA, Widory D, David F, Ohte N. Respective contribution of urban wastewater and mangroves on nutrient dynamics in a tropical estuary during the monsoon season. Marine Pollution Bulletin 2020; 160:Article No.111652.

Tanaka K, Choo PS. Influences of nutrient outwelling from the mangrove swamp on the distribution of phytoplankton in the Matang Mangrove Estuary, Malaysia. Journal of Oceanography 2000;56(1):69-78.

Trang CTT, Kha PT, Torreton JP, Nghi DT, Luu VT. Water Quality in Cam-Bach Dang Estuary Area, IRD Symposium on Marine Science. Hai Phong, Vietnam: Publishing House for Science and Technology; 2013.

Wösten J, De Willigen P, Tri N, Lien T, Smith S. Nutrient dynamics in mangrove areas of the Red River Estuary in Vietnam. Estuarine, Coastal and Shelf Science 2003;57(1-2): 65-72.

Environment and Natural Resources Journal

Volume 23
Issue 1
2025

Roughness Variation Impact on the Morphological Evolution at the Medjerda River: Telemac 2D-Sisyphe Modeling

Hammami Saber[1,2], Romdhane Hela[1], Soualmia Amel[1*], and Kourta Azeddine[2]

[1]National Institute of Agronomy of Tunisia, University of Carthage, 43 Avenue Charles Nicolle, 1082 Tunis, Tunisia
[2]University of Orléans, INSA-CVL, PRISME, EA 4229, 45072, Orléans, France

ARTICLE INFO

Received: 20 Feb 2024
Received in revised: 4 Nov 2024
Accepted: 11 Nov 2024
Published online: 3 Jan 2024
DOI: 10.32526/ennrj/23/20240043

Keywords:
Telemac-Sisyphe Model/ Sediment transport/ Vegetation/ River stability/ Medjerda River

*** Corresponding author:**
E-mail: amel.inat@hotmail.fr

ABSTRACT

Sediment transport plays a vital role in river management and flood protection, particularly in regions prone to erosion and deposition. The study aims to assess the impact of roughness modification on the sediment transport process in the Medjerda, Tunisia's longest perennial river, following a decade of dredging activities implemented for flood protection measures in the Boussalem city. We used the Telemac Sisyphe model to stimulate sediment 17.8 km section, which regularly undergoes dredging crossing the city of Boussalem. This section contains two distinct parts: first a smooth riverbed followed by the variable roughness on both sides of the banks, which is influenced by the existing vegetation cover. The study developed four simulation scenarios, with a smooth riverbed maintained in call cases while the roughness of the second part increasing from smooth to rough. The model-generated outputs facilitated a comprehensive longitudinal and transverse comparative analysis, focusing on flow velocity, shear stress, and bed evolution profile in response to varying roughness levels. The results show a reduction in erosion and deposition phenomena as the roughness as the bank's roughness increases. this the crucial role of vegetation in stabilizing river banks by, strengthening the cohesion of the riverbed, thus minimizing erosion risks and excessive sediment transport, ultimately maintaining the riverbed's integrity. These findings contribute to understanding of sedimentation patterns in the Medjerda River and facilitated the prediction of potential impacts on its fluvial morphology.

1. INTRODUCTION

Erosion processes, sediment supply, and their transport are essential elements of river system functioning (Nazi et al., 2016), significantly influencing river morphology by altering their shape and structure over time. The mechanisms of aggradation, characterized by sediment accumulation, and degradation, resulting from bed erosion, contribute to the development of a distinct topography within the riverbed (Mugade Mugade and Sapkale, 2015). These dynamic processes, which are influenced by the movement and redistribution of sediment particles (Vargas-Luna et al., 2019), play a key role in the continuous evolution of river morphology, leading to a distinct and recognizable geomorphological configuration. However, the transport capacity of a river channel can diminish when large quantities of sediment accumulate in the riverbed, increasing the risk of the rivercourse shifting into adjacent areas (Badoux et al., 2014; Rickenmann et al., 2016). Typically, sediment transport rates are estimated using empirical equations (Meyer-Peter and Müller, 1948; van Rijn, 1984; Einstein, 1950; Wilcock and Crowe, 2003), which are largely based on laboratory experiments that often oversimplify real-world conditions. More recent equations, which incorporate some field data, offer improved accuracy in representing natural processes (Recking, 2013).

Riverbanks provide a particularly favorable environment for vegetation. This vegetation increases

Citation: Saber H, Hela R, Amel S, Azeddine K. Roughness variation impact on the morphological evolution at the Medjerda River: Telemac 2D-Sisyphe Modeling. Environ. Nat. Resour. J. 2025;23(1):65-79. (https://doi.org/10.32526/ennrj/23/20240043)

local roughness, alters flow patterns, and adds additional resistance, thereby reducing bed shear stress and promoting local sediment deposition (Luca et al., 2020). Roughness increases with the height and density of the vegetation. Vegetation significantly reduces sediment transport rates, especially when vegetation density is high (Penna et al., 2022; Li et al., 2022). Fortes et al. (2022) demonstrated, using a dynamic roughness model, that the water level profile increased by an average of 7.03%, thereby inferring the seasonal effect of vegetation. Fan et al. (2023) studied the relative roughness of riverbanks compared to the bed roughness, a key factor in the anti-erosion of river boundaries, using a rectangular cross-sectional model. The results reveal an optimal width-to-depth ratio for each value of relative roughness (λ). Thus, an increase in λ leads to a 36.46% reduction in river width and a 28% increase in depth. Furthermore, Fan et al. (2020) demonstrated that varying the bank angle from 0° to 60° results in a 34.84% increase in channel width and a 13.29% decrease in depth, with other hydraulic parameters remaining relatively constant.

In recent decades, rivers worldwide have been subjected to significant anthropogenic interventions, such as bank reinforcement, dam construction, urban expansion in floodplains, agricultural development, and deforestation practices (Nanson et al., 2010). Morphological models coupled with hydrodynamic models (Reisenbüchler et al., 2019) have now been applied to various rivers of different sizes and characteristics to examine channel evolution (Guan et al., 2016; Tu et al., 2017; Ramirez et al., 2020). For example, Yassine et al. (2023) developed a 2D hydromorphodynamic model with the TELEMAC-MASCARET system for the section of Lac des Gaves in the Hautes-Pyrénées to reproduce bed changes following the 2018 flood. Their study showed that the Meyer-Peter-Müller and Recking sediment transport equations, coupled with Ferguson and Strickler friction laws, are crucial for realistic simulations. Meanwhile, Nazarjani et al. (2023) revealed significant instability in 71% of the Kashafrood River sections in Iran, with high erosion potential exacerbated by human activities such as land use changes and dredging. This instability has already led to the demolition of some infrastructure due to severe erosion, highlighting the impact of human interventions on fluvial conditions.

The Medjerda is the only perennial river in Tunisia, collecting half of the country's exploitable surface water from the north. Significant sediment deposits, partly due to frequent moderate floods and hydraulic structures, have led to modifications in the riverbed (Gharbi, 2016). Various studies have analyzed sediment transport processes in the Medjerda, notably Gharbi et al. (2016), who used Telemac 2D and Sisyphe to study sediment transport during floods and its effects on river morphology, demonstrating a close link with flood issues. Morri et al. (2016) applied the same model to simulate flow, sediment transport, and morphological changes in the presence of vegetation, integrating hydraulic resistance through an adapted friction coefficient in the Medjerda.

In our previous work, we modeled flows in the Medjerda River using TELEMAC 2D and HEC-RAS to map floods and assess the impact of dredging works, as well as to create scenarios and risk maps for return periods up to 100 years. Our calibration results revealed the Manning's coefficient values for the different studied areas as follows: minor bed (without vegetation): 0.033 s/m⅓, middle bed occupied by Tamarix: 0.10 s/m⅓, cleared middle bed: s/m⅓, major bed (agricultural zone): s/m⅓, and major bed (urban zone): 0.2 s/m⅓ (Hammami et al., 2022; Hammami et al., 2023; Hammami et al., 2024). Consequently, the roughness of the riverbanks ranges between 0.03 s/m⅓ (smoother, dredged) and 0.10 s/m⅓ (rougher, dense vegetation). The objective of this study is to determine the impact of the relative roughness of the banks on the morphology of the wadi, shear stress, and consequently, on sediment transport in the river. To achieve this, the Telemac2D hydrodynamic model was coupled with the Sisyphe sediment transport model. This combination allows for detailed simulation of the complex interactions between water flow, bank roughness, and sediment transport processes, to better understand and predict morphological changes in the riverbed under different conditions. To this end, we maintained the river's minor bed smooth while progressively increasing the roughness of the banks from 0.03 s/m⅓ to 0.09 s/m⅓. This approach allows for the analysis of the effects of increasing bank roughness on hydrodynamic and sedimentary parameters.

2. METHODOLOGY

2.1 Study area

A stretch of the Medjerda River passing through the city of Boussalem, located between the coordinates 36°36'40" N, 8°58'11" E, within the alluvial plain of the upper Medjerda Valley, has been selected to

illustrate the aforementioned impacts, where the Medjerda River undergoes regular dredging works to combat flooding. The total length of this section is 17.8 km. The study area is situated 20 km upstream from the Sidi Salem Dam (Figure 1), which has a significant influence on sedimentation in the study section. Indeed, since its construction and impoundment, the dam has resulted in the formation of a sediment plug at the entrance of the reservoir, requiring approximately the Boussalem City to be reached for the dam's impact to dissipate.

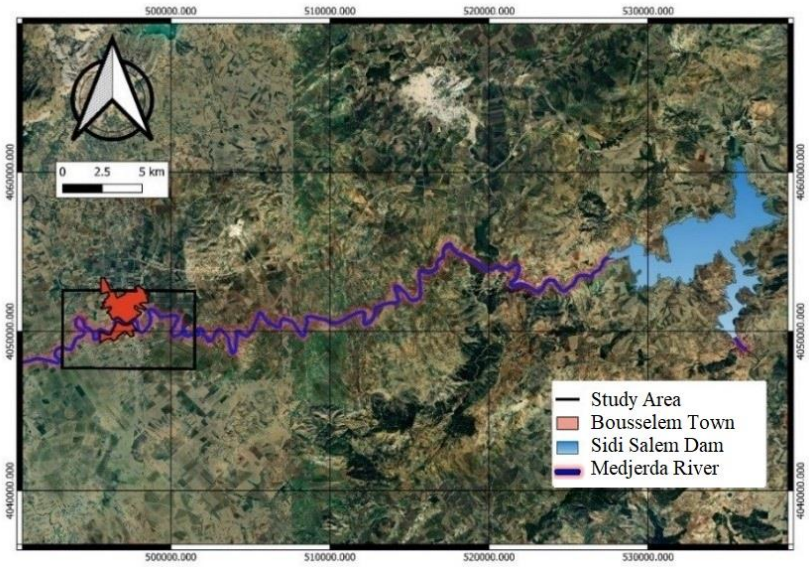

Figure 1. Location of the study area (Boussalem City: 36°36′40″ N, 8°58′11″ E)

2.2 Model and conceptual scheme

The TELEMAC-MASCARET system, an open-source software, is used for numerical simulations, including free surface flows, sediment transport, waves, and water quality (Hervouet, 2003). To model hydrodynamic and morphodynamic processes, we have selected the TELEMAC2D and SISYPHE modules. TELEMAC2D is used to simulate free surface flows and hydrodynamic interactions, while SISYPHE is employed to model sediment transport and morphological changes in the riverbed. The integration of these two modules allows for a comprehensive and coherent analysis of river dynamics under different roughness conditions, providing a powerful tool for studying riverbed evolution and sediment interactions.

For suspended sediment transport, SISYPHE solves the advection-diffusion equation for sediment concentration, accounting for turbulence effects and settling velocities, which is essential for simulating the movement of particles in the water column. Meanwhile, bedload transport is modeled using specific equations, such as the Meyer-Peter and Müller equation, to represent the movement of sediments along the riverbed under the influence of flow forces.

2.2.1 Hydrodynamic module

TELEMAC 2D solves the Saint-Venant equations to simulate free surface flows, which are decomposed into mass and momentum conservation equations.

$$\frac{\partial h}{\partial_t} + u \times \nabla(h) + h\nabla \times (u) = 0$$

$$\frac{\partial u}{\partial_t} + u \times \nabla(u) = -gd_x\, zf - gS_{f,x} + h^{-1}\nabla \times (hv_t \nabla u)$$

$$\frac{\partial v}{\partial_t} + u \times \nabla(v) = -gd_y\, zf - f\, S_{f,y} + h^{-1}\nabla \times (hv_t \nabla v)$$

Where; t [s] is the time, $\nabla = \partial x, \partial y)$ is the gradient field, g = 9.81 ms^{-2} is the acceleration due to gravity, h [m] is the water depth, u=(u,v) [m/s] is the average depth velocity vector with u and v [ms^{-1}] being the components along the longitudinal x and transverse y axes, respectively, with {u} [ms^{-1}] being the magnitude of u, and v_t [m^2s^{-1}] is the turbulent viscosity term.

2.2.2 The 2D sediment transport model

In SISYPHE, there are two sediment transport modes based on transport mechanisms: bed load and suspended load:

$$q_t = q_b + q_s$$

Where; q_t is the total sediment transport, q_b is the bed load transport, and q_s is the suspended load transport.

2.2.3 Suspended sediment transport module

Suspended transport is the portion of sediment carried by a liquid flow that settles slowly enough that it almost never touches the bed. It is kept in suspension due to the turbulence of the moving water and typically consists of fine sand particles, silt, and clay. Suspended sediment transport is accounted for by SISYPHE by solving the two-dimensional advection-diffusion equation, expressed by:

$$\frac{\partial hC}{\partial t} + \frac{\partial huC}{\partial x} + \frac{\partial hvC}{\partial y} = \frac{\partial}{\partial x}\left(h\varepsilon_s \frac{\partial C}{\partial x}\right) + \frac{\partial}{\partial y}\left(h\varepsilon_s \frac{\partial C}{\partial y}\right) + E - D$$

Where; c=c(x, y, t) is the depth-averaged concentration expressed as a volume percentage (-), and ε_s is the turbulent diffusivity of sediments, often related to the turbulent viscosity $\varepsilon_s = \frac{v_t}{\sigma_c}$, with σ_c being the Schmidt number, equal to 1.0 in SISYPHE. The non-cohesive deposition rate is $D = w_s C_{Z_{ref}}$, where w_s is the sedimentation velocity and Z_{ref} is the concentration near the bed, assessed at the interface between bed load and suspended load transport, $=Z_{ref}$. The non-cohesive erosion rate is $=w_s C_{eq}$, where C_{eq} is the equilibrium concentration near the bed determined using an empirical formula.

2.2.4 Bedload sediment transport

The term "bedload" refers to the particles in a moving fluid (typically water) that are transported along the bed. Bedload moves through rolling, sliding, and/or saltation (hopping). The morphodynamic module is based on the Exner equation (Exner, 1920), which can be coupled with the hydrodynamic module equation.

$$(1-\gamma)\frac{\partial z_b}{\partial t} + \nabla \times Q_b = 0$$

With Q_b being the volumetric transport rate per unit width without pores (m^2/s), Z_b the bed elevation (m), and γ the bed porosity. The dimensionless sediment transport rate induced by the current q_b^* is expressed by:

$$q_b^* = \frac{Q_b}{\sqrt{g\left(\frac{\rho_s}{\rho}-1\right)d^3}}$$

With ρ_s being the sediment density (kg/m^3); ρ the water density (kg/m^3); and d the grain diameter ($=d_{50}$ for a uniform sediment distribution (m)). Bedload transport formulas are generally calculated based on the Shields number θ, given by the formula:

$$\theta = \frac{\mu\tau_b}{(\rho_s - \rho)\, gd}$$

With τ_b being the bed shear stress [Pa] and μ the correction factor for surface friction. The Meyer-Peter-Müller equation is a threshold equation, and its original formulation considers a critical Shields parameter equal to 0.047. The equation is written as follows:

$$q_b^* = 8(\theta - \theta_{cr})^{3/2} = 8(\tau^* - \tau_c^*)^{3/2}$$

Where; τ^* is the critical bed shear stress, expressed as $\tau^* = \frac{\tau}{(\rho_s - \rho)d_{50}}$ and $\tau_c{}^*$=0.047 is the minimum shear stress required to initiate sediment particle movement, often called the critical shear stress, which is a key parameter in sediment transport. It corresponds to the force exerted by the water flow on the sediment particles that is sufficient to overcome resisting forces, such as cohesion and weight, thereby causing the onset of particle movement.

Knowing that:

- The hydraulic friction coefficient Manning-Strickler is $= \frac{U}{R_h^{3/2} S^{1/2}}$, where U [$ms^{-1}$] is the average flow velocity, S [mm^{-1}] is the bed slope, and R_h [m] is the hydraulic radius.
- The grain roughness coefficient can be estimated based on the grain size distribution as $K' = \frac{26}{d_{90}^{1/6}}$, where d_{90} is the diameter corresponding to approximately 90% by weight of the grains.

The Meyer-Peter-Müller equation is written as follows:

$$q_b^* = 8\left[\left(\frac{K'}{K}\right)^{3/2}\tau^* - 0.47)\right]^{3/2}$$

The Telemac-Sisyphe coupling is designed to address a set of morphodynamic issues (sediment transport and bed evolution) and is particularly suited for assessing sediment stock response to hydrodynamic conditions, notably bed shear stress. This coupling represents an integrated approach for the numerical modeling of free-surface flows and sediment transport in riverine, estuarine, and coastal

environments. These two models are often used synergistically to provide a more comprehensive representation of hydrodynamic and sedimentary processes.

The coupling is achieved in a chained fashion with an update of the domain geometry for each time step. In other words, the hydrodynamic module is executed first, followed by the morphodynamic module using the hydrodynamic results (Gharbi et al., 2016). Subsequently, an update of the domain geometry is performed before the next time step (Figure 2).

2.3 Roughness calibration

In our previous work, we modeled flows in the Medjerda River using TELEMAC 2D and HEC-RAS to map floods and assess the impact of dredging operations. The calibration results provide Manning's roughness coefficient values for the different studied areas: minor bed (without vegetation): 0.033 s/m⅓, middle bed occupied by Tamarix: 0.10 s/m⅓, dredged middle bed: 0.4 s/m⅓, major bed (agricultural area): 0.6 s/m⅓, and major bed (urban area): 0.2 s/m⅓ (Hammami et al., 2023). Therefore, the roughness of the banks ranges from 0.03 s/m⅓ (smoother, dredged) to 0.10 s/m⅓ (rougher, dense vegetation).

We chose a simplified configuration of the river section containing two distinct parts: the first part, located at the riverbed, which is completely smooth with a roughness coefficient of 0.03 s/m⅓, and includes the minor bed and the dredged middle bed. The second part, located on both sides of the banks, has variable roughness depending on the pre-existing vegetation cover (Figure 3). The scenarios we studied were designed with a fixed roughness for the riverbed, kept smooth, while the roughness of the banks was varied from the smoothest to the roughest. Four simulation scenarios were established, progressively increasing the roughness of the banks with respective values of 0.03 s/m⅓, 0.05 s/m⅓, 0.07 s/m⅓, and 0.09 s/m⅓.

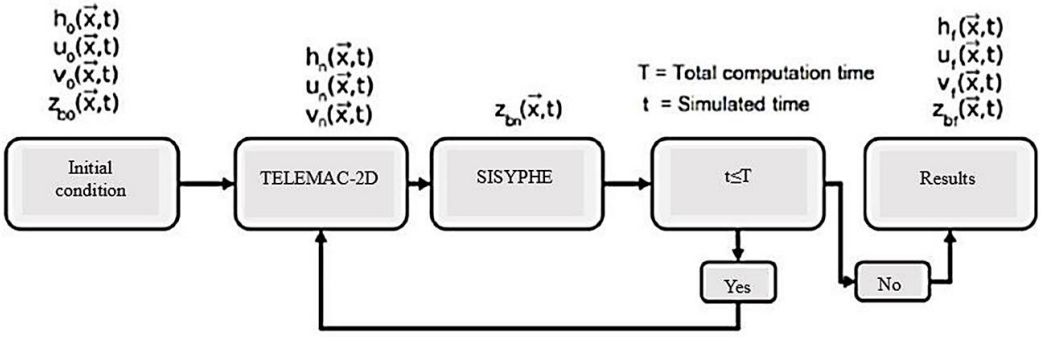

Figure 2. Simplified diagram of the Telemac-Sisyphe coupling

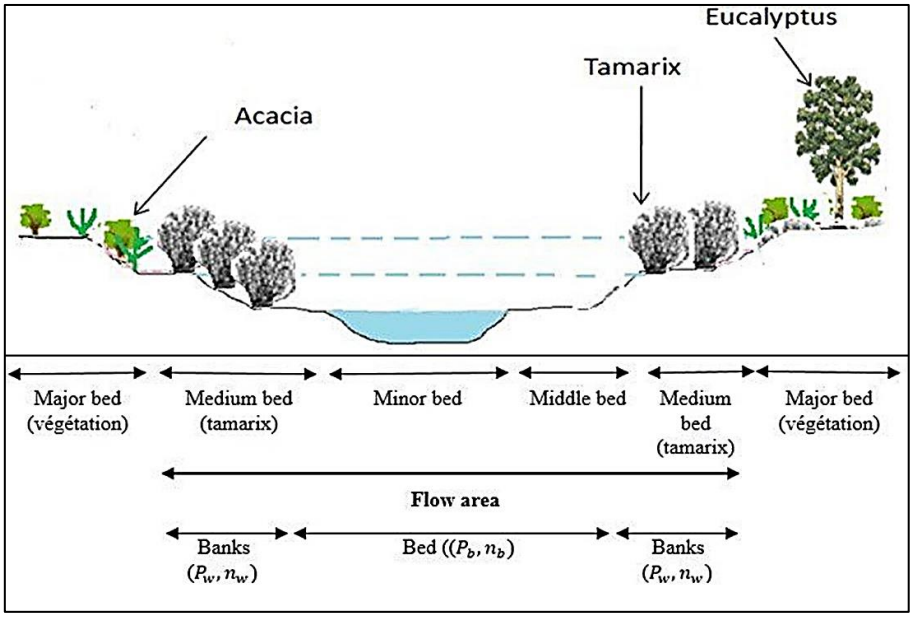

Figure 3. Roughness distribution in the Medjerda Section

To assess the impact of the non-uniform distribution of boundary roughness on the river morphology, we selected Einstein's method (Einstein, 1942; Einstein, 1950), which suggested using hydraulic radius segmentation to partition boundary resistance. This method incorporates Manning's formula for channel resistance segmentation. The specific formulation is as follows:

$$(n)^{3/2}P = (n_b)^{3/2} P_b + (n_w)^{3/2} P_w$$

Where; n_b and n_w are respectively the overall roughness coefficient of the cross-section, the roughness coefficient of the riverbed, and the roughness coefficient of the bank, and P, P_b, and P_w are respectively the wetted perimeter of the entire cross-section, the riverbed, and the bank.

$$P = P_b + P_w$$

The relative roughness of the banks compared to the riverbed is represented by the variable λ, defined as follows:

$$\lambda = (n_w)^{3/2}/(n_b)^{3/2}$$

2.4 Data and post-processing

This research requires primary data, particularly post-processing of topographic data. The considered area covers an equal surface of 40.71 km² with a river length of approximately 17.8 km. We created an unstructured surface mesh using the Blue Kenue model, based on the finite element method. This mesh was generated from a set of points derived from a LIDAR survey covering the area of interest, including riverbeds and floodplains. The LIDAR data was obtained from the Ministry of Agriculture.

Given the main objective of our study, which focuses on flows in the minor channel with relatively low discharge that does not impact floodplains, we opted for a variable mesh. More specifically, we chose a finer mesh for the minor channel, with a mesh size of approximately 5 m longitudinally to accurately represent flows along the main direction. For the rest of the domain, the mesh size is maintained at around 50 m. The grid, illustrated in the figure, consists of 54,279 nodes and 108,211 elements (Figure 4).

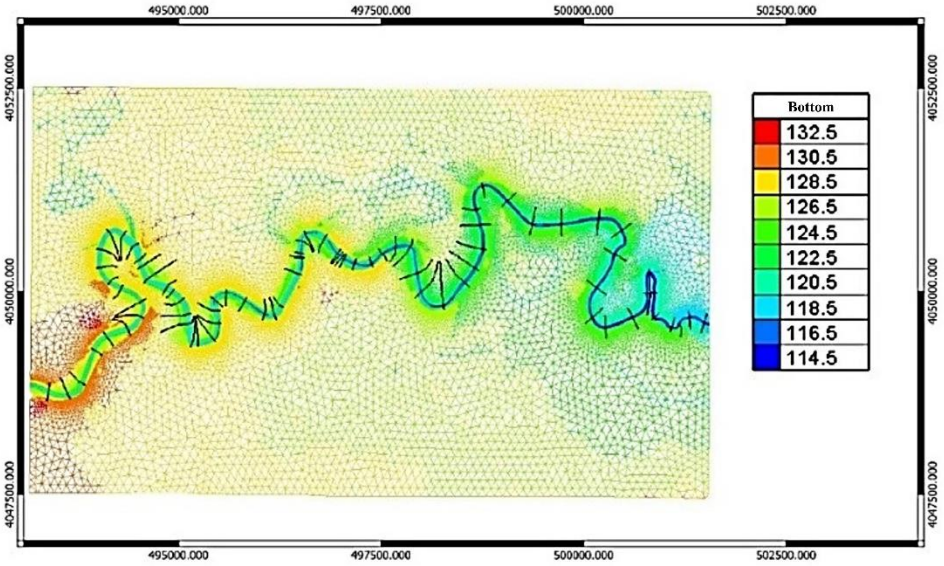

Figure 4. Study area grid with Telemac 2D

2.5 Sediment size distribution

A crucial aspect of sediment transport modeling is visualizing the evolution of sediment composition in relation to variations in flow. This visualization helps to better understand how changes in flow conditions affect the grain size distribution of sediments, their erosion, deposition, and consequently, the morphological evolution of the riverbed over time. The grain size distribution of sediments in the Oued Medjerda was determined through sieving and sedimentation after a sampling campaign under different flow conditions. These analyses, conducted by DGRE (2004), are used in this study.

For evaluating sediment transport rates, unlike conventional models that consider only a single average diameter, SISYPHE offers a non-uniform (multi-size) model. These non-uniform sediment models rely on a complex sedimentary description,

considering several granulometric fractions that closely resemble real-world conditions.

While suspended sediment transport is predominant, the impact of bedload sediment transport on the morphological evolution of the Medjerda should not be overlooked. Downstream of the confluence with the Oued Tessa, coarser sediments, sometimes up to 5 cm in diameter, have been observed up to 2 km downstream. Sandbanks have also been observed near the Bousalem Bridge. This indicates that significant flood events can transport these bedload sediments. The percentage of sediment transport by bedload can reach 20 to 25% of the total sediment transport during exceptional flows (Gharbi, 2016). Therefore, we used these 5 classes of mean diameter for each scenario. Given the significant variation in particle diameters transported by bedload, we chose a diameter of 1 mm for sand particles (Table 1).

Table 1. Variation in sediment diameters based on water discharge

Q (m^3/s)	% Clay (< 2 µm)	% Fine silt (2-20 µm)	% Coarse silt (20-50 µm)	Sand (> 50-2,000 µm)
100	25	32	29	14
200	26	28	27	19

2.6 Simulation scenarios and boundary conditions

The configuration of this section contains two distinct parts: the first part, located at the riverbed with a width less than 10 m, is entirely smooth with a roughness coefficient of 0.03 $s/m^{1/3}$. The second part, situated on both sides of the banks, exhibits variable roughness depending on the pre-existing vegetation cover. Four simulation scenarios were established, keeping the riverbed smooth and gradually increasing the roughness of the second part, with respective values of 0.03 $s/m^{1/3}$, 0.05 $s/m^{1/3}$, 0.07 $s/m^{1/3}$, and 0.09 $s/m^{1/3}$. These four scenarios are replicated for two constant discharge values of 100 m^3/s and 200 m^3/s, chosen as open boundaries at the model inlet. The output data is assigned to height data corresponding to the rating curve of the last section. Calibration results from our previous studies in the analysis and mapping of floods in the Boussalem city will be taken into account.

2.7 Sediment transport analysis

The longitudinal profile analysis of the studied section of the Medjerda provides significant insights, highlighting a notable change in slope near the old bridge of Boussalem (Figure 5), where a slight increase from 0.24% to 0.36% is identified. Sandbars have also been observed near the Boussalem Bridge. Since the bed of the Medjerda, is mainly composed of silts and clays, the very low slopes of the riverbed do not allow for significant transport of coarser sediments by bedload.

Figure 5. Sediment deposits in the Medjerda River (downstream view of the old bridge of Boussalem)

The comparison between the 2007 and 2019 profiles reveals, upstream of the old bridge of Boussalem, moderate sedimentation with rates of 3.4 and 2.5 m³/mL/year (Figure 6). These rates, relatively low, take into account the dredging works carried out in the relevant sections, making it difficult to provide a precise quantitative estimation of the sedimentation process in this part. However, on the lower part, sedimentation increases significantly, reaching 9.5 m³/mL/year; this section corresponds to the entry of the influence zone of the dam on the longitudinal profile of the Medjerda. Given the limited changes in the longitudinal profile and the modest volumes transported by bedload, the observed changes in the sections are primarily attributable to variations (sedimentation/erosion) of fine particles within the sections.

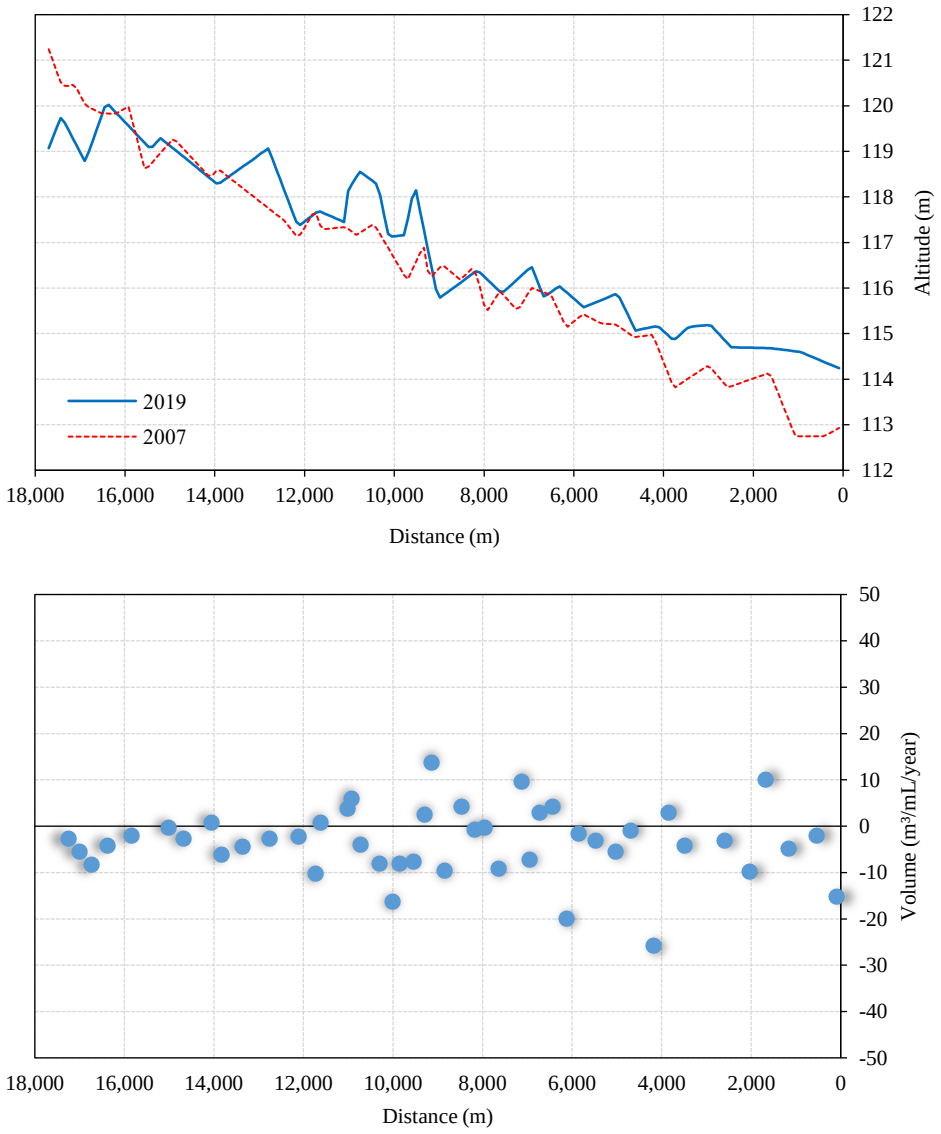

Figure 6. The riverbed evolution between 2007 and 2019 in the study area

3. RESULTS

The outputs generated by the model allowed us to conduct a comprehensive comparative analysis, focusing on flow velocity, shear stress, and bed evolution along the longitudinal profile and within each section. This helps in better understanding sedimentation patterns, predicting potential impacts on fluvial morphology, and aiding in the development of sustainable water resource management strategies in the Medjerda Basin.

3.1 Velocity, shear stress, and bed evolution in a dredged riverbed

Figure 7 illustrates the velocity evolution along the longitudinal profile of the flow section in the first scenario, where the riverbed is considered completely

smooth. This scenario reflects the immediate reality on the ground after the completion of dredging works. It can be observed that the velocity undergoes multiple fluctuations, resulting from various factors such as slope, flow section width, depth, and changes in flow direction. The velocity decreases by approximately 0.2 m/s on average between the two discharges along the longitudinal profile.

Figure 7 also presents the calculated shear stress values for both discharges and at each section. Shear stress, representing the force per unit area acting parallel to the flow direction, influences the movement or retention of sediments on the riverbed. Despite the observed fluctuations due to different factors governing the flow, there is a clear increase in shear stress, with an average of 2.3 N/m² with the increase in discharge.

The bed Shear stress is directly related to sediment transport capacity. An increase in shear stress leads to an increase in sediment transport and deposition, as clearly illustrated in Figure 8 where the longitudinal bed evolution is compared for the two discharges. It is observed that this evolution is more pronounced with the increase in discharge, reaching an average difference of 20 cm. This increase is explained by the increased force, causing erosion of the banks. The particles thus eroded subsequently undergo sedimentation in the flow bed.

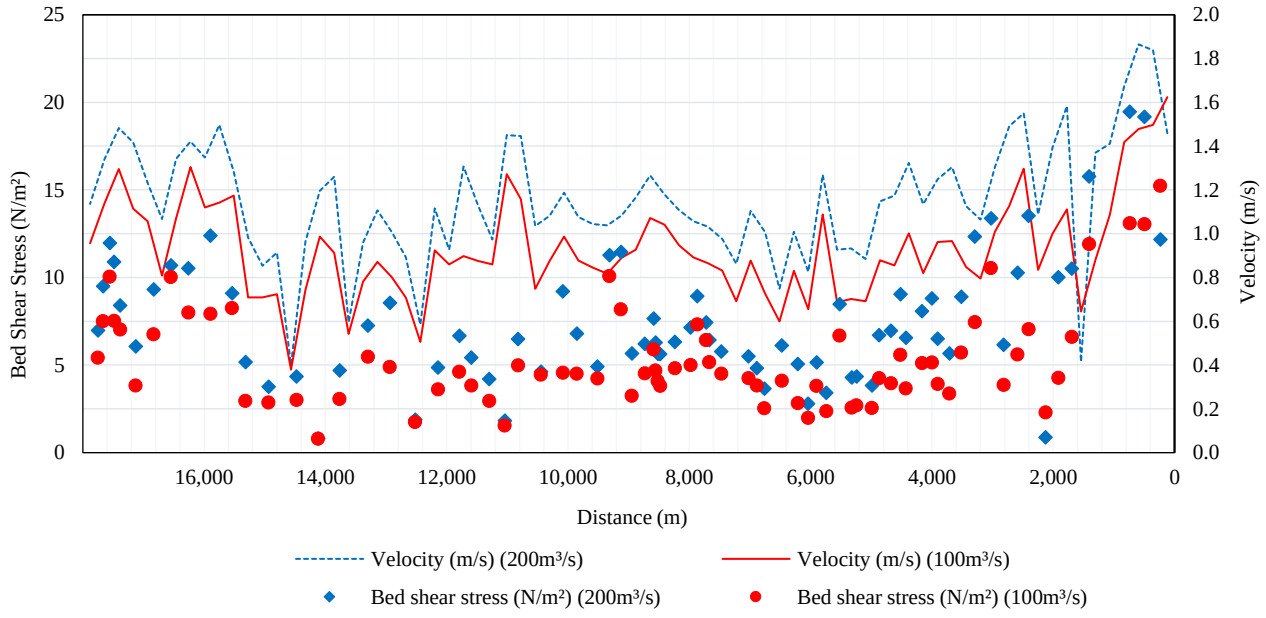

Figure 7. Velocity and longitudinal shear stress in a dredged riverbed for Q=100 m³/s and Q=200 m³/s

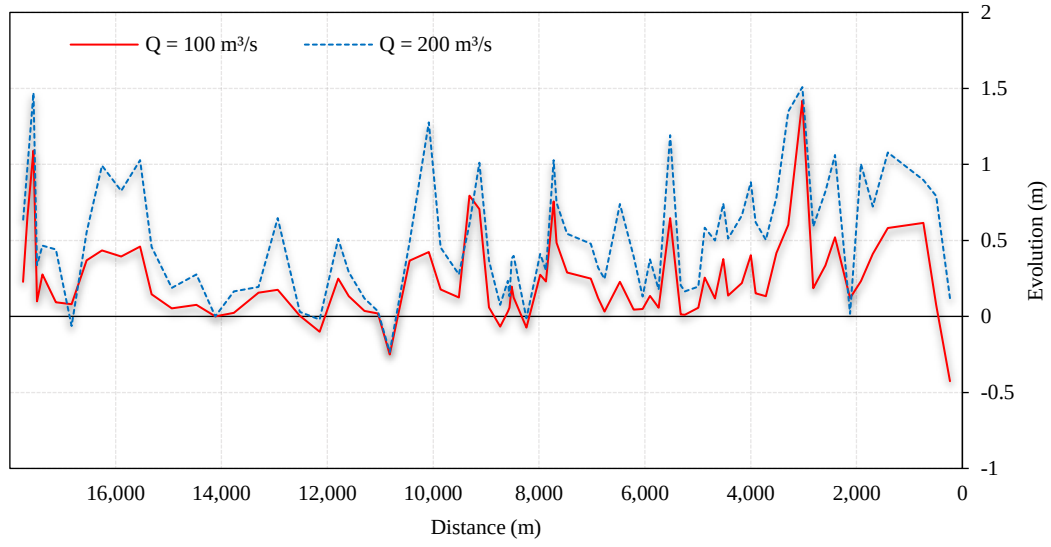

Figure 8. Longitudinal bed evolution in a dredged riverbed for Q=100 m³/s and Q=200 m³/s

3.2 Effect of roughness variation on velocity, shear stress, and bed evolution in transverse sections

Roughness increases in tandem with vegetation development. To assess the influence of vegetation on particle transport, we kept the riverbed smooth and gradually increased the roughness on both banks. Values of 0.03 s/m⅓, 0.05 s/m⅓, 0.07 s/m⅓, and 0.09 s/m⅓ were respectively assigned to the vegetated area (Figure 9).

A cross-sectional analysis of the three parameters, namely velocity, shear stress, and bed evolution, was conducted for the four scenarios. As for the velocity (Figure 10), it exhibits a parabolic increase, reaching zero at the ends of both banks and attaining its maximum value in the middle of the section for the maximum water height. On the banks, we observe that the speed decreases as the roughness increases.

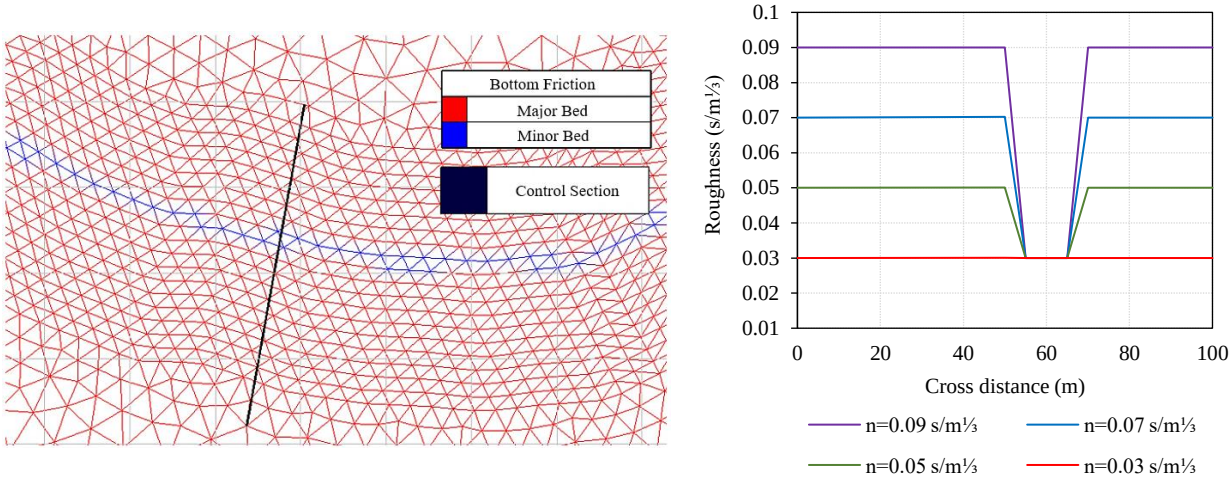

Figure 9. Variation of bed roughness in a cross-section

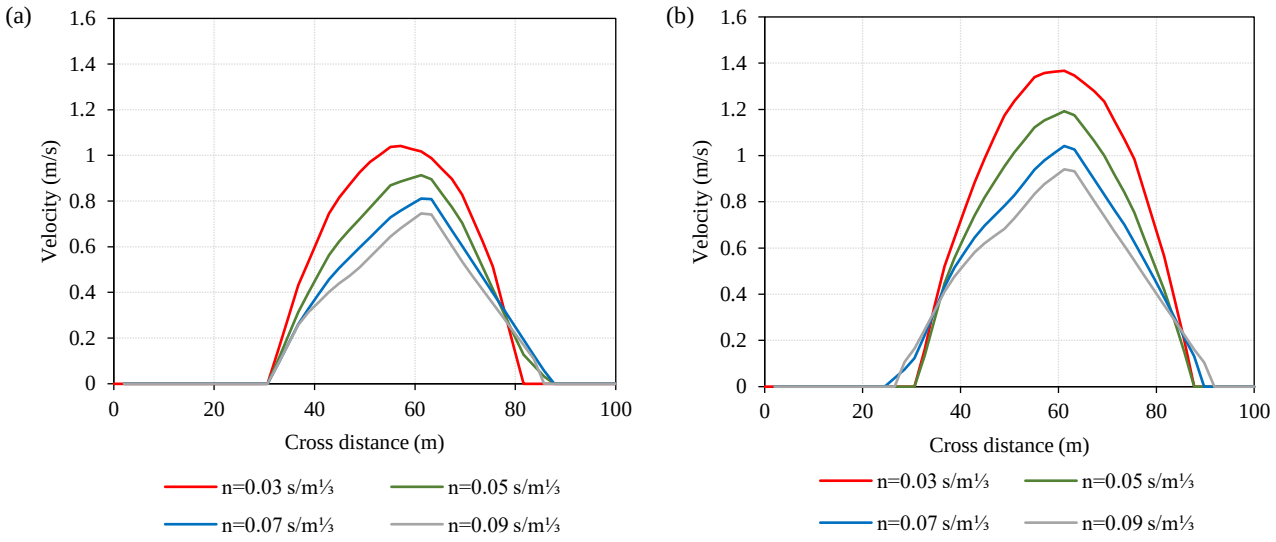

Figure 10. The average velocity Evolution in a cross-section as a function of roughness change for Q=100 m³/s (a) and Q=200 m³/s (b)

Furthermore, the evolution of the bed reveals the presence of two distinct regions. A deposition zone is observed on the smooth bed, while an erosion zone is noted along both banks, with a proportional decrease as roughness increases. For instance, under a discharge condition of 200 m³/s, erosion decreases from 50 cm in the first scenario to 8 cm in the second scenario, almost disappearing in the last two scenarios. Meanwhile, the calculated maximum deposits are 80 cm, 41 cm, 28 cm, and 17 cm respectively for the four scenarios. This trend naturally stems from the reduction in the quantity of sediment transported by the water (Figure 11).

For the shear stress (Figure 12), it is observed that it increases as the roughness increases along the banks of the wadi. For a flow rate of 100 m³/s, the respective values are 6.1, 8.2, 10.2, and 12 N/m² for the four scenarios. In the middle part of the flow where the bed remains smooth, it is observed that the shear stress decreases for the four scenarios, with respective values of 6, 4.2, 3.1, and 2.6 N/m².

Analyzing these results, it becomes clear that vegetation plays a crucial role in preserving bank stability by acting as an effective barrier against particle detachment and suspension. This conclusion is particularly reinforced by the observation in the last graph, where shear stress increases proportionally with the roughness coefficient on both banks. These findings suggest that the vegetation contributes to enhance the cohesion of the riverbed, minimizing the risks of erosion and excessive sediment transport (Figures 11 and 12). The combined effect of vegetation-induced roughness appears to play a crucial role in preserving bank stability, which can have significant implications for the management and preservation of river ecosystems

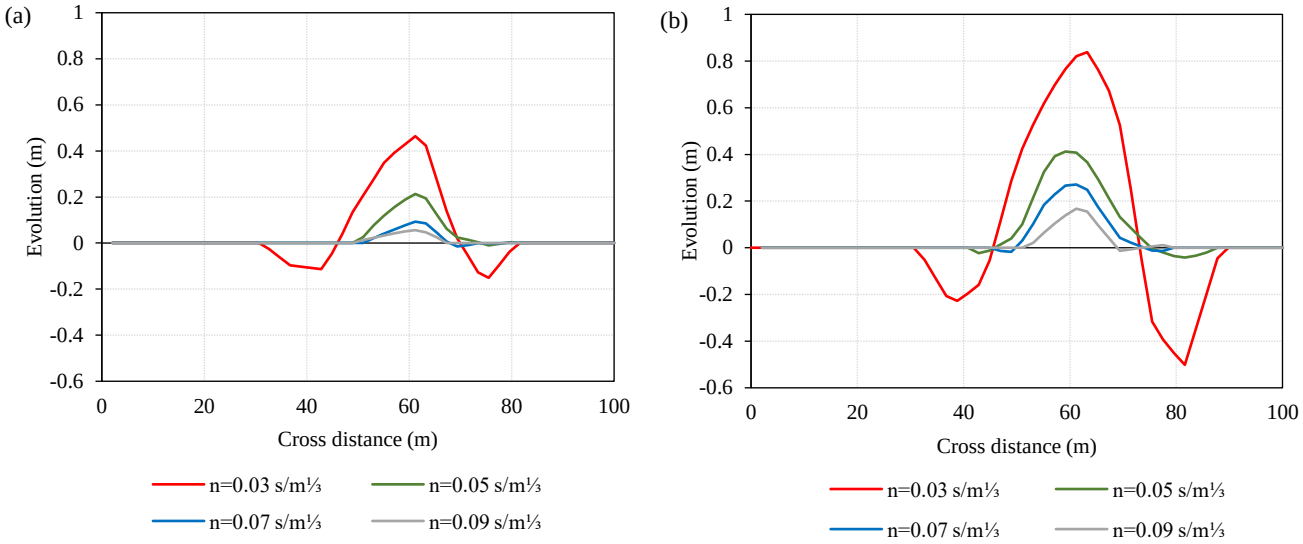

Figure 11. Bed evolution in a cross-section as a function of roughness change for Q=100 m³/s (a) and Q=200 m³/s (b)

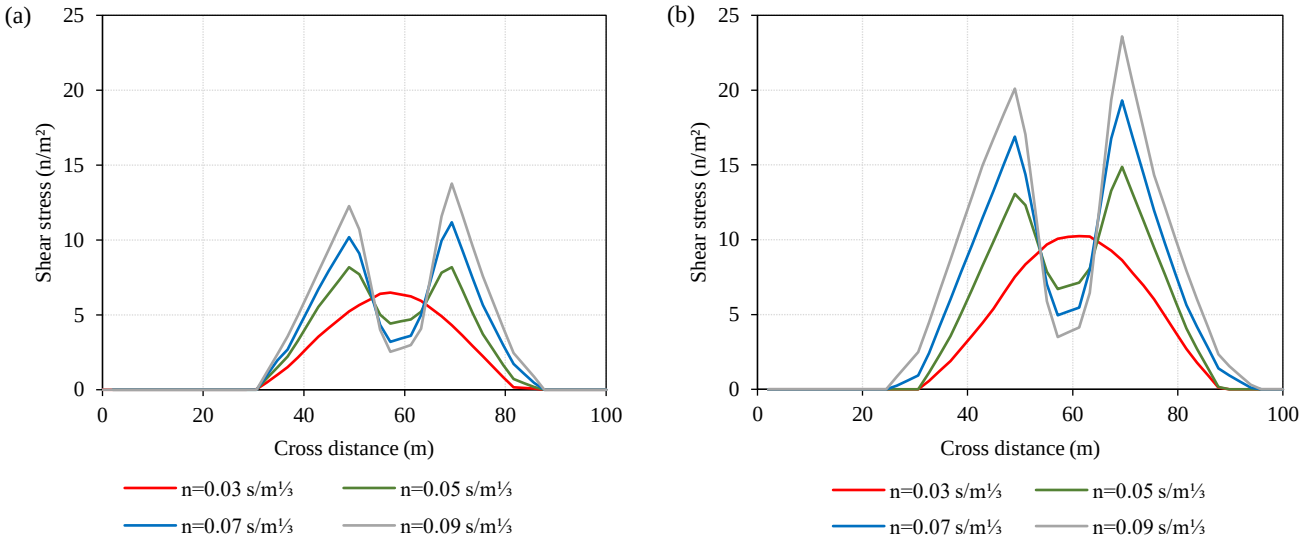

Figure 12. Bed shear stress evolution in a cross-section as a function of roughness change for Q=100 m³/s (a) and Q=200 m³/s (b)

3.3 Effect of roughness variation on the longitudinal evolution of the bed

The Figures 13 and 14 present a detailed analysis of the longitudinal evolution of the riverbed in response to variations in bank roughness under different scenarios and for the two distinct imposed flow rates. For a flow rate of 100 m³/s, the maximum deposition decreases to values of 141 cm, 60 cm, 15 cm, and 8 cm,

respectively, while the maximum erosion decreases to values of 28 cm, 25 cm, 22 cm, and 11 cm. For a flow rate of 200 m³/s, the maximum deposition decreases to values of 150 cm, 72 cm, 42 cm, and 23 cm, respectively, and the maximum erosion decreases to values of 31 cm, 28 cm, 25 cm, and 22 cm, respectively. The observation of the data reveals a significant relationship between bank roughness and erosion and deposition phenomena in the riverbed.

When bank roughness increases, a noticeable trend emerges: the magnitude of erosion and deposition processes decreases. This observation suggests a substantial effect of the bank roughness on the sedimentary dynamics of the watercourse. It is essential to notice that this trend is observed while keeping hydraulic parameters constant for the different scenarios studied, confirming the specificity of the effect of the bank roughness on the sediment transport.

The reduction in the magnitude of erosion and deposition phenomena indicates a relative stabilization of the riverbed as the bank roughness increases. This stabilization can be attributed to a decrease in the local flow velocity and an increase in shear stresses along the riverbed, resulting from increased roughness. These changes in hydraulic dynamics influence the river's ability to transport and deposit sediments.

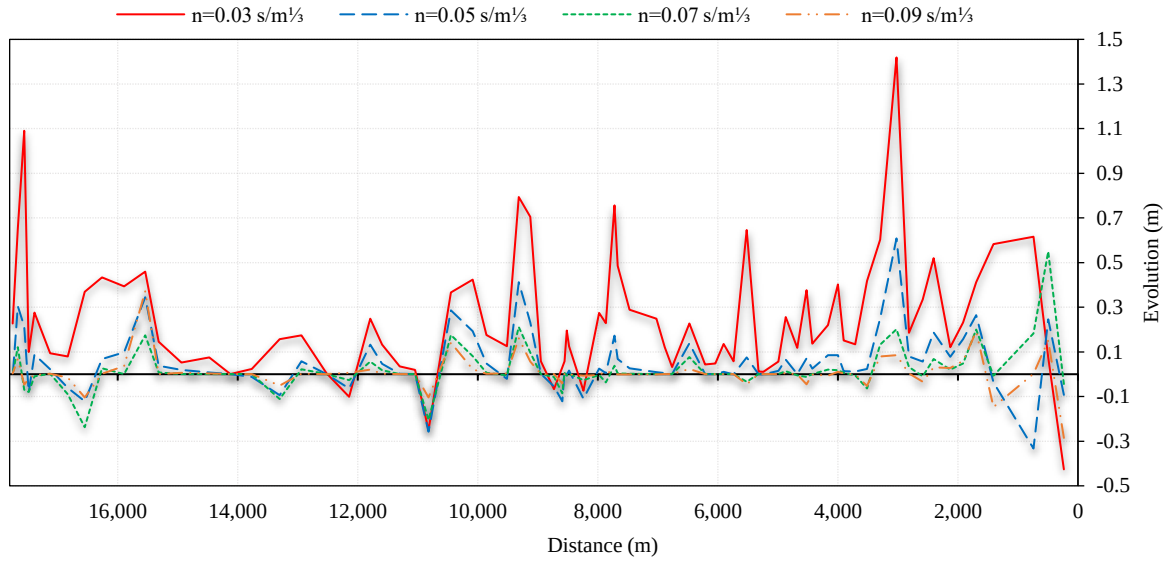

Figure 13. Evolution of longitudinal bed level in relation to variations in roughness for Q=100 m³/s.

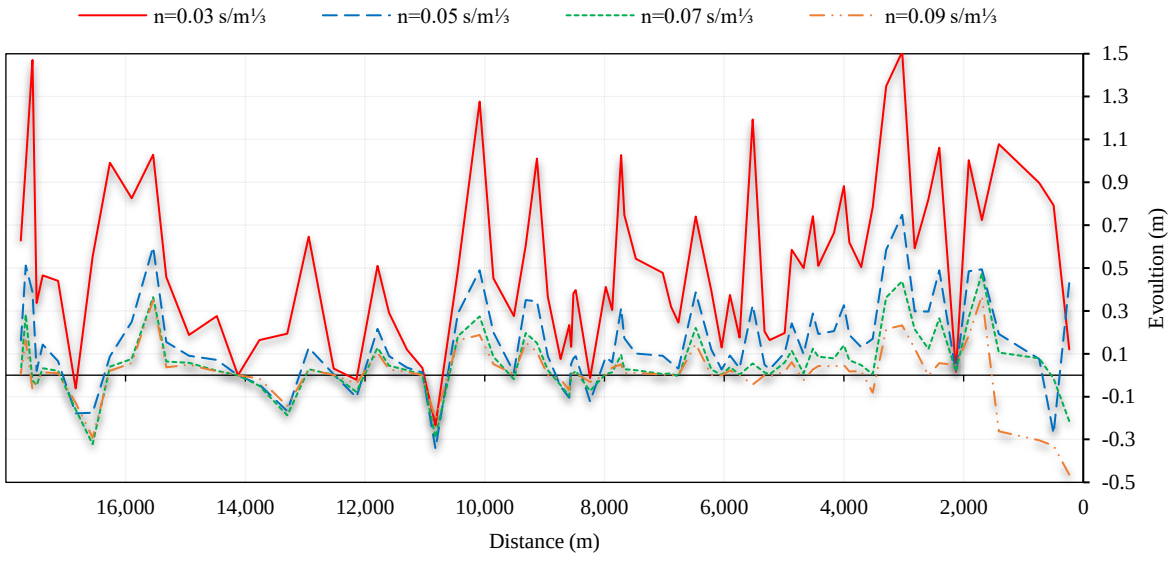

Figure 14. The longitudinal bed level evolution in relation to variations in roughness for Q=200 m³/s.

4. DISCUSSION

To better understand the impact of relative roughness on the morphology of the Oued, we calculated the following in the table: the average bed elevation (ζ_{mb}), the average bed shear stress (τ_{mb}), and the corresponding bed flow velocity (U_{mb}) for each scenario and for both discharge rates.

As relative roughness (λ) increases, the average bed shear stress (τ_{mb}) significantly decreases for a discharge of 100 m³/s, dropping from 5.34 N/m² to 4.89 N/m², which is a reduction of approximately 8.4%. Similarly, for a discharge of 200 m³/s, τ_{mb} decreases from 7.46 N/m² to 6.52 N/m², representing a reduction of 12.6% with the increase in relative roughness (Table 2). This trend indicates that increasing relative roughness reduces the stress exerted by the flow on the smooth riverbed.

Table 2. Impact of relative roughness on bed elevation, shear stress, and flow velocity

	Q= 100 m³/s				Q= 200 m³/s			
	ζ_{mb} [m]	τ_{mb} [Nm^{-2}]	U_{mb} [ms^{-1}]	q_b^*[m³s^{-1}] (E-05)	ζ_{mb} [m]	τ_{mb} [Nm^{-2}]	U_{mb} [ms^{-1}]	q_b^*[m³s^{-1}] (E-05)
λ_1=1	0.241	5.34	0.93	1.72	0.431	7.46	1.15	3.32
λ_2=2.15	0.053	5.28	0.84	0.92	0.150	7.08	1.02	2.02
λ_3=3.56	0.018	5.05	0.74	0.36	0.054	6.83	0.94	1.49
λ_4=5.19	0.007	4.89	0.68	0.20	0.010	6.52	0.88	0.98

The average bed elevation (ζ_{mb}) decreases markedly with increasing relative roughness (λ). For a discharge of 100 m³/s, ζ_{mb} drops from 0.241 m to 0.007 m. Similarly, for a discharge of 200 m³/s, ζ_{mb} decreases from 0.431 m to 0.010 m. Given that the flow depth is around 3.32 m, the increase in relative roughness λ represents a depth increase of 7% and 12% respectively for the 100 m³/s and 200 m³/s flows (Table 2).

The bedload discharge significantly decreases with increasing relative roughness. For a discharge of 100 m³/s, q_b^* decreases from 1.72×10^{-5} m³/s to 0.20×10^{-5} m³/s as λ increases, representing a reduction of about 88%. Similarly, for a discharge of 200 m³/s, q_b^* decreases from 3.32×10^{-5} m³/s to 0.98×10^{-5} m³/s, which is a reduction of approximately 70% (Table 2). This marked decrease in bedload discharge with increasing relative roughness indicates the significant role of vegetated banks in reducing transported sediment. Our analyses suggest that dredging, although often used to increase flow discharge during flood events, could compromise bank stability by disrupting the natural sediment transport balance, potentially having adverse effects on the morphology of the Oued and on downstream reservoirs

Our results reflect the trends observed by Fan et al. (2023) regarding the increase in depth with increasing relative roughness. However, a direct comparison is challenging due to the variability in river dimensions on one hand, and the use of different particle diameter classes on the other. Despite these differences, our results confirm the validity of previous observations in a slightly modified context.

Although our model simulates static roughness for different scenarios, the results obtained can serve as a foundation for initiating a dynamic roughness model. If we have real-time data on vegetation variability, this model would allow us to analyze the corresponding morphodynamic effects. For example, Fortes et al. (2022), through a dynamic model, demonstrated that the water level profile increased by an average of 7.03% over a one-year period, thereby highlighting the seasonal effect of vegetation

5. CONCLUSIONS

The objective of this study was to demonstrate how changes in bed roughness influence the morphodynamic evolution of the bed in response to sediment displacement. The study employed hydro-sedimentary numerical modeling using the hydrodynamic (TELEMAC 2D) and morphodynamic (SISYPHE) modules of the TELEMAC-MASCARET modeling system.

To highlight the effect of vegetation installed on the riverbanks on sediment transport and morphological deformation, we simulated scenarios with fixed roughness for the smooth bed and variable roughness for the banks, ranging from the smoothest to the roughest. Four simulation scenarios were established, progressively increasing the bank roughness with respective values of 0.03 s/m⅓, 0.05 s/m⅓, 0.07 s/m⅓, and 0.09 s/m⅓.

We analyzed the results on a control transverse section, as well as along the profile of the river. This analysis mainly focused on parameters of velocity, evolution, and shear stress. The results reveal two distinct zones in the evolution of the riverbed: a deposition zone on the smooth bed and an erosion zone along the banks. Erosion along the banks decreases proportionally with increasing roughness. This trend naturally results from the decrease in shear stress, which leads to a reduction in the amount of sediment transported by the water.

To assess the impact of the non-uniform distribution of bed roughness on the river's morphology, we used Einstein's method, which suggested using hydraulic radius segmentation to partition boundary resistance. For each relative bank roughness (λ), we calculated the average bed elevation (ζ_{mb}), the average bed shear stress (τ_{mb}), the flow velocity at the bed (U_{mb}), and the bedload discharge (q_b^*) for each scenario.

The results showed that the average bed elevation (ζ_{mb}) decreases significantly with increasing relative roughness (λ). Given that the flow depth is around 3.32 m, increasing the relative roughness λ from 1 to 5.19 results in an increase in depth of 7% and 12% respectively for flow rates of 100 and 200 m³/s. Our results reflect previously observed laboratory trends regarding the increase in depth with increasing relative roughness. However, direct comparison is challenging due to variability in river dimensions and the use of different particle diameter classes. Despite these differences, our results confirm the validity of previous observations in a slightly modified context.

The results also show that:

- With increasing relative roughness (λ), the average shear stress (τ_{mb}) decreases significantly by about 8.4% and 12.6% respectively for flow rates of 100 and 200 m³/s.
- The bedload discharge (q_b^*) decreases significantly with reductions of approximately 88% and 70% respectively for flow rates of 100 and 200 m³/s.

Although dredging works combat flooding by facilitating flow transit, they lead to increased amounts of transported sediments that will deposit downstream in the dams due to the removal of vegetation, which is crucial for the morphological stability of the river. This reduces the exploitable water volume in the dams and accelerates its silting. The results obtained can serve as a foundational basis for initiating a dynamic roughness model if real-time roughness variability data is available.

REFERENCES

Badoux A, Andres N, Turowski JM. Damage costs due to bedload transport processes in Switzerland. Natural Hazards and Earth System Sciences 2014;14(2):279-94.

Exner FM. On the Physics of Dunes. Vienna, Austria: Proceedings of the Academy of Sciences in Vienna; 1920 (in German).

Einstein HA. Formula for transportation of bed load. Transactions of the American Society of Civil Engineers 1942;107(1): 561-97.

Einstein HA. The bed load function for sediment transportation in open channel flows. In: Technical Bulletin. USA: U.S. Department of Agriculture; 1950. p. 71.

Fan J, Huang H, Yu G, Su T. River channel forms in relation to bank steepness: A theoretical investigation using a variational analytical method. Water 2020;12(5):Article No. 1250.

Fan J, Luo Q, Bai Y, Liu X, Li R. Investigating the influence of the relative roughness of the riverbanks to the riverbed on equilibrium channel geometry in Alluvial Rivers: A variational approach. Water 2023;15:Article No. 4029.

Fortes AA, Hashimoto M, Udo K, Ichikawa K, Sato S. Dynamic roughness modeling of seasonal vegetation effect: Case study of the Nanakita River. Water 2022;14:Article No. 3649.

Gharbi M, Soualmia A, Dartus D, Masbernat L. Floods effects on rivers morphological changes: Application to the Medjerda River in Tunisia. Journal of Hydrology and Hydromechanics 2016;64(1):56-66.

Gharbi M. Study of Floods and Associated Sediment Transport - Application to the Medjerda Watershed [dissertation]. Toulouse: National Polytechnic Institute of Toulouse; 2016.

Guan M, Carrivick JL, Wright NG, Sleigh PA, Staines KE. Quantifying the combined effects of multiple extreme floods on river channel geometry and on flood hazards. Journal of Hydrology 2016;538:256-68.

Hammami S, Romdhane H, Soualmia A, Kourta A. 1D/2D coupling model to assess the impact of dredging works on the Medjerda River Floods, Tunisia. Journal of Materiel and Environmental Science 2022;13(7):825-39.

Hammami S, Soualmia A, Kourta A. Analysis and forecasting flood risk mapping of the Medjerda River at Boussalem Town, in Tunisia. Engineering and Applied Science Research 2023;50(5):449-57.

Hammami S, Soualmia A, Kourta A. Telemac 2D modeling of pollutant transport in the Medjerda River: Impact of Tamarix Vegetation, Bousselem, Tunisia. European Journal of Environment and Earth Sciences 2024;5(3):47-54.

Hervouet J-M. Hydrodynamics of Free Surface Flows: Numerical Modeling with the Finite Element Method. Paris, France: Presses de l'École Nationale des Ponts et Chaussées; 2003.

Li J, Claude N, Tassi P, Cordier F, Vargas-Luna A, Crosato A, et al. Effects of vegetation patch patterns on channel morphology: A numerical study. Journal of Geophysical Research: Earth Surface 2022;127(5):e2021JF006529.

Luca M, Diego R, Walter B. The role of vegetation and large wood on the topographic characteristics of braided river systems. Geomorphology 2020;367:Article No. 107299.

Meyer-Peter E, Müller R. Formulas for bed-load transport. Proceedings of the 2nd Meeting of the International

Association for Hydraulic Structures Research; 1948 May 7; Stockholm; 1948.

Morri M, Soualmia A, Belleudy P. Mean velocity predictions in vegetated flows. Journal of Applied Fluid Mechanics 2016;9(3):1273-83.

Mugade U, Sapkale J. Influence of aggradation and degradation on river channels: A review. International Journal of Engineering and Technical Research 2015;3(6):209-12.

Nanson RA, Nanson GC, Huang HQ. The hydraulic geometry of narrow and deep channels: Evidence for flow optimization and controlled peatland growth. Geomorphology 2010;117 (1-2):143-54.

Nazarjani M, Saremi A, Eslami AR, Yazdani V. Analysis of the impact of roughness coefficient changes due to land use changes on the hydraulics of the Kashafrood River. AQUA - Water Infrastructure, Ecosystems and Society 2023; 72(11):1969-86.

Nazi MHM, Awang S, Shaaban AJ, Yahaya NKEM, Jusoh AM, Arumugam MARMA, et al. Sediment transport dynamic in a meandering fluvial system: Case study of Chini River. IOP Conference Series: Materials Science and Engineering 2016;136:Article No. 012072.

Penna N, Coscarella F, D'Ippolito A, Gaudio R. Effects of fluvial instability on the bed morphology in vegetated channels. Environmental Fluid Mechanics 2022;22(2):619-44.

Ramirez JA, Zischg AP, Schürmann S, Zimmermann M, Weingartner R, Coulthard T, et al. Modeling the geomorphic response to early river engineering works using CAESAR-Lisflood. Anthropocene 2020;32:Article No. 100266.

Recking A. An analysis of nonlinearity effects on bedload transport prediction. Journal of Geophysical Research 2013;118:1264-81.

Reisenbüchler M, Bui MD, Skublics D, Rutschmann P. Enhancement of a numerical model system for reliably predicting morphological development in the Saalach River. International Journal of River Basin Management 2019;18(3):335-47.

Rickenmann D, Badoux A, Hunzinger L. Significance of sediment transport processes during piedmont floods: the 2005 flood events in Switzerland. Earth Surface Processes and Landforms 2016;41(2):224-30.

Tu T, Carr KJ, Ercan A, Trinh T, Kavvas ML, Nosacka J. Assessment of the effects of multiple extreme floods on flow and transport processes under competing flood protection and environmental management strategies. Science of the Total Environment 2017;607-608:613-22.

Van Rijn LC. Sediment transport, Part I: Bed load transport. Journal of Hydraulic Engineering 1984;110(10):1431-56.

Vargas-Luna A, Crosato A, Byishimo P, Uijttewaal WSJ. Impact of flow variability and sediment characteristics on channel width evolution in laboratory streams. Journal of Hydraulic Research 2019;57(1):51-61.

Wilcock PR, Crowe JC. Surface-based transport model for mixed-size sediment. Journal of Hydraulic Engineering 2003; 129(2):120-8.

Yassine R, Cassan L, Roux H, Frysou O, Pérès F. Numerical modelling of the evolution of a river reach with a complex morphology to help define future sustainable restoration decisions. Earth Surface Dynamics 2023;11(6):1199-221.

Environment and Natural Resources Journal

Volume 23
Issue 1
2025

Spatial Dynamics and Risk Mapping of Forest Fires in Madhesh Province, Nepal: A Multi-Criteria Decision Approach

Gunjan Adhikari[1], Khagendra Prasad Joshi[2], Dristee Chad[1], Ashish Ghimire[1], and Sandeep Mahara[1*]

[1]Institute of Forestry, Pokhara Campus, Tribhuvan University, Pokhara, Nepal
[2]Central Department of Hydrology and Meteorology, Tribhuvan University, Nepal

ARTICLE INFO

Received: 30Apr 2024
Received in revised: 22 Nov 2024
Accepted: 2 Dec 2024
Published online: 6 Jan 2025
DOI: 10.32526/ennrj/23/20240124

Keywords:
AHP/ Forest fire/ GIS/ MODIS

*** Corresponding author:**
E-mail: maharas450@gmail.com

ABSTRACT

Forest fires in Nepal are a pressing environmental concern, impacting ecosystems and community livelihoods. This research aims to understand forest fires, their trends, distribution, and relation with selected variables found in the sub-tropical forests of Madhesh Province of Nepal, and then identify potential fire risks and vulnerable areas. The selected fire incidents were analyzed using fire points produced by the moderate resolution imaging spectroradiometer (MODIS) sensor. Following the analytic hierarchy process (AHP) approach, this research investigates topographic, climatic, biophysical, and anthropogenic variables to create a fire risk map. Throughout the 22-year research period (2001-2023), 6,368 fire incidents and 6,158.22 km^2 of total burnt area were reported in the study area. Overall, the Mann-Kendall test showed an increasing trend for regional fire incidents. It has been found that about 24% of the province is either at high or very high risk for fire. The validity of the prediction map was confirmed with an AUC value of 0.798. The findings of the study will be valuable to local, state, and federal governments, policymakers, forest fire managers, researchers, and land planners in building a landscape-level forest fire management plan for high-risk areas.

1. INTRODUCTION

Wildfire or forest fire, although an important component of biome development in forest ecosystem (Dawson et al., 2001; Doerr and Santín, 2016) has been a driving factor for forest degradation globally, and a major risk to Nepal's forest cover (Singh, 2017). Recurrent forest fires destroy non-timber forest products, severely harming and hindering seedling regeneration and growth, and, in some situations, facilitating the spread of exotic species (MoFSC, 2016).

Monitoring and assessment of forest fires and prone areas with remote sensing has been an effective approach for evaluating, regulating, and predicting fire risks (Qadir et al., 2021). Numerous geosynchronous satellites, including the along track scanning radiometer (ATSR) onboard, ERS-1 and 2 (European Remote Sensing Satellite 1 and 2), the moderate resolution imaging spectroradiometer (MODIS) onboard the Terra and Aqua Satellites have been frequently used in monitoring forest fires (Curkovic, 2012). MODIS, acquiring its synoptic source of information from routine satellite observation on various temporal scales, has proven to be advantageous for the monitoring of forest fires (Reeves et al., 2006). In line with this, Pradhan et al. (2007) produced a susceptibility map based on the correlation between MODIS fire incident points and the associated contributing factors.

Among many techniques for calculating and modeling fire risk areas, multi-criterion decision analysis (MCDA) and geographic information system (GIS) have been most adopted (Wang et al., 1990; Joerin et al., 2001; Yu et al., 2011; Zolekar and Bhagat, 2018), where MCDA techniques offer solutions with user-defined needs. Different literatures

Citation: Adhikari G, Joshi KP, Chad D, Ghimire A, Mahara S. Spatial dynamics and risk mapping of forest fires in Madhesh Province, Nepal: A multi-criteria decision approach. Environ. Nat. Resour. J. 2025;23(1):80-94. (https://doi.org/10.32526/ennrj/23/20240124)

have prompted the use of MCDA techniques including analytical hierarchy process (AHP), Fuzzy AHP, and ANP (citations of papers using AHP, Fuzzy AHP, and ANP). Among others, AHP is a thorough structured technique for multi-criteria decision analysis (Kumar and Garg, 2017). Most importantly, integrating GIS and remote sensing with AHP approaches can give policymakers, social networks, forest fire managers, and other stakeholders credible information on when and where fires are predicted to occur.

Despite being a small nation with an area of 147,516 km^2, 44.74% of Nepal's total land area is covered with forests and woodlands (FAO, 2020). Recent years have shown a growing trend of forest fires, where 2021 hit the worst-case scenario as compared to past trends (Parajuli et al., 2020). Madhesh Province represents the Terai region of Nepal and is second to the Chure range in terms of fire hotspots in Nepal (Ranabhat et al., 2022), however, no research work has addressed the recurrent wildfire patterns of the province. Thus, this study responds to the necessity of accurately mapping the wildfire risk zones to abate the possible abrasion of forest fires in the province. Such mapping of forest fire risk zones would eventually benefit Nepal's disaster preparedness measures (Parajuli et al., 2020). The current study considers the province for the most recent trends in forest fires way forwarding further opportunities for filling the research void in forest fire dynamics of the province. This research identifies where and when the fires are most likely to occur in the study area, providing a crucial foundation for improving current forest fire control strategies.

2. METHODOLOGY

2.1 Study area

Madhesh province occupies the southern part of Nepal within an elevation range of 1,000-3,300 feet, located between 22.9734°N and 78.6569°E, and bordered by the Siwalik hills on the north, India in the south, the Koshi River in the east, and Bagmati Pradesh in the west. The province's lower tropical climate dominates over 90% of its total geographical area, with the remaining portion experiencing the upper tropical climate. Approximately 27.29% of the total land area is covered by forest in the province (DFRS, 2015). The major forest cover is occupied by *Shorea robusta* forest, followed by the forests of *Terminalia* and *Anogeissus*, *Dalbergia sissoo-Acacia catechu*, and Bombax riverine. The study primarily focuses on the forest region of the area as shown in Figure 1. Simultaneously Figure 2 provides the overall framework of methodological steps involved in this study.

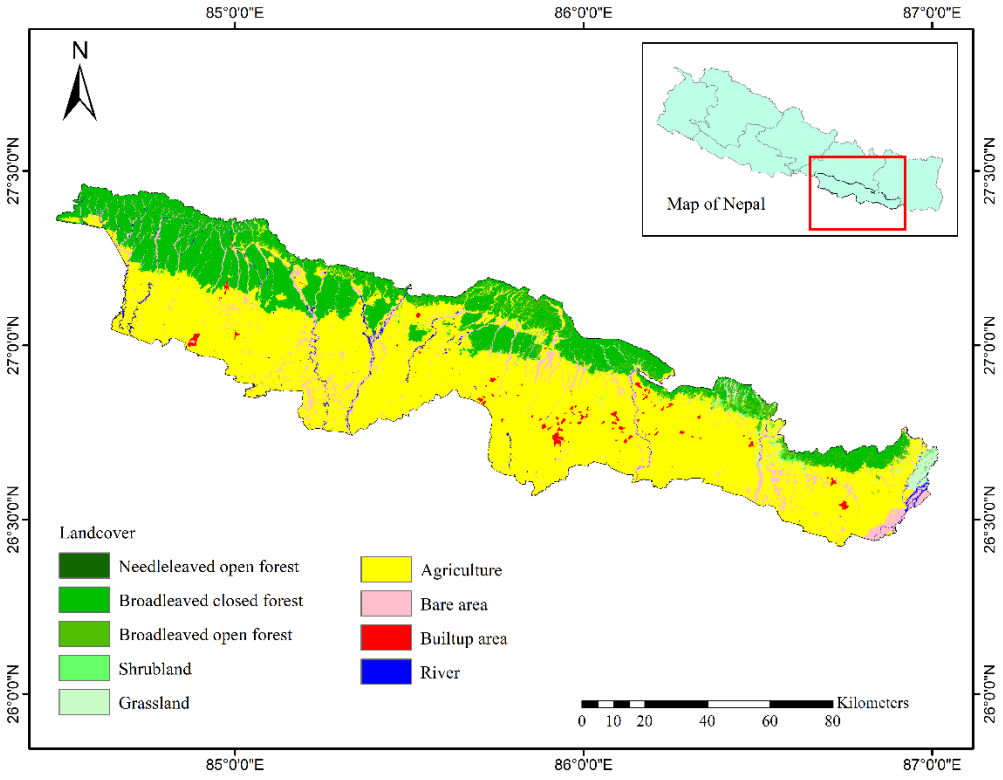

Figure 1. Landcover map of the study area (Source: ICIMOD, 2013)

2.2 Acquisition of dataset

Data available on active fires were extracted using the MODIS. The MODIS active fire product detects fires burning in 1×1 km^2 pixels under cloud-free conditions (Giglio et al., 2015; Giglio et al 2006). The fire incidences from 2001 to 2023 were obtained from https://firms.modaps.eosdis.nasa.gov/active_fire/ which provides the data for spatial-temporal analysis (Qadir et al., 2021). In MODIS, there are different levels of confidence from 0 to 100 in the detection intervals showing the accuracy of the data. We used the data exceeding 30% confidence level in this study to avoid false incidents but not ignore small fires before previous studies (Giglio et al., 2015; Parajuli et al., 2020).

In the current study, satellite data as well as other vector and raster data products were utilized. The parameters were divided into topographical (elevation, aspect, and slope), climatic (temperature), anthropogenic (distance from road and closeness to settlement), and biophysical categories (land cover). For the topographical data, Aster global DEM model V003 was downloaded from the USGS website (https://earthexplorer.usgs.gov/) (LP DAAC, 2019) and the area of interest was then mosaiced, projected, and then clipped consecutively. Then, using the slope and aspect function in the ArcGIS 10.8 spatial analyst tool (ESRI, 2022), the slope and aspect were obtained from the DEM map. The data for land surface temperature was obtained by compiling MODIS data (MOD11C3) (Wan, 2014). The ArcGIS cell statistics tool was used to assemble and integrate the monthly data. For effectiveness, a distinct layer was created by averaging the mean monthly temperature for each year's pre-monsoon season (March-May) since the majority of forest fire cases occur in this season (Matin et al., 2017; Parajuli et al., 2020). Similarly, landcover data for the year 2010 was obtained from (ICIMOD, 2013) providing the classification of all the forest types. The data from this year was used since no other open-source layers provided the classification of the forest types. The dataset on roads and settlements was obtained from the Department of Survey (https://opendatanepal.com/dataset), and the vector polyline and points shapefile were further rasterized using the Euclidean distance method under the spatial analyst tool. Table 1 provides information on the data model and the sources of the various criteria maps. All the variables used in the study are visualized in Figure 2.

Table 1. Datasets used and their sources

Variable type	Data	Format	Data period	Resolution	Sources/References
Dependent variable	Fire occurrence data	SHP	2001-2023	1,000 m	MODIS
Topographical	ASTER DEM	TIFF	2019	30 m	NASA/LAADSDAAC/USGS (V003) (LP DAAC, 2019)
	Slope	TIFF	2019	30 m	
	Aspect	TIFF	2019	30 m	
Climatic	Land surface temperature	HDF	2001-2023	1,000 m	MODIS (Wan, 2014)
	Precipitation	TIFF	2000-2018	4.5 km	Worldclim
Bio-physical	Landcover (2010)	TIFF	2010	30 m	ICIMOD (ICIMOD, 2013)
Anthropogenic	Proximity of settlement	SHP	2015	1:25,000	Department of Survey
	Distance from road	SHP	2015	1:250,000	Department of Survey

2.3 Preparation of variables

Before running any model, it is imperative to statistically test the multicollinearity among the response variables as it may later impact the model estimation (Chang et al., 2013). In multiple regression models, multicollinearity refers to the level of linear intercorrelation between the explanatory variables (Kim, 2019). So, before relying on the input variable's authenticity, a multicollinearity test was conducted to observe the correlation among the independent variables in response to the dependent fire count, to accurately validate the data and obtain a reliable conclusion. All the independent explanatory variables were classified as categorical variables before running the multicollinearity test. We calculated the Variation Inflation Factor (VIF) among the variables since it shows the severity of collinearity among the variables. The study of Davis et al. (2017) states that the variables with VIF<5 have insignificant levels of multicollinearity. As visible in Table 2, since the VIF for all the eight independent variables ranged below 1.6, thus indicating a low correlation between the input variables, all the variables were used for fire risk mapping.

As for the trend analysis of forest fire for the years 2001-2023, the Man-Kendall test was used for both the fire incidents and the burnt area. It assesses the significance of the Theil-Sen slope (Mann, 1945) and indicates the presence of a trend when the TS slope quantifies its magnitude. Different studies like Mishra et al. (2014) and Zhu et al. (2023), have used it for forest fire and burnt area trend and significance estimation. Furthermore, to analyze the spatial distribution of forest fire counts across different variables, Arc GIS 10.8 (ESRI, 2022) was used to overlay the incidents and variables.

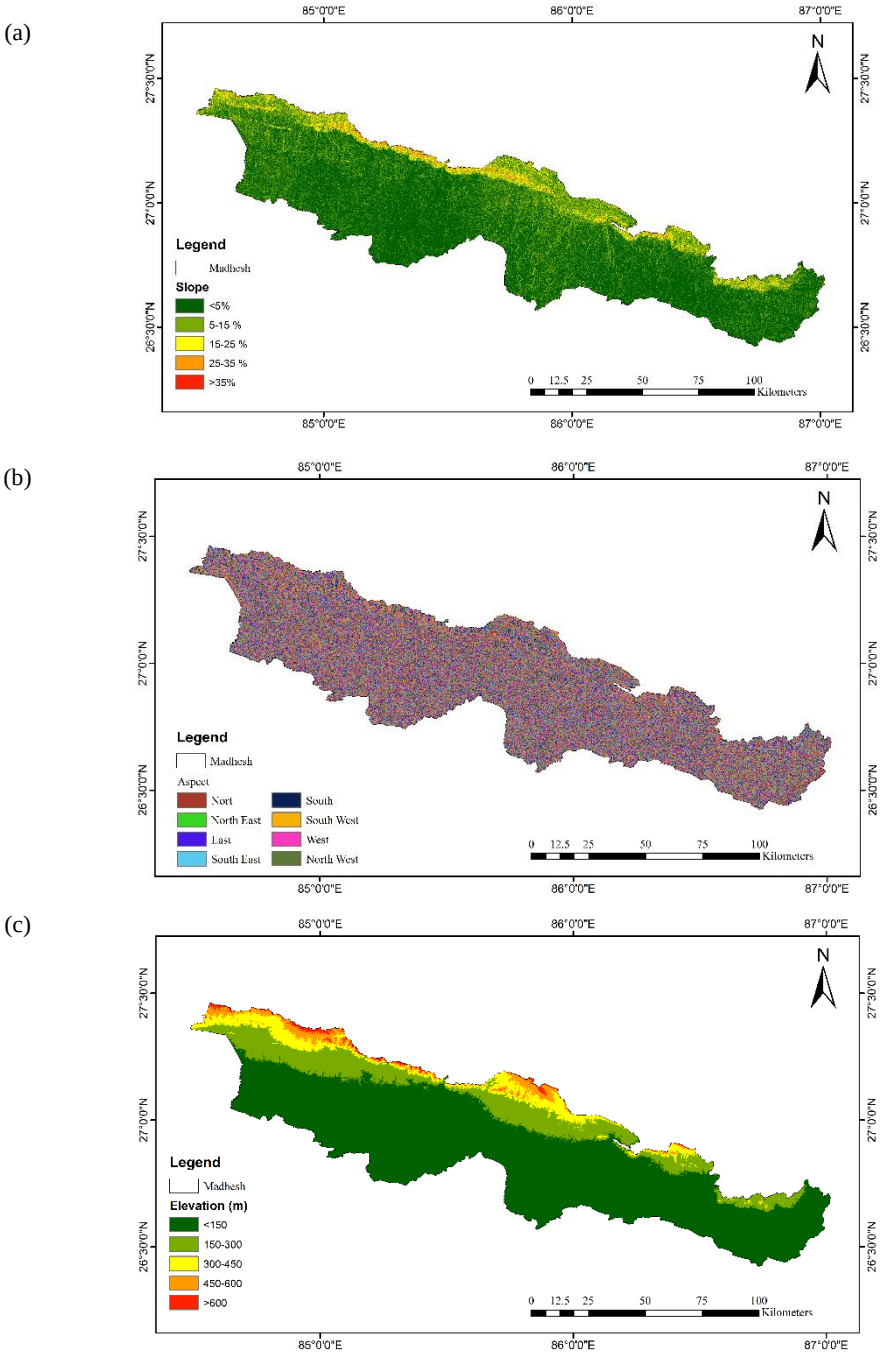

Figure 2. Variables (a) slope, (b) aspect, (c) elevation, (d) land surface temperature, (e) proximity of settlement, (f) distance from road, and (g) precipitation

(d)

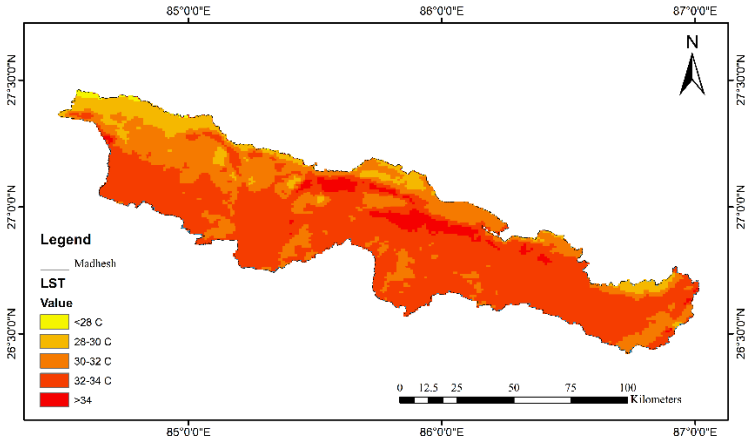

(e)

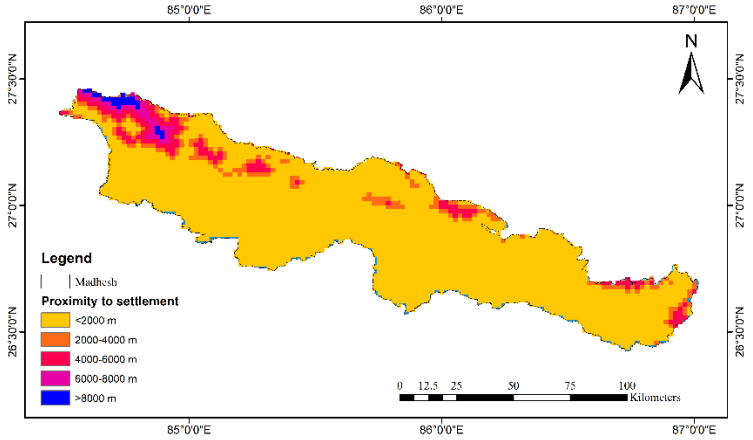

(f)

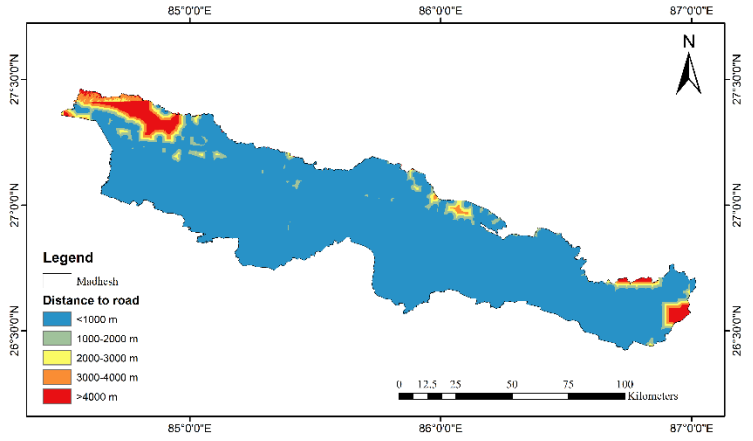

(g)

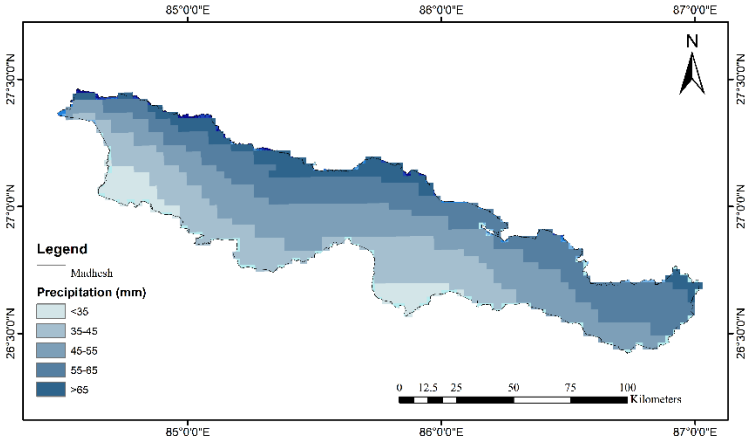

Figure 2. Variables (a) slope, (b) aspect, (c) elevation, (d) land surface temperature, (e) proximity of settlement, (f) distance from road, and (g) precipitation (cont.)

Table 2.VIF test of all the independent variables

Type of variable	Variable name	Collinearity statistics	
		Tolerance	VIF
Independent Explanatory Variables	Slope	0.968	1.033
	Settlement	0.728	1.374
	Road distance	0.656	1.524
	LST	0.650	1.538
	Elevation	0.999	1.001
	Land cover	0.808	1.237
	Aspect	0.999	1.001
	Precipitation	0.989	1.203

*Dependent variable: Fire count

2.4 Assignment of weights for risk model

The weight ranking of each variable was done using the AHP method which is a pairwise comparison-based measurement theory and establishes the significance of each criterion (Saaty, 1994; Saaty, 1977; Saaty, 1988; Saaty and Vargas, 1991). Individual criteria and their subclasses are given relative weights based on previously acquired knowledge of the criteria's features, local field experience, firsthand observation, specifics of the chosen research area, and expert suggestions. A pair-wise comparison matrix was made to compare all factors against each other based on their importance (equal, moderate, strong, very strong, and extremely strong). A standard Saaty's 1-9 scale was used to determine the relative importance values for all themes and their respective features, where value '1' denotes "equal importance" between the two themes, and the value '9' denotes the "extreme importance" of one theme compared to another as shown in Table 3.

Table 3. Scale for a pair-wise comparison matrix (Saaty, 1988)

Intensity importance	Linguistic variables
1	Equal importance
2	Equal to moderate importance
3	Moderate importance
4	Moderate to strong importance
5	Strong importance
6	Strong to the very strong importance
7	Very strong importance
8	Very to the extremely strong importance
9	Extreme importance

Mathematical description of the different steps is summarized in the following steps.

(1) Sum the values in each column of the pair-wise comparison matrix using the formula:

$$Lij = \sum_{n=1}^{n} Cij \quad (1)$$

Where; Lij is the total column value of the pair-wise comparison matrix and Cij is the criteria used for the analysis.

(2) Divide each element in the matrix by its total row to generate a normalized pair-wise comparison matrix (Table 5) as shown in:

$$Xij = \frac{Cij}{Lij} \quad (2)$$

Where; Xij=normalized pair-wise comparison matrix.

(3) Divide the sum of the normalized row of the matrix by the number of criteria/parameter (N) to generate the standard weight by using the following formula:

$$Wij = \frac{\sum_{j=1}^{n} Xij}{N} \quad (3)$$

Where; Wij=standard weight.

(4) For calculating the consistency vector values, the following formula was used:

$$\lambda = \sum_{n=1}^{n} CVij \quad (4)$$

Where; λ=consistency vector.

(5) Consistency index (CI) was used as a deviation or degree of consistency which was then calculated using the following Equation 5 and Consistency ratio (Cr) was calculated by using the formula Equation 6 (Kanga et al., 2017; Kayet et al., 2018).

$$CI = \frac{\lambda - n}{n-1} \quad (5)$$

Where; CI=consistency index, n=number of criteria.

(6) For calculating the Consistency ratio (Cr)

$$Cr = \frac{CI}{RI} \quad (6)$$

If the value of the Consistency ratio (Cr) is less than or equal to 0.10, then the inconsistency is acceptable (Barzilai, 1998). Random inconsistency (RI) values for 'n' number of criteria, i.e., the number of parameters are shown in Table 4.

Table 4. Random index (RI) for different number of criteria (n)

n	1	2	3	4	5	6	7	8	9	10
RI	0	0	0.58	0.9	1.12	1.24	1.32	1.41	1.45	1.49

Table 5. Pairwise and normalized comparison matrix

	LULC	PS	DR	Elevation	LST	Slope	Aspect	Rainfall
LULC	1	3	3	5	5	6	7	7
PS	0.33	1	3	4	5	5	6	7
DR	0.33	0.33	1	3	3	4	5	5
Elevation	0.2	0.25	0.33	1	3	3	5	6
LST	0.2	0.2	0.33	0.33	1	2	3	7
Slope	0.17	0.2	0.25	0.33	0.5	1	3	5
Aspect	0.14	0.17	0.2	0.2	0.33	0.33	1	5
Rainfall	0.14	0.14	0.2	0.17	0.14	0.2	0.2	1

	LULC	PS	DR	Elevation	LST	Slope	Aspect	Rainfall	Total weight	Normal weight
LULC	0.4	0.57	0.36	0.36	0.28	0.28	0.23	0.16	2.64	0.33
PS	0.13	0.19	0.36	0.29	0.28	0.23	0.2	0.16	1.84	0.22
DR	0.13	0.06	0.12	0.21	0.17	0.19	0.17	0.12	1.17	0.15
Elevation	0.08	0.05	0.04	0.07	0.17	0.14	0.17	0.14	0.86	0.11
LST	0.08	0.04	0.04	0.02	0.06	0.09	0.1	0.16	0.59	0.07
Slope	0.07	0.04	0.03	0.02	0.03	0.05	0.1	0.12	0.46	0.06
Aspect	0.06	0.03	0.02	0.01	0.02	0.02	0.03	0.12	0.33	0.04
Rainfall	0.06	0.03	0.02	0.01	0.01	0.01	0.01	0.02	0.17	0.02

Finally, the weight was assigned to the variables accordingly. The Cr value was calculated within the acceptable range of less than 0.01 (Barzilai, 1998). Relative weights were assigned to different classes of variables from local field experience, personal observation, previous research in similar regions, literature (Parajuli et al., 2020; Parajuli et al., 2023; Tiwari et al., 2021), and expert's suggestions. The expert group was constituted of four members including the expert personnel from the District Forest office, the Institute of Forestry, and the Ministry of Tourism and Environment. Finally, the weight was assigned as shown in Table 6. For each variable, the classes for the impact of forest fire were classified into five different categories: Very High, high, medium, low, and very low based on the suggestions from experts, distribution of forest fire points (Figure 6), and different literature review (Parajuli et al., 2020; Parajuli et al., 2023; Tiwari et al., 2021). The methodological framework utilized in the study is given in Figure 3 which was used for obtaining the final risk map.

Table 6. Weight ranking for the different classes of the variables

Variable	Normalized weight	Class	Value assigned	Fire rating classes
Land cover	0.33	Broadleaved closed forest	1	Very high
		Broadleaved open forest	2	High
		Grassland	3	Medium
		Shrubland	4	Low

Table 6. Weight ranking for the different classes of the variables (cont.)

Variable	Normalized weight	Class	Value assigned	Fire rating classes
Land cover	0.33	Needle leaved open forest	4	Low
		Other	5	Very low
Slope (%)	0.06	<5	1	Very high
		5-15	2	High
		15-25	3	Medium
		25-35	4	Low
		>35	5	Very low
Distance to road (m)	0.15	<1,000	1	Very high
		1,000-2,000	2	High
		2,000-3,000	3	Medium
		3,000-4,000	4	Low
		4,000-5,000	5	Very low
Proximity to settlement (m)	0.22	<2,000	1	Very high
		2,000-4,000	2	High
		4,000-6,000	3	Medium
		6,000-8,000	4	Low
		>8,000	5	Very low
Elevation (m)	0.11	<150	1	Very high
		150-300	2	High
		300-450	3	Medium
		450-600	4	Low
		>600	5	Very low
LST	0.07	<28	5	Very low
		28-30	3	Medium
		30-32	2	High
		32-34	2	High
		>34	1	Very high
Aspect	0.04	South	1	Very high
		Southwest	1	Very high
		Southeast	2	High
		West	3	Medium
		East	3	Medium
		Northwest	4	Low
		Northeast	4	Low
		North	5	Very low
Precipitation (mm)	0.02	<35 mm	1	Very high
		35-45 mm	2	High
		45-55 mm	3	Medium
		55-65 mm	4	Low
		>65 mm	5	Very low

3. RESULTS AND DISCUSSION

3.1 Trend analysis of fire incidents in Madhesh Province

From 2001 to 2023, altogether 6,796 fire incidents occurred across 6,158.22 km^2 in Madesh Province. However, only the data with detection confidence greater than 30% accounted for 6,368 fire incidents, as illustrated in Figure 4. This study recorded the year 2021 with the highest fire incidents, while Parajuli et al. (2020) had regarded the year 2016 with the most fire incident occurrence, where Parajuli et al. (2023) has signified that both 2016 and 2021 witnessed severe drought conditions, pointing out as primary reason for sudden surge of fire incidents.

Previously, the research of Parajuli et al. (2015) and Matin et al. (2017) showed that the year 2009 had high frequency of fire incidents due to persisting lower moisture regimes.

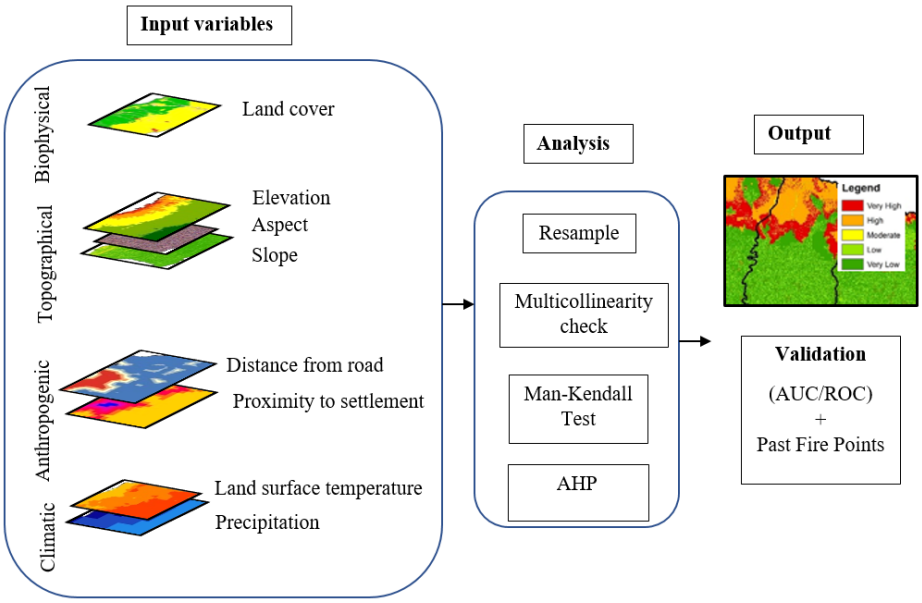

Figure 3. Methodological framework for forest fire risk map

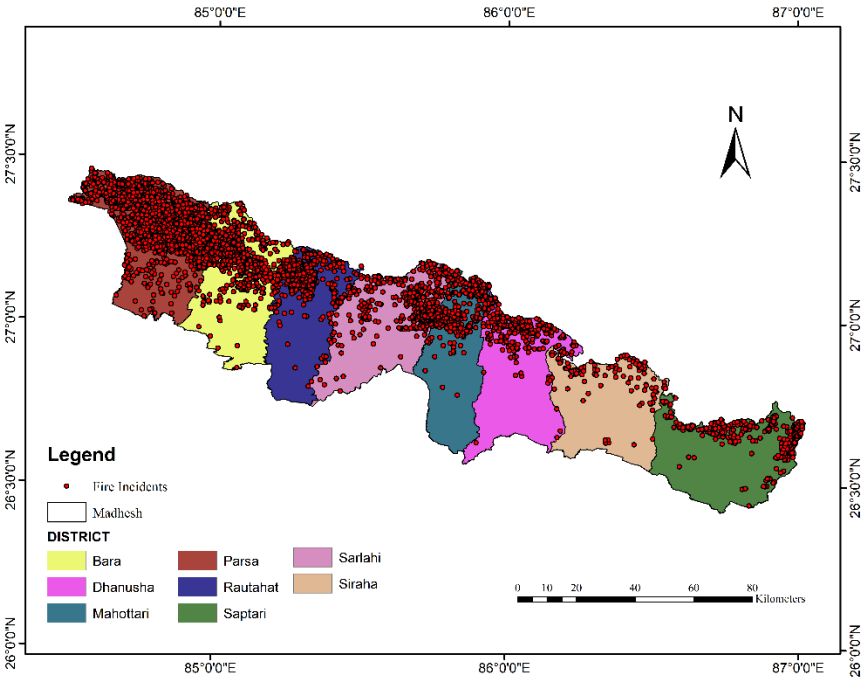

Figure 4. Fire incidents in Madhesh Province for the study period (2001-2023)

We used the Mann-Kendall trend analysis (Mishra et al., 2014) for burnt area analysis and it revealed a decreasing trend with Kendall's tau value of -0.11 and a Sen's slope value of -0.52 (Figure 5(a)). However, this decrease is of relatively low magnitude. Importantly, the observed negative trend in the burnt area is statistically insignificant (p=0.92 at a 5% significance level). In Figure 5(b), the Mann-Kendall trend analysis of fire incidents highlights a statistically significant trend (p=0.02) of increasing forest fire incidence in the region. This is evidenced by the positive value of Kendall's tau (0.351) and Sen's slope value (10.5). The positive trend signifies a notable increase in forest fire incidents over the analyzed period.

Such phenomena may result from improved fire management and suppression efforts, which limit the spread of fires despite higher incident rates (Mishra et al., 2014). Additionally, factors like changes in land use and vegetation dynamics, as well as climatic variations, may play a role in causing inconsistencies between burn area and fire incidence as seen in Figure 5 (Bowman et al., 2009; Westerling et al., 2006). These findings indicate a complex interplay of factors influencing fire dynamics, thus, requiring further investigation into the underlying causes of these trends.

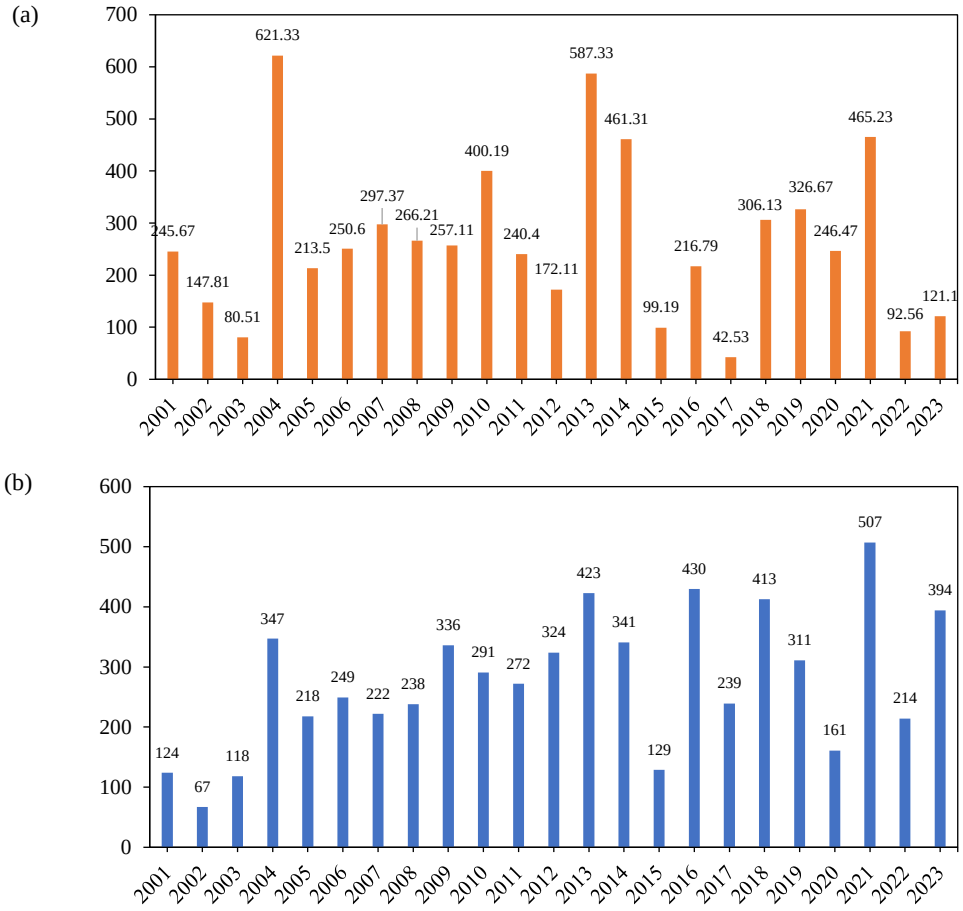

Figure 5. Year-wise trend analysis of forest fire in Madhesh Province: (a) Burnt area (per km^2) and (b) Fire incidence reported by MODIS

3.2 Variables effect on forest fire incidents

Each factor concerned with forest fire has been discussed and analyzed separately. The land cover class map shows that around 16% of the study area was forested with broad-leaved closed forest comprising the majority area of approximately 83%. Figure 6(a) shows that the broad-leaved closed forest was intercepted with the highest number of forest fire counts consisting 74% of the total incidents. This was due to the presence of dried Sal (*Shorea robusta*) leaves serving as active fuel material, comprising almost 90% of the continuous fuel in the forest of this region (Sharma and Hussin, 1996).

The fire incidents witnessed a decreasing trend with the slope increment as shown in Figure 6(b). In case of plain lands, as of Terai Region of Nepal, the study of Matin et al. (2017) recorded that 72% of the fires occurred in the areas with temperature above 30°C and a slope of less than 5%. Similar findings were recorded in this study where a majority of incidents occurred in the areas where temperature was around 30-32°C. Further, the southern side receives more sunshine, thus, raises the temperature and makes fuel drier (Prasad et al., 2008; Parajuli et al., 2020). Majority of the Madesh Province falls in the Terai Region with some extension in the Chure hills up to 918 m, fire incidents decreased with an increase in the elevation. As evident in Figure 6(c), only a quarter of fire incidents occurred in the areas with slope greater than 15%. Similar findings were reported by Ariapour and Shariff (2014), where 65% of fires occurred within 1,000 m elevation. Further, this study showed that the areas within the proximity of 2,000 m from settlements, there were relatively high fire incidents

comprising almost 45%. Interestingly, a slight increment from 1369 to 1428 is seen in fire incident occurrence between 2,000-6,000 m which later decreases to only about 14.5% incidents. According to research by Hussin et al. (2008), people seldom light fires at distances greater than 2000 m from where they live which may be the reason for lesser frequency of fire incidents above 2,000 m as shown in Figure 6(g). The study of Ariapour and Shariff (2014) documented 40% of fire incidents within 1 km from the road. Likewise, in this study, Figure 6(h) shows that around 65% of fire incidents were within 1 km from the road. The incidence of fire to activities such as throwing unlit cigarettes onto dry litter, and heating bitumen/asphalt for road surfacing are subjected to higher occurrences of forest fires within closer proximity of road (Jaiswal et al., 2002; Ariapour and Shariff, 2014).

Various researchers have employed different variables and assigned varying degrees of importance. Tiwari et al. (2021), for instance, accorded the highest weight to elevation, whereas Feizizadeh et al. (2015) prioritized slope. Further, Hassan et al. (2020) emphasized rainfall and temperature. However, Kodandapani et al. (2008) acknowledged that forest type plays a pivotal role in fire occurrence and highlighted those broad-leaved forests are highly susceptible to fire during dry seasons. This research discovered that relatively higher impacts are constrained by land cover, followed by proximity to settlement, elevation, road distance, as shown by Figure 6 and the risk map. We found that the risk areas mostly comprised forest areas with almost 90% of the forest area under high and very high-risk areas in the province (Figure 7).

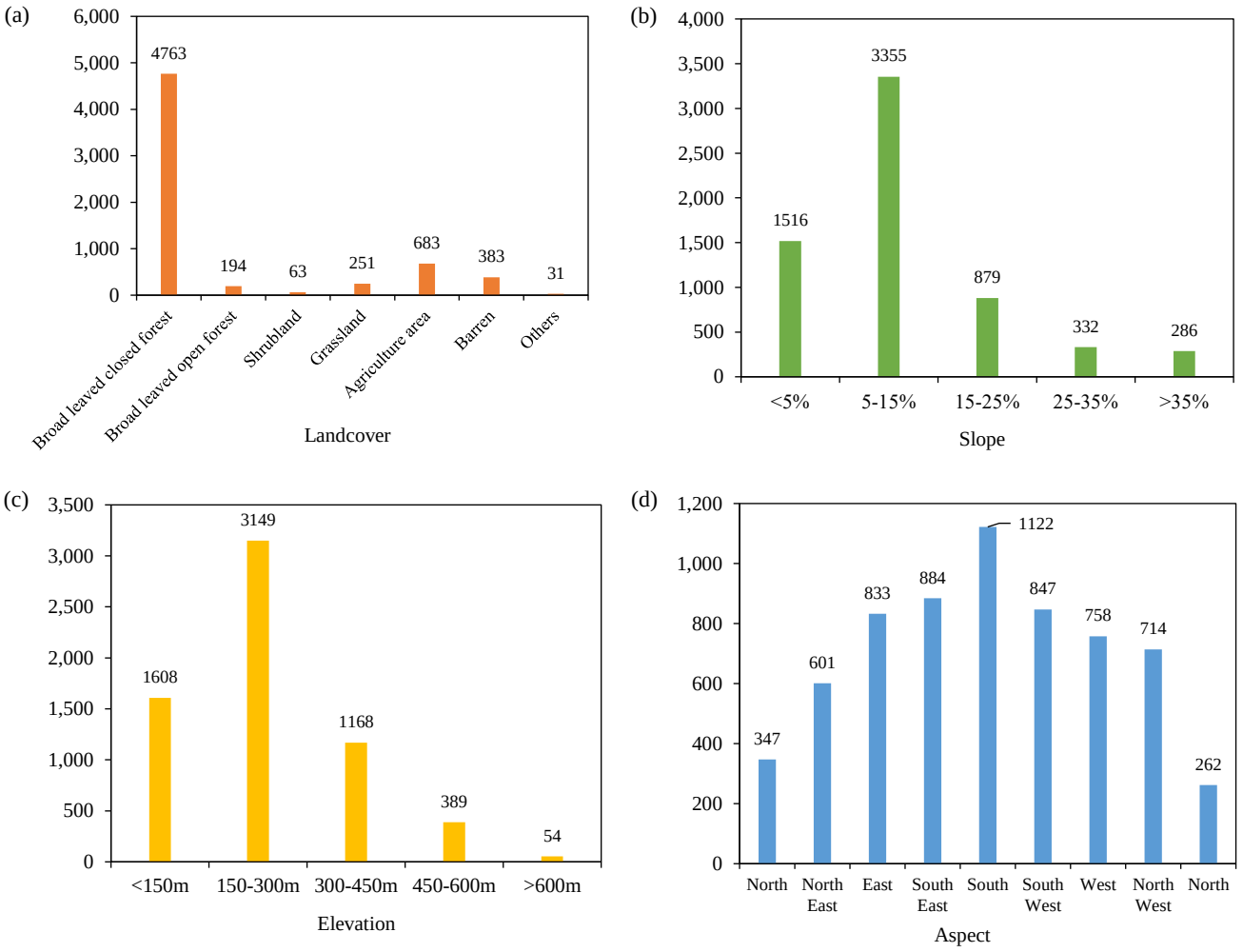

Figure 6. Forest fire incidents (a) land cover classes, (b) slope, (c) elevation, (d) aspect, (e) land surface temperature, (f) precipitation (g) proximity to settlement, and (h) distance to road

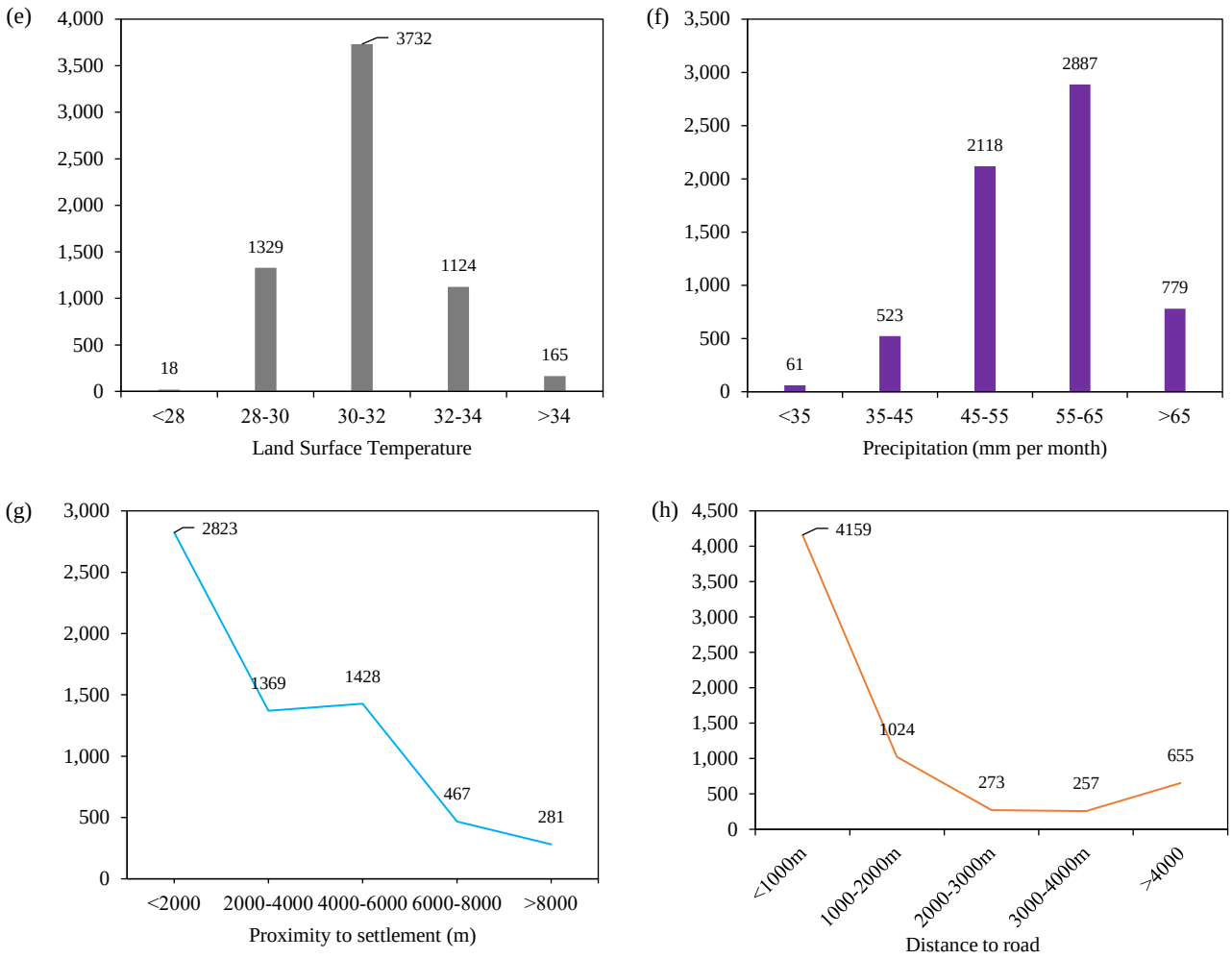

Figure 6. Forest fire incidents (a) land cover classes, (b) slope, (c) elevation, (d) aspect, (e) land surface temperature, (f) precipitation (g) proximity to settlement, and (h) distance to road (cont.)

3.3 Fire risk map

As accord to Table 6 weightage value obtained from the AHP method, the risk map of Madhesh was obtained. Based on the weightage given to each variable class as per their influence on forest fire**,** all the thematic variables were added using the weightage overlay method in ArcGIS as shown in Figure 7, where the area is classified into five categories ranging from very high, high, moderate, and low to very low. The Table 7 demonstrates that, although the area under very high and high category is just 24.5%, however, it accounts for 72.5% of total fire incidents, which is in concordant with the output of Mann-Kendal trend analysis.

Table 7. Fire incidents in risk areas

Value	Area (km^2)	% of area	No. of total fire counts	% of total fire counts	Fire density per km^2
Very high	660.43	7.26	1,002	15.74	1.51
High	1566.52	17.24	3,679	56.78	2.34
Medium	193.36	2.13	556	8.73	2.87
Low	1430.45	15.72	558	8.76	0.39
Very low	5243.51	57.65	573	8.99	0.10

3.4 Validation

For the validation process, past data points were overlaid on the map, revealing a concentration of fire incidents in the high-risk zone. This validation method aligns with approaches utilized by various researchers, including Higgins et al. (2013), Feizizadeh et al. (2015), Ajin et al. (2016), Pourghasemi (2020), and Lamat et al. (2021). Additionally, to ascertain the

accuracy of the results, the area under curve (AUC) curve was employed, as depicted in Figure 6. This study employed the AUC validation technique, like the approach utilized by Parajuli et al. (2023) and has yielded significant results. The ArcSDM tool (ESRI, 2022) was used in ArcGIS for AUC calculation and the prediction map scored the AUC value of 0.798 (79.8%) (Figure 8) which shows the produced results are acceptable. Notably, this AUC value is comparable to that reported by (Tiwari et al., 2021) with 81.75% for AHP method.

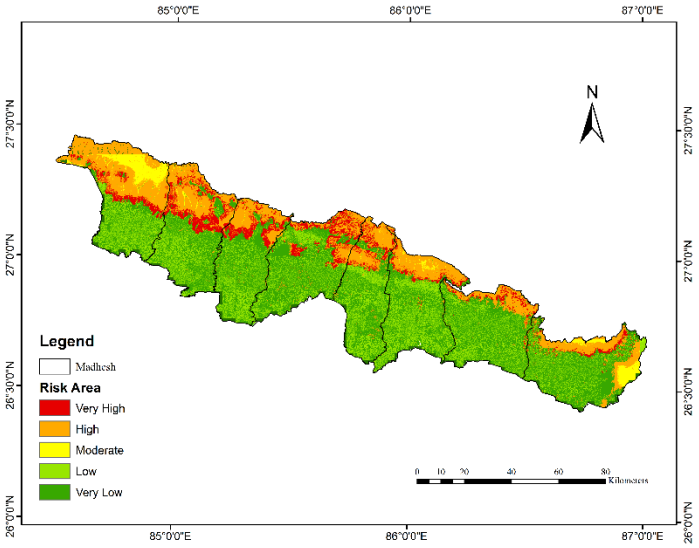

Figure 7. Forest fire risk map index combining all influencing variables

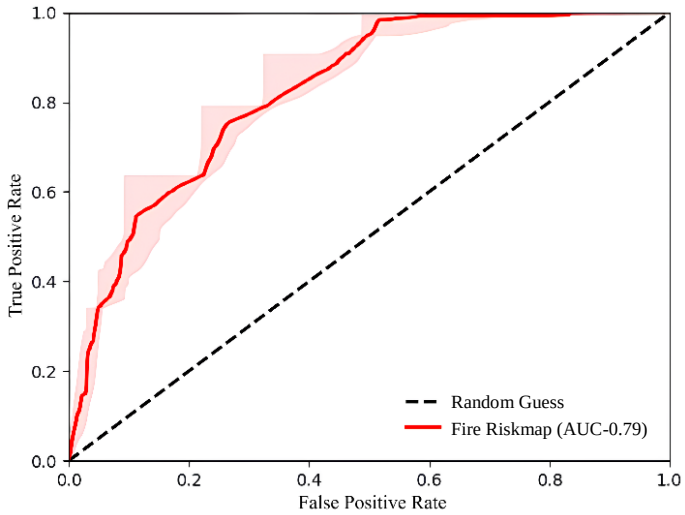

Figure 8. Receiver Operating Characteristic (ROC) curve of fire risk map

4. CONCLUSION

The research gives insights to spatial dynamics of forest fires in various influencing variables in the sub-tropical forests of Madhesh Province of Nepal. The MODIS fire incidence analysis showed highest incidence in 2021 while highest burnt area was reported in 2004. Overall, the broadleaved forests appeared vulnerable to fire incidents occurrence, with nearly 90% of the forested area falling into high or very high-risk category, so mitigatory strategies are suggested to be applied to lessen the damage incurred. The weight ranking shows that land cover, proximity to settlement, and elevation are highly sensitive to forest fire risk presumed in the Madhesh Province. Furthermore, the forest fire risk map index, based on the weightage of various variables, reveals that the forest area of the Madesh Province is vulnerable, and overall, 7.26% area is under very high-risk, 17.24% under high risk. Moreover, the Man Kendal trend analysis of burn area and fire incidence reveal that

further intricated studies are required to understand the underlying factors affecting the variables associated with forest fires.

ACKNOWLEDGEMENTS

This research acknowledges Department of Forest, Madhesh Province and Institute of Forestry Pokhara for providing necessary support and guidance throughout the research.

AUTHOR CONTRIBUTIONS

- Conceptualization: Adhikari G and Joshi KP
- Data curation: Adhikari G;
- Formal analysis: Adhikari G and Joshi KP
- Funding acquisition: Not applicable
- Investigation: Adhikari G and Joshi KP
- Methodology: Adhikari G and Chad D
- Project administration: Not applicable
- Visualization: Adhikari G and Joshi KP
- Roles/Writing-original draft: Adhikari G, Mahara S, and Chad D
- Writing-review and editing: Mahara S, Adhikari G, and Ghimire A

DECLARATION OF COMPETING INTEREST

The authors declare no conflict of interest.

REFERENCES

Ajin RS, Loghin AM, Vinod PG, Jacob MK. RS and GIS based forest fire risk zone mapping in the Periyar Tiger Reserve, Kerala, India. Journal of Wetlands Biodiversity 2016;6:139-48.

Ariapour A, Shariff AR. Rangeland fire risk zonation using remote sensing and geographical information system technologies in Boroujerd Rangelands, Lorestan Province, Iran. Ecopersia 2014;2(4):805-18.

Barzilai J. Consistency measures for pairwise comparison matrices. Journal of Multi-Criteria Decision Analysis 1998; 7(3):123-32.

Bowman DM, Balch JK, Artaxo P, Bond WJ, Cochrane MA, D'Antonio CM, et al. Fire in the Earth system. Science 2009;324(5926):481-4.

Chang Y, Zhu ZL, Bu RC, Chen HG, Feng YT, Li YH, et al. Predicting fire occurrence patterns with logistic regression in Heilongjiang Province. Landscape Ecology 2013;28(10): 1989-2004.

Curkovic S. Sustainable development: Authoritative and leading edge content for environmental management. In: Leblon B, Chavez LB, Ayanz JSM, editors. Use of Remote Sensing in Wildfire Management. Croatia: InTech; 2012. p. 55-82.

Davis R, Yang Z, Yost A, Belongie C, Cohen W. The normal fire environment-modeling environmental suitability for large forest wildfires using past, present, and future climate normals. Forest Ecology and Management 2017;390:173-86.

Dawson TP, Butt N, Miller F. The ecology of forest fires. ASEAN Biodiversity: The Newsmagazine of the ASEAN Regional Centre for Biodiversity Conservation 2001;1(3):18-21.

Department of Forest Research and Survey (DFRS). State of Nepal's Forests. Forest Resource Assessment (FRA) Nepal. Kathmandu, Nepal: DFRS; 2015.

Doerr SH, Santín C. Global trends in wildfire and its impacts: Perceptions versus realities in a changing world. Philosophical Transactions of the Royal Society B: Biological Sciences 2016;371(1696):Article No. 20150345.

Environmental Systems Research Institute (ESRI). ArcGIS Deskop 10.8 [Internet]. 2022 [cited 2023 Mar 12]. Available from: https://desktop.arcgis.com/en/arcmap/latest/get-started/installation-guide/installing-on-your-computer.htm.

Feizizadeh B, Omrani K, Aghdam FB. Fuzzy analytical hierarchical process and spatially explicit uncertainty analysis approach for multiple forest fire risk mapping. Giforum 2015;1:72-80.

Giglio L, Schroeder W, Hall JV, Justice CO. MODIS Collection 6 Active Fire Product User's Guide Revision A. Maryland: Department of Geographical Sciences, University of Maryland; 2015. p. 9.

Giglio L, Van der Werf GR, Randerson JT, Collatz GJ, Kasibhatla P. Global estimation of burned area using MODIS active fire observations. Atmospheric Chemistry and Physics 2006; 6(4):957-74.

Food and Agriculture Organization of the United Nations (FAO). Global Forest Resource Assessment [Internet]. 2020 [cited 2023 Mar 12]. Available from: http://www.fao.org/forest-resources-assessment/2020.

GoN/Ministry of Forests and Soil Conservation (MoFSC). Conservation landscapes of Nepal. Singha Durbar, Kathmandu, Nepal: Ministry of Forests and Soil Conservation; 2016.

Hassan AH, Feizizadeh B, Blaschke T. GIS-based forest fire risk mapping using the analytical network process and fuzzy logic. Journal of Environmental Planning and Management 2020;63(3):481-99.

Higgins E, Taylor M, Jones M, Lisboa P. Understanding community fire risk: A spatial model for targeting fire prevention activities. Fire Safety Journal 2013;62:20-9.

Hussin YA, Matakala M, Zagdaa N. The applications of remote sensing and GIS in modeling forest fire hazard in Mongolia. Proceedings of the 21st ISPRS Congress 2008: Silk Road for Information from Imagery; 2008 July 3-11; Beijing: China; 2008.

International Centre for Integrated Mountain Development (ICIMOD). Land Cover of Nepal 2010. ICIMOD; 2013.

Jaiswal RK, Mukherjee S, Raju KD, Saxena R. Forest fire risk zone mapping from satellite imagery and GIS. International Journal of Applied Earth Observation and Geoinformation 2002;4(1):1-10.

Joerin F, Thériault M, Musy A. Using GIS and outranking multicriteria analysis for land-use suitability assessment. International Journal of Geographical Information Science 2001;15(2):153-74.

Kanga S, Tripathi G, Singh SK. Forest fire hazards vulnerability and risk assessment in Bhajji forest range of Himachal Pradesh (India): A geospatial approach. Journal of Remote Sensing and GIS 2017;8(1):1-6.

Kayet N, Chakrabarty A, Pathak K, Sahoo S, Dutta T, Hatai B. Comparative analysis of multi-criteria probabilistic FR and AHP models for forest fire risk (FFR) mapping in Melghat Tiger Reserve (MTR) forest. Journal of Forestry Research 2018;31:565-79.

Kim JH. Multicollinearity and misleading statistical results. Korean Journal of Anesthesiology 2019;72(6):558-69.

Kodandapani N, Cochrane MA, Sukumar R. A comparative analysis of spatial, temporal, and ecological characteristics of forest fires in seasonally dry tropical ecosystems in the Western Ghats, India. Forest Ecology and Management 2008;256(4):607-17.

Kumar D, Garg CP. Evaluating sustainable supply chain indicators using fuzzy AHP: Case of Indian automotive industry. Benchmarking: An International Journal 2017;24(6):1742-66.

LP DAAC. ASTER Global Digital Elevation Model V003 [Internet]. 2019 [cited 2023 Mar 12]. Available from: https://lpdaac.usgs.gov/products/astgtmv003/.

Lamat R, Kumar M, Kundu A, Lal D. Forest fire risk mapping using analytical hierarchy process (AHP) and earth observation datasets: A case study in the mountainous terrain of Northeast India. SN Applied Sciences 2021;3(4):Article No. 425.

Mann HB. Nonparametric tests against trend. Econometrica 1945;13(3):245-59.

Matin MA, Chitale VS, Murthy MSR, Uddin K, Bajracharya B, Pradhan S. Understanding forest fire patterns and risk in Nepal using remote sensing, geographic information system and historical fire data. International Journal of Wildland Fire 2017;26(4):276-86.

Mishra B, Babel MS, Tripathi NK. Analysis of climatic variability and snow cover in the Kaligandaki River Basin, Himalaya, Nepal. Theoretical and Applied Climatology 2014;116: 681-94.

Parajuli A, Chand DB, Rayamajhi B, Khanal R, Baral S, Malla Y. Spatial and temporal distribution of forest fires in Nepal. Proceedings of the 14th World Forestry Congress; 2015 Sep 7-11; Durban: South Africa; 2015.

Parajuli A, Gautam AP, Sharma SP, Bhujel KB, Sharma G, Thapa PB, et al. Forest fire risk mapping using GIS and remote sensing in two major landscapes of Nepal. Geomatics, Natural Hazards and Risk 2020;11(1):2569-86.

Parajuli A, Manzoor SA, Lukac M. Areas of the Terai Arc landscape in Nepal at risk of forest fire identified by fuzzy analytic hierarchy process. Environmental Development 2023;45:Article No. 100810.

Pourghasemi HR, Kariminejad N, Amiri M, Edalat M, Zarafshar M, Blaschke T, et al. Assessing and mapping multi-hazard risk susceptibility using a machine learning technique. Scientific Reports 2020;10(1):Article No. 3203.

Pradhan B, Suliman MDHB, Awang MAB. Forest fire susceptibility and risk mapping using remote sensing and geographical information systems (GIS). Disaster Prevention and Management: An International Journal 2007;16(3): 344-52.

Prasad VK, Badarinath K, Eaturu A. Biophysical and anthropogenic controls of forest fires in the Deccan Plateau, India. Journal of Environmental Management 2008;86(1):1-13.

Qadir A, Talukdar NR, Uddin MM, Ahmad F, Goparaju L. Predicting forest fire using multispectral satellite measurements in Nepal. Remote Sensing Applications: Society and Environment 2021;23:Article No. 100539.

Ranabhat S, Pokhrel A, Neupane A, Singh B, Gahatraj S. Forest fire risk assessment and proposal for fire stations in different Geographical Regions of Central Nepal. Journal of Forest and Livelihood 2022;21(1):46-59.

Reeves MC, Zhao M, Running SW. Applying improved estimates of MODIS productivity to characterize grassland vegetation dynamics. Rangeland Ecology and Management 2006; 59(1):1-10.

Saaty TL. A scaling method for priorities in hierarchical structures. Journal of Mathematical Psychology 1977;15(3):234-81.

Saaty TL. Some mathematical topics in the analytic hierarchy process. In: Mathematical Models for Decision Support. Berlin, Heidelberg: Springer; 1988.

Saaty TL. How to make a decision: The analytic hierarchy process. Interfaces 1994;24(6):19-43.

Saaty TL, Vargas LG. Prediction, Projection and Forecasting. Boston, USA: Kluwer Academic; 1991.

Sharma N, Hussin Y A. Spatial Modelling for Forest Fire Hazard Prediction, Management and Control in Corbett National Park, India. University of Twente Research Information; 1996.

Singh BK. Land tenure and conservation in Chure. Journal of Forest and Livelihood 2017;15(1):87-102.

Tiwari A, Shoab M, Dixit A. GIS-based forest fire susceptibility modeling in Pauri Garhwal, India: A comparative assessment of frequency ratio, analytic hierarchy process and fuzzy modeling techniques. Nat Hazards 2021;105(2):1189-230.

Wan Z. New refinements and validation of the collection-6 MODIS land-surface temperature/emissivity product. Remote Sensing of Environment 2014;140:36-45.

Westerling AL, Hidalgo HG, Cayan DR, Swetnam TW. Warming and earlier spring increase western US forest wildfire activity. Science 2006;313(5789):940-3.

Wang F, Hall GB, Subaryono. Fuzzy information representation and processing in conventional GIS software: Database design and application. International Journal of Geographical Information System 1990;4(3):261-83.

Yu J, Chen Y, Wu J, Khan S. Cellular automata-based spatial multi-criteria land suitability simulation for irrigated agriculture. International Journal of Geographical Information Science 2011;25(1):131-48.

Zolekar RB, Bhagat VS. Multi-criteria land suitability analysis for plantation in Upper Mula and Pravara basin: remote sensing and GIS approach. Journal of Geographical Studies 2018;2(1):12-20.

Zhu H, Zhang Z, Yang S, Zhu ZP, Zeng AC, Guo FT. Temporal and spatial distribution of forest fire and the dynamics of fire danger period in southern and northern China: A case study in Heilongjiang and Jiangxi Provinces. Chinese Journal of Ecology 2023;42(1):Article No. 198-207.

Environment and Natural Resources Journal

Volume 23
Issue 1
2025

Study of Crystal Structure, Lattice Strain, and Elemental Content of Natural Iron Sand Nanoparticles Synthesized by the Coprecipitation Method

Tulus Na Duma[1], Syahrul Humaidi[1*], Erna Frida[1], Mohd. Mustafa Awang Kechik[2], Muhammadin Hamid[3], Martha Rianna[1], Novita[1], Rahmadhani Banurea[1], Norazimah Mohd Yusof [4], and Nur Jannah Azman[4]

[1]Postgraduate Program (Physics), FMIPA, Universitas Sumatera Utara, Jl. Bioteknologi No.1, Medan 20155, Indonesia
[2]Department of Physics, Faculty of Science, Universiti Putra Malaysia, 43400 UPM Serdang, Selangor, Malaysia
[3]Department of Physics, Universitas Sumatera Utara, Jl. Bioteknologi No.1, Medan 20155, Indonesia
[4]Faculty of Applied Sciences, Universiti Teknologi MARA, Cawangan Negeri Sembilan, Kampus Kuala Pilah 72000, Kuala Pilah, Negeri Sembilan, Malaysia

ARTICLE INFO

Received: 13 May 2024
Received in revised: 29 Nov 2024
Accepted: 3 Dec 2024
Published online: 14 Jan 2025
DOI: 10.32526/ennrj/23/20240141

Keywords:
Crystal structure/ Coprecipitation/ Iron sand/ Lattice strain/ Magnetite nanoparticles

*** Corresponding author:**
E-mail: syahrul1@usu.ac.id

ABSTRACT

GRAPHICAL ABSTRACT

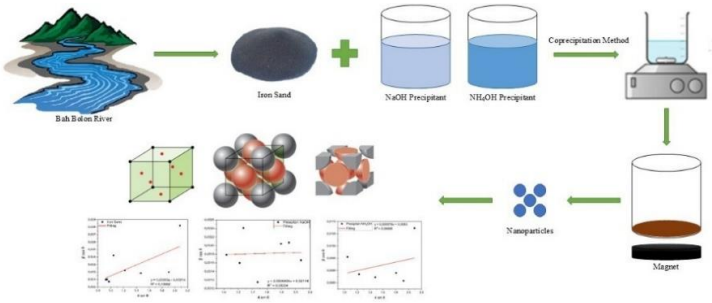

This study was conducted to investigate the synthesis of magnetite nanoparticles from iron sand collected from the Bah Bolon River in Indonesia, using the coprecipitation method with NaOH and NH_4OH as precipitants. The results showed that based on SEM-EDX (scanning electron microscopy coupled with energy-dispersive x-ray spectroscopy) analysis, the Fe content of the raw iron sand, initially at 34.76%, increased to 45.50% following synthesis with NH_4OH, indicating enhanced purity in the final product. SEM observations found average particle sizes of approximately 53 nm for nanoparticles synthesized with NaOH and 20 nm for those synthesized with NH_4OH. X-ray diffraction (XRD) analysis confirmed that the synthesized nanoparticles retain the magnetite (Fe_3O_4) phase with a face-centered cubic (FCC) spinel structure. Crystallite size calculations using the Scherrer equation yielded average crystallite sizes of 80.194 nm for NaOH-synthesized samples and 15.124 nm for NH_4OH-synthesized samples, demonstrating that NH_4OH favors the formation of smaller crystallites. Lattice strain analysis through the Williamson-Hall method showed positive tensile strain values for all samples, indicating structural tension within the crystal lattice. The NH_4OH-synthesized nanoparticles had slightly higher lattice strain, suggesting that synthesis conditions impact both crystallite size and lattice tension. In conclusion, this study demonstrated that NH_4OH was more effective than NaOH in producing high-purity, small-crystallite magnetite nanoparticles from natural iron sand, with potential implications for enhanced material properties.

Citation: Duma TN, Humaidi S, Frida E, Kechik MMA, Hamid M, Rianna M, Novita, Banurea R, Yusof NM, Azman NJ. Study of crystal structure, lattice strain, and elemental content of natural iron sand nanoparticles synthesized by the coprecipitation method. Environ. Nat. Resour. J. 2025;23(1):95-104. (https://doi.org/10.32526/ennrj/23/20240141)

1. INTRODUCTION

Magnetic materials are of significant interest in the field of nanotechnology due to the unique properties, which facilitate application for a variety of advanced purposes. These materials are typically composed of elements such as iron, cobalt, nickel, and alloys, which have intrinsic magnetic behaviors potentially manipulated and enhanced at the nanoscale. Magnetic materials, when synthesized as nanoparticles show characteristics including superparamagnetism, a phenomenon defined as a loss of magnetization in the absence of an external magnetic field, which is advantageous for applications requiring precise control. Additionally, magnetic nanoparticles tend to have higher saturation, facilitating more responsiveness to external magnetic fields. The increased surface area promotes higher reactivity and allows for functionalization, enabling tailored applications in various fields (Díez et al., 2022).

Among magnetic materials, magnetite (Fe_3O_4) has demonstrated particular potential for further development. Fe_3O_4 nanoparticles are widely studied due to the strong magnetic properties, biocompatibility, and versatility in application. The application cuts across a range of fields, including targeted drug delivery, where magnetic properties allow for controlled movement to specific locations in the body. In magnetic resonance imaging (MRI), the nanoparticles act as contrast agents to improve image clarity (Zhang et al., 2022). Other uses include hyperthermia therapy for cancer, where localized heating of tumor cells is achieved through magnetic induction (Wang et al., 2021), and environmental remediation, where magnetic separation can efficiently remove pollutants from water (Fatimah et al., 2023; Tlili et al., 2023).

An important advantage of magnetite is that it can be sourced from nature, providing a potentially sustainable and cost-effective resource for nanoparticle synthesis. Natural deposits of Fe_3O_4 are found in coastal regions, riverbeds, volcanic areas, and green synthesis making it readily available for large-scale production (Elaoud et al., 2024; Novita et al., 2024). Although significant studies have been conducted on Fe_3O_4 nanoparticles synthesized from coastal stands (Yuwanda et al., 2022), data on using river sand as a source are relatively scarce. This gap suggests an opportunity for further investigation into river sands as an alternative natural source of Fe_3O_4, which could expand the availability of sustainable raw materials for magnetite nanoparticle production and open new pathways for applications in nanotechnology.

Various synthesis methods have been used to produce magnetite nanoparticles, each offering unique advantages and influencing the final characteristics. Prominent methods include coprecipitation (Gutierrez et al., 2024; Hamid et al., 2022; Parvathy Namboothiri and Vasundhara, 2023), sol-gel (Hu et al., 2019; Polla et al., 2023), high-energy milling (Calderón Bedoya et al., 2021; Melinia et al., 2022; Rianna et al., 2022), and laser ablation (Al-Salih et al., 2021; Alkallas et al., 2023; Dadashi et al., 2015). Among these methods, coprecipitation is particularly popular due to the simplicity, cost-effectiveness, and ability to yield nanoparticles with controlled size, morphology, and elemental composition. The coprecipitation method entails mixing iron salts in an alkaline medium, allowing for precise manipulation of reaction parameters such as temperature, pH, and the type of precipitating agent used. These parameters play a crucial role in determining the particle size, distribution, and magnetic properties of the resulting nanoparticles, making coprecipitation an adaptable and highly effective method for synthesizing magnetite nanoparticles at both laboratory and industrial scales (Tukan et al., 2023). Although Fe_3O_4 is already present in raw river sand, the coprecipitation method is essential to enhance purity, control particle size, and improve the crystallinity of the synthesized nanoparticles. These improvements are necessary for applications that demand high-purity and consistent particle properties, justifying the use of coprecipitation for refining natural Fe_3O_4 sources.

Studies on magnetite nanoparticle synthesis have shown that the choice of precipitant significantly impacts the characteristics of the final product. Previous studies by Ba-Abbad et al. (2022) explored the effects of different precipitants, such as sodium hydroxide (NaOH) and ammonium hydroxide (NH_4OH), on the morphology and size of magnetite nanoparticles. The results underscore how varying the precipitant can allow fine-tuning of nanoparticle properties, which is essential for tailoring to specific applications. Iron chloride hexahydrate and iron sulfate heptahydrate are commonly used as precursors, reacting with an alkaline solution to form magnetite. However, only a few studies have examined the impact of different precipitants specifically for nanoparticles synthesized from natural iron sand. Examining the effects of different precipitants could

provide valuable insights into controlling the structural and magnetic properties of magnetite nanoparticles, particularly those synthesized from natural, sustainable resources.

Understanding the structural characteristics, lattice strain, and elemental composition of magnetite nanoparticles derived from natural iron sand is crucial for optimizing performance across various applications. The crystal structure, for instance, influences magnetic properties and surface reactivity, which are critical for applications such as MRI and targeted drug delivery. Lattice strain, often induced by particle size reduction or imperfections within the crystal lattice, potentially impacts the stability and performance of nanoparticles, making it a key parameter to assess in any synthesis process. Additionally, the elemental composition determines the chemical stability and interaction of nanoparticles with the environment, which is especially relevant in biomedical and environmental applications where compatibility and longevity are essential. By comprehensively characterizing these properties, synthesis methods can be refined to produce nanoparticles with tailored properties, ultimately broadening applicability in scientific and technological fields (Nguyen et al., 2021).

This study aimed to synthesize magnetite nanoparticles from natural iron sand using the coprecipitation method, with a focus on examining the effects of different precipitants, namely NaOH and NH_4OH. A review of existing literature suggests that these precipitants are commonly used for magnetite nanoparticle synthesis, though there are limited studies on the specific effects when applied to natural iron sand sources. This study will investigate how the choice of precipitant influences the crystal structure, lattice strain, and elemental composition of nanoparticles. To achieve this, characterization methods such as x-ray diffraction (XRD) were used to analyze crystal structure and lattice strain while scanning electron microscopy coupled with energy-dispersive x-ray spectroscopy (SEM-EDX) was used to assess particle morphology, size, and elemental content. The results will provide new insights into the potential of natural iron sand as a raw material for high-quality magnetite nanoparticles, paving the way for more sustainable production practices in nanotechnology.

2. METHODOLOGY

2.1 Materials

The natural iron sand used was obtained from the Bah Bolon River, Simalungun Regency of North Sumatra, Indonesia. A previous study focused on analyzing the mineral composition and magnetic characteristics of iron sand (Novita et al., 2023). However, to date, the synthesis of magnetite nanoparticles River has not been undertaken. Further investigation is warranted to examine additional properties of the iron sand after the conversion into magnetite nanoparticles. For the synthesis process, ammonium hydroxide (NH_4OH) at a concentration of 25% (75 mL) and sodium hydroxide (NaOH) at 3 g dissolved in 20 mL of distilled water was used. Additionally, 20 mL of 37% hydrochloric acid (HCl) was utilized.

2.2 Synthesis of magnetite nanoparticles

The synthesis of magnetite nanoparticles was conducted through the coprecipitation method. Initially, 10 g of iron sand were measured and dissolved in 20 mL of 37% HCl. The addition of HCl facilitated the dissolution of iron sand, releasing Fe ions necessary for the formation of magnetite nanoparticles. The acid treatment aided in breaking down the iron sand structure, enhancing the availability of iron for the subsequent reaction steps with NaOH or NH_4OH. This preparation step is crucial for ensuring a homogenous solution of iron ions, which facilitates efficient nanoparticle formation. The dissolution of iron oxides in HCl can be represented by the reactions:

$$Fe_2O_3 + 6HCl \rightarrow 2Fe^{3+} + 3H_2O + 6Cl^-$$
$$FeO + 2HCl \rightarrow Fe^{2+} + H_2O + 2Cl^-$$

The solution of iron sand and HCl was stirred at 70°C for 30 min, with agitation maintained at a speed of 500 rpm. Subsequently, a preheated solution of NaOH at 70°C for 10 min was gradually added to the iron sand solution while heating and stirring were continued for an additional hour. This procedure was repeated using 75 mL of 25% NH_4OH solution in place of NaOH. The addition of the base raised the pH, precipitating Fe^{2+} and Fe^{3+} ions as Fe_3O_4 according to the reaction:

$$2Fe^{3+} + Fe^{2+} + 8OH^- \rightarrow Fe_3O_4 + 4H_2O$$

The use of NaOH and NH_4OH as the precipitant introduced a buffering effect, which stabilizes the pH and supports controlled growth of Fe_3O_4 particles, resulting in nanoparticles with desired purity and size. The synthesized solutions were then allowed to settle, followed by washing of the precipitate with distilled water to eliminate the solvent. Finally, the separated precipitate was dried in an oven at 100°C for 3 h.

2.3 Characterization of magnetite nanoparticles

SEM-EDX analysis, facilitated by Image-J and OriginLab software, was used to examine elemental composition, surface morphology, and particle size. X-ray diffraction (XRD) with CuKα radiation (λ=1.5406 Å) was used to analyze crystal structure and lattice strain, scanning within the range of 20-80° for an angle of 2θ. The crystal size of the synthesized samples was determined using the Scherrer equation (Equation 1), while lattice strain values were assessed using the Williamson-Hall method (Mustapha et al., 2019).

$$d = \frac{K\lambda}{\beta \cos\theta} \quad (1)$$

In the Scherrer equation, K represents Scherrer's constant (K=0.9), β denotes the peak width at half maximum in radians, λ signifies the x-ray wavelength (λ=1.5406 Å), and θ indicates the Bragg diffraction angle measured in radians (Humaidi et al., 2023).

3. RESULTS AND DISCUSSION

3.1 SEM-EDX analysis

SEM-EDX analysis was used to investigate the particle size, surface morphology, and elemental composition of magnetite nanoparticles synthesized from natural iron sand. Figure 1 shows the SEM images at 1,000x magnification, with clear distinctions between the pre- and post-synthesis states of the particles. The raw iron sand (Figure 1(a)) has irregular shapes, asymmetrical protrusions, and a rough surface, likely due to environmental factors including erosion, sediment transport, and deposition in river currents. Following synthesis, the magnetite nanoparticles showed significantly reduced particle size but lacked a fully uniform morphology.

For samples synthesized with NaOH as the precipitant, SEM images showed a moderate reduction in surface roughness, yielding a comparatively smoother texture. In contrast, synthesis with NH_4OH produced smaller particles with reduced surface irregularity and a more porous structure. This morphology may be attributed to NH_4OH which created a more controlled pH environment, resulting

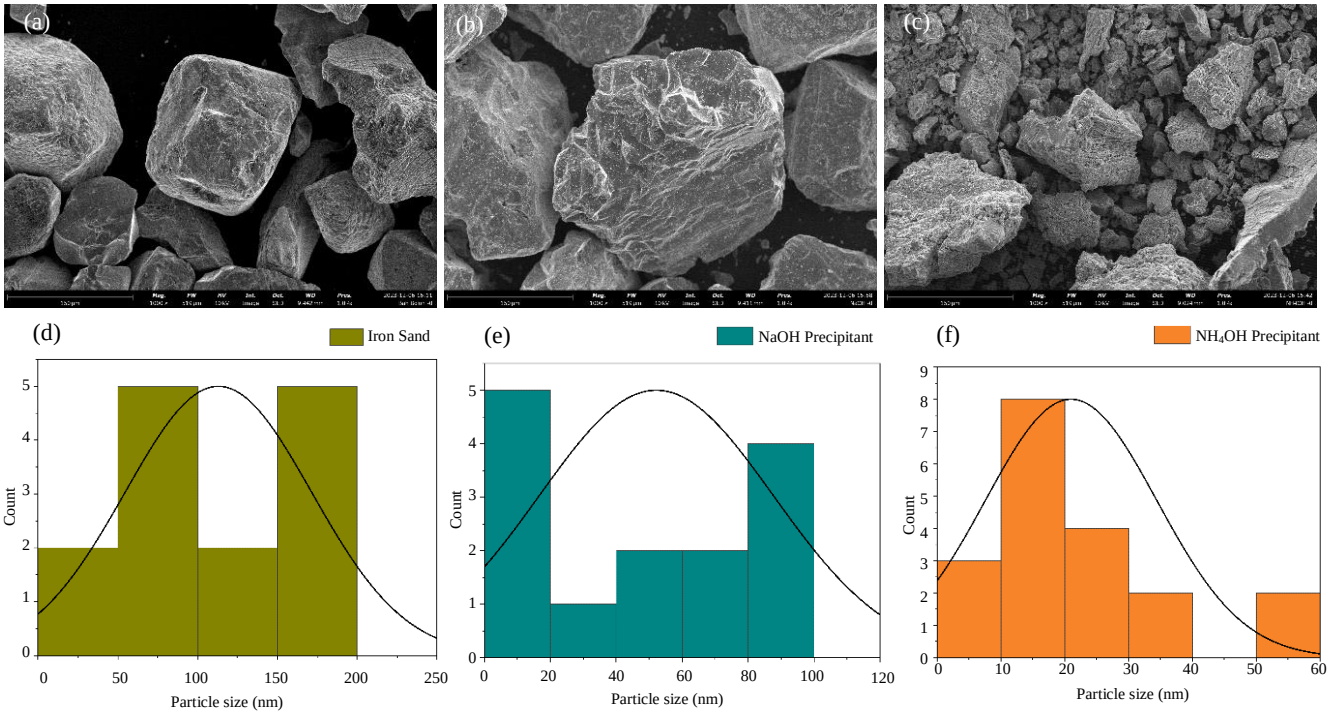

Figure 1. SEM morphology and particle size distribution of natural iron sand and synthesized magnetite nanoparticles (1,000x magnification). SEM images of (a) raw iron sand; (b) iron sand synthesized with NaOH; (c) iron sand synthesized with NH4OH. Histogram of particle size distribution for (d) raw iron sand; predominantly ranging from 100-150 nm; (e) iron sand synthesized with NaOH, with a distribution of 40-80 nm; and (f) iron sand synthesized with NH4OH, exhibiting a narrower range of 20-40 nm.

in slower nucleation and growth, as well as limited particle size. NH_4OH releases ammonia gas during synthesis, which may promote the formation of microvoids within the particles, leading to a porous structure. Although nanoparticle agglomeration is often expected due to high surface energy and particle instability, the SEM images do not show pronounced agglomeration (Figure 1(b) and Figure 1(c)). This may be due to the stabilizing effect of NH_4OH, which supports the formation of dispersed nanoparticles with lower surface energy, reducing visible aggregation despite theoretical tendencies.

Using Image-J and OriginLab software for particle size analysis (Figure 1(d-f)), the average particle size of the iron sand before synthesis was approximately 122 nm. After synthesis, particle size decreased to around 53 nm and 20 nm with NaOH and NH_4OH as precipitants, respectively. NH_4OH yielded smaller particle sizes, attributed to the more acidic reaction environment, which accelerates nanoparticle formation (Mardana et al., 2023). The synthesized particles are larger than those from synthetic precursors namely iron chloride hexahydrate but remain within the nanoscale range, supporting classification as nanoparticles.

EDX analysis was used to examine the elemental composition of the iron sand before and after synthesis into magnetite nanoparticles (Figure 2) (Taufiq et al., 2020). In the natural state, the iron sand sourced from the Bah Bolon River contained 34.76% iron (Fe) and 58.30% oxygen (O), along with trace elements, namely aluminum (Al), silicon (Si), and titanium (Ti), possibly derived from geological and sedimentary processes within the river environment. After synthesis, the Fe content increased to 40.76% and 45.50% with NaOH and NH_4OH as precipitants respectively. This increase indicates successful conversion to magnetite, with NH_4OH demonstrating higher efficiency in promoting Fe incorporation.

The elevated Fe content post-synthesis is consistent with previous studies on natural iron sand sources, which also report increased Fe percentage after processing. Amiruddin and Prayitno (2019) reported a Fe content of 55.33% in iron sand synthesized from Kata Pariaman Beach using the ball milling method. Prasetyowati et al. (2021) observed Fe content up to 60.96% for coastal sand-based magnetite from Kulon Progo Beach. Although the Fe content of magnetite synthesized from Bah Bolon River iron sand is slightly lower than in studies using coastal sources, it still falls within an acceptable range for natural sources, confirming the suitability of river sand for nanoparticle production.

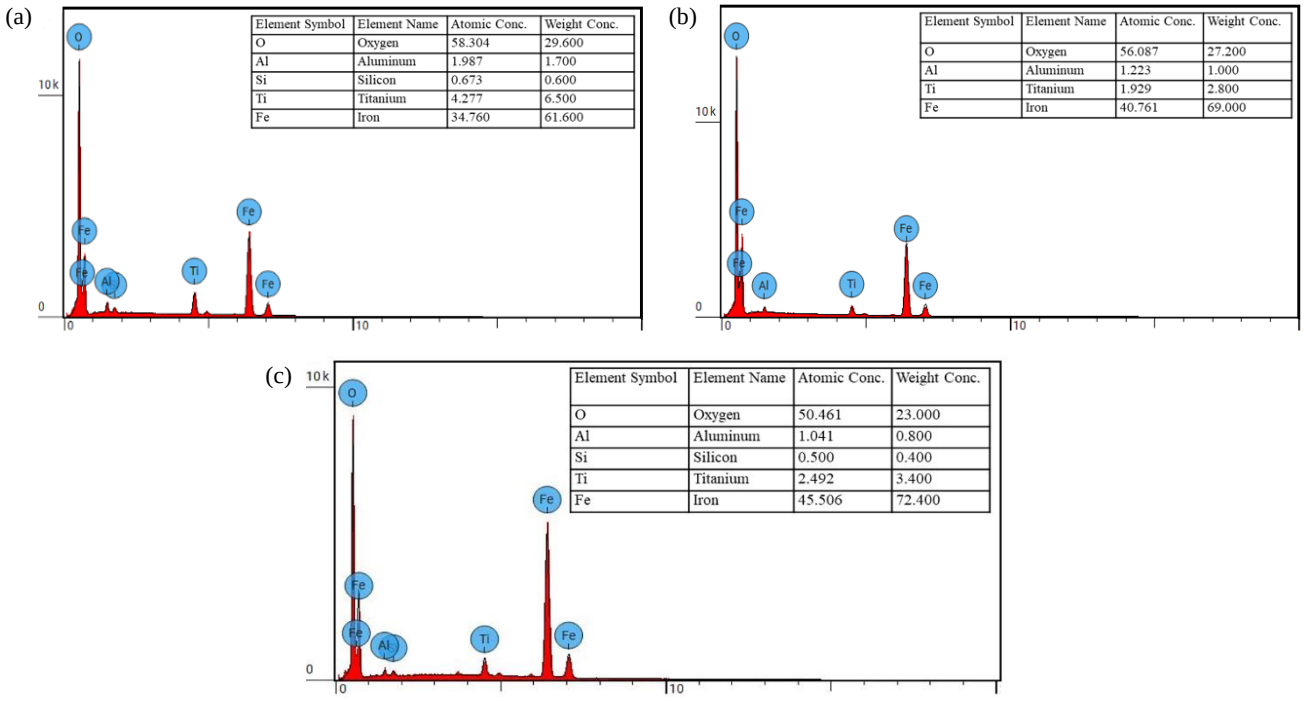

Figure 2. EDX analysis of natural iron sand and synthesized magnetite nanoparticles, displaying elemental composition changes. EDX spectrum of (a) raw iron sand; (b) iron sand synthesized with NaOH; and (c) iron sand synthesized with NH_4OH.

The coprecipitation process used in this study enhanced the Fe content of the final magnetite nanoparticles by facilitating the deposition of ions into a stable Fe_3O_4 crystal structure. The natural iron sand serves as the primary Fe source, containing various iron oxides and other minerals. During the synthesis process, Fe ions are first extracted from the iron sand matrix through dissolution in HCl, which breaks down the mineral structure and releases the ions into solution. The selection of precipitant (NaOH or NH_4OH) plays a critical role. After the addition, the precipitant raises the pH of the acidic Fe ion solution, inducing controlled nucleation and growth of Fe_3O_4 particles through coprecipitation.

In particular, the use of NH_4OH as the precipitant led to a higher Fe content in the nanoparticles compared to NaOH. This effect can be attributed to the greater reactivity and buffering capacity of NH_4OH, which stabilizes the pH more effectively and allows for a more controlled and complete reaction between Fe ions and OH^- ions. Therefore, NH_4OH promotes a faster and more efficient precipitation process, leading to higher Fe incorporation in the magnetite structure. The resulting Fe_3O_4 nanoparticles had a higher Fe density due to the compact magnetite structure formed during precipitation, leading to an increased Fe content compared to the initial iron sand material. Additionally, NH_4OH buffering properties helped limit excessive particle growth, resulting in smaller and more uniform Fe_3O_4 nanoparticles. This controlled environment minimized the presence of other mineral impurities from the iron sand, producing a purer Fe_3O_4 phase with higher Fe content. NH_4OH demonstrated greater efficacy in synthesizing magnetite nanoparticles from natural iron sand by enhancing Fe incorporation, accelerating reaction rates, and producing smaller, more uniformly dispersed particles.

3.2 X-Ray diffraction (XRD) analysis

X-ray diffraction (XRD) analysis provided insight into the crystalline phases, crystallite size, and lattice strain in both the initial iron sand sample and the synthesized magnetite nanoparticles. In this analysis, diffraction peaks were formed from the interaction of X-rays with specific crystal planes within the material, which are identified by the Miller indices (Hamid et al., 2023). Figure 3 shows the diffraction peaks corresponding to the Miller indices. Both the raw iron sand and the synthesized samples showed diffraction peaks corresponding to the Fe_3O_4 (magnetite) phase, suggesting that the material is polycrystalline. Distinct peaks for the magnetite phase appear at (220), (311), (400), (422), (511), and (440) reflections, consistent with the face-centered cubic (FCC) crystal structure in the Fd-3m space group, often referred to as the spinel structure (Sinaga et al., 2023). This phase identification is consistent with the standard reference JCPDS Card No. 19-0629 (Girardet et al., 2022). Additionally, the raw iron sand contains extra peaks corresponding to SiO_2 and α-FeOOH (goethite) phases, identified with Miller indices (111), as per JCPDS Cards No. 46-1045 and No. 29-0713. The presence of SiO_2 is in line with the natural impurities commonly found in iron sands from river sources.

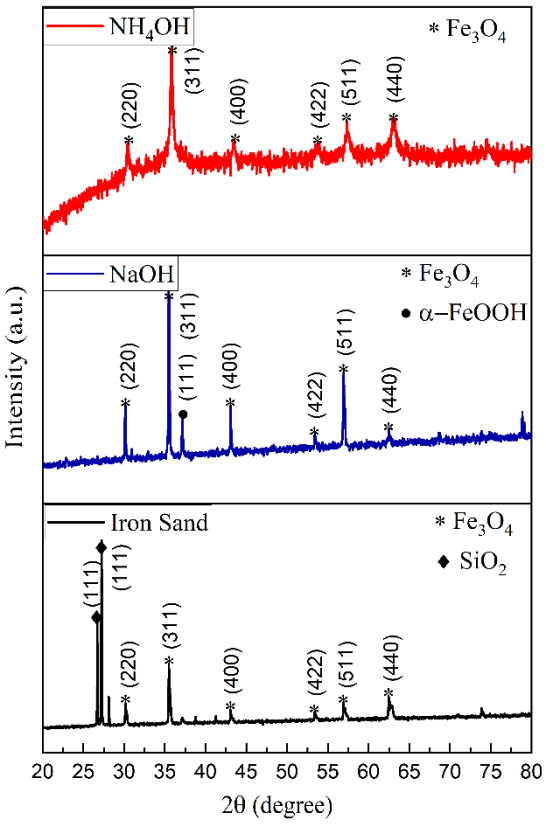

Figure 3. XRD diffraction patterns of natural iron sand and synthesized magnetite nanoparticles. XRD spectra show diffraction peaks corresponding to Fe_3O_4 for both the raw and synthesized samples, indicating a polycrystalline magnetite structure.

For samples synthesized through the coprecipitation method, the XRD pattern for the NaOH-synthesized nanoparticles showed distinct peaks of magnetite along with minor peaks associated with goethite (α-FeOOH). The presence of goethite in this sample suggests that NaOH does not fully reduce

iron compounds to the magnetite phase under the synthesis conditions used, potentially leaving behind residual iron oxide impurities. This partial reduction could be attributed to the lower reactivity of NaOH compared to NH_4OH, which might result in a less efficient transformation process. In contrast, the NH_4OH-synthesized sample showed only magnetite peaks, indicating a higher phase purity. This phase purity can be beneficial in applications requiring high magnetic purity, as it minimizes interference from non-magnetic phases including goethite.

The (311) reflection showed the highest peak intensity across all samples, which becomes more pronounced after synthesis. This indicates an alignment preference along the (311) lattice plane in the synthesized magnetite nanoparticles. The diffraction peaks of the NaOH-synthesized nanoparticles are sharper and narrower than those of the NH_4OH-synthesized ones, implying a higher degree of crystallinity and structural regularity in the NaOH sample (Jain et al., 2022). Table 1 shows a comparison of crystallinity percentages and average crystallite sizes for each sample.

Table 1. Comparison of crystallinity and crystal size of each sample

Sample	Crystallinity (%)	Crystallite size (nm)
Iron sand	74.54	90.608
NaOH precipitant	48.94	80.194
NH_4OH precipitant	40.53	15.124

The crystallite size was calculated using the Scherrer formula (Equation 1). The size values obtained were approximately 80.194 nm and 15.124 nm for the sample synthesized using NaOH and NH_4OH respectively. This distinction in crystallite size reflects the influence of precipitant choice on crystal growth, with NH_4OH favoring smaller crystallite formation, possibly due to a more controlled reaction environment. Importantly, this measurement pertains to the average crystallite size rather than the particle, as calculated using the Scherrer equation (Abdel-Mohsen et al., 2022). Crystallite size represents the coherent diffraction domain, which may differ from particle size when particles consist of multiple crystallites.

According to SEM analysis, the average particle sizes are larger than the XRD-determined crystallite sizes, indicating that the nanoparticles may be polycrystalline, consisting of multiple crystallites within a single particle. This observation is especially relevant for magnetite nanoparticles synthesized with NaOH, which show larger crystallite sizes. Polycrystalline particles can impact magnetic properties by reducing the superparamagnetic behavior typically observed in single-crystalline nanoparticles at smaller scales. This suggests that NH_4OH-synthesized nanoparticles, with smaller crystallites and potentially single-domain structures, might show more favorable magnetic properties, such as enhanced superparamagnetic behavior and higher magnetic saturation.

The crystallinity of each sample was analyzed based on the intensity and sharpness of the XRD peaks. The NH_4OH-synthesized sample showed broader peaks, particularly in the (311) reflection, which implies a smaller crystallite size but also may indicate higher lattice strain. This refers to distortions within the crystal lattice, which can be quantified by analyzing peak broadening. In nanostructured materials, lattice strain is often associated with surface defects and structural irregularities that arise during the synthesis process.

Lattice strain can have significant implications for the physical properties of magnetite nanoparticles. To further understand the lattice strain, the Williamson-Hall method was used. Lattice strain, which signifies deformation within the crystal lattice, can arise due to defects, stress, or other imperfections. The Williamson-Hall plot, where $4 \sin\theta$ is plotted against $\beta \cos\theta$, was used to estimate strain (Patel et al., 2024). The lattice strain values calculated were 0.00363 for raw iron sand, 0.0000469 for NaOH-synthesized, and 0.000576 for NH_4OH-synthesized nanoparticles (Figure 4). The positive strain values across samples indicate tensile strain within the lattice. The reduction in lattice strain post-synthesis implies a relaxation in structural tension as the raw iron sand transforms into magnetite nanoparticles. However, the NH_4OH-synthesized sample shows a slightly higher tensile strain than the NaOH-synthesized sample, indicating that NH_4OH promotes a degree of structural

strain, possibly due to rapid nanoparticle formation under more acidic conditions.

Higher lattice strain in the NH_4OH-synthesized sample may enhance surface reactivity and catalytic activity, which is advantageous for applications in environmental remediation and biomedical fields where surface interactions are crucial. It also significantly impacts the material mechanical and magnetic properties by increasing stored energy, which can affect mechanical strength, elasticity, and plastic deformation. Additionally, lattice strain introduces localized magnetic anisotropies within the nanoparticles, potentially enhancing the performance in magnetic hyperthermia applications where controlled heating is essential. Strain can further influence properties such as coercivity, magnetoresistance, and atomic diffusion rates, which in turn impact chemical reactivity. Therefore, the choice of precipitant not only affects crystallite size but also plays a key role in determining the structural and functional characteristics of the synthesized nanoparticles.

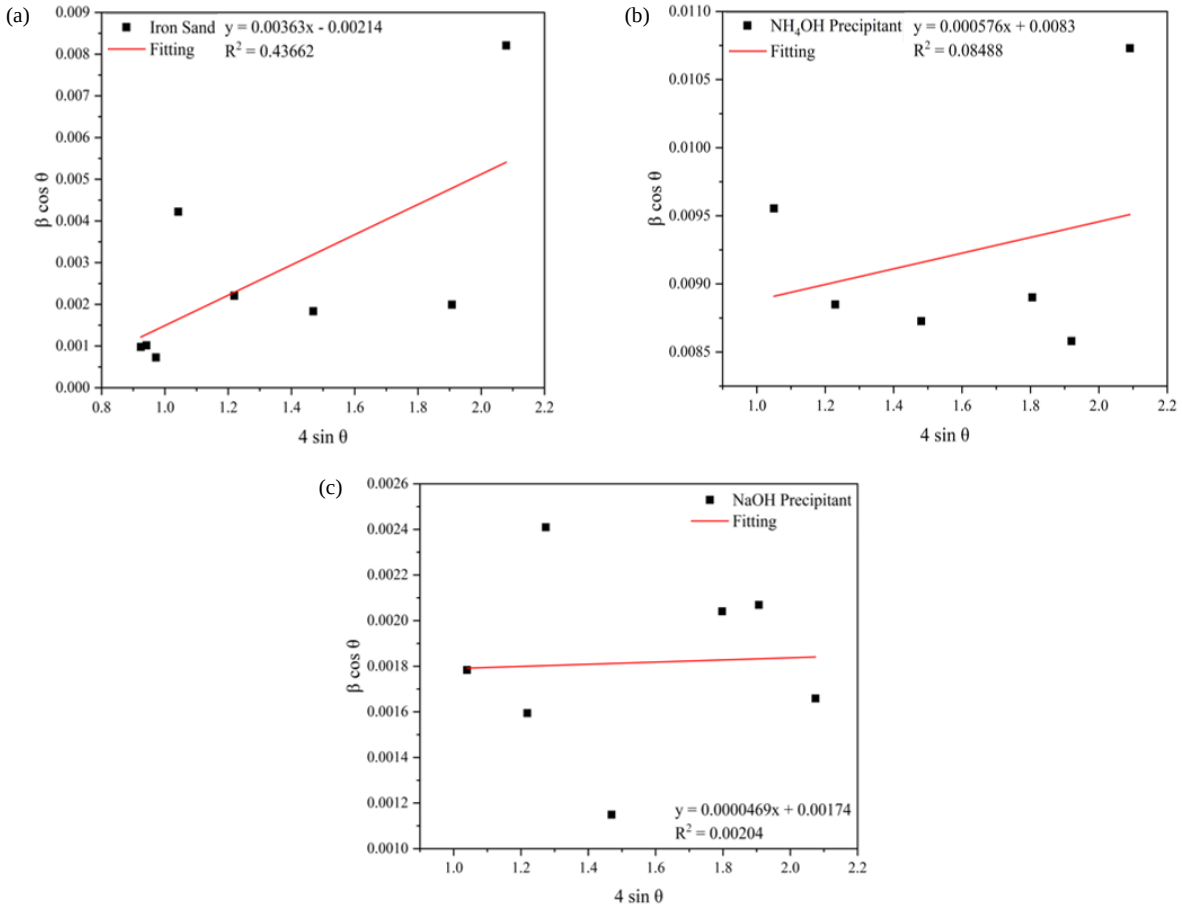

Figure 4. W-H Plot (Williamson-Hall Plot) for estimating lattice strain of natural iron sand and synthesized magnetite nanoparticles. Raw iron sand (a) exhibits the hightest strain due to impurities and distortions. NH_4OH-synthesized magnetite (b) shows reduced strain; while NaOH-synthesized magnetite (c) has the lowest strain. All samples display positive lattice strain, indicating tensile strain within the crystal lattice.

4. CONCLUSION

In conclusion, the successful synthesis of magnetite nanoparticles from natural iron sand was achieved through the coprecipitation method using two distinct precipitants, namely NaOH and NH_4OH. The results showed that the choice of precipitant significantly impacted the shape and size of the resulting magnetite nanoparticles. NH_4OH precipitant demonstrated higher performance in synthesizing magnetite nanoparticles from natural iron sand compared to NaOH, as evidenced by an increase in Fe content, accelerated reaction kinetics, and production of smaller particle sizes. Moreover, the NH_4OH precipitant yielded purer magnetite nanoparticles with a more regular crystal structure and higher crystallinity relative to NaOH. Iron sand samples synthesized with NH_4OH precipitant also showed a higher level of tensile strain. The selection of

precipitants in the synthesis process of magnetite nanoparticles from natural iron sand significantly influenced the crystal structure, lattice strain, and elemental composition.

ACKNOWLEDGEMENTS

The authors are grateful to the Postgraduate Program of Physics, FMIPA, Universitas Sumatera Utara, Indonesia, and the Department of Physics, FMIPA, Universitas Sumatera Utara, Indonesia for the support and encouragement to complete this project through the facilities provided and PMDSU Program Batch VII Year of 2023.

REFERENCES

Abdel-Mohsen LH, Lafta SH, Hashim MS. Comparing the role of NaOH and NH_4OH on structural and magnetic properties of spinel ba ferrite synthesized by autocombustion method. Journal of Physics: Conference Series 2022;2322:Article No. 012081.

Al-Salih M, Samsudin S, Arshad SS. Synthesis and characterizations iron oxide carbon nanotubes nanocomposite by laser ablation for anti-microbial applications. Journal of Genetic Engineering and Biotechnology 2021;19(1):Article No. 76.

Alkallas FH, Alghamdi SM, Rashed EA, Trabelsi ABG, Nafee SS, Elsharkawy WB, et al. Nanocomposite Fe_3O_4-MWCNTs based on femtosecond pulsed laser ablation for catalytic degradation. Diamond and Related Materials 2023;140(PA):Article No. 110445.

Amiruddin E, Prayitno A. The synthesis of magnetic nanoparticles from naturaliron sand of Kata Beach Pariaman West Sumatera using ball milling method as environmental material. MATEC Web of Conferences 2019;276:Article No. 06014.

Ba-Abbad MM, Benamour A, Ewis D, Mohammad AW, Mahmoudi E. Synthesis of Fe_3O_4 nanoparticles with different shapes through a co-precipitation method and their application. Journal of the Minerals, Metals and Materials Society 2022;74(9):3531-9.

Calderón Bedoya PA, Botta PM, Bercoff PG, Fanovich MA. Magnetic iron oxides nanoparticles obtained by mechanochemical reactions from different solid precursors. Journal of Alloys and Compounds 2021;860:Article No. 157892

Dadashi S, Poursalehi R, Delavari H. Structural and optical properties of pure iron and iron oxide nanoparticles prepared via pulsed Nd:YAG laser ablation in liquid. Procedia Materials Science 2015;11:722-6.

Díez AG, Rincón-Iglesias M, Lanceros-Méndez S, Reguera J, Lizundia E. Multicomponent magnetic nanoparticle engineering: The role of structure-property relationship in advanced applications. Materials Today Chemistry 2022;26: Article No. 101220.

Elaoud A, Mechi A, Tlili H, Ferhi M, Hassen H Ben. Green synthesis and characterization of magnetite nanoparticles using eucalyptus globulus leaves for water treatment and agronomic valorization. Environmental Monitoring and Assessment 2024;196(9):Article No. 786.

Fatimah S, Juharni J, Wahyuni ASH. Green synthesis of Fe_3O_4 nanoparticles based on natural sand as methylene blue degradation by electrocoagulation method. Positron 2023;13(1):86-94.

Girardet T, Venturini P, Martinez H, Dupin JC, Cleymand F, Fleutot S. Spinel magnetic iron oxide nanoparticles: Properties, synthesis and washing methods. Applied Sciences 2022;12(16):Article No. 8127.

Gutierrez FV, Lima IS, De Falco A, Ereias BM, Baffa O, Diego de Abreu Lima C, et al. The effect of temperature on the synthesis of magnetite nanoparticles by the coprecipitation method. Heliyon 2024;10(4):e25781.

Hamid M, Rianna M, Rangkuti WR, Sembiring T, Sebayang P. Study and characterization RGO/Fe_3O_4 in microstructure and magnetic properties. South African Journal of Chemical Engineering 2022;42:280-2.

Hamid M, Susilawati, Amaturrahim SA, Dalimunthe IB, Daulay A. Synthesis of magnetic activated carbon-supported cobalt(II) chloride derived from pecan shell (*Aleurites Moluccana*) with co-precipitation method as the electrode in supercapacitors. Materials Science for Energy Technologies 2023;6:429-36.

Hu P, Chang T, Chen WJ, Deng J, Li SL, Zuo YG, et al. Temperature effects on magnetic properties of Fe_3O_4 nanoparticles synthesized by the sol-gel explosion-assisted method. Journal of Alloys and Compounds 2019;773:605-11.

Humaidi S, Hamid M, Wijoyo H. Study and characterization of $BaFe_{12}O_{19}$-PVDF materials prepared by co-precipitation for supercapacitor electrodes applications. Authorea 2023; DOI: 10.22541/au.169887066.61389194/v1.

Jain R, Kumar S, Meena SK. Precipitating agent (NaOH and NH_4OH) dependent magnetic properties of cobalt ferrite nanoparticles. AIP Advances 2022;12:Article No. 095109.

Mardana IBP, Lutfiyah YN, Yasa P, Widiantara GKA. Synthesis and characterization of magnetite Fe_3O_4 nanoparticles from natural iron sand in Gelar River. Indonesian Physical Review 2023;6(1):114-23.

Melinia LA, Puspita E, Naibaho M, Ramlan R, Ginting M. Analysis of natural iron sand from Musi River, South Sumatra. Journal of Scientific Research 2022;24(3):Article No. 122.

Mustapha S, Ndamitso MM, Abdulkareem AS, Tijani JO, Shuaib DT, Mohammed AK, et al. Comparative study of crystallite size using williamson-hall and debye-scherrer plots for ZnO nanoparticles. Advances in Natural Sciences: Nanoscience and Nanotechnology 2019;10(4):Article No. 045013.

Nguyen MD, Tran H-V, Xu S, Lee TR. Fe_3O_4 nanoparticles : structures, synthesis, magnetic properties, surface functionalization, and emerging applications. Applied Sciences 2021;11:Article No. 11301.

Novita N, Naibaho M, Puspita E, Ramlan R, Ginting M, Humaidi S. Analysis of mineral content and magnetic properties of iron sand of Bah Bolon Simalungun River, North Sumetera. Asian Journal of Engineering, Social and Health 2023;2(12):1633-9.

Novita, Ramlan, Naibaho M, Ginting M, Humaidi S, Duma TN. Fe_2O_3 review: Nanostructure, synthesis methods, and applications. International Journal of Social Service and Research 2024;04(02):539-59.

Parvathy Namboothiri PM, Vasundhara M. Synthesis and characterization of nano-hematite. Materials Today: Proceedings 2023;92:1459-63.

Patel K, Patel A, Jethwa VP, Patel H, Solanki GK. X-Ray diffraction analysis of orthorhombic SnSe nanoparticles by

Williamson-Hall, Halder-Wagner and Size-Strain plot methods. Chemical Physics Impact 2024;8:Article No. 100547.

Polla MB, Nicolini JL, Venturini J, da Cas Viegas A, Zen Vasconcellos MA, Montedo ORK, et al. Low-temperature sol-gel synthesis of magnetite superparamagnetic nanoparticles: influence of heat treatment and citrate-nitrate equivalence ratio. Ceramics International 2023;49(5):7322-32.

Prasetyowati R, Widiawati D, Swastika PE, Ariswan A, Warsono W. Synthesis and characterization of magnetite (Fe_3O_4) nanoparticles based on iron sands at Glagah Beach Kulon Progo with coprecipitation methods at various NH_4OH concentrations. Journal of Basic Science 2021;10(2):57-61.

Rianna M, Hamid M, Handayani F, Sebayang AMS, Rangkuti WR, Situmorang M, et al. Study and characterization of Fe_3O_4 synthesized from natural iron sand in Sumatera Utara. Journal of Aceh Physics Society 2022;11(2):45-8.

Sinaga JEE, Budianto G, Pritama VL, Suhendra. Particle Size and Lattice Strain Effect on the Optical Constants of Fe_3O_4 Nanoparticles. Indonesian Physical Review 2023;6(1):114-23.

Taufiq A, Nikmah A, Hidayat A, Sunaryono S, Mufti N, Hidayat N, et al. Synthesis of magnetite/silica nanocomposites from natural sand to create a drug delivery vehicle. Heliyon 2020;6(4):e03784.

Tlili H, Elaoud A, Asses N, Horchani-naifer K, Ferhi M, Goya GF, et al. Reduction of oxidizable pollutants in waste water from the Wadi El Bey River Basin using magnetic nanoparticles as removal agents. Magnetoche 2023;9(6):Article No. 157.

Tukan DN, Rosmainar L, Kustomo K, Rasidah R. A review: optimum conditions for magnetite synthesis (Fe_3O_4). Journal of Scientific Periodicals of Science and Applied Chemistry 2023;17(2):Article No. 15.

Wang W, Li F, Li S, Hu Y, Xu M, Zhang Y, et al. M2 macrophage-targeted iron oxide nanoparticles for magnetic resonance image-guided magnetic hyperthermia therapy. Journal of Materials Science and Technology 2021;81:77-87.

Yuwanda AN, Rahmayuni R, Visgun DA, Rahmi A, Rifai H, Dwiridal L. Characterization of magnetic minerals of iron sand Pasia Nan Tigo Padang Beach using X-Ray diffraction (XRD). Indonesian Journal of Applied Physics 2022;12(1):35-47.

Zhang W, Zhang Z, Lou S, Chang Z, Wen B, Zhang T. Hyaluronic acid-stabilized Fe_3O_4 nanoparticles for promoting In vivo magnetic resonance imaging of tumors. Frontiers in Pharmacology 2022;13:Article No. 918819.

INSTRUCTION FOR AUTHORS

Publication and Peer-reviewing processes of Environment and Natural Resources Journal

Environment and Natural Resources Journal is a peer reviewed and open access journal that is published in six issues per year. Manuscripts should be submitted online at https://ph02.tci-thaijo.org/index.php/ennrj/about/submissions by registering and logging into this website. Submitted manuscripts should not have been published previously, nor be under consideration for publication elsewhere (except conference proceedings papers). A guide for authors and relevant information for the submission of manuscripts are provided in this section and also online at: https://ph02.tci-thaijo.org/index.php/ennrj/author. All manuscripts are refereed through a **single-blind peer-review** process.

Submitted manuscripts are reviewed by outside experts or editorial board members of **Environment and Natural Resources Journal**. This journal uses double-blind review, which means that both the reviewer and author identities are concealed from the reviewers, and vice versa, throughout the review process. Steps in the process are as follows:

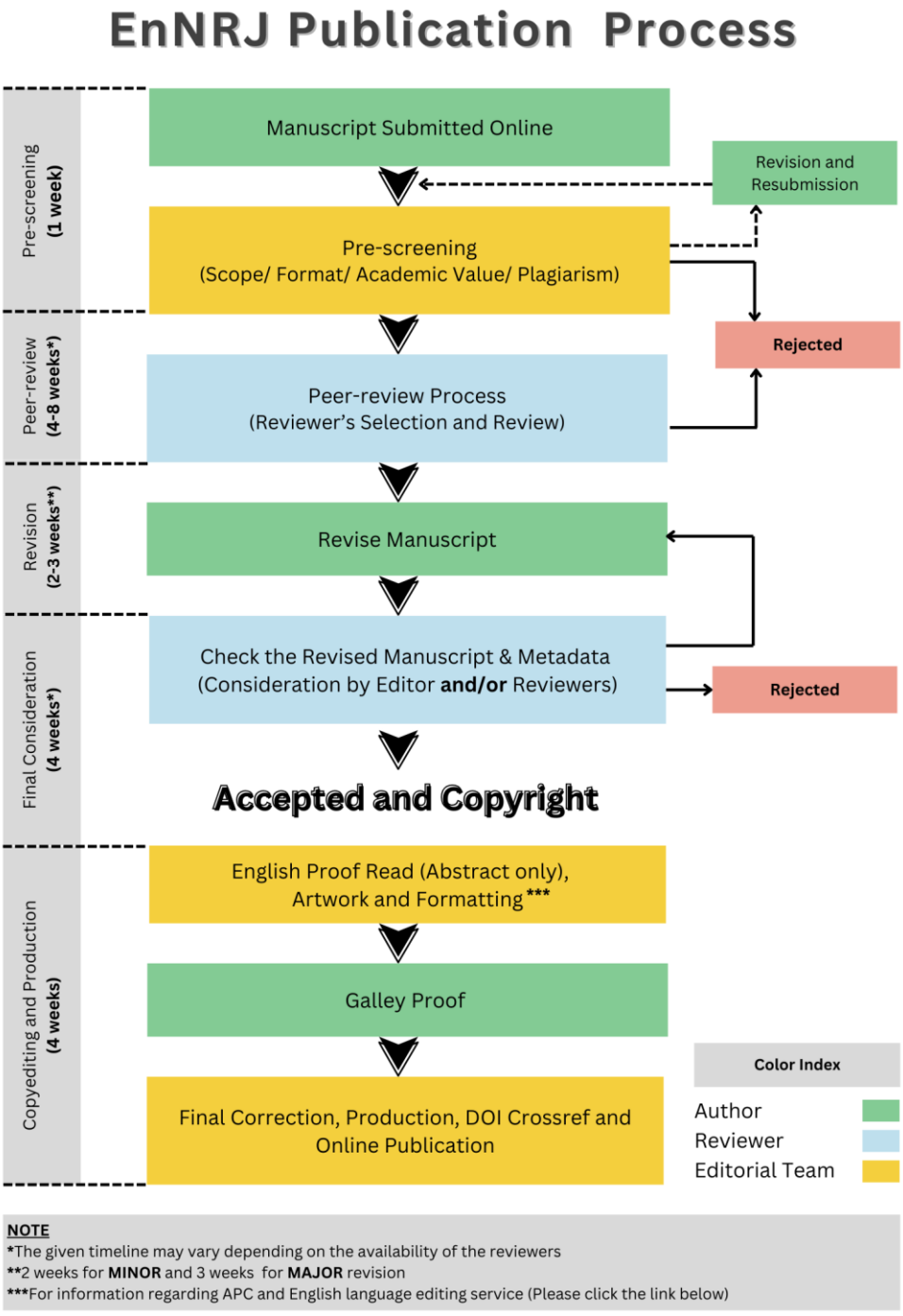

The Environment and Natural Resources Journal (EnNRJ) considers and accepts two types of articles for publication as follows:

- *Original Research Article*: This is the most common type of article. It showcases new, innovative or unique findings surrounding a focused research question. Manuscripts should not exceed 4,000 words (excluding references) - see more details in the Preparation of Manuscript section below.
- *Review Article (by invitation)*: This type of article focuses on the in-depth critical review of a special aspect of an environmental-related research question, issue, or topic. It provides a synthesis and critical evaluation of the state of the knowledge of the subject. Manuscripts should not exceed 6,000 words (excluding references).

Submission of Manuscript

The items that the author needs to upload for the submission are as follows:

Manuscript: The manuscript must be submitted as a Microsoft Word file (.doc or .docx). Refer to the **Preparation of Manuscript** section below for detailed formatting instructions.

Cover Letter: The letter should address the Editor and include the following: a statement declaring that the author's paper has not been previously published and is not currently under consideration by another journal.

- a brief description of the research the author reports in the paper, including why the findings are important and why the journal readers should be interested
- contact information of the author and any co-authors
- a confirmation that the author has no competing interests to disclose

Graphical Abstract (Optional): The author is encouraged to submit a graphical abstract with the manuscript. The graphical abstract depicts the research and findings with visuals. It attracts more potential readers as it lets them understand the overall picture of the article within a few glances. Note that the graphical abstract must be original and unpublished artwork. It should be a high-quality illustration or diagram in any of the following formats: TIFF, PDF, JPEG, or PNG. The minimum required size is 750 × 750 pixels (height × width). The size should be of high quality (600 dpi or larger) in order to reproduce well.

Reviewers Suggestion (mandatory): Please provide the names of three potential reviewers, with information about their affiliations as well as their email addresses. The recommended reviewers should not have any conflict of interest with the authors. Each reviewer must represent a different affiliation and not have the same nationality as the author. Please note that the editorial board retains the sole right to decide whether or not the recommended reviewers will be selected.

Declaration of Competing Interest: The author must include a declaration of competing interest form during submission. If there is no conflict of interest, please state, "The authors declare no conflict of interest." Otherwise, authors should declare all interests to avoid inappropriate influence or bias in their published work. Examples of potential conflicts of interest in research projects include but are not limited to financial interests (such as employment, consultancies, grants, and other funding) and non-financial interests (such as personal or professional relationships, affiliations, and personal beliefs).

CrediT (Contributor Roles Taxonomy) Author Statement or Author Contributions: For research articles with several authors, we require corresponding authors to provide co-author contributions to the manuscript using the relevant CRediT roles. CRediT is a taxonomy that shows the contributions of the author and co-author(s), reduces possible authorship disputes, and facilitates collaboration among research team members. The CRediT taxonomy includes 14 different roles describing each contributor's specific contribution to the scholarly output.

The roles are: Conceptualization; Data curation; Formal analysis; Funding acquisition; Investigation; Methodology; Project administration; Resources; Software; Supervision; Validation; Visualization; Roles/Writing – original draft; and Writing – review & editing.

Note that authors may have contributed through multiple roles, and those who contributed to the research work but do not qualify for authorship should be listed in the acknowledgments.

An example of a CRediT author statement is given below:
"Conceptualization, X.X. and Y.Y.; Methodology, X.X.; Software, X.X.; Validation, X.X., Y.Y. and Z.Z.; Formal Analysis, X.X.; Investigation, X.X.; Resources, X.X.; Data Curation, X.X.; Writing – Original Draft Preparation, X.X.; Writing – Review & Editing, X.X.; Visualization, X.X.; Supervision, X.X.; Project Administration, X.X.; Funding Acquisition, Y.Y."

Artwork for the Journal Cover: The author may provide and propose a piece of artwork (with a description) for the journal issue cover. This is an excellent opportunity for the author to promote their article, if accepted, on the cover of a published issue. Alternatively, the editorial team may invite the author to submit a piece of artwork for the cover after their manuscript has been accepted for publication. The final cover artwork selection will be made by the editorial team.

Final Author Checks: In addition to the basic requirements, the author should review this checklist before submitting their manuscript. Following it ensures the manuscript is complete and in accordance with all standards.

Preparation of Manuscript

Format and Style

The manuscript should be prepared strictly as per the guidelines given below. Any manuscript with an incorrect format will be returned, and the corresponding author may have to resubmit a new manuscript with the correct format.

Overall Format

The manuscript must be submitted as a Microsoft Word file (.doc or .docx). The formatting should be as follows:

- File format - .doc or .docx
- Page size - A4
- Page orientation - portrait (some landscape pages are accepted if necessary)
- Page margin - 2.54 cm (left and the right margin) and 1.9 cm (bottom and the top margin)
- Page number (bottom of the page)
- Line number
- Line spacing - 1.5
- Font - 12 point, Times New Roman (unless stated otherwise)

Unit - The use of abbreviation must follow the International System of Units (SI Unit) format.

- The unit separator is a virgule (/) and not a negative coefficient: 10 mg/L not 10 mgL^{-1}
- Liter always has a capital letter: mg/L

Equations

- Insert equations using the dedicated tool in Microsoft Word. Do not use pictures or text boxes.
- Equations that are referenced in the text should be identified by parenthetical numbers, such as (1), and should be referred to in the manuscript as “Equation 1”.

Inclusive Language: The language used in the manuscript acknowledges diversity, promotes equal opportunity, respects all people, and is sensitive to all aspects of differences. The manuscript content should not make assumptions about the beliefs or commitments of any individual. It should not imply superiority regarding age, race, ethnicity, culture, gender, sexual orientation, disability, or health conditions. Moreover, the manuscript must be free from bias, stereotypes, slang, and derogatory terms.

Reference Style: Vancouver style should be used for the reference list and in-text citations throughout the manuscript. Please follow the format of the sample references and citations, as shown in the Body Text Sections portion below.

Front Page

Title: The title of the manuscript should be concise and not longer than necessary. The title should be bold, 12-point size, and Times New Roman. The first letter of major words should be capitalized (as in standard title case).

Author(s) Name: The first and last names of all authors must be given, in bold, Times New Roman, and 12-point font.

Affiliation of All Author(s): Affiliation(s) must be in italics, Times New Roman, and 11-point font. Specify the Department/School/Faculty, University, City/Province/or State, and Country of each affiliation. Do not include positions or fellowships, or postal zip codes.
Each affiliation should be indicated with superscript Arabic numerals. The Arabic numeral(s) should appear immediately after the author’s name, and represent the respective affiliation(s).

Corresponding Author: One author should be responsible for correspondence, and their name must be identified in the author list using an asterisk (*).

- All correspondence with the journal, including article submission and status updates, must be handled by the corresponding author.

- The online submission and all associated processes should be operated by the corresponding author.

*Corresponding author: followed by the corresponding author's email address.

Example:

Papitchaya Chookaew[1], Apiradee Sukmilin[2], and Chalor Jarusutthirak[1*]
[1]Department of Environmental Technology and Management, Faculty of Environment, Kasetsart University, Bangkok, Thailand
[2]Environmental Science and Technology Program, Faculty of Science and Technology, Phranakhon Rajabhat University, Bangkok, Thailand
**Corresponding author: abcxx@xx.ac.th*

Abstract Page

Abstract: The abstract should include the significant findings paired with relevant data. A good abstract is presented in one paragraph and is limited to 250 words. Do not include a table, figure, or references.
Keywords - Up to six keywords are allowed, and they should adequately index the subject matter.

Highlights: Please include 3-5 concise sentences describing innovative methods and the findings of the study. Each sentence should contain at most 85 characters (not words).

Body Text Sections
The main body text of the manuscript normally includes the following sections: 1. Introduction 2. Methodology 3. Results and Discussion 4. Conclusions 5. Acknowledgments 6. Author Contributions 7. Declaration of Competing Interests 8. References

Introduction should include the aims of the study. It should be as concise as possible, with no subheadings. The significance of the problem and the essential background should also be given.

Methodology is sufficiently detailed so that the experiments can be reproduced. The techniques and methods adopted should be supported with standard references.
There should be no more than three levels of headings in the **Methodology and Results and Discussion** sections. Main headings are in bold letters, second-level headings are in bold and italic letters, and third-level headings are in normal letters.

Here is an example:

2. Methodology
2.1 Sub-heading
2.1.1 Sub-sub-heading

Results presents the key findings in figures and tables with descriptive explanations in the text.

Tables
- Tables - look best if all the cells are not bordered; place horizontal borders only under the legend, the column headings, and the bottom.

Figures
- Figures - should be submitted in color. The author must ensure that the figures are clear and understandable. Regardless of the application used to create them, when electronic artworks are finalized, please 'save as' or convert the images to TIFF or JPG and send them separately to EnNRJ. Images require a resolution of at least 600 dpi (dots per inch) for publication. The labels of the figures and tables must be Times New Roman, and their size should be adjusted to fit the figures without borderlines.
- Graph - The font style in all graphs must be Times New Roman, 9-10 size, and black color. Please avoid bold formatting, and set the border width of the graphs to 0.75 pt.

- Graph from MS Excel: Please attach an editable graph from MS Excel within your manuscript. Then please also submit the full MS Excel file used to prepare the graph as a separate document. This helps us customize our layout for aesthetic beauty.
- Graph from another program: Feel free to use whichever program best suits your needs. But as noted above, when your artwork is finalized, please convert the image to TIFF or JPG and send them separately Again, images should be at least 600 dpi. Do not directly cut and paste.

***All figures and tables should be embedded in the text, and also mentioned in the text.**

Discussion shows the interpretation of findings with supporting theory and comparisons to other studies. The Results and Discussion sections can be either separated, or combined. If combined, the section should be named Results and Discussion. **Conclusions** should include a summary of the key findings and take-home messages. This should not be too long, or repetitive but this section is absolutely necessary so that the argument of the manuscript is not uncertain or left unfinished.

Acknowledgments should include the names of those who contributed substantially to the work, but do not fulfill the requirements for authorship. It should also include any sponsor or funding agency that supported the work.

Author Contributions: For research articles with several authors, we require corresponding author contributions listed using the relevant CRediT roles. This should be done by the author responsible for correspondence.

Declaration of Competing Interest: The author must include a declaration of competing interest form during submission. If there is no conflict of interest, please state, "The authors declare no conflict of interest." Otherwise, authors should declare all interests to avoid inappropriate influence or bias in their published work.

References should be cited in the text by the surname of the author(s) and the year. This journal uses the author-date method of citation. The author's last name and date of publication are inserted in the text in the appropriate place. If there are more than two authors, “et al.” must be added after the first author’s name. Examples: (Frits, 1976; Pandey and Shukla, 2003; Kungsuwas et al., 1996). If the author’s name is part of the sentence, only the date is placed in parentheses: “Frits (1976) argued that . . .”

Please ensure that every reference cited in the text is also in the reference list (and vice versa).

In the list at the end of the manuscript, complete references must be arranged alphabetically by the surnames of the first author in each citation. Examples are given below.

Book

Tyree MT, Zimmermann MH. Xylem Structure and the Ascent of Sap. Heidelberg, Germany: Springer; 2002.

Chapter in a book

Kungsuwan A, Ittipong B, Chandrkrachang S. Preservative effect of chitosan on fish products. In: Steven WF, Rao MS, Chandrkachang S, editors. Chitin and Chitosan: Environmental and Friendly and Versatile Biomaterials. Bangkok: Asian Institute of Technology; 1996. p. 193-9.

Journal article

Muenmee S, Chiemchaisri W, Chiemchaisri C. Microbial consortium involving biological methane oxidation in relation to the biodegradation of waste plastics in a solid waste disposal open dump site. International Biodeterioration and Biodegradation 2015;102(3):172-81.

Journal article with Article Number

Sah D. Concentration, source apportionment and human health risk assessment of elements in $PM_{2.5}$ at Agra, India. Urban Climate 2023;49:Article No. 101477.

Non-English articles

Suebsuk P, Pongnumkul A, Leartsudkanung D, Sareewiwatthana P. Predicting factors of lung function among motorcycle taxi drivers in the Bangkok metropolitan area. Journal of Public Health 2014;44(1):79-92 (in Thai).

Article in press

Dhiman V, Kumar A. Biomass and carbon stock estimation through remote sensing and field methods of subtropical Himalayan Forest under threat due to developmental activities. Environment and Natural Resources Journal 2024. DOI: 10.32526/ennrj/22/20240018.

Published in conference proceedings

Wiwattanakantang P, To-im J. Tourist satisfaction on sustainable tourism development, Amphawa floating market Samut Songkhram, Thailand. Proceedings of the 1st Environment and Natural Resources International Conference; 2014 Nov 6-7; The Sukosol hotel, Bangkok: Thailand; 2014.

Ph.D./Master thesis

Shrestha MK. Relative Ungulate Abundance in a Fragmented Landscape: Implications for Tiger Conservation [dissertation]. Saint Paul, University of Minnesota; 2004.

Website

Orzel C. Wind and temperature: why doesn't windy equal hot? [Internet]. 2010 [cited 2016 Jun 20]. Available from: http://scienceblogs.com/principles/2010/08/17/wind-and-temperature-why-doesn/.

Report organization

Intergovernmental Panel on Climate Change (IPCC). IPCC Guidelines for National Greenhouse Gas Inventories: Volume 1-5. Hayama, Japan: Institute for Global Environmental Strategies; 2006.

Royal Gazette

Royal Gazette. Promotion of Marine and Coastal Resources Management Act 2059. Volume 132, Part 21, Dated 26 Mar B.E. 2558. Bangkok, Thailand: Office of the Council of State; 2015a. (in Thai).

Remark

** Please be note that manuscripts should usually contain at least 15 references and some of them must be up-to-date research articles.*

** Please strictly check all references cited in text, they should be added in the list of references. Our Journal does not publish papers with incomplete citations.*

Changes to Authorship

This policy of journal concerns the addition, removal, or rearrangement of author names in the authorship of accepted manuscripts:

Before the accepted manuscript

For all submissions, that request of authorship change during review process should be made to the form below and sent to the Editorial Office of EnNRJ. Approval of the change during revision is at the discretion of the Editor-in-Chief. The form that the corresponding author must fill out includes: (a) the reason for the change in author list and (b) written confirmation from all authors who have been added, removed, or reordered need to confirm that they agree to the change by signing the form. Requests form submitted must be consented by corresponding author only.

After the accepted manuscript

The journal does not accept the change request in all of the addition, removal, or rearrangement of author names in the authorship. Only in exceptional circumstances will the Editor consider the addition, deletion or rearrangement of authors after the manuscript has been accepted.

Copyright transfer

The copyright to the published article is transferred to Environment and Natural Resources Journal (EnNRJ) which is organized by Faculty of Environment and Resource Studies, Mahidol University. The accepted article cannot be published until the Journal Editorial Officer has received the appropriate signed copyright transfer.

Online First Articles

The article will be published online after receipt of the corrected proofs. This is the official first publication citable with the Digital Object Identifier (DOI). After release of the printed version, the paper can also be cited by issue and page numbers. DOI may be used to cite and link to electronic documents. The DOI consists of a unique alpha-numeric character string which is assigned to a document by the publisher upon the initial electronic publication. The assigned DOI never changes.

Mahidol University

Wisdom of the Land

Faculty of Environment and Resource Studies, Mahidol University, Thailand
999 Phutthamonthon Sai 4 Rd, Salaya, Phutthamonthon District, Nakhon Pathom 73170
E-mail: ennrjournal@gmail.com